



HAL
open science

Catalytic application of decatungstate for photodegradation and selective oxidation of organic compounds

Peng Cheng

► **To cite this version:**

Peng Cheng. Catalytic application of decatungstate for photodegradation and selective oxidation of organic compounds. Analytical chemistry. Université Clermont Auvergne, 2021. English. NNT : 2021UCFAC102 . tel-03813711

HAL Id: tel-03813711

<https://theses.hal.science/tel-03813711v1>

Submitted on 13 Oct 2022

HAL is a multi-disciplinary open access archive for the deposit and dissemination of scientific research documents, whether they are published or not. The documents may come from teaching and research institutions in France or abroad, or from public or private research centers.

L'archive ouverte pluridisciplinaire **HAL**, est destinée au dépôt et à la diffusion de documents scientifiques de niveau recherche, publiés ou non, émanant des établissements d'enseignement et de recherche français ou étrangers, des laboratoires publics ou privés.



Catalytic application of decatungstate for photodegradation and selective oxidation of organic compounds

This dissertation is submitted to the
Université Clermont Auvergne

For the degree of doctor of University

By the candidate

Peng CHENG

Faculty: **Fundamental Sciences**

Specialization: **Theoretical, Physical and Analytical chemistry**

Date of Ph.D defense: **17 December 2021**

Composition of the jury:

Rapporteurs: Alessandra Bianco Prevot, Professor at University of Turin, Italy

Feng Wu, Professor at Wuhan University, China

Examiners: Christine Mousty, CNRS Research Director Emeritus, France

Yanlin Wu, Associate Professor at Fudan University, China

Thesis director: Gilles Mailhot, CNRS Research Director, France

Thesis co-director: Mohamed Sarakha, Professor at University Clermont Auvergne, France

Catalytic application of decatungstate for photodegradation and selective oxidation of organic compounds

Abstract:

Decatungstate is a kind of highly efficient catalyst/photocatalyst that is widely used in organic depollution and synthesis. Hence, studying the applications of decatungstate for photodegradation and selective oxidation of organic compounds is of great values and significance. In the first part of this work, the photodegradation of sulfapyridine and sulfasalazine in the presence of sodium decatungstate (NaDT) and H_2O_2 was investigated. The effects of various parameters such as pH, H_2O_2 concentration, NaDT concentration and substrate concentration were studied. In the second part of this work, the photodegradation of sulfapyridine in the presence of sodium decatungstate (NaDT) and Potassium Persulfate (PS) was explored. The different reduced NaDT species produced in photocatalytic process, the reaction of generated reduced NaDT species with PS and the photodegradation of sulfapyridine in the presence of NaDT and PS were also studied. In the third part, the ternary catalytic system (NaDT/ $\text{Fe}_3\text{O}_4/\text{H}_2\text{O}_2$) was constructed to selectively oxidize amine substrates to nitroso compounds. The mechanism of this system was deeply investigated via FTIR, XPS, cyclic voltammetry experiments. The different parameters such as pH, H_2O_2 concentration, NaDT concentration, amount of Fe_3O_4 were studied. Finally, in the fourth part and in order to recycle decatungstate, the water insoluble Tetra-n-butylammonium decatungstate (TBADT) was used. Catalytic complex M-T (Fe_3O_4 -TBADT) was prepared to selectively oxidize amine compounds to nitroso compounds. The different parameters such as pH, H_2O_2 concentration and amount of M-T were deeply studied.

Key words: Decatungstate, Photodegradation, Selective Oxidation, H_2O_2 , Fe_3O_4 , Persulfate

Application catalytique du decatungstate pour la photodégradation et l'oxydation sélective de composés organiques

Résumer:

Le decatungstate est un type de catalyseur/photocatalyseur très efficace qui a été largement utilisé dans la dépollution et la synthèse organique. Par conséquent, l'étude de l'application du decatungstate pour la photodégradation et l'oxydation sélective des composés organiques revêt une grande importance. Dans la première partie de ce travail, la photodégradation de la sulfapyridine et de la sulfasalazine en présence de decatungstate de sodium (NaDT) et de H_2O_2 a été étudiée. Les effets de différents paramètres tels que le pH, la concentration en H_2O_2 , la concentration en NaDT et la concentration en substrat ont été étudiés. Dans la deuxième partie de ce travail, la photodégradation de la sulfapyridine en présence de decatungstate de sodium (NaDT) et de persulfate de potassium (PS) a été explorée. Les différentes espèces réduites de NaDT produites dans le processus photocatalytique, la réaction des espèces réduites de NaDT générées avec le PS et la photodégradation de la sulfapyridine en présence de NaDT et de PS ont également été étudiées. Dans la troisième partie de ce travail, le système catalytique ternaire (NaDT/ Fe_3O_4/H_2O_2) a été mis en place pour oxyder sélectivement les composés aminés en composés nitroso. Le mécanisme de ce système a été étudié en profondeur via des expériences de FTIR, XPS, voltammétrie cyclique. Les différents paramètres tels que le pH, la concentration en H_2O_2 , la concentration en NaDT, la quantité de Fe_3O_4 ont été explorés. Dans la quatrième partie et afin de recycler le decatungstate, le Tetra-n-butylammonium decatungstate (TBADT), insoluble dans l'eau, a été utilisé. Le complexe catalytique M-T (Fe_3O_4 -TBADT) a été préparé pour oxyder sélectivement les composés aminés en composés nitroso. Les différents paramètres tels que le pH, la quantité de H_2O_2 de M-T ont été étudiés.

Mots clés : Decatungstate, Photodégradation, Oxydation sélective, H_2O_2 , Fe_3O_4 , Persulfate

十聚钨酸盐在有机化合物光降解和选择性氧化中的催化应用

摘要:

十聚钨酸盐($W_{10}O_{32}^{4-}$)是一种高效的催化剂/光催化剂,被广泛用于有机物的降解净化和有机合成。因此,十聚钨酸盐在有机化合物的光降解和选择性氧化中的应用具有重要的价值和意义。在这项工作的第一部分,研究了磺胺吡啶和磺胺嘧啶在十聚钨酸钠(Sodium decatungstate, NaDT)和双氧水(H_2O_2)存在下的光降解情况。研究了如 pH 值、 H_2O_2 浓度、NaDT 浓度和底物浓度等各种实验参数对光降解效率的影响。在这项工作的第二部分,探讨了在十聚钨酸钠(NaDT)和过硫酸钾(PS)存在的条件下磺胺吡啶的光降解问题。同时研究了在光催化过程中产生的不同的 NaDT 还原态物种,以及生成的还原态 NaDT 物种与 PS 的氧化还原反应,最后对在 NaDT 和 PS 存在下的磺胺的光降解进行了初步探究。第三部分,构建了三元催化体系(NaDT/ Fe_3O_4 / H_2O_2)来选择性地将胺类底物氧化成亚硝基化合物。通过傅里叶红外吸收光谱(FTIR)、X 射线光电子能谱(XPS)、循环伏安法实验(CV)深入研究了该体系的机理。同时研究了不同的参数,如 pH 值、 H_2O_2 浓度、NaDT 浓度、 Fe_3O_4 的量。最后,在第四部分,为了回收十聚钨酸盐,合成并使用了不溶于水的四正丁基十聚钨酸铵(Tetra-n-butylammonium decatungstate, TBADT)。以该十聚钨酸盐为材料,制备了复合催化剂 M-T (Fe_3O_4 -TBADT),并利用该复合材料选择性氧化胺类化合物以制备亚硝基化合物。系统地研究了不同的参数如 pH 值、 H_2O_2 浓度和 M-T 量等对选择性催化氧化的影响。

关键字: 十聚钨酸盐, 光降解, 选择性氧化, H_2O_2 , Fe_3O_4 , 过硫酸盐

Table of Contents

Chapter 1: Introduction	1
1.1. Background	2
1.2. Objective	4
1.3. Thesis organization	5
References	7
Chapter 2: Bibliographic Study	13
2.1. Photochemistry	14
2.1.1. The law of photochemistry	15
2.1.2. Light-matter interaction	16
2.1.3. Electronic excited state	17
2.1.4. Deactivation of electronic excited state	20
2.2. Antibiotic contamination	21
2.2.1. Current status of antibiotic consumption	22
2.2.2. Antibiotics in the environment	23
2.2.3. The hazards of antibiotic contamination	25
2.3. Advanced oxidation processes (AOPs)	26
2.3.1. Photocatalysis processes	28
2.3.2. The advantages and limitations of photocatalytic processes	34
2.4. Polyoxometalate	36
2.4.1. Structural characteristics of POMs	37
2.4.2. Redox activity of POMs	41
2.4.3. Photochemistry of POMs	42
2.4.4. Application of POMs as catalysts	44
2.5. Decatungstate	46
2.5.1. Mechanistic aspects of decatungstate ($W_{10}O_{32}^{4-}$) photoexcitation	46
2.5.2. The application of decatungstate	47

References	55
Chapter 3: Methods and Materials	82
3.1. Chemical reagents	83
3.1.1. Commercial reagents	83
3.1.2. Synthetic reagents	83
3.2. Laboratory equipments	86
3.2.1. Irradiation reactor	86
3.2.2. Analytical instruments	89
3.2.3. Other equipments	90
3.3. Preparation of solution	90
3.4. Characterization	94
3.4.1. Purity of catalyst testing	94
3.4.2. Phase analysis	94
3.4.3. Morphological and size	95
3.5. Experimental methods	96
3.5.1. Photodegradation in presence of decatungstate (NaDT) and H₂O₂	96
3.5.2. Photodegradation in presence of decatungstate (NaDT) and S₂O₈²⁻	97
3.5.3. Selective sulfapyridine oxidation via decatungstate/magnetite/H₂O₂ system.	98
3.6. Analytical Methods	102
3.6.1. High Performance Liquid Chromatography (HPLC) Method	102
3.6.2. Determination of H₂O₂ concentration	106
3.6.4. Quantification of nitroso-sulfapyridine (N-SPD) by NMR	108
3.6.5. HPLC-MS	108
3.6.6. Determination of Total organic carbon (TOC)	109
3.6.7. pH measurement	111
References	112

Chapter 4: Results and Discussion	114
Manuscript 1	115
Enhancement of the photocatalytic activity of Decatungstate, $W_{10}O_{32}^{4-}$, for the oxidation of sulfasalazine/sulfapyridine in the presence of hydrogen peroxide	115
Abstract	116
1. Introduction	117
2. Materials and Methods	120
2.1. Materials	120
2.2. Preparation and characterization of sodium decatungstate	120
2.3. Irradiation experiments and photoreactor	121
2.4. HPLC Analysis	122
2.5. TOC Analysis	123
3. Results	123
3.1. Characterization and photochemistry behavior of the photocatalyst .	123
3.2. photodegradation of SSZ and SPD by NaDT, H_2O_2 or NaDT/H_2O_2 systems	125
3.3. Effect of different amount of decatungstate	129
3.4. Effect of different concentrations of H_2O_2	130
3.5. Effect of different SSZ and SPD concentrations	132
3.6. Effect of different initial pH	133
3.7. Elucidation of the initial products and degradation pathways for the pollutant disappearance	134
3.8. Total organic carbon analysis	139
4. Conclusion	140
Acknowledgements	140
References	141
Supporting Information	148

Manuscript 2	151
Decatungstate photocatalyst: simultaneous reduction of persulfate and oxidation of organic pollutants	151
1. Introduction	152
2. Materials and Methods	153
2.1. Materials	153
2.2. Preparation of sodium decatungstate (NaDT)	153
2.3. Irradiation experiments and photoreactor	154
3. Results and Discussions	156
3.1. Photoreduction of $W^{10}O_{32}^{4-}$	156
3.2. Reaction between reduced decatungstate and persulfate ($S_2O_8^{2-}$)	160
3.3 Irradiation experiments	162
3.4 Products analysis by HPLC	164
4. Conclusion	166
5. Proposal	166
References	167
Manuscript 3	171
Abstract	172
1. Introduction	173
2. Experimental	175
2.1. Materials	175
2.2. Preparation of sodium decatungstate (NaDT) and Fe_3O_4	176
2.3. Characterization	177
2.4. Catalytic tests: sulfapyridine (SPD) oxidation	178
2.5. Preparative LC, NMR Spectroscopy, HRMS-UHPLC and HPLC	179
2.6. Electrochemical measurements	180
3. Results and Discussion	181
3.1. Characterization	181
3.2. Conversion of SPD in different systems	184

3.3. Optimization of the experimental parameters for the ternary system	187
3.4. Recycling experiments	187
3.5. Investigation of the interactions in the ternary system	188
3.6. Mechanistic scheme	197
4. Conclusion	200
Acknowledgements	201
References	202
Supporting Information	210
Manuscript 4	227
Tetra-n-butylammonium decatungstate supported magnetite nanoparticles: a novel magnetically nano-catalyst for green synthesis of nitroso compound	227
Abstract	228
1. Introduction	230
2. Materials and Methods	232
2.1. Materials	232
2.2. Preparation of magnetite, TBADT and M-T complex	233
2.3. Characterization	234
2.4. Catalytic tests: sulfapyridine (SPD) oxidation	235
2.5. Preparative liquid chromatography, NMR Spectroscopy and HPLC	236
2.6. Electrochemical measurement	238
3. Result and Discussions	239
3.1. Characterization	239
3.2. Comparison experiment of sulfapyridine conversion	248
3.3. Effect of main experimental parameters	250
3.4. Investigation of Electrochemical behavior of M-T, magnetite and TBADT	254
3.5. Comparison between soluble decatungstate with insoluble decatungstate	257
3.6. Mechanistic scheme	258

4. Conclusion	260
5. Proposal	260
References	261
Supporting Information	269
Chapter 5: Conclusion	280

Table of Figures

Chapter 2: Bibliographic study

Fig. 2-1. The solar radiation spectrum	16
Fig. 2-2. Light-matter interaction	17
Fig. 2-3. Diagram of the HOMO and LUMO of a molecule	18
Fig. 2-4. An orbital correlation diagram for hydrogen.....	19
Fig. 2-5. Different transitions between the bonding and anti-bonding electronic states.....	20
Fig. 2-6. A typical Jablonski diagram showing the possible radiative and non-radiative transitions	21
Fig. 2-7. Routes of transmission of antibiotics.....	25
Fig. 2-8. Photocatalytic process over TiO ₂	35
Fig. 2-9. Polyoxoanion-forming elements.....	38
Fig. 2-10. Polyoxometalates (POMs) structures in polyhedral representations	38
Fig. 2-11. Building-up process from the α -Keggin to the A- α -Dawson structure	40
Fig. 2-12. Various pathways involved in catalytic and photocatalytic process with POMs. ...	44
Fig. 2-13. Time resolved UV-vis spectra showing the photoreduction of [P ₂ W ₁₇ O ₆₁ ¹⁰⁻]	45
Fig. 2-14. The structure of the decatungstate	48

Chapter 3: Materials and Methods

Fig. 3-1. The irradiation reactor I setup	87
Fig. 3-2. Emission spectrum of the Philips HPW, 15W tube.....	87
Fig. 3-3. The 365 nm irradiation setup.....	88
Fig. 3-4. Emission spectrum of the MAZDA MAW 125 W lamp.....	88
Fig. 3-5. The molecular formula of SPD.....	91
Fig. 3-6. The molecular formula of SSZ	91
Fig. 3-7. The Calibration curve of SPD	103
Fig. 3-8. The Calibration curve of SSZ.....	105

Fig. 3-9. The Calibration curve of TAOH.....	106
Fig. 3-10. The Calibration curve of H ₂ O ₂	107
Fig. 3-11. The Calibration curves of TC and IC	111

Chapter 4: Results and Discussion

Manuscript 1

Fig. 1. Emission spectrum of lamps used in the reactor and UV-visible absorption spectra of SSZ, SPD and decatungstate (NaDT).....	125
Fig. 2. Degradation kinetics of (A) SSZ and (B) SPD in the different systems.....	127
Fig. 3. Formation of Hydroxyterephthalic acid by excitation of decatungstate (40 μM) at 365 nm in the presence of H ₂ O ₂	129
Fig. 4. Effect of decatungstate concentration on SSZ (A) and SPD (B) removal in the presence of H ₂ O ₂	132
Fig. 5. Initial degradation rates of SSZ and SPD as a function of their initial concentrations	135
Fig. 6. Evolution of TOC in a SSZ or/and SPD solution in decatungstate/H ₂ O ₂ system.....	139

Supporting information

Fig. S1. The 365 nm irradiation setup.....	149
Fig. S2. The infrared spectrum of the decatungstate.....	149
Fig. S3. UV-Vis spectra of decatungstate and its reduced specie	150
Fig. S4. Effect of different pH on pollutants removal.....	150

Manuscript 2

Fig. 1. Scheme of the 365 nm irradiation setup.....	154
Fig. 2. Emission spectrum of the MAZDA MAW 125 W lamp	155
Fig. 3. UV-Vis absorption spectra of NaDT at different concentrations	157

Fig. 4. UV-Vis spectra of sodium decatungstate ($W_{10}O_{32}^{4-}$) in aqueous solution under irradiation at $\lambda = 365$ nm in the presence of methanol and in deoxygenated solution	158
Fig. 5. Kinetics of NaDT, $NaDT^{1-}$ and $NaDT^{2-}$ concentration in aqueous solution in the presence of methanol without oxygen and under irradiation at 365 nm	160
Fig. 6. Absorbance of $NaDT^{1-}/NaDT^{2-}$ at 775 nm and kinetics change of its absorbance after adding persulfate solution at different concentrations.	161
Fig. 7. Comparison of sulfapyridine degradation experiments.	162
Fig. 8. Comparison of sulfapyridine degradation experiments in the dark	163
Fig. 9. Chromatogram of HPLC after 90 min of irradiation in three different systems.....	165
Fig. 10. Chromatogram of the NaDT/PS/SPD system at different irradiation times	165

Manuscript 3

Fig. 1. XRD patterns of Fe_3O_4 and NaDT	183
Fig. 2. FTIR spectra of NaDT and/or Fe_3O_4	183
Fig. 3. Conversion kinetics of SPD in the different systems.....	185
Fig. 4. Effect of 2-propanol on the conversion of SPD	186
Fig. 5. XPS spectra a) Fe_3O_4 before and after reaction. High resolution spectra of Fe_3O_4 after reaction of (b) Fe 2p, (c) O 1s and (d) W 4f.....	192
Fig. 6. CVs of PGE baseline in 0.1 M $LiClO_4$ pH 2.6 under Ar (a), with 1 mM NaDT (b) and in the presence of 1.0 mM (c), 2.0 mM (d), 5.0 mM (e) of H_2O_2 ($v = 10$ mV s^{-1}).....	196
Fig. 7. CVs of 1 mM NaDT in presence of 5.0 mM H_2O_2 recorded at bare PEG (a) and at M-PGE (b).....	197

Supporting information

Fig. S1. UV-vis absorption spectrum of sodium decatungstate (NaDT).....	211
Fig. S2. TEM image of Fe_3O_4	211
Fig. S3. Longer conversion kinetics of SPD with NaDT or Fe_3O_4 in presence of H_2O_2	212

Fig. S4. The UPLC-MS chromatograms of the sulfapyridine (SPD) in the ternary system at 0 min and 120 minutes	212
Fig. S5. NMR spectrum of N-SPD (a) and TPSD ₄ (b) after 120 minutes of reaction	213
Fig. S6. Effect of H ₂ O ₂ concentration on SPD conversion in NaDT/Fe ₃ O ₄ /H ₂ O ₂ system.....	217
Fig. S7. Effect of the amount of Fe ₃ O ₄ on SPD conversion in NaDT/Fe ₃ O ₄ /H ₂ O ₂ system...	218
Fig. S8. Effect of different NaDT concentrations	218
Fig. S9. The UPLC chromatogram of the sulfapyridine (SPD) in the ternary system.....	219
Fig. S10. High resolution XPS spectra of Fe ₃ O ₄ before reaction of (a) Fe 2p, and (b) O 1s.	219
Fig. S11. CVs recorded with M-PGE modified electrode in 0.1 M LiClO ₄ pH = 2.6 under Ar (a) and in the presence of 1 mM NaDT (b) ($v = 10 \text{ mV s}^{-1}$).....	220
Fig. S12. The UV-Vis spectra of NaDT in the absence or presence of H ₂ O ₂ within 2 hours at pH = 3.0. (a) NaDT (77 μM), (b) NaDT (77 μM) /H ₂ O ₂ (5.0 mM) and (c) The absorbance of NaDT (77 μM) at 321nm in the presence of H ₂ O ₂ (5.0 mM) before and after irradiation at $\lambda = 310 \text{ nm}$	221

Manuscript 4

Fig. 1. XRD patterns of TBADT, magnetite and M-T complex before and after reaction	241
Fig. 2. FTIR spectra of TBADT(a), magnetite (b) and M-T complex (c).....	242
Fig. 3. XPS profile of M-T complex (before reaction) (a), and the high-resolution spectra of Fe 2p (b), O 1s (c) and W 4f (d).....	245
Fig. 4. SEM images and SEM-EDS element mapping of M-T complex before and after reaction	248
Fig. 5. Kinetics of sulfapyridine (SPD) disappearance under various experimental conditions	249
Fig. 6. The CVs of A) T-PGE and B) M-T-PGE in the absence (a and a') or presence of 5 mM (b, b') H ₂ O ₂ in 0.1 M LiClO ₄ (pH = 3.5) under Ar, $v = 10 \text{ mV s}^{-1}$. The dash line (curve c) corresponds to the PGE baseline in 0.1 M LiClO ₄ pH 3.5 under Ar.....	254

Supporting information

Fig. S1. UV-vis spectra of different concentration of TABDT.....	270
Fig. S2. TEM images of the Magnetite (a), TBADT (b) and the M-T complex before (c) and after (d) reaction.....	270
Fig. S3. Adsorption experiments of TBADT, magnetite and M-T complex	271
Fig. S4. NMR spectrum of N-SPD (a) and TSPd ₄ (b).....	272
Fig. S5. Effect of the ratio between magnetite and TBADT on the conversion of SPD.....	273
Fig. S6. Effect of pH on the conversion of SPD.	274
Fig. S7. Effect of hydrogen peroxide concentration on the conversion of SPD.	274
Fig. S8. Effect of the amount of M-T ₂₋₁ on the conversion of SPD.	275
Fig. S9. The CVs of M-PGE in the absence (a) and in the presence (b) of 5 mM H ₂ O ₂ in 0.1 M LiClO ₄ (pH = 3.5) under Ar, $v = 10 \text{ mV s}^{-1}$. The dash line (curve c) corresponds to the PGE baseline in 0.1 M LiClO ₄ pH 3.5 under Ar.	275
Fig. S10. Ten cycles of CVs of M-T-PGE in the absence (a) and presence of 5mM H ₂ O ₂ (b) in 0.1 M LiClO ₄ (pH = 3.5) under Ar, $v = 10 \text{ mV s}^{-1}$	276
Fig. S11. Six consecutive of CVs of M-T-PGE in the presence of 5mM H ₂ O ₂ in 0.1 M LiClO ₄ (pH = 3.5) under Ar, $v = 10 \text{ mV s}^{-1}$. Insert shows the cathodic currents I_{pc1} (⊗) and I_{pc2} (⊠) at each cycle time.	276

Table of Tables

Chapter 3: Methods and Material

Table 3-1. The reagents used in the experiment.....	84
Table 3-2. The table of analytical instrument performing in the experiment	89
Table 3-3. The table of other instruments using in the experiment.....	90
Table 3-4. HPLC conditions for Analyzing of SPD.....	103
Table 3-5. HPLC conditions for Analyzing of SSZ.....	104
Table 3-6. UHPLC-MS conditions for Analyzing of SPD and SSZ.....	110

Chapter 4: Results and Discussion

Manuscript 1

Table 1. SSZ and SPD initial degradation rates as a function of H ₂ O ₂ concentration.....	131
Table 2. MS analysis of SPD and SSZ by-products and suggested structures.....	136

Manuscript 2

Table 1. Molar adsorption coefficients of decatungstate (NaDT) and reduced species (NaDT ¹⁻ and NaDT ²⁻).....	159
--	-----

Manuscript 3

Table 1. The conversion and selectivity of SPD in repeated experiments within 2h.....	188
Table 2. The ratios of Fe ²⁺ and Fe ³⁺ in Fe ₃ O ₄ before and after 4 times reuse and the fitting peak position of Fe ²⁺ , Fe ³⁺ and satellite peak in Fe 2p _{3/2} and Fe 2p _{1/2} spectrum respectively.....	193
Table 3. The fitting peak position of O 1s in Fe ₃ O ₄ before and after 4 times reuse.....	193

Supporting information

Table S1. MS analysis of SPD products and suggested structures	222
Table S2. NMR information of N-SPD and TSPD ₄	223
Table S3. Effect of pH on SPD conversion and yield of N-SPD formation in 2h	223
Table S4. Effect of [H ₂ O ₂] on SPD conversion and yield of N-SPD formation in 2h.....	224
Table S5. Effect of amount of Fe ₃ O ₄ on SPD conversion and yield of N-SPD formation in 2h	224
Table S6. Effect of [NaDT] on SPD conversion and yield of N-SPD formation in 2h	225

Manuscript 4

Table 1. The ratios of Fe ²⁺ and Fe ³⁺ in magnetite and M-T complex	246
Table 2. The fitting peak position of O 1s in TBADT, magnetite and M-T complex.....	247
Table 3. Effect of the ratio between magnetite and TBADT on SPD conversion and N-SPD production in 2h	252
Table 4. Effect of pH on SPD conversion and N-SPD production in 2h	252
Table 5. Effect of H ₂ O ₂ concentration on SPD conversion and N-SPD production in 2h.....	253
Table 6. Effect of H ₂ O ₂ concentration on SPD conversion and yield in 2h.....	253
Table 7. Comparison of selective oxidation parameters in soluble and insoluble W ₁₀ O ₃₂ ⁴⁻ synergistic magnetite and H ₂ O ₂	258

Supporting information

Table S1. The fitting peak position of W _{4f} in TBADT and M-T complex.....	277
Table S2. MS analysis of SPD products and suggested structures	277
Table S3. NMR information of N-SPD and TSPD ₄	278

Abbreviations

HOMO	Highest Occupied Molecular Orbital
LUMO	Lowest Unoccupied Molecular Orbital
MO	Molecular orbitals
WWTPs	Waste Water Treatment Plants
DDD	The defined daily dose
WTO	World Health Organization
APUA	Alliance for the Prudent Use of Antibiotics
AOPs	Advanced oxidation processes
LMCT	Ligand-to-metal charge transfer
LUMO	Lowest Unoccupied Molecular Orbital
OMCT	Oxygen to metal charge transfer bands
PS	Persulfate
PS-AOPs	Persulfate-based advanced oxidation processes
DT	Decatungstate
NaDT	Sodium decatungstate ($\text{Na}_4\text{W}_{10}\text{O}_{32}^{4-}$)
NaDT¹⁻	The reduced state of NaDT with one electron won ($\text{W}_{10}\text{O}_{32}^{5-}$)
NaDT²⁻	The reduced state of NaDT with two electrons won ($\text{W}_{10}\text{O}_{32}^{6-}$)
M	Magnetite
TBADT	Tetra-n-butylammonium decatungstate
TBABr	Tetra-n-butylammonium bromide
M-T	Magnetite and Tetra-n-butylammonium decatungstate complex

SPD	Sulfapyridine
N-SPD	Nitroso-sulfapyridine
SSZ	Sulfasalazine
TA	Terephthalic acid
TAOH	2-hydroxyterephthalic acid
PGE	Pyrolytic graphite electrode
M-PGE	PGE modified with a magnetite coating
T-PGE	PGE modified with a TBADT coating
M-T-PGE	PGE modified with a M-T complex coating
TSPd₄	3-(Trimethylsilyl) propionic acid-d ₄ sodium salt
ROS	Reactive oxygen species
RSD	Relative standard deviation

Acknowledgments

This project officially started in Université Clermont Auvergne on November 12, 2018. Writing of this thesis was one of the most significant academic challenges that I have ever had to face. Without the support, patience and guidance of the following people, I would not have been able to complete it, I owe them my sincere gratitude.

I would like to express the deepest gratitude to my supervisors Professors Gilles Mailhot and Mohamed Sarakha, who provided academic support and facilities for me to carry out researches in Université Clermont Auvergne. Their mentorship is paramount in providing a well-rounded experience consistent my long-term career goal. They encouraged me to not only grow as a researcher but also to become an independent thinker.

I am extremely grateful to Prof. Marcello Brigante in the laboratory. Although he was not my supervisor, he gave me instructions on laboratory experiments and had brilliant suggestions to solve various problems. I am extremely grateful to Mr. Guillaume Voyard, an excellent engineer in the laboratory. He taught me how to use HPLC (in the laboratory), and when there was a problem (with HPLC), he patiently taught me, how to solve it. I am extremely grateful to Dr. Yara Arbid, my best friend in the Lab. She was an excellent doctoral student; we both were working in the same office. She helped me a lot in the experiment operations and the correction of the papers.

Many heartfelt thanks to all the members of the laboratory (Institut Chimie de Clermont Ferrand) in France. Ms. Yajie Wang, Yufang Tao, Yanlin Wu and Arezou Fazli Mr Xavier Farges; Mr. Davide Palama, Étienne Bourgart, et al; DR. Claire RiChard, Prof. Mohamad Sleiman. They all helped me a lot. A Great thanks to DR. Christine Mousty and Prof. Pierre

Bonnet who gave help during my experiments. I would like to thank my friends, Mr. Qiulin Chen, Yunliang Yu. Our friendship began 2018, we met in Shanghai, where we were studying French. At that time, we were living in the same dormitory. After we all came to France, we kept visiting each other and had fun together, even if we didn't live in the same city. I would like to thank my old friends Ms. Yue Wang and her husband Mr Bastien (Duoyu Wang) too. This old friendship goes back to more than 10 years. I met Yue in Anhui Normal University in 2011, and magically we still could meet in France and have fun with in Chambéry or Clermont-Ferrand. I still can remember, at that time in the university, I was a real handsome boy so that Yue really admired me immensely and she was overwhelmed by my appearance and talent. But she turned away from me after meeting Mr Bastien, who was more handsome than me. Obviously, I was disappointed in Yue, but to tell you the truth I like Mr Duoyu Wang, he is a nice French guy and I guess that he likes Chinese culture more than Chinese girls. Mr. Samuel Collin-Nechansky, a very nice guy of French and German nationality, he's been helping me a lot in Clermont. I really thank him for inviting me and Alicia Zhang to travel to Germany last year. I really enjoyed the happy time in Germany with him. In addition, a lot of thanks to my friends, Mr Kai Zhang, Dongwei Zhai, Mingjuan Cai, Mengwei Li, Xiaowei Liu and Xuehua Zou.

Thanks to the funding support from China scholarship Council (CSC), I really appreciate this opportunity to study in France. I would also like to thank Prof. Dong Chen and Prof. Tianhu Chen. They were my supervisors when I was a master student in China. Thank you for giving me the opportunity to carry out academic cooperation and provide some support for my research during my Ph.D.

Finally, and most importantly, I would like to thank my family. A greatest thank to my parents for giving me life, they put me on this earth where I can enjoy my happy life. My parents' support and encouragement were undeniably the bedrock upon which my life has been built. A great thanks to my dear grandfather Mingyou Mei. My dear grandfather passed away last year due to illness, and I was unable to return home for his funeral due to the global COVID-19 pandemic. I am sure he will be proud of me. whsh he be free from pain in another world. I would like to honor my dear grandfather with this doctoral Thesis. I would also like thank my fiancée Xiaoyu Zhang (Alicia), I couldn't tackle these challenges without her support. We fell in love 10 years ago, and we got together again in 2019 after breaking up for some silly reasons. Thank you very much for following me to France, in order to be with me. You had to come to a strange country and to overcome all kinds of challenges and difficulties. I proposed to her on the day of my Ph.D. defense, and obviously I am still a romantic person, and I am very grateful that she accepted my proposal. Here I would like to use a passage from "All this I did Without You" to express my love for her and my expectations for our future life. I want nothing else in this life than to be with you, to listen and watch you (your beautiful voice, your beauty), to argue with you, to laugh with you, to show you things and share things with you, to explore your magnificent mind, to explore your wonderful body, to help you, protect you, serve you, and bash you on the head when I think you are wrong.

Chapter 1: Introduction

1.1. Background

➤ AOPs

The oxidation reaction belongs to the whole content of organic chemistry [1]. Concerning advanced oxidation processes (AOPs), also known as deep oxidation technology, they represent a family of organic pollutants treatment technologies that emerged in the early 1980s. These technologies generate free radicals with strong oxidizing ability under various experimental conditions: high temperature, high pressure, electricity, sound, light irradiation or catalyst reaction conditions. The most important of these oxidizing species is the hydroxyl radical also noted $\bullet\text{OH}$ ($E = 2.80 \text{ V}$) [2,3]. This species is able to oxidize the majority of organic molecules up to the mineralization, namely formation of water and carbon dioxide [4]. According to the presence or absence of irradiation, the process of free radical generation can be divided into photochemical processes and non-photochemical processes. Non-photochemical advanced oxidation processes include ozone (O_3) oxidation [5,6], Fenton/Fenton-like oxidation [7,8], electrochemical oxidation [9], catalytic wet oxidation [10,11], ultrasonic oxidation [12], etc. While photochemical advanced oxidation processes involve UV radiations of O_3 [13,14], H_2O_2 [15], TiO_2 [16,17] and photo-Fenton process [18–20].

➤ Selective oxidation

Selective oxidations, also known as partial oxidations, refers to a process in which some hydrogen atoms (or carbon atoms) in hydrocarbons and their derivatives react with oxidants, while other hydrogen atoms (or carbon atoms) do not. In these reactions, the chemical-

Introduction

selectivity, regioselectivity, stereo-selectivity and enantio-selectivity can be controlled under relatively mild reaction conditions, and the product can be obtained with the best yield [1]. The selective oxidation of organic compounds is a prominent challenge in the chemical industry [21].

Nitroso compounds are known to be highly valuable chemical intermediates, which are versatile building blocks in polymer, dyes, agrochemicals and pharmaceuticals industries [22]. They can be easily prepared from inexpensive starting material [23]. Among the preparation methods, catalytic oxidation of primary amines appears to be one of the widely used method with a variety of oxidizing agents [24–26]. H_2O_2 as a milder oxidant is largely used in “green synthesis”, since H_2O and O_2 represent the main reaction products [23,27]. In addition, the less amount of complex mixtures of over-oxidized, non-regio and chemo-selective side products is produced with H_2O_2 [23]. In the last years, the most popular methodology to prepare nitroso compounds was the transition metal-catalyzed oxidation, with tungstate (W) [23,28], molybdenum (Mo) [22,29], vanadium (V) [29], zirconium (Zr) [30], gold (Au) [31] as metal, in combination with hydrogen peroxide.

Polyoxometalates (POMs) are a class of inorganic, anionic, nanometer size metal-oxide cluster compounds with great variety in charge and framework structure [32]. POMs as an excellent catalyst widely used in organic selective oxidation and water depollution attracted more and more attention this decade.

Decatungstate ($\text{W}_{10}\text{O}_{32}^{4-}$) is one kind of the isopolyoxometalates, which has an octahedral structure. Due to the promising photocatalytic activity, the $\text{W}_{10}\text{O}_{32}^{4-}$ was chosen as the catalyst in organic synthesis and water depollution [33]. The illumination of $\text{W}_{10}\text{O}_{32}^{4-}$ under UV light

Introduction

(ranged at 300-400 nm), leads to the formation of excited state of decatungstate ($W_{10}O_{32}^{4-*}$) that has an oxygen-to-metal charge transfer (LMCT) character. This character can be highlighted by nano- and microsecond laser flash photolysis experiments [33]. $W_{10}O_{32}^{4-*}$ as the primary LMCT excited state, was formed upon absorption of a UV photon, which was demonstrated by the picosecond flash excitation experiments [34]. In addition, this excited species can survive within 30 ps in both aerated and deaerated acetonitrile and aqueous solution, then can decay to an extremely reactive non-emissive transient (a dark state tagged wO), which has a lifetime τ_{wO} of 65 ± 5 ns in the case of sodium decatungstate. Its formation quantum yield Φ_{wO} is evaluated to 0.57 [35]. The reaction between wO and appropriate hydrogen or/and electron donor leads to the formation of the one electron reduced form of decatungstate $W_{10}O_{32}^{5-}$ that absorbs in the visible region with a maximum at 778 nm. The reduction of molecular oxygen to superoxide anion by such species is an efficient process that permits the regeneration of the starting catalyst, $W_{10}O_{32}^{4-}$.

The two main fields where decatungstate salts (ammonium, potassium, sodium, etc.) were used upon solar light absorption are (i) synthesis (formation of C-C, C-N, or C-O bonds, photo-oxidations) and (ii) water depollution [33].

1.2. Objective

This thesis is a high-level university Ph.D program which subsidized by the China Scholarship Council and carried out under the supervision of Prof. Gilles Mailhot and Mohamed Sarakha from the photochemistry group of the Institut de Chimie de Clermont Ferrand (ICCF, UMR 6296 CNRS/UCA) at the Université Clermont Auvergne, France.

According to the above-mentioned background, the aim of this study is to investigate the catalytic application of decatungstate in photo-degradation and selective oxidation. The specific details of the goals can be divided into the following: **i)** to improve the photocatalytic efficiency of sodium decatungstate by adding hydrogen peroxide (H_2O_2) and persulfate (PS) **ii)** to prepare heterogeneous decatungstate-magnetite complex **iii)** to selectively oxidize aromatic amine compounds with this new material in the presence of H_2O_2 .

1.3. Thesis organization

The present work has been organized as follows:

Chapter 1 is the present chapter

Chapter 2 brings a comprehensive literature review on

- i)** The laws of photochemistry, the generation of excited states, the law of electronic transitions and the process of annihilation of excited states;
- ii)** Current consumption status, environmental chemistry process and harm of antibiotic;
- iii)** The concepts of reactive oxygen species (ROS) involved in AOPs; the photochemistry process based on typical homogeneous and heterogeneous AOPs; the advantages and limitations of photocatalytic process.
- iv)** The concept of structure, redox activity and photochemistry of POMs, the application of the POMs as catalysts.
- v)** The structure of decatungstate, mechanistic aspects of decatungstate photoexcitation and the application of decatungstate.

Chapter 3 describe the detailed experimental methods adopted in this thesis.

Chapter 4 exhibits the results and discussion, which is separated as follows:

Manuscript 1: This section is dedicated to the description of the enhancement of the photocatalytic activity of sodium decatungstate, for the oxidation of sulfasalazine/sulfapyridine in the presence of hydrogen peroxide.

Manuscript 2: In this section, simultaneous reduction of persulfate and oxidation of organic pollutants was investigated with decatungstate as a photocatalyst.

Manuscript 3: In this section, innovative decatungstate/magnetite/H₂O₂ ternary catalytic system was synthesized and applied to selective oxidation of aromatic amine compounds.

Manuscript 4: In this section, Tetrabutyl-n-ammonium decatungstate (TBADT) supported on magnetite nanoparticles was prepared as a novel magnetically nano-catalyst (M-T) to selectively oxidize aromatic amine compounds in the presence of H₂O₂.

Finally, a conclusion, as well as some perspectives for possible improvement of the work are provided.

References

- [1] D. Lenoir, Selective Oxidation of Organic Compounds—Sustainable Catalytic Reactions with Oxygen and without Transition Metals?, *Angewandte Chemie International Edition*. 45 (2006) 3206–3210. <https://doi.org/10.1002/anie.200502702>.
- [2] W.R. Haag, J. Hoigné, Photo-sensitized oxidation in natural water via •OH radicals, *Chemosphere*. 14 (1985) 1659–1671. [https://doi.org/10.1016/0045-6535\(85\)90107-9](https://doi.org/10.1016/0045-6535(85)90107-9).
- [3] T.A. Kurniawan, W. Lo, G.Y.S. Chan, Radicals-catalyzed oxidation reactions for degradation of recalcitrant compounds from landfill leachate, *Chemical Engineering Journal*. 125 (2006) 35–57. <https://doi.org/10.1016/j.cej.2006.07.006>.
- [4] J. Peller, O. Wiest, P.V. Kamat, Sonolysis of 2,4-Dichlorophenoxyacetic Acid in Aqueous Solutions. Evidence for •OH-Radical-Mediated Degradation, *J. Phys. Chem. A*. 105 (2001) 3176–3181. <https://doi.org/10.1021/jp003478y>.
- [5] S. Zhu, B. Dong, Y. Yu, L. Bu, J. Deng, S. Zhou, Heterogeneous catalysis of ozone using ordered mesoporous Fe₃O₄ for degradation of atrazine, *Chemical Engineering Journal*. 328 (2017) 527–535. <https://doi.org/10.1016/j.cej.2017.07.083>.
- [6] S.A. Snyder, E.C. Wert, D.J. Rexing, R.E. Zegers, D.D. Drury, Ozone Oxidation of Endocrine Disruptors and Pharmaceuticals in Surface Water and Wastewater, *Ozone: Science & Engineering*. 28 (2006) 445–460. <https://doi.org/10.1080/01919510601039726>.
- [7] Y. Liu, Y. Zhao, J. Wang, Fenton/Fenton-like processes with in-situ production of hydrogen peroxide/hydroxyl radical for degradation of emerging contaminants: advances and prospects, *Journal of Hazardous Materials*. 404 (2021) 124191.
- [8] B.M. Esteves, C.S. Rodrigues, F.J. Maldonado-Hódar, L.M. Madeira, Treatment of high-strength olive mill wastewater by combined Fenton-like oxidation and

- coagulation/flocculation, *Journal of Environmental Chemical Engineering*. 7 (2019) 103252.
- [9] C.A. Martínez-Huitle, M. Panizza, Electrochemical oxidation of organic pollutants for wastewater treatment, *Current Opinion in Electrochemistry*. 11 (2018) 62–71. <https://doi.org/10.1016/j.coelec.2018.07.010>.
- [10] J.J. Rueda Márquez, I. Levchuk, M. Sillanpää, Application of Catalytic Wet Peroxide Oxidation for Industrial and Urban Wastewater Treatment: A Review, *Catalysts*. 8 (2018) 673. <https://doi.org/10.3390/catal8120673>.
- [11] B. Xing, H. Chen, X. Zhang, Efficient degradation of organic phosphorus in glyphosate wastewater by catalytic wet oxidation using modified activated carbon as a catalyst, *Environmental Technology*. 39 (2018) 749–758. <https://doi.org/10.1080/09593330.2017.1310935>.
- [12] Y. Zhang, C. Yang, Y. Li, Y. Huang, J. Zhang, Y. Zhang, Q. Li, Ultrasonic extraction and oxidation characteristics of functional groups during coal spontaneous combustion, *Fuel*. 242 (2019) 287–294. <https://doi.org/10.1016/j.fuel.2019.01.043>.
- [13] Y. Wang, H. Li, P. Yi, H. Zhang, Degradation of clofibric acid by UV, O₃ and UV/O₃ processes: Performance comparison and degradation pathways, *Journal of Hazardous Materials*. 379 (2019) 120771.
- [14] W. Yao, S.W.U. Rehman, H. Wang, H. Yang, G. Yu, Y. Wang, Pilot-scale evaluation of micropollutant abatements by conventional ozonation, UV/O₃, and an electro-peroxone process, *Water Research*. 138 (2018) 106–117.
- [15] Y.-M. Lee, G. Lee, K.-D. Zoh, Benzophenone-3 degradation via UV/H₂O₂ and

- UV/persulfate reactions, *Journal of Hazardous Materials*. 403 (2021) 123591.
<https://doi.org/10.1016/j.jhazmat.2020.123591>.
- [16] M.R. Al-Mamun, S. Kader, M.S. Islam, M.Z.H. Khan, Photocatalytic activity improvement and application of UV-TiO₂ photocatalysis in textile wastewater treatment: A review, *Journal of Environmental Chemical Engineering*. 7 (2019) 103248.
<https://doi.org/10.1016/j.jece.2019.103248>.
- [17] C.H. Wu, C.Y. Kuo, C.D. Dong, C.W. Chen, Y.L. Lin, Removal of sulfonamides from wastewater in the UV/TiO₂ system: effects of pH and salinity on photodegradation and mineralization, *Water Science and Technology*. 79 (2019) 349–355.
<https://doi.org/10.2166/wst.2019.053>.
- [18] Y. Ahmed, J. Lu, Z. Yuan, P.L. Bond, J. Guo, Efficient inactivation of antibiotic resistant bacteria and antibiotic resistance genes by photo-Fenton process under visible LED light and neutral pH, *Water Research*. 179 (2020) 115878.
- [19] C.-H. Han, H.-D. Park, S.-B. Kim, V. Yargeau, J.-W. Choi, S.-H. Lee, J.-A. Park, Oxidation of tetracycline and oxytetracycline for the photo-Fenton process: Their transformation products and toxicity assessment, *Water Research*. 172 (2020) 115514.
- [20] R. Mosteo, A.V. Lopez, D. Muzard, N. Benitez, S. Giannakis, C. Pulgarin, Visible light plays a significant role during bacterial inactivation by the photo-fenton process, even at sub-critical light intensities, *Water Research*. 174 (2020) 115636.
- [21] A.E. Wendlandt, S.S. Stahl, Quinone-Catalyzed Selective Oxidation of Organic Molecules, *Angewandte Chemie International Edition*. 54 (2015) 14638–14658.
<https://doi.org/10.1002/anie.201505017>.

- [22] A.V. Biradar, T.V. Kotbagi, M.K. Dongare, S.B. Umbarkar, Selective N-oxidation of aromatic amines to nitroso derivatives using a molybdenum acetylide oxo-peroxo complex as catalyst, *Tetrahedron Letters*. 49 (2008) 3616–3619. <https://doi.org/10.1016/j.tetlet.2008.04.005>.
- [23] M. Jadidi Nejad, E. Yazdani, M. Kazemi Miraki, A. Heydari, Tungstate-supported silica-coated magnetite nanoparticles: a novel magnetically recoverable nanocatalyst for green synthesis of nitroso arenes, *Chem. Pap.* 73 (2019) 1575–1583. <https://doi.org/10.1007/s11696-019-00708-x>.
- [24] R.R. Holmes, R.P. Bayer, A Simple Method for the Direct Oxidation of Aromatic Amines to Nitroso Compounds¹, *J. Am. Chem. Soc.* 82 (1960) 3454–3456. <https://doi.org/10.1021/ja01498a054>.
- [25] B.G. Gowenlock, W. Lüttke, Structure and properties of C-nitroso-compounds, *Q. Rev. Chem. Soc.* 12 (1958) 321–340. <https://doi.org/10.1039/QR9581200321>.
- [26] Y. Shiraishi, H. Sakamoto, K. Fujiwara, S. Ichikawa, T. Hirai, Selective Photocatalytic Oxidation of Aniline to Nitrosobenzene by Pt Nanoparticles Supported on TiO₂ under Visible Light Irradiation, *ACS Catal.* 4 (2014) 2418–2425. <https://doi.org/10.1021/cs500447n>.
- [27] M. M. Heravi, N. Ghalavand, E. Hashemi, Hydrogen Peroxide as a Green Oxidant for the Selective Catalytic Oxidation of Benzylic and Heterocyclic Alcohols in Different Media: An Overview, *Chemistry*. 2 (2020) 101–178. <https://doi.org/10.3390/chemistry2010010>.
- [28] P.L. Gkizis, I. Kalara-Lafkioti, D. Varelas, I. Tamiolakis, G.S. Armatas, I.N. Lykakis, Efficient and selective oxidation of aromatic amines into nitrosoarenes catalyzed by

- supported polyoxometalates., *Biointerface Research in Applied Chemistry*. 4 (2014) 857–860.
- [29] V. Conte, B. Floris, Vanadium and molybdenum peroxides: synthesis and catalytic activity in oxidation reactions, *Dalton Trans.* 40 (2011) 1419–1436. <https://doi.org/10.1039/C0DT00706D>.
- [30] K. Krohn, Zirconium Alkoxide Catalyzed Oxidation of Phenols, Alcohols, and Amines, *Synthesis*. 1997 (1997) 1115–1127. <https://doi.org/10.1055/s-1997-1333>.
- [31] S. Fountoulaki, P.L. Gkizis, T.S. Symeonidis, E. Kaminioti, A. Karina, I. Tamiolakis, G.S. Armatas, I.N. Lykakis, Titania-Supported Gold Nanoparticles Catalyze the Selective Oxidation of Amines into Nitroso Compounds in the Presence of Hydrogen Peroxide, *Advanced Synthesis & Catalysis*. 358 (2016) 1500–1508. <https://doi.org/10.1002/adsc.201500957>.
- [32] X. Chen, Y. Zhou, V.A. Roy, S.-T. Han, Evolutionary metal oxide clusters for novel applications: toward high-density data storage in nonvolatile memories, *Advanced Materials*. 30 (2018) 1703950.
- [33] D. Ravelli, S. Protti, M. Fagnoni, Decatungstate Anion for Photocatalyzed “Window Ledge” Reactions, *Acc. Chem. Res.* 49 (2016) 2232–2242. <https://doi.org/10.1021/acs.accounts.6b00339>.
- [34] D.C. Duncan, T.L. Netzel, C.L. Hill, Early-Time Dynamics and Reactivity of Polyoxometalate Excited States. Identification of a Short-Lived LMCT Excited State and a Reactive Long-Lived Charge-Transfer Intermediate following Picosecond Flash Excitation of $[W_{10}O_{32}]^{4-}$ in Acetonitrile, *Inorg. Chem.* 34 (1995) 4640–4646.

<https://doi.org/10.1021/ic00122a021>.

- [35] I. Texier, J.A. Delaire, C. Giannotti, Reactivity of the charge transfer excited state of sodium decatungstate at the nanosecond time scale, *Phys. Chem. Chem. Phys.* 2 (2000) 1205–1212. <https://doi.org/10.1039/A908588B>.

Chapter 2: Bibliographic Study

2.1. Photochemistry

Photochemistry is a field of science that may be presented with two connected meanings:

- C. H. Wells defined that "photochemistry studies chemical behaviors and physical processes experienced by molecules that absorb ultraviolet or visible light [1]".
- N. J. Turro believed that "photochemistry studies the chemical behavior and physical processes of electronically excited molecules [2]".

Thus, photochemistry is then concerned with all the possible reactions that are initiated by the absorption of suitable radiations in the UV and visible regions of the spectrum and that lead to the generation of the electronically excited molecules. It played and still playing a very important role in our life with the sun as the central unit: photobiology (photosynthesis, phototaxis, vision) [3,4]. Owing to its greater efficiency and selectivity, photochemistry has also been used in a variety of applications in science and technology: photosynthesis, photoinitiation of polymerization, lithoprinting, photochromic materials [5–9]. Moreover, several processes that may result from the absorption of radiations in the UV and visible regions, more commonly called photophysical processes such as fluorescence and phosphorescence have also found several applications in technology field [5,10–13]. Photochemistry may also play a major role in the environment. It is deeply involved in the majority of the reactions in the atmosphere, natural surface waters and to a lesser extent in soils [14–18]. Such reactions contribute in a harmonious way to the equilibrium of our planet. Such aspect of photochemistry has then positively been used by taking advantage of its versatility to study the fate of organic pollutants in natural waters [19,20] and also to decontaminate polluted waters up the total

mineralization by employing specific and suitable techniques [21–23]. The use of solar light for such benefits appears to be a challenging topic.

The available energy in sunlight can initiate photochemistry reactions in almost all the environmental media. It is considered as a polychromatic electromagnetic wave with a composition of terrestrial sunlight from 250 to 2500 nm (**Fig. 2-1**). The wavelengths within the range 300-400 nm correspond to energies that can be considered adequate to break many type of chemicals bonds. The high flux of photons in this wavelength range is another parameter that can be considered important from the reaction rate point of view.

Moreover, photochemical reactions been classified into two different aspects: direct photoreactions and indirect photoreactions. In the former case, the substrate of interest directly absorbs the solar light and undergoes photochemical reactions while in the last case, a substance other than the substrate of interest absorbs solar light leading to highly reactive species (oxidant or reductant). These generated species react in their turn with the desired substrate leading to its degradation. In the case where the reactive species is formed in a continuous manner (photocatalysis process), the process may go on a sufficiently high efficiency till the mineralization of the contaminated aqueous solution.

2.1.1. The law of photochemistry

The principle of photochemical activation (Grotthus Draper's law) - a photochemical reaction can occur only after the radiation absorbed by a molecule. The law of actinic equivalence (Einstein-Stark law) - the number of activated molecules or atoms is equal to the quantum number of lights absorbed. The energy of a photon is given by the equation (2-1):

$$E = h\nu \quad (2-1)$$

Where h is Planck's constant ($h = 6.626 \times 10^{-34} \text{ J s}^{-1}$) and $\nu(\text{cm}^{-1})$ is the frequency of the radiation.

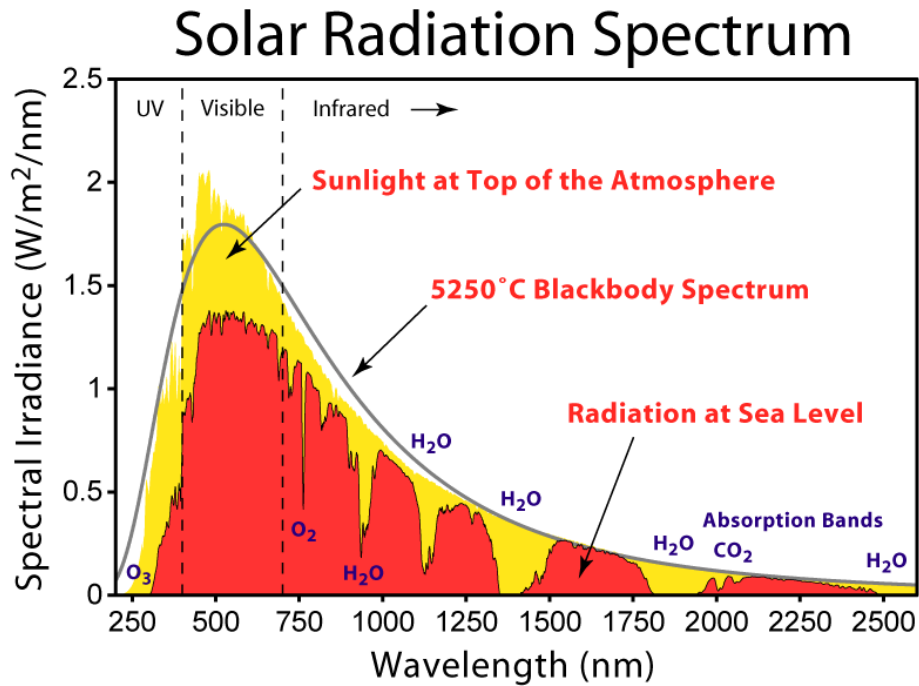


Fig. 2-1 The solar radiation spectrum. Extracted from:

https://commons.wikimedia.org/wiki/File:Solar_Spectrum.png

2.1.2. Light-matter interaction

When the light interacts with a substrate, there is a reduction of the incident photonic flux (I_0). Such reduction can be explained by various phenomena of diffusion (I_d) and absorption (I_a) (Fig. 2-2). It represents the transmitted intensity as given in equation (2-2):

$$I_0 = I_a + I_d + I_t \quad (2-2)$$

When using solutions, the diffusion process is generally neglected and thus, the absorbance at a given wavelength, A_λ , may be defined with Beer Lambert law, which is shown by the equation (2-3):

$$A_\lambda = \log \frac{I_t}{I_o} = \epsilon \times c \times l \quad (2-3)$$

with A = absorbance, I_t = transmitted light intensity, I_o = incident light intensity, ϵ = molar absorption coefficient ($L \text{ mol}^{-1} \text{ cm}^{-1}$), c = solution concentration (mol L^{-1}) and l = path length (cm). When dealing with a mixture of several components (i chemical species) and in the absence of physical interactions and photochemical reactions, the total absorbance, A_{total} is then defined as, shown in equation (2-4):

$$A_\lambda = \sum_i A_i \quad (2-4)$$

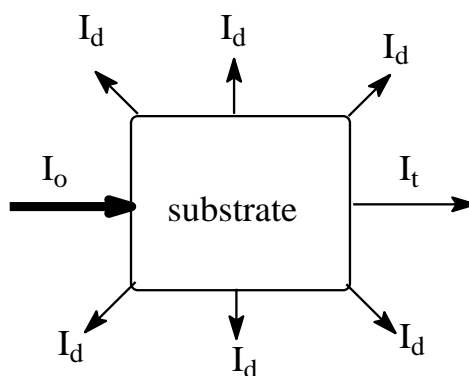


Fig. 2-2. Light-matter interaction

2.1.3. Electronic excited state

The low-energy stable state of atoms and molecules is named the ground state. The electronic excited state in photochemistry refers to the state formed by transferring the low-

energy orbit of an electron to a high-energy orbit. The most relevant to photochemical reactions are the Highest Occupied Molecular Orbital (HOMO) and the Lowest Unoccupied Molecular Orbital (LUMO), shown in **Fig. 2-3**.

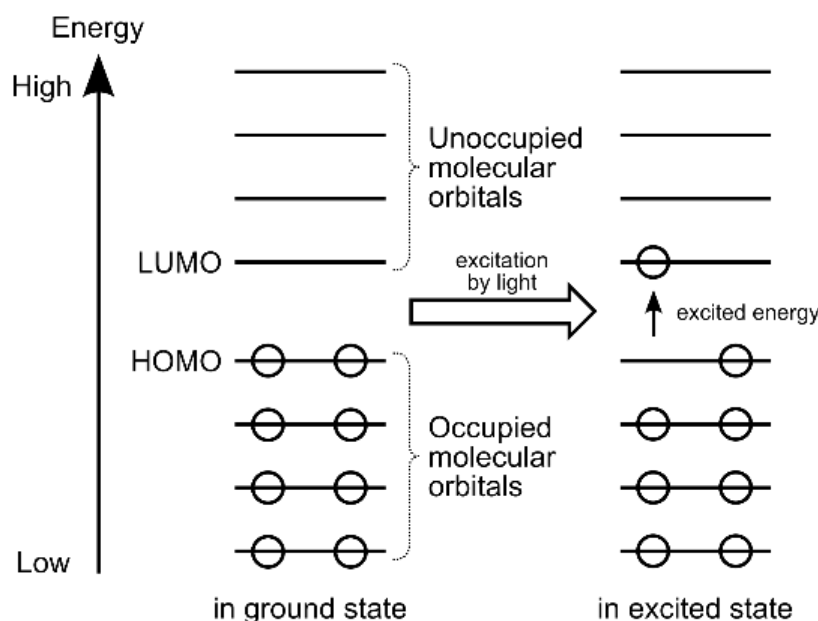


Fig. 2-3. Diagram of the HOMO and LUMO of a molecule. Each circle represents an electron in an orbital; when light of a high enough frequency is absorbed by an electron in the HOMO, it jumps to the LUMO. Extracted from: https://en.wikipedia.org/wiki/HOMO_and_LUMO

Electron transitions between different energy levels occur, when a molecule absorbs a certain energy of light radiation. Usually, two atomic orbitals can be linearly combined into two molecular orbitals. One of the molecular orbitals (MO) called the bonded molecular orbital has a lower energy than the atomic orbitals that compose it. The other molecular orbital has higher energy than the atomic orbitals that compose it. We call it the anti-bond molecular orbital and mark it with "*". Taking the H atom as an example, the molecular orbital theory can be visually shown in **Fig. 2-4**.

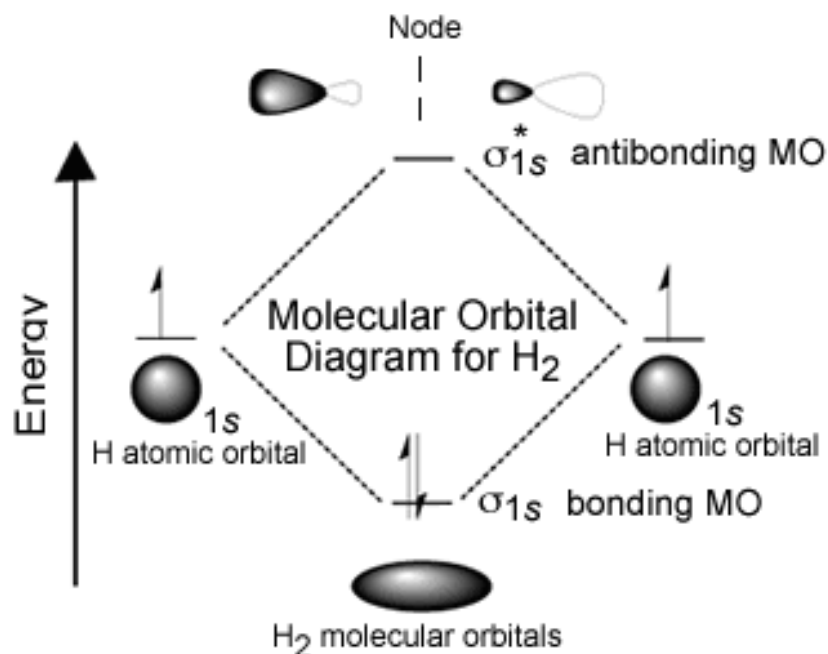


Fig. 2-4. An orbital correlation diagram for hydrogen. Extracted from:

<https://sites.google.com/site/sciencewise/classes/tiger---chemistry/4-quantum-numbers/4-quantum-numbers---page-12/molecular-orbital-theories>

According to the calculation results of molecular orbital theory, the order of the energy levels of molecular orbitals is shown in **Fig. 2-5**. When the molecule is irradiated with light of the appropriate wavelength and thus appropriate energy, the electrons on the low-energy bonding σ , π orbitals and n orbitals will transfer to the anti-bonding π^* , σ^* orbitals, which may produce $\sigma \rightarrow \sigma^*$, $\pi \rightarrow \pi^*$, $n \rightarrow \pi^*$, $n \rightarrow \sigma^*$ and $\sigma \rightarrow \pi^*$ and $\pi \rightarrow \sigma^*$ six electronic transition modes. Thus, the absorption of photon in the UV-visible region (220 – 800 nm) by a molecule leads to a new electronic distribution since several combinations are possible permitting the formation of various excited states (singlet and/or triplet). Moreover, the efficiency of the absorption is characterized by the molar absorption coefficient which depends on the molecular structure and on the involved electronic transition. As a matter of fact, the absorption is deeply

dependent on a molecular pattern named chromophores that consist on a specific arrangement of bonds and atoms.

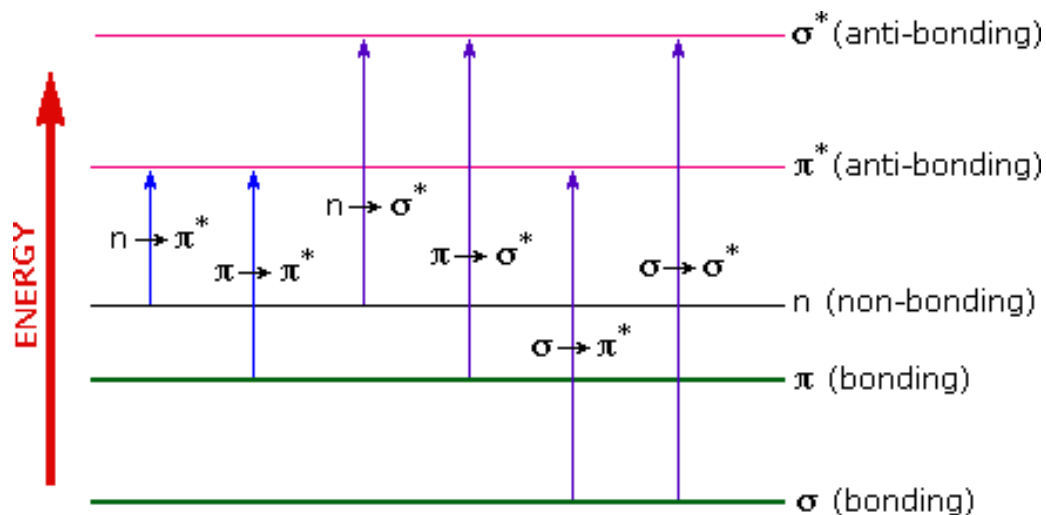
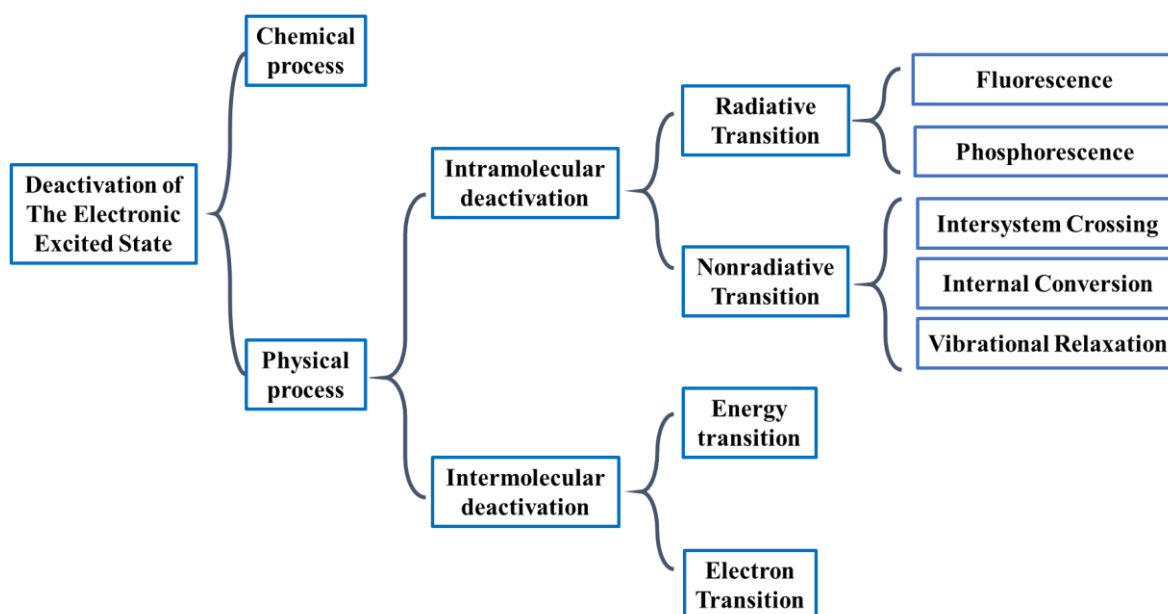


Fig. 2-5. Different transitions between the bonding and anti-bonding electronic states [24].

2.1.4. Deactivation of electronic excited state

After excitation, the return to the energetic equilibrium of an excited molecule can be obtained by degradation of the molecule (photochemistry) or return to the ground state (stable state) via the emission of photons leading to fluorescence (singlet excited state to singlet ground state) or phosphorescence processes (triplet excited state to singlet ground state) or internal energy conversion. Studying the behaviour of a molecule is thus equivalent to studying the chemical behaviour and the different ways of deactivation of its excited states since the deactivation can occur in a physical and a chemical process. The various pathways of deactivation or decay of excited state molecules can be summarized with the following scheme (Scheme 2-1) and Jablonski diagram (Fig. 2-6).



Scheme 2-1. Scheme of deactivation of the electronic excited state

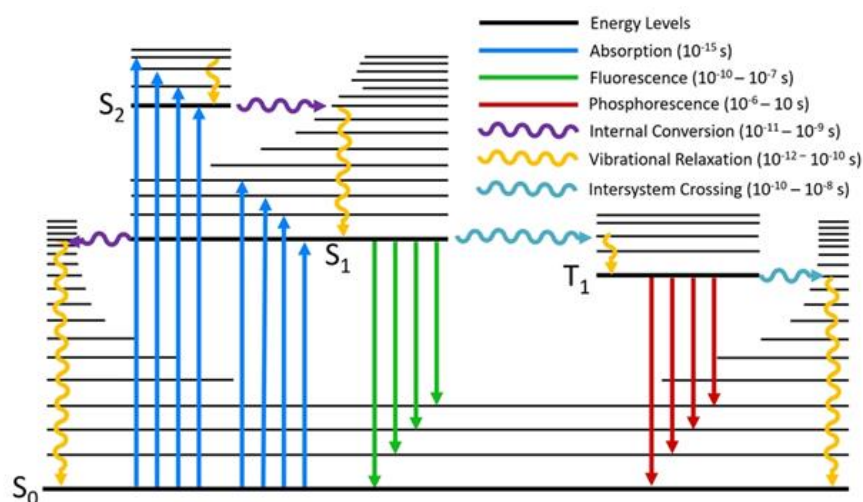


Fig. 2-6. A typical Jablonski diagram showing the possible radiative and non-radiative

transitions. Extracted from: <https://www.edinst.com/blog/jablonski-diagram/>

2.2. Antibiotic contamination

In 1928, Alexander Fleming discovered penicillin, which is the first time of discovery of antibiotics. These products represent one kind of antimicrobial substance that produced by

microorganisms (including bacteria, fungi, actinomycetes) or higher animals and plants during their lives [25].

Antibiotics were extensively used during the second world war for treating injured soldiers. Thousands of infected people have been cured, but the widespread use of antibiotics has also brought new problems, such as environmental pollution [26–28]. Various antibiotics have been reported in different environmental compartments, such as waste waters from treatment plants (WWTPs) [29–31], livestock farms [32,33], river waters and sediments [31,34–36] and soils [37,38]. For example, the antibiotics were widely present in the main rivers of Hong Kong. The Ofloxacin was the most frequently detected in the rivers, with a detection rate of 69.6% and a median concentration of 0.7 ng L⁻¹ but also Sulfadimidine (concentration up to 580.4 ng L⁻¹) and doxycycline (concentration up to 82.2 ng L⁻¹), with detection frequencies of 65.2% and 30.4% respectively [35].

2.2.1. Current status of antibiotic consumption

Antibiotics are mainly used in the prevention and treatment of human, livestock diseases, agricultural diseases prevention and control, and aquaculture [39–41]. E. Y. Klein, et.al analyzed the trends and drivers of antibiotic consumption from 2000 to 2015 in 76 countries and projected total global antibiotic consumption through 2030 [42]. This study indicated that global antibiotic consumption increased by 65% between 2000 and 2015, from 21.1 to 34.8 billion DDDs (The defined daily dose (DDD)), while the antibiotic consumption rate increased of 39% from 11.3 to 15.7 DDDs per 1,000 inhabitants per day over the study period. They

estimated that the global antibiotic consumption in 2030 would increase from 32% to 55.6 billion DDDs.

In addition, As the most populated country in the world, China is the largest producer and user of antibiotics in the world [43,44]. The total consumption of antibiotics in this country represents 162,000 tons in 2013 [45,46]. Q. Zhang, et.al systematically studied the national consumption, emissions and multimedia fate of 36 frequently detected antibiotics [46]. They conclude that the total usage for the 36 chemicals was 92700 tons in 2013, an estimated 54000 tons of the antibiotics was excreted by human and animals, and eventually 53800 tons of them entered into the receiving environment following various wastewater treatments

2.2.2. Antibiotics in the environment

The World Health Organization (WHO) has established a special Alliance for the Prudent Use of Antibiotics (APUA) in order to regulate the use of antibiotics. The abuse of antibiotics can generate many problems such as, threatening human health and causing environmental pollution. The routes of antibiotic entering the environment and transmission of antibiotics are shown in **Fig. 2-7**. Antibiotics contaminations mainly have main three sources, such as human and animal excrements, hospital medical wastewater and wastewater produced by pharmaceutical industries.

The excess antibiotics are excreted with excrement, which is due to humans and animals can not completely metabolize antibiotics [47,48]. The antibiotics mainly exist in hospital domestic wastewater and the water that used to clean the medical equipments [49,50]. Moreover,

the wastewater produced by antibiotics pharmaceutical factory is known to contain high concentrations of antibiotics [51,52].

➤ **Residual antibiotics enter the environment with the effluent discharged by WWTPs**

First, the wastewaters from hospital, pharmaceutical industry and domestic uses will be transferred to the waste water treatment plants (WWTPs) in order to reduce the amount of the antibiotics to a safe level [53–55]. Since most sewage treatment plants currently use biodegradation processes, and antibiotics have an inhibitory effect on microorganisms in water, it is difficult for antibiotic wastewaters to be 100% degraded. The antibiotics enter the environment with the effluent from the WWTPs. Hence, the presence of antibiotics in effluent of WWTPs is often reported [56,57].

➤ **Antibiotics enter the environment through manuring and aquaculture**

Due to the improvement of the economic level, livestock and aquaculture have been developed tremendously. Hence, antibiotics are often added to animal feed, such as chicken feed and fish feed, as growth regulators to prevent and treat common diseases to obtain maximum economic benefits [58].

For the livestock, antibiotics that cannot be completely metabolized are excreted from the body with animal excrement [59]. Since the residual antibiotics cannot be totally degraded in the process of sterilization, they enter soil environment after manuring with this organic fertilizer. In the case of aquaculture, the antibiotics inserted in the feed could be dissolved in the water which represents the possibility of the antibiotic to enter water environment [60,61],

shown in **Fig. 2-7**. In addition, antibiotics in water and soil will transfer via irrigation, leaching and erosion processes [62].

Moreover, we can be aware of the fact that antibiotics entering the environment will reach the human body again through the drinking water and food chain [63,64]. Like persistent organic pollution and heavy metal pollutants, antibiotics have a bioaccumulation effect [65,66].

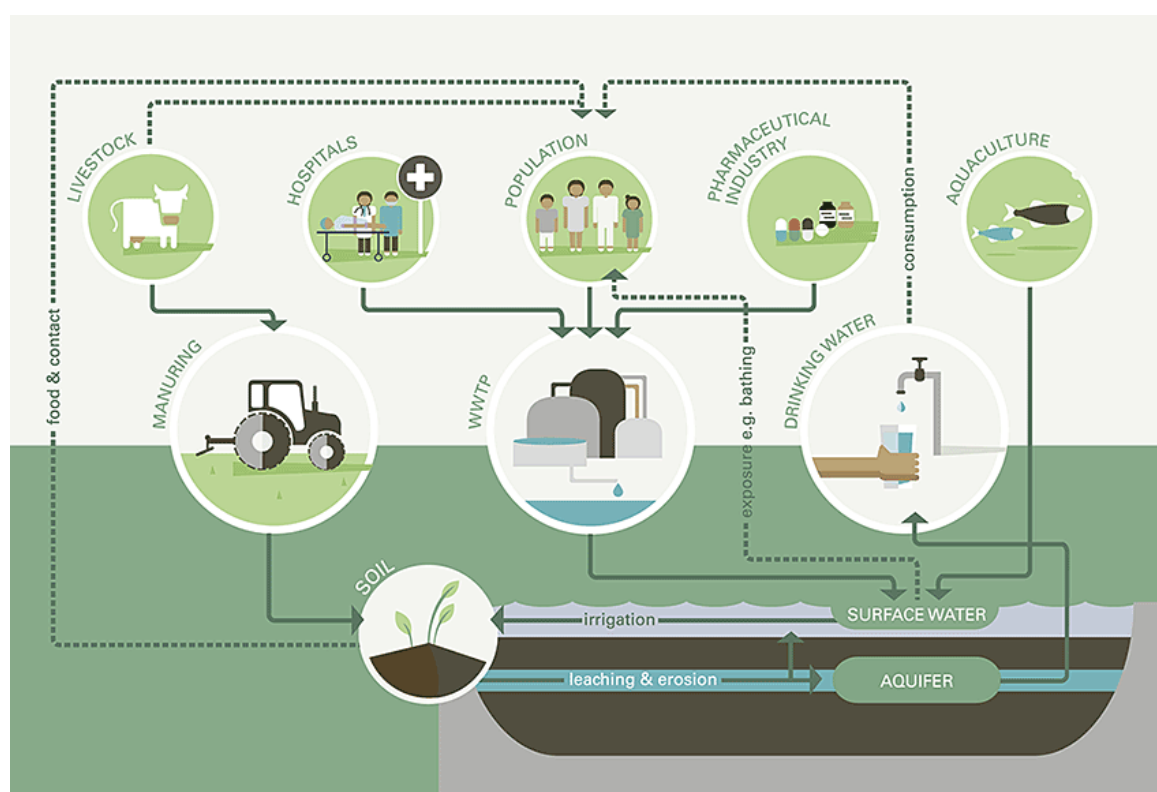


Fig. 2-7. Routes of transmission of antibiotics Extracted from:

<https://www.eawag.ch/en/departement/surf/projects/antibiotics/>

2.2.3. The hazards of antibiotic contamination

The hazards of abuse of antibiotics are mainly reflected in the following three aspects: aggravating resistance, threatening human life and health, and endangering the environment.

➤ **Aggravating antibiotic resistance**

The long-term and large-scale use of antibiotics will produce antibiotic resistance. It can cause that the antibiotics are not available for killing some bacteria. For example, super antibiotic resistance bacteria appear on the environment and are be very dramatic like operating table [67,68].

➤ **Threatening life and health**

The abuse of antibiotics can cause malignancy, vomiting, liver and kidney failure, allergies, and adverse reactions caused by drug interactions, as well as carcinogenic, teratogenic, and mutagenic side effects [69].

➤ **Endangering the environment**

The hazards of antibiotics to the environment are mainly reflected in the transmission and enrichment through the food chain, which can have side effect on human health at the end, and the impact on microorganisms in soil and water, for example, tetracycline is toxic to algae, mainly reflected in the ability of tetracycline to inhibit the protein and chlorophyll of algae [70].

2.3. Advanced oxidation processes (AOPs)

Advanced oxidation processes (AOPs), also known as deep oxidation technology, represent an organic pollutant treatment technology that emerged in the 1980s. The concept of AOPs was established by Glaze et al who defined AOPs as processes involving the generation of highly reactive oxidizing species able to attack and degrade organic substances [71,72]. This

technology generates free radicals with strong oxidizing ability under high temperature, high pressure, electricity, sound, light irradiation or catalyst reaction conditions, the most important of radicals is $\bullet\text{OH}$ ($E = 2.80 \text{ V}$) [73,74]. This species is able to degrade the majority of organic molecules up to the mineralization, leading namely to the formation of water and carbon dioxide [75].

According to the presence or absence of irradiation, the process of free radical generation can be divided into photochemical processes and non-photochemical processes. Non-photochemical advanced oxidation processes include ozone (O_3) oxidation [76,77], Fenton/Fenton-like oxidation [78,79], electrochemical oxidation [80], catalytic wet oxidation [81,82], ultrasonic oxidation [83], etc. While photochemical advanced oxidation processes include UV/ O_3 [84,85], UV/ H_2O_2 [86,87], UV/ TiO_2 [88,89] and photo-Fenton process [90–92]. In addition, generation of sulfate radicals ($\text{SO}_4\bullet^-$) to this set of process is attracting more and more attentions [93–95].

The typical mechanisms of reaction between $\bullet\text{OH}$ with organic pollutants are: **a)** Hydrogen abstraction reaction between hydroxyl radicals and organic pollutants, H_2O and corresponding organic radical are producing in this reaction. **b)** addition of $\bullet\text{OH}$. **c)** electron transfer from organic pollutants to $\bullet\text{OH}$.

The typical mechanism for sulfate radicals ($\text{SO}_4\bullet^-$) attack the organic pollutants is due to the lone pair of electrons of sulfate radicals ($\text{SO}_4\bullet^-$). The radical chain reaction is similar to the $\bullet\text{OH}$.

AOPs are used to treat organic matter, especially non-biodegradable organic matter, such as organic dyes, antibiotics, pesticides, and landfill leachate. The main advantages of AOPs are

as follows: high degradation efficiency, non-selectivity and low price. More and more people are using these processes or combining several AOPs technologies to achieve higher degradation efficiency.

2.3.1. Photocatalysis processes

The principle of photocatalysis is based on the oxidation-reduction ability of photocatalysts under light radiation, which can achieve the purposes of degradation of pollutants, substance synthesis and transformation. Under normal circumstances, photocatalytic oxidation reactions use semiconductors as catalysts and light as energy to degrade organic matter into carbon dioxide and water [96]. The photocatalysis process can be divided to homogeneous and heterogeneous photocatalysis process, according to the solubility of the catalyst in the aqueous solution.

2.3.1.1. AOPs based on homogeneous photocatalytic degradation

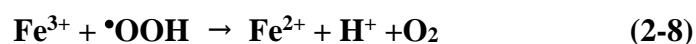
Homogeneous photocatalysis consists of a soluble molecular catalyst including a light-absorbing system (photosensitizer), catalytic sites for oxidation, and reduction processes, all in a single form (solution) [97]. Typical homogeneous photocatalysis processes include photo-Fenton reaction, UV/H₂O₂ process and O₃/UV process, etc.

➤ Photo-Fenton reaction

The chemical oxidation based on iron plays an important role in the advanced oxidation processes (AOPs), and occupies an important position [98–100]. Well known, iron element is

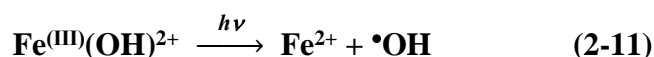
one of the most common elements in the crust, which can be found in different media and forms. For example, it widely presents in natural waters. Moreover, it is reported that the iron has been tested in rivers, lakes and even in the fog water and rain water [101]. Therefore, the effective application of iron in AOPs will be an important development direction for the future wastewater treatment.

About 110 years ago, chemist Mr. H.J.H Fenton discovered that the solution mixed with Fenton reagent (namely Fe(II) and H₂O₂) had strong oxidation capacity, which could oxidize many kinds of organic compounds and efficiently mineralize them to CO₂, H₂O and inorganic compounds [101,102]. But it would not attract attention of researchers in that moment until in the 1970s and 1980s. Fenton reaction was used in the degradation of refractory organic pollutants, such as pesticides, antibiotics, dyes, etc [103–107]. The chain reaction in Fenton process is shown in following equations [101]:



Moreover, iron (Fe) as a photoreactive species is widely used in photodegradation due to that it can produce some reactive oxygen species (ROS), such as $\bullet\text{OH}$, $\bullet\text{OOH}$ and $\text{O}_2\bullet^-$ radicals through direct or indirect photochemical reactions. As well known, these oxidizing active

radicals are the key species for the degradation of pollutants. The iron hydroxyl complex is the main species when ferric iron (Fe^{3+}) is dissolved into water in the pH of range of 2.5 - 5.0, and this main form of dissolved Fe^{3+} can generate hydroxyl radical ($\bullet\text{OH}$) through its photolysis. The process is shown in equation (2-11):



The quantum yield of its photolysis is reportedly at around 0.075 at 360 nm UV light [108], while Lee reported that the quantum yield of its photolysis is reportedly at around 0.065 at 254 nm [109]. These studies show that the quantum yield is low. Shown in above equation (2-6), the ferrous ion ($\text{Fe}(\text{II})$) was generated by the photo reduction process, then it can be oxidized and regenerate $\text{Fe}(\text{III})$ by oxygen in the solution. Therefore, the $\text{Fe}(\text{III})/\text{Fe}(\text{II})$ redox cycle will continuously generate oxidation free radicals ($\bullet\text{OH}$) in the solution, and these free radicals will unselectively attack the organic pollutants in water.

In the 1990s, according to the mechanism of Fenton reaction and photolysis of $\text{Fe}(\text{III})$, researchers combined UV/ $\text{Fe}(\text{III})$ and H_2O_2 to form a higher oxidation efficient technology, named photo-Fenton reaction, it was efficiently applied in the removal of organic pollutants.

➤ UV/ H_2O_2 Process

In 1818, L.J. Rhenard discovered that hydrogen peroxide (H_2O_2) was generated before water when water-based inorganic and organic matter oxidize, or when the organism breathes oxygen [110]. H_2O_2 is a strong oxidant and is generally used in medical, leather, textile, organic synthesis and rocket propulsion. For example, 3% H_2O_2 solution can be used to disinfect

wounds. 10% H₂O₂ solution can be used as a bleaching agent and deodorant for textiles and leather. H₂O₂ is easily available, cheap and easy to transport, and the product in the use process is water, so it is called a green oxidant. And the hydroxyl radicals ($\bullet\text{OH}$) are produced in the decomposition process have strong oxidizing properties, so H₂O₂ is mostly used in the treatment of organic wastewater by AOPs.

The UV/H₂O₂ system consists of adding hydrogen peroxide (H₂O₂) in the presence of UV light to generate hydroxyl radicals ($\bullet\text{OH}$) through the homolytic bond scission [86,87,111]. The main advantage of using UV/H₂O₂ for water and wastewater systems resides in the fact that UV radiation can work simultaneously as a disinfectant, by physically inactivating microorganisms, and helping in the photolysis of peroxide, breaking it into the highly reactive hydroxyl radicals ($\bullet\text{OH}$).

The photochemical advanced oxidation process using UV light and hydrogen peroxide is a quite well-established technology for water and wastewater treatment. This process relies on the production of an effective oxidant, the hydroxyl radical ($\bullet\text{OH}$), through the irradiation of the hydrogen peroxide with ultraviolet (UV) radiation. The process is shown in equation (2-12):

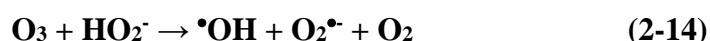
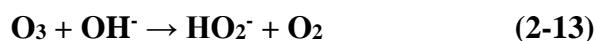


➤ O₃/UV process

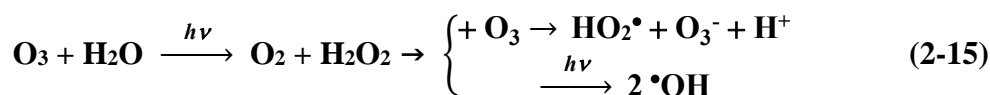
Ozone (O₃) is an allotrope of oxygen (O₂). O₃ is a colorless gas with a special smell at room temperature. As a strong oxidant, ozone has been successfully used to disinfect and decompose dissolved organic compounds [76,77]. Ozone can oxidize organics and inorganics in water under any pH conditions. There are two ways for it to interact with organics. One is slow and selective direct oxidation. The second is •OH radicals generated after ozone decomposition, which indirectly reacts with organic matter. The latter has stronger oxidizing ability, which is more rapid and non-selective [73,74].

The decomposition of the ozone solution in pure water is caused by OH⁻. The reaction leads to the generation of free radicals-free radicals or free radicals-solute reactions. [112,113].

The reaction process is expressed as follows equations:



The above reactions do not have a significant effect when oxidizing organics with complex structures [112]. The target organics are difficult to completely degrade, especially under low pH conditions. Therefore, ozone is often used in combination with other technologies. O₃/UV process is the process of further accelerating ozone decomposition through ultraviolet radiation. In the water phase, O₃ photolysis produces H₂O₂ as the main product. Then it can be directly photodegraded into •OH radicals, and the radicals can react with O₃ aqueous solution to generate •O₂H radicals, as shown below:



2.3.1.2. AOPs based on heterogeneous photocatalytic degradation

Homogeneous photocatalytic systems show high activity and fast catalytic reaction rate in photocatalytic degradation [114,115]. However, there are many inherent shortcomings, such as catalysts are difficult separation, recovery and reuse, relatively high pH requirements of the reaction system, and quantum yield on the low side [115–117].

In most cases, heterogeneous catalysts are better than homogeneous catalysts, because heterogeneous catalysts have strong stability [118], are simple and easy to separate and the catalyst can be recycled. Among all semiconductor photocatalyst materials, TiO₂ is the most commonly used in heterogeneous catalysis. TiO₂ has excellent photocatalytic yield, excellent stability and suitable band edge capabilities [88,119,120], shown in **Fig. 2-8**.

In heterogeneous photocatalysis system (TiO₂), the electron transition will occur between energy bands after the electron of semiconductors absorbs light energy greater than its band gap. Subsequently, forming the electron-hole pairs when electrons are excited to the conduction band and holes are generated in the valence band [121]. The part of electron-hole pairs that migrate to the surface of the semiconductor will separate and take part in the redox reaction respectively [122]. The organic compounds adsorbed on the surface of the semiconductor are oxidized by the valence band holes. In addition, the H₂O/OH⁻ are oxidized by the valence band holes as well to produce the hydroxyl radicals (•OH) [123]. At the same time, the unmatched electrons quickly combine with oxygen on the semiconductor surface to obtain superoxide radical anion (O₂^{•-}) [124]. Two highly reactive oxidizing species superoxide radical (O₂^{•-}) and

hydroxyl radical ($\bullet\text{OH}$) in photocatalytic process over TiO_2 , which non-selectively degrade and mineralize organic pollutants. While the electron and hole recombination (annihilation) occurs when the nuclear power carrier migrates [125]. There are several factors that may affect the efficiency of the process. One can distinguish four main factors that will be discussed as follows [126].

a) Light response range. As we all know, solar radiation energy is mainly distributed in the visible, ultraviolet and infrared regions, 50% of which is in the visible region (400 - 760nm), 43% in the infrared region, and 7% in the ultraviolet region. According to Planck's law, the light in the visible and infrared region has a longer wavelength and so the smaller energy. Hence the probability of electron transition is lower.

b) The efficiency of generating photo-generated carriers and quantum yield.

c) The recombination rate of electron-hole pairs and the lifetime of photogenerated carriers.

d) The ability to overcome the effects of photocorrosion, namely, the stability of the catalyst.

2.3.2. The advantages and limitations of photocatalytic processes

➤ Advantages of photocatalytic oxidation method

(1) The photocatalytic reaction conditions are mild and its oxidation capacity is strong.

(2) The photocatalytic reaction can tolerate a high organic wastewater loading, which means it can treat both dilute and high concentrated organic wastewater.

(3) The photocatalytic reaction can be efficiently applied to oxidize the organic compounds into inorganic small molecules, achieving the goal of wastewater depollution.

(4) The photocatalytic reaction can be used as a deep treatment for the drinking water. It can completely destroy organic compounds and remove all kinds of microorganisms, like bacteria and molds in water, and convert them into H_2O and CO_2 for discharge.

(5) The photocatalytic reaction is a very clean treatment method, almost no or a small number of substances will be introduced into the system.

(6) The photocatalytic reaction can be used to treat some highly toxic substances, such as cyanide, various organic chelating agents and additives commonly used in electroplating, and achieve harmlessness.

(7) The photocatalytic reaction also has broad application for the removal of many inorganic substances, such as CN^- , $\text{Au}(\text{CN})_2^-$, I^- , SCN^- , $\text{Cr}_2\text{O}_7^{2-}$, $\text{Hg}(\text{CH}_3)_2$, Hg^{2+} , etc.

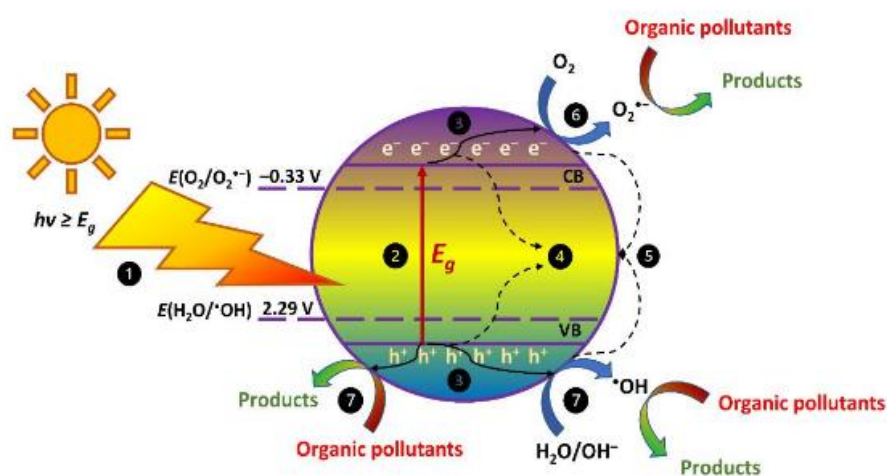


Fig. 2-8. Photocatalytic process over TiO_2

- ① Photon absorption; ② Generation and separation of electron-hole pairs (e^- and h^+); ③ Transport of electrons and holes in the bulk to the photocatalyst surface; ④ Recombination of electrons and holes in the bulk; ⑤ Surface recombination of electrons and holes; ⑥ Reduction reaction on TiO_2 surface; ⑦ Oxidation reactions on TiO_2 surface [127].

➤ Disadvantages of photocatalytic oxidation

(1) The absorption range of ultraviolet light is narrow, and the utilization rate of light energy is low. The efficiency of photocatalytic reaction is also limited by the property of the catalyst, ultraviolet wavelength and reactor. Short-wave ultraviolet (wavelength less than 270 nm) is better than long-wave, but short-wave ultraviolet light is more difficult to obtain, expensive and dangerous.

(2) The transmittance of solution can affect the photocatalytic efficiency. While some suspended solids and darker chromaticity in some wastewater, like dyeing wastewater, can decrease the light transmission and cause a low photocatalytic efficiency.

(3) Most of the currently used catalysts are nano-particles in order to get higher degradation efficiency. But these catalysts are difficult to recover from the solution. In addition, the electron-hole pairs are easily recombined and deactivated in a nano scale catalyst.

(4) Some ions in the actual wastewater can react with the free radicals generated in the photocatalytic reaction, which can reduce the efficiency of sewage degradation.

2.4. Polyoxometalate

Polyoxometalates (POMs) are a class of inorganic, anionic, nanometer size metal-oxide cluster compounds with great variety in charge and framework structure [128]. POMs are produced by condensation and dehydration of simple oxo acid salts under certain pH conditions [129]. Among them, the isopolyoxometalates are produced by dehydration of one oxo acid salt, and the heteropolyoxometalates are produced by the dehydration of two or more oxo acid salts [129].

The first times description of polyoxometalates (POMs), yellow precipitate formed from a mixture of arsenate and phosphate with molybdic acid, namely the ammonium salt of the anion $[\text{PMo}_{12}\text{O}_{40}]^{3-}$, was done by J. J. Berzelius [130]. Later, two isomers of 12-tungstosilicic acid (namly α and β isomers of $[\text{SiW}_{12}\text{O}_{40}]^{4-}$) were prepared and correctly analyzed by Marignac, which was the first systematic study of polyoxometalates [131].

Fig. 2-9 shows that the main elements that can form POMs are concentrated in the early transition metals (V, Nb, Ta, Cr, Mo, W) and certain p-block elements (B, Si, Ge, P, As, Sb, Te, I), usually these POMs can be expressed in a general formula $\text{M}_x\text{O}_y^{n-}$ while the other properties rarely have similarities.

2.4.1. Structural characteristics of POMs

In 1892, Blomstrand proposed the structure of phosphomolybdic acid and other poly-acids as a chain or ring configuration [132]. Alfred Werner, tried to describe the structure of silicotungstic acid, by using the coordination compound ideas of Copaux. He speculated that $[\text{SiO}]^{4+}$ as a central group were encased by four $[\text{RW}_2\text{O}_6]^+$ roundly, which linked to the central group via primary valences, while two more $\text{R}_2\text{W}_2\text{O}_7$ groups were linked to the central group by secondary valences, where R is a unipositive ion [133].

Due to the development of new synthetic methods and new characterization methods, the tremendous development of POMs chemistry has been promoted, leading to the discovery of a large number of new POMs structures and the development of molecules and composite materials used in different fields [134].

Bibliographic Study

In fact, the basic structural units of POMs are mainly MO_6 octahedrons or MO_4 tetrahedrons. The polyhedrons are connected by co-angle, co-edge or co-planar to produce a large number of different polymeric structures [129]. **Fig. 2-10** shows the six main typical structure of POMs.

<i>H</i>																	<i>He</i>
<i>Li</i>	<i>Be</i>											<i>B</i>	<i>C</i>	<i>N</i>	<i>O</i>	<i>F</i>	<i>Ne</i>
<i>Na</i>	<i>Mg</i>											<i>Al</i>	<i>Si</i>	<i>P</i>	<i>S</i>	<i>Cl</i>	<i>Ar</i>
<i>K</i>	<i>Ca</i>	<i>Sc</i>	<i>Ti</i>	<i>V</i>	<i>Cr</i>	<i>Mn</i>	<i>Fe</i>	<i>Co</i>	<i>Ni</i>	<i>Cu</i>	<i>Zn</i>	<i>Ga</i>	<i>Ge</i>	<i>As</i>	<i>Se</i>	<i>Br</i>	<i>Kr</i>
<i>Rb</i>	<i>Sr</i>	<i>Y</i>	<i>Zr</i>	<i>Nb</i>	<i>Mo</i>	<i>Tc</i>	<i>Ru</i>	<i>Rh</i>	<i>Pd</i>	<i>Ag</i>	<i>Cd</i>	<i>In</i>	<i>Sn</i>	<i>Sb</i>	<i>Te</i>	<i>I</i>	<i>Xe</i>
<i>Cs</i>	<i>Ba</i>	<i>La</i>	<i>Hf</i>	<i>Ta</i>	<i>W</i>	<i>Re</i>	<i>Os</i>	<i>Ir</i>	<i>Pt</i>	<i>Au</i>	<i>Hg</i>	<i>Tl</i>	<i>Pb</i>	<i>Bi</i>	<i>Po</i>	<i>At</i>	<i>Rn</i>
<i>Fr</i>	<i>Ra</i>	<i>Ac</i>															

Fig. 2-9. Polyoxoanion-forming elements

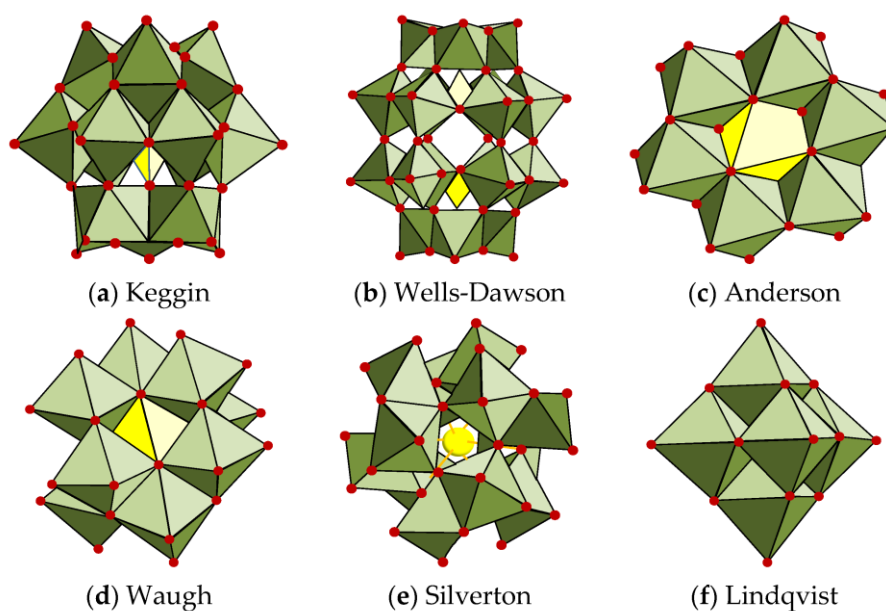


Fig. 2-10. Polyoxometalates (POMs) structures in polyhedral representations [135].

➤ Keggin structure

Keggin structure is perhaps the most commonly adopted structure which has a diameter of 1.2 nm. As shown in the **Fig. 2-10(a)** [136] it is composed of 12 vertices and edge-sharing MO_6 octahedra surrounding a central XO_4 tetrahedron. Its general formula is $[\text{XM}_{12}\text{O}_{40}]^n$, ($\text{X} = \text{P}, \text{Si}, \text{Ge}$, etc. $\text{M} = \text{W}, \text{Mo}$), for example, $\text{PW}_{12}\text{O}_{40}^{3-}$, $\text{SiW}_{12}\text{O}_{40}^{4-}$ and $\text{PMo}_{12}\text{O}_{40}^{3-}$. Pauling took the first step in understanding the structure of polyoxometalates anions in 1929 [137]. He proposed that the structure of the 12-tungsto anions were based on a central PO_4 or SiO_4 tetrahedron surrounded by WO_6 octahedra according to the rules he developed for complex ionic crystals. In 1933, Keggin reported the structure of $\text{H}_3\text{PW}_{12}\text{O}_{40} \cdot 5\text{H}_2\text{O}$ (which was much later shown to be the hexahydrate) [138]. A year later Signer & Gross demonstrated that $\text{H}_4\text{SiW}_{12}\text{O}_{40}$, $\text{H}_5\text{BW}_{12}\text{O}_{40}$ and $\text{H}_6[\text{H}_2\text{W}_{12}\text{O}_{40}]$ formed hydrates that were isomorphous with Keggin's structure.

➤ Wells-Dawson structure

The second kind of common structure is called Wells-Dawson structure, as shown in the **Fig. 2-10(b)**. The general formula is $[\text{X}_2\text{M}_{18}\text{O}_{62}]^n$, ($\text{X} = \text{P}, \text{As}$, etc. $\text{M} = \text{Mo}, \text{W}$, etc.), it can be seen as derived from the Keggin structure. In 1953, Dawson used X-ray analysis to determine the structure of $\text{K}_6\text{P}_2\text{W}_{18}\text{O}_{62} \cdot 14 \text{H}_2\text{O}$ [139]. Wells-Dawson structure is based on the truncated XM_9O_{34} Keggin unit (XM_9 in short): two of these fragments can be assembled symmetrically to form the X_2M_{18} cluster [140], as shown in **Fig. 2-11**. The most typical compositions associated to the Well-Dawson structure derive from the phosphotungstate and molybdate anions, $[\text{P}_2\text{M}_{18}\text{O}_{62}]^{6-}$ (P_2M_{18} , $\text{M} = \text{W}, \text{Mo}$). Compounds containing As or S instead of phosphorus have also been reported [141].

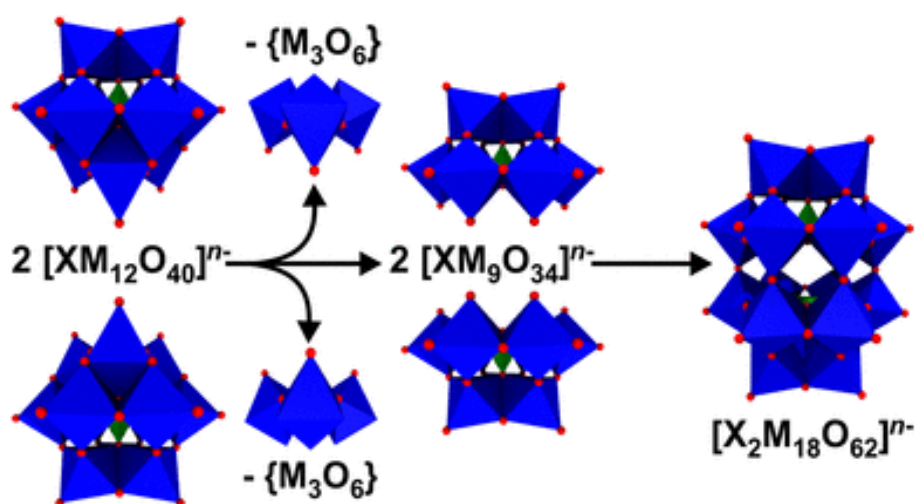


Fig. 2-11. Building-up process from the α -Keggin to the A- α -Dawson structure. *Blue* octahedra are MO_6 units ($M = W, Mo$), and *green* tetrahedra are XO_4 anions [142].

➤ Anderson structure

The third kind of common structure is called Anderson structure, as shown in the **Fig. 2-10(c)**. The general formula is $[XM_6O_{24}]^{n-}$, ($X = Cr^{3+}, Mn^{4+}, Co^{3+}, Cu^{2+}, Zn^{2+}, Te^{4+}$ and Pt^{4+} ; $M = Mo, W$) [143].

➤ Waugh structure

The fourth kind of common structure is called Waugh structure, as shown in the **Fig. 2-10(d)**. The general formula is $[XM_9O_{32}]^{n-}$, ($M = Mo$; $X = Mn^{4+}, Ni^{4+}$) [129].

➤ Silverton structure

The fifth kind of common structure is called Silverton structure, as shown in the **Fig. 2-10(e)**. The general formula is $[XMo_{12}O_{42}]^{9-}$, ($X = Ce^{3+}, Gd^{3+}$) [129]. More specifically, Baker et al. reported the first Silverton-type compound in 1953 with the formula of

$(\text{NH}_4)_2\text{H}_6[\text{CeMo}_{12}\text{O}_{42}] \cdot 12\text{H}_2\text{O}$ and then this structure was further explored by Silverton et al [144]. Subsequently, this configuration was defined as “Silverton” type POM, in which the $[\text{CeMo}_{12}\text{O}_{42}]^{8-}$ anion is constructed by six corner-sharing $\{\text{Mo}_2\text{O}_9\}$ groups and a twelve-coordinated Ce^{4+} ion.

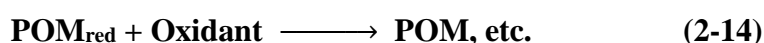
➤ Lindqvist structure

The sixth kind of common structure is called Lindqvist structure, as shown in the **Fig. 2-10(f)**. The general formula is $[\text{M}_6\text{O}_{19}]^n$, ($\text{M} = \text{Mo}, \text{W}, \text{Nb}, \text{Ta}$) [129].

2.4.2. Redox activity of POMs

One of the characteristics of POMs is that they can undergo multiple "reversible" multi-electron redox reactions, which are reversible in the sense that their structure remains intact [145]. Therefore, they can be used as electronic relays and oxygen relays to participate in redox reactions [129].

As a general rule, POMs participate in heterogeneous redox reactions involving oxygen, mainly as oxygen relays, and almost exclusively as electron relays in homogeneous photocatalytic reactions. The basic reactions involved in the two situations are shown in following equations:



After combining the above two equations, the following results can be obtained:



where S = Organic substrate. The best and mildest oxidant is molecular oxygen. Therefore, in a heterogeneous reaction, equation (2-13) mainly carries oxygen from POM to pollutants. While, the lost oxygen is supplemented by atmospheric oxygen or oxygen from other oxidants, shown in equation (2-14) [129]. In homogeneous photocatalytic reaction, equation (2-13) and equation (2-14) are strictly related to the transfer of electrons [129].

2.4.3. Photochemistry of POMs

The photosensitive properties of polyoxometalates were first discovered by Rindl in 1916 [146]. Systematic work on the photochemistry and radiation chemistry of POMs began about more than 50 years ago (in the early 1970's). Papaconstantinou was the first person who conducted to detailed study on the photocatalytic process and illustrated that the reduced polyoxometalate can be re-oxidized in the air to form the POM catalytic cycle process [147]. In addition, it turns out that the photocatalytic processes with POMs may be divided, roughly, into two categories: (a) selective and (b) non selective.

As a matter of fact, the ability of POMs to mineralize organic pollutants (to CO₂, H₂O and inorganic anions) was recognized in 1990s [129]. Since then, research on POM photocatalytic degradation of organic halides, pesticides and other pollutants in water has been rapidly developed [147].

Fig. 2-12 shows various pathways involved in catalytic and photocatalytic process with POMs. The whole picture of POMs photocatalysis is introduced, and then the involved photocatalysis process will be discussed in turn as follows [129]:

There is ample evidence that irradiation with visible light and near-ultraviolet light (into oxygen to metal charge transfer bands (LMCT)) makes POMs powerful oxidant (POMs*, called a soluble anodes) that can oxidize a variety of organic compounds [148]. The POMs are reduced to colored, generally, blue species in this process, simultaneously. Continuous photolysis leads in further oxidation of the organic compounds with concomitant accumulation of electrons on the POMs [149].

The POMs can regenerate from reduced state in solution in presence of a species can accept electrons from POMs, thus, the closing of photocatalytic cycle completes. In addition, the process continues until the substance in the solution cannot accept electrons from the POMs or until the organic substance cannot be further oxidized [129]. This results, with minor exceptions, in mineralization of organic pollutants.

The photochemistry of POM can be described by the following photocatalytic cycle (**Fig. 2-12**). As mentioned earlier, we briefly discuss it here so that we can understand the chemical reactions involved. Path I (**Fig. 2-12**) shows that after mixing POM and S (S = organic substrate), a pre-association complex or pre-association equilibrium is established [150]. Path II shows that the exposure of POM under irradiation (visible and near UV light) leads to formation of oxidation species of S (S_{ox}) and reduction species of POM (POM(e^-)). The reduced POM can be also produced thermally by various reducing reagents (Path IV). The electrons accumulated on POM can be taken out by various electron acceptors and close the photocatalytic cycle (Path V). In the absence of a strong oxidant (such as, in a deoxygenated solution), the reduced POM appears blue, and it is easy to track the photoreaction by spectrophotometry, as shown in **Fig.**

2-13. Dioxygen (O_2) is the most common benign oxidant and undergoes reductive activation during the process ($O_2^{\bullet-}$) that initiates further oxidation (Path VI).

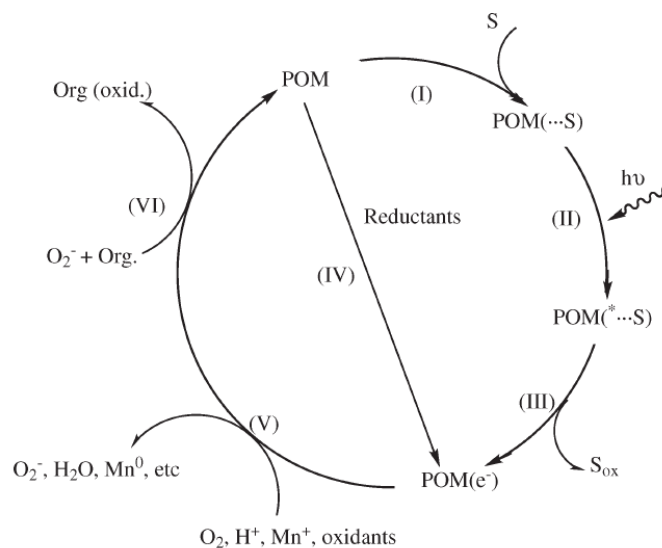


Fig. 2-12. Various pathways involved in catalytic and photocatalytic process with POMs
 Path(I)-Pre-association; (II)-Excitation; (III)-Photoredox reaction; (IV)-Thermal redox reaction; (V)-Reoxidation, regeneration of catalyst; (VI)-Further oxidations through $O_2^{\bullet-}$ radical [129].

2.4.4. Application of POMs as catalysts

POMs have a wide range of applications in structural chemistry, analytical chemistry, food chemistry, surface science, medicine, electrochemistry, photochemistry and catalysis [152]. Especially in the field of catalysis, more than 80% of the reported patents of POMs are related to catalysis. POMs can become catalytic materials with excellent performance and have many characteristics that traditional catalysts do not have [153]. Kind of excellent characteristics, mainly including the following aspects:

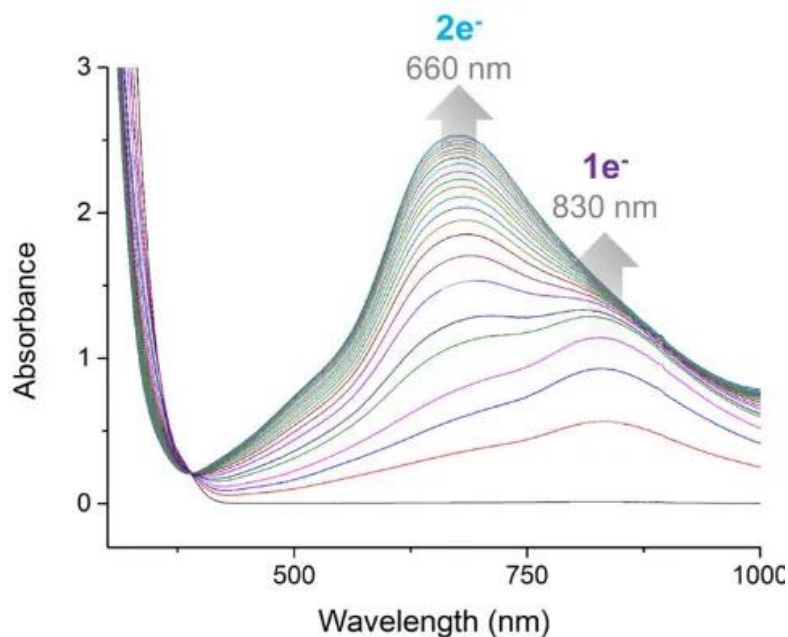


Fig. 2-13. Time resolved UV-vis spectra showing the photoreduction of $[P_2W_{17}O_{61}]^{10-}$

Over 1 h in degassed n-dimethylformamide under irradiation at $\lambda > 390$ nm. Notably, the metal-functionalized clusters are readily reduced by up to two electrons under visible light in the absence of oxygen. Data is shown at 2 minutes intervals [151].

1. POMs have a definite and stable structure, which is conducive to the design and synthesis of catalysts at the molecular and atomic levels [154].
2. POMs have both acidic and oxidizing properties. It can be acid, oxidant or bifunctional catalyst. Under the condition of not changing the anion structure of POMs, by selecting the constituent elements (coordinating atom, central atom and counter ion, etc.), the catalytic performance can be system regulation [155].
3. POMs are soluble in polar solvents and can be used in homogeneous and heterogeneous reaction systems [156].

4. POMs Have a unique reaction field. In a solid-phase catalytic reaction, polar molecules can enter the bulk phase of the catalyst and have a "pseudo-liquid phase" behavior that turns the entire bulk phase into a reaction field [157].

5. The softness of heteropolyanions. Heteropolyanions are soft bases, as ligands for metal ions or organometals, they have unique coordination capabilities and can stabilize reaction intermediates [158].

By the early part of the twentieth century several hundred "heteropoly" compounds had been prepared and analyzed by many research groups [159]. Polyoxometalates (POMs) form a large and distinctive class of molecular inorganic compounds of unrivaled electronic versatility and structural variation, that impacts many fields of science and technology, such as chemistry, catalysis, materials science, biology, and medicine. These substances continue to attract increasing attention worldwide [129].

2.5. Decatungstate

Decatungstate ($W_{10}O_{32}^{4-}$) is one kind of the isopolyoxometalates, which has an octahedral structure, shown in the **Fig. 2-14**. Due to the promising photocatalytic activity, the $W_{10}O_{32}^{4-}$ was chosen as the catalyst in organic synthesis and water depollution [160].

2.5.1. Mechanistic aspects of decatungstate ($W_{10}O_{32}^{4-}$) photoexcitation

The decatungstate ($W_{10}O_{32}^{4-}$) photoexcitation performance has attracted the attention of many researchers. The UV-Vis spectra and laser transient absorption spectroscopy could be used to characterize decatungstate [162]. Illumination of $W_{10}O_{32}^{4-}$ under UV light (ranged at

300-400 nm), leads to the formation of excited state of decatungstate ($W_{10}O_{32}^{4-*}$) that has an oxygen-to-metal charge transfer (LMCT) character. And this character can be highlighted by nano- and microsecond laser flash photolysis experiments [160]. $W_{10}O_{32}^{4-*}$ as the primary LMCT excited state, was formed upon absorption of a UV photon, which was demonstrated by the picosecond flash excitation experiments [163]. In addition, this excited species can survive for ca. 30 ps in both aerated and deaerated acetonitrile and aqueous solution, then can decay to an extremely reactive non-emissive transient (a dark state tagged wO), which has a lifetime τ_{wO} of 65 ± 5 ns in the case of sodium decatungstate and its formation quantum yield Φ_{wO} is 0.57 [164]. And this intermediate triplet state is the actual chemically active species and shares an oxyradical-like character ($\bullet wOH$), due to the presence of an electron-deficient oxygen center [165]. While wO cannot be quenched by O_2 , so it is claimed as a relaxed state. And the singlet oxygen can neither be produced when initial species ($W_{10}O_{32}^{4-}$) nor can it be formed when wO is generated under illumination in O_2 -saturated acetonitrile solution [165]. Such reaction between wO and appropriate hydrogen or/and electron donor leads to the formation of the one electron reduced form of decatungstate $W_{10}O_{32}^{5-}$ that absorbs in the visible region with a maximum at 778 nm. The reduction of molecular oxygen to superoxide anion by such species is an efficient process for the regeneration of the starting catalyst, $W_{10}O_{32}^{4-}$.

2.5.2. The application of decatungstate

The two main fields where decatungstate salts (ammonium, potassium, sodium, etc.) were used upon solar light absorption are (i) synthesis (formation of C-C, C-N, or C-O bonds, photo-oxidations) and (ii) depollution [160].

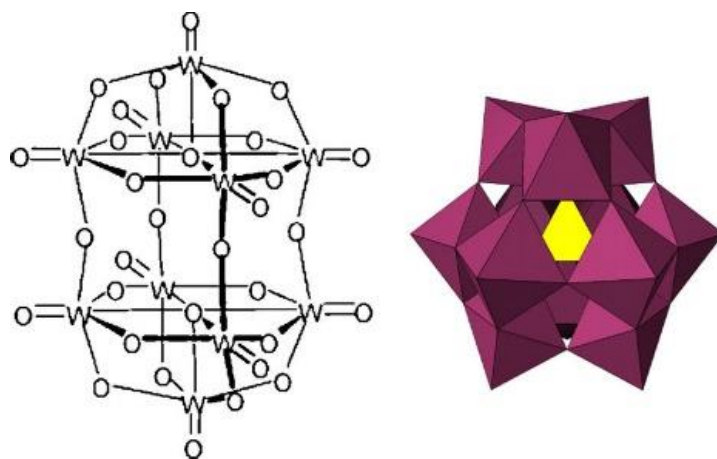


Fig. 2-14. The structure of the decatungstate [161].

2.5.2.1. Recent works on the application of decatungstate in depollution

Monilari et al. studied [166] the degradation of emerging concern contaminants in water by heterogeneous photocatalysis with $\text{Na}_4\text{W}_{10}\text{O}_{32}$. A new photocatalytic method for removal of atenolol, levofloxacin and trimethoprim (target molecules) from water is proposed. The photoactive species is decatungstate anion both in solution and immobilized on modified silica particles. The degradation process is studied at ambient temperature, atmospheric pressure and at pH values similar to that of natural waters. The $\cdot\text{OH}$ radicals was proved as the reactive oxygen species (ROS) in degradation process. The heterogeneous catalyst is stable and can be recycled without a significant loss of efficiency thus opening the possibility of developing new solid materials with interesting photocatalytic performance.

Yang et al. studied [167] visible-near-infrared-responsive $\text{g-C}_3\text{N}_4\text{H}_x^+$ reduced decatungstate with excellent performance for photocatalytic removal of petroleum hydrocarbon. They demonstrated a well-defined visible-near-infrared-responsive $\text{g-C}_3\text{N}_4\text{H}_x^+$ reduced decatungstate charge-transfer salt (RCD-CTS), which possess efficient light-absorption ability

ranging from visible light to the near infrared region. The RCD-CTS photocatalyst exhibits excellent performance for photocatalytic removal of petroleum hydrocarbon. The strong chemical interaction between components and partly reduction of decatungstate cause the plasmonic properties and the absorption of near infrared light was confirmed by the structural characterization and theoretical calculation

Wang et al. studied [168] the electrostatic polypyridine–ruthenium(II)···decatungstate dyads: structures, characterizations and photodegradation of dye. Two hybrids, $[\text{Ru}(\text{bpy})_2(\text{CH}_3\text{CN})_2]_2[\text{W}_{10}\text{O}_{32}] \cdot 2\text{CH}_3\text{CN}$ (RuW-1) and $[\text{Ru}(\text{bpy})_3]_2[\text{W}_{10}\text{O}_{32}]$ (RuW-2) (bpy = 2,2'-bipyridine), were synthesized by the reaction of (2,2'-dipyridyl) ruthenium complexes and decatungstate. Photodegradation experiments were performed on Rhodamine B (RhB) dye, spectrophotometric analysis showing an absorbance decrease at 544 nm, with a pseudo-first-order rate constant in the range of 10^{-3} to 10^{-2} s^{-1} . These results demonstrate that the hybrids have effective activity and reusability for the photodegradation of RhB.

Yang et al. studied [169] constructing a novel ternary composite $(\text{C}_{16}\text{H}_{33}(\text{CH}_3)_3\text{N})_4\text{W}_{10}\text{O}_{32}/\text{g}-\text{C}_3\text{N}_4/\text{rGO}$ with enhanced visible-light-driven photocatalytic activity for degradation of dyes and phenol. A novel binary $(\text{C}_{16}\text{H}_{33}(\text{CH}_3)_3\text{N})_4\text{W}_{10}\text{O}_{32}/\text{g}-\text{C}_3\text{N}_4$ and a ternary $(\text{C}_{16}\text{H}_{33}(\text{CH}_3)_3\text{N})_4\text{W}_{10}\text{O}_{32}/\text{g}-\text{C}_3\text{N}_4/\text{rGO}$ photocatalysts were successfully constructed. The photocatalytic properties were evaluated in photodecomposition of aqueous methyl orange and phenol under visible-light irradiations. It has been shown that the obtained binary photocatalytic system exhibited improved photocatalytic activity and enhanced reduced charge recombination as compared with those of $\text{g}-\text{C}_3\text{N}_4$ and $(\text{C}_{16}\text{H}_{33}(\text{CH}_3)_3\text{N})_4\text{W}_{10}\text{O}_{32}$. The ternary photocatalyst was superior to that of the binary one, due to the introduction of graphene

revealed a synergistic effect between the $(C_{16}H_{33}(CH_3)_3N)_4W_{10}O_{32}$ species, g- C_3N_4 and graphene with stronger visible-light absorption and more reduced charge combination. Finally, ternary system can be used six times without loss of activity recycling, this revealed that the ternary composite photocatalyst was not only highly efficient but also robust.

Da Silva et al. studied [170] heterogeneous photocatalytic degradation of pesticides using decatungstate intercalated macroporous layered double hydroxides. Decatungstate $W_{10}O_{32}^{4-}$ was efficiently intercalated between the layers of three-dimensionally ordered macroporous Mg_2Al -layered double hydroxide. The photocatalytic properties of immobilized $W_{10}O_{32}^{4-}$ within Mg_2Al structure were investigated using 2-(1-naphthyl) acetamide (NAD) as a model of pesticide. The influence of different parameters such as amount of catalyst, pH and oxygen concentration were investigated. For example, an optimal NAD degradation was obtained with a photocatalyst concentration of 60 mg L^{-1} . Under our experimental conditions, this heterogeneous photocatalyst induces photodegradation of 60 % of NAD after 17 h of irradiation at 365 nm and at pH 6.6. Interestingly, pesticide photodegradation leads to the mineralization of substrates to H_2O and CO_2 and the photocatalyst can be recycled and reused without any loss of activity over four cycles.

Allaoui et al. studied [171] efficient degradation of methabenzthiazuron photoinduced by decatungstate anion in water: they investigated the elimination of methabenzthiazuron (MBTU) photocatalysed by sodium decatungstate salts in aqueous solution under irradiation at 365 nm. 90% of MBTU (10^{-4} M) is mineralised in the presence of the photocatalyst ($2 \times 10^{-4} \text{ M}$) after 7 days under exposure and the formation of nitrate, sulphate and ammonium confirmed this phenomenon. In aerated conditions, the photodegradation rate of MBTU clearly increased by a

factor of 40 when compared to direct photolysis with $\Phi_{\text{MBTU}} = 2.5 \times 10^{-2}$ and $t_{1/2}(\text{MBTU}) = 1.4$ h. Oxygen appeared essential since 2 times inhibition of MBTU disappearance and the photocatalytic cycle interrupt were observed in the absence of oxygen. Two processes were implied in the degradation: electron transfer and H atom abstraction reactions both involving excited state species. In the primary steps of the degradation, the aromatic ring hydroxylation was observed by electron transfer leading to OH-MBTU isomers and H atom abstraction reaction gave benzthiazuron and a supposed demethylated product. Secondary oxidations permitted the hydroxylation of both products.

Pasti et al. studied [172] an advanced oxidation process by photoexcited heterogeneous sodium decatungstate for the degradation of drugs present in aqueous environment. The ability of decatungstate anion ($\text{W}_{10}\text{O}_{32}^{4-}$) to photoproduce $\bullet\text{OH}$ radicals from water is retained when the polyoxoanion is immobilized on solid supports and can be exploited as a heterogeneous photocatalytic process aimed to water remediation. However, they illustrated that interaction between $\bullet\text{OH}$ radicals and drug molecules depend on the physical chemical properties of the chosen support. And they demonstrate that silica particles covered by decatungstate anions are not efficient in the degradation of organic compounds at operating pH of 6. On the contrary, entrapment of $\text{W}_{10}\text{O}_{32}^{4-}$ inside a mesoporous organosilica matrix leads to a heterogeneous photocatalytic system with proper characteristic of hydrophobicity. Organic molecules enter mesopores and easily leave the aqueous environment. Inside pores, the reaction between photoproduced $\bullet\text{OH}$ radicals is favored. Mono- and di-hydroxylated products precede fragmentation and degradation of the investigated drug.

2.5.2.2 Recent works on the application of decatungstate in selective oxidation

Yang et al. studied [173] the influence of tetraalkylammonium cations on quality of decatungstate and its photocatalytic property in visible light-triggered selective oxidation of organic compounds by O_2 . Three decatungstates were conveniently synthesized respectively using quaternary ammonium cations of tetramethyl, tetrapropyl and tetrabutyl as counterions (marked as TMADT, TPADT and TBADT). The photo-catalysis activity of decatungstate anion for these oxidations gradually increases with the shortening of its cationic alkyl chain, which is attributed to the continuous improvement of its quality from TBADT to TMADT. Furthermore, the addition of water and 12 M hydrogen chloride (HCl) solution and especially the mixture of both can markedly promote the decatungstate-photocatalyzed oxidations and such promotion presents an enhancing trend from TBADT to TMADT.

Xie et al. studied [174] decatungstate-mediated solar photooxidative cleavage of C=C bond using air as an oxidant in water. They first report the combination of direct utilization of solar energy, decatungstate as catalyst, air as the oxidant and water as the solvent for the selective cleavage of C=C double bonds in aryl olefins. Various α -methyl styrenes, diaryl alkenes as well as terminal styrenes are well tolerated in this green and sustainable strategy and furnished the desired carbonyl products in satisfactory yields. Like heterogeneous catalysis, this homogeneous catalytic system could also be reused and it retains good activity even after repeating three times. Mechanism investigations indicated that both $O_2^{\bullet-}$ and 1O_2 were involved in the reaction. Based on these results, two possible mechanisms, including the electron transfer pathway and the energy transfer pathway, were proposed.

Yang et al. studied [175] that adjusting effect of additives on decatungstate-photocatalyzed 5-hydroxymethylfurfural (HMF) oxidation with O₂ under visible light illumination. They disclosed that decatungstate can efficiently catalyze the visible light-triggered oxidation of 5-hydroxymethylfurfural (HMF) with O₂ in MeCN under normal temperature and pressure, affording 2,5-diformylfuran (DFF) and 2,5-furandicarboxylic acid (FDCA) as the oxygenated products. The photo-catalytic efficiency of decatungstate anion depends on its counter cations-regulated synthetic quality and is adjusted significantly by the additives. Among the additives examined, NaBr, dimethyl sulfoxide (DMSO) and 1-butyl-3-methyl-imidazolium chloride ([Bmim]Cl) may obviously improve the carbon balance yield (CBY) of this photo-catalytic oxidation owing to their restraining effect on the light-induced HMF polymerization.

Laudadio et al. studied [176] selective C(sp³)-H aerobic oxidation enabled by decatungstate photocatalysis in flow. A mild and selective C(sp³)-H aerobic oxidation enabled by decatungstate photocatalysis has been developed. The reaction can be significantly improved in a microflow reactor enabling the safe use of oxygen and enhanced irradiation of the reaction mixture. Their method allows for the oxidation of both activated and unactivated C-H bonds (30 examples). The ability to selectively oxidize natural scaffolds, such as (-)-ambroxide, pregnenolone acetate, (+)-sclareolide, and artemisinin, exemplifies the utility of this new method.

Ravelli et al. studied [177] site-selective C-H functionalization by decatungstate anion photocatalysis: synergistic control by polar and steric effects expand the reaction scope. The synergistic control of the S_H² transition states of hydrogen abstraction by polar and steric effects provides a promising strategy in achieving site-selective C(sp³)-H functionalization under

Bibliographic Study

decatungstate anion photocatalysis. By using this photocatalytic approach, the C–H bonds of alkanes, alcohols, ethers, ketones, amides, esters, nitriles, and pyridylalkanes were functionalized site-selectively. In the remarkable case of a 2,4-disubstituted cyclohexanone bearing five methyl or five methylene, and three methine C–H bonds, one methine C–H bond in the isoamyl ether was selectively functionalized.

Summery

Hence, in this study, on the premise of fully grasping the basic principles of photochemistry and the basic properties of decatungstate, the decatungstate prepared in the laboratory was used as the photocatalyst, the deep research has been carried out on the catalytic application of deca-tungstate for photodegradation and selective oxidation of organic compounds.

References

- [1] C.H.J. Wells, Introduction to molecular photochemistry, Chapman and Hall, London, 1972.
- [2] N.J. Turro, Modern Molecular Photochemistry, University Science Books, 1991.
- [3] J.J. Wolken, Photoprocesses, Photoreceptors, and Evolution, Academic Press, 2016.
- [4] E. Kohen, R. Santus, J.G. Hirschberg, Photobiology, Elsevier, 1995.
- [5] P.-M. Li, H.-Y. Gao, R.J. Strasser, [Application of the fast chlorophyll fluorescence induction dynamics analysis in photosynthesis study], *Zhi Wu Sheng Li Yu Fen Zi Sheng Wu Xue Xue Bao.* 31 (2005) 559–566.
- [6] Y. Yagci, S. Jockusch, N.J. Turro, Photoinitiated Polymerization: Advances, Challenges, and Opportunities, *Macromolecules.* 43 (2010) 6245–6260.
<https://doi.org/10.1021/ma1007545>.
- [7] N.S. Allen, Photochemistry and Photophysics of Polymeric Materials, John Wiley & Sons, 2010.
- [8] R.C. Evans, P. Douglas, H.D. Burrow, Applied photochemistry, Springer, 2013.
- [9] Y. Liang, A. S. Dvornikov, P. M. Rentzepis, Synthesis and photochemistry of photochromic fluorescing indol-2-ylfulgimides, *Journal of Materials Chemistry.* 10 (2000) 2477–2482. <https://doi.org/10.1039/B002374O>.
- [10] J. Steffens, E. Landulfo, L.C. Courrol, R. Guardani, Application of Fluorescence to the Study of Crude Petroleum, *J Fluoresc.* 21 (2011) 859–864.
<https://doi.org/10.1007/s10895-009-0586-4>.

- [11] Y. Matsuda, V.M. Chapman, Application of fluorescence in situ hybridization in genome analysis of the mouse, *ELECTROPHORESIS*. 16 (1995) 261–272. <https://doi.org/10.1002/elps.1150160142>.
- [12] R. Tomaschek, On the application of phosphorescence spectra to the investigation of the structure of solids and solutions, *Transactions of the Faraday Society*. 35 (1939) 148–154.
- [13] Z. Zhou, D. Li, H. Yang, Y. Zhu, S. Yang, Synthesis of d–f coordination polymer nanoparticles and their application in phosphorescence and magnetic resonance imaging, *Dalton Transactions*. 40 (2011) 11941–11944.
- [14] E. De Laurentiis, M. Minella, V. Maurino, C. Minero, D. Vione, Effects of climate change on surface-water photochemistry: a review, *Environ Sci Pollut Res*. 21 (2014) 11770–11780. <https://doi.org/10.1007/s11356-013-2343-0>.
- [15] M. Sturini, A. Speltini, F. Maraschi, L. Pretali, A. Profumo, E. Fasani, A. Albini, Environmental photochemistry of fluoroquinolones in soil and in aqueous soil suspensions under solar light, *Environ Sci Pollut Res*. 21 (2014) 13215–13221. <https://doi.org/10.1007/s11356-013-2124-9>.
- [16] C. George, M. Ammann, B. D’Anna, D.J. Donaldson, S.A. Nizkorodov, Heterogeneous Photochemistry in the Atmosphere, *Chem. Rev*. 115 (2015) 4218–4258. <https://doi.org/10.1021/cr500648z>.
- [17] S. Rayne, K. Forest, K.J. Friesen, Mechanistic aspects regarding the direct aqueous environmental photochemistry of phenol and its simple halogenated derivatives. A review, *Environment International*. 35 (2009) 425–437. <https://doi.org/10.1016/j.envint.2008.09.004>.

- [18] J. Levine, *The Photochemistry of Atmospheres*, Elsevier, 2012.
- [19] L. Carlos, D.O. Mártire, M.C. Gonzalez, J. Gomis, A. Bernabeu, A.M. Amat, A. Arques, Photochemical fate of a mixture of emerging pollutants in the presence of humic substances, *Water Research*. 46 (2012) 4732–4740. <https://doi.org/10.1016/j.watres.2012.06.022>.
- [20] J.J. Guerard, Y.-P. Chin, H. Mash, C.M. Hadad, Photochemical Fate of Sulfadimethoxine in Aquaculture Waters, *Environ. Sci. Technol.* 43 (2009) 8587–8592. <https://doi.org/10.1021/es9020537>.
- [21] L. Carena, S. Comis, D. Vione, Geographical and temporal assessment of the photochemical decontamination potential of river waters from agrochemicals: A first application to the Piedmont region (NW Italy), *Chemosphere*. 263 (2021) 127921. <https://doi.org/10.1016/j.chemosphere.2020.127921>.
- [22] S. Malato, J. Blanco, D.C. Alarcón, M.I. Maldonado, P. Fernández-Ibáñez, W. Gernjak, Photocatalytic decontamination and disinfection of water with solar collectors, *Catalysis Today*. 122 (2007) 137–149. <https://doi.org/10.1016/j.cattod.2007.01.034>.
- [23] B. David, M. Lhote, V. Faure, P. Boule, Ultrasonic and photochemical degradation of chlorpropham and 3-chloroaniline in aqueous solution, *Water Research*. 32 (1998) 2451–2461. [https://doi.org/10.1016/S0043-1354\(97\)00477-6](https://doi.org/10.1016/S0043-1354(97)00477-6).
- [24] K.C. Le, *Raman spectroscopy of soot produced in low pressure flames : ex situ Analyses and Online Gas Phase Studies*, 2017.
- [25] J. Bérdy, Bioactive Microbial Metabolites, *J Antibiot.* 58 (2005) 1–26. <https://doi.org/10.1038/ja.2005.1>.

- [26] S. Li, W. Shi, W. Liu, H. Li, W. Zhang, J. Hu, Y. Ke, W. Sun, J. Ni, A duodecennial national synthesis of antibiotics in China's major rivers and seas (2005–2016), *Science of The Total Environment*. 615 (2018) 906–917. <https://doi.org/10.1016/j.scitotenv.2017.09.328>.
- [27] E. Felis, J. Kalka, A. Sochacki, K. Kowalska, S. Bajkacz, M. Harnisz, E. Korzeniewska, Antimicrobial pharmaceuticals in the aquatic environment - occurrence and environmental implications, *European Journal of Pharmacology*. 866 (2020) 172813. <https://doi.org/10.1016/j.ejphar.2019.172813>.
- [28] Y. Hu, H. Cheng, S. Tao, Environmental and human health challenges of industrial livestock and poultry farming in China and their mitigation, *Environment International*. 107 (2017) 111–130. <https://doi.org/10.1016/j.envint.2017.07.003>.
- [29] L. Gao, Y. Shi, W. Li, H. Niu, J. Liu, Y. Cai, Occurrence of antibiotics in eight sewage treatment plants in Beijing, China, *Chemosphere*. 86 (2012) 665–671. <https://doi.org/10.1016/j.chemosphere.2011.11.019>.
- [30] P.K. Mutiyar, A.K. Mittal, Occurrences and fate of selected human antibiotics in influents and effluents of sewage treatment plant and effluent-receiving river Yamuna in Delhi (India), *Environ Monit Assess*. 186 (2014) 541–557. <https://doi.org/10.1007/s10661-013-3398-6>.
- [31] H. Jiang, D. Zhang, S. Xiao, C. Geng, X. Zhang, Occurrence and sources of antibiotics and their metabolites in river water, WWTPs, and swine wastewater in Jiulongjiang River basin, south China, *Environ Sci Pollut Res*. 20 (2013) 9075–9083. <https://doi.org/10.1007/s11356-013-1924-2>.

- [32] J. Sun, X.-P. Liao, A.W. D'Souza, M. Boolchandani, S.-H. Li, K. Cheng, J.L. Martínez, L. Li, Y.-J. Feng, L.-X. Fang, Environmental remodeling of human gut microbiota and antibiotic resistome in livestock farms, *Nature Communications*. 11 (2020) 1–11.
- [33] N. Wang, X. Guo, J. Xu, X. Kong, S. Gao, Z. Shan, Pollution characteristics and environmental risk assessment of typical veterinary antibiotics in livestock farms in Southeastern China, *Journal of Environmental Science and Health, Part B*. 49 (2014) 468–479.
- [34] B. Eduardo-Correia, H. Morales-Filloo, J.P. Abad, Bacteria From the Multi-Contaminated Tinto River Estuary (SW, Spain) Show High Multi-Resistance to Antibiotics and Point to *Paenibacillus* spp. as Antibiotic-Resistance-Dissemination Players, *Frontiers in Microbiology*. 10 (2020) 3071. <https://doi.org/10.3389/fmicb.2019.03071>.
- [35] W. Deng, N. Li, H. Zheng, H. Lin, Occurrence and risk assessment of antibiotics in river water in Hong Kong, *Ecotoxicology and Environmental Safety*. 125 (2016) 121–127. <https://doi.org/10.1016/j.ecoenv.2015.12.002>.
- [36] R. Zhang, G. Zhang, Q. Zheng, J. Tang, Y. Chen, W. Xu, Y. Zou, X. Chen, Occurrence and risks of antibiotics in the Laizhou Bay, China: Impacts of river discharge, *Ecotoxicology and Environmental Safety*. 80 (2012) 208–215. <https://doi.org/10.1016/j.ecoenv.2012.03.002>.
- [37] K.-L. Chen, L.-C. Liu, W.-R. Chen, Adsorption of sulfamethoxazole and sulfapyridine antibiotics in high organic content soils, *Environmental Pollution*. 231 (2017) 1163–1171. <https://doi.org/10.1016/j.envpol.2017.08.011>.

- [38] M. Uddin, J. Chen, X. Qiao, R. Tian, Y. Arafat, X. Yang, Bacterial community variations in paddy soils induced by application of veterinary antibiotics in plant-soil systems, *Ecotoxicology and Environmental Safety*. 167 (2019) 44–53. <https://doi.org/10.1016/j.ecoenv.2018.09.101>.
- [39] Y. Shao, Y. Wang, Y. Yuan, Y. Xie, A systematic review on antibiotics misuse in livestock and aquaculture and regulation implications in China, *Science of The Total Environment*. 798 (2021) 149205. <https://doi.org/10.1016/j.scitotenv.2021.149205>.
- [40] M. Qiao, G.-G. Ying, A.C. Singer, Y.-G. Zhu, Review of antibiotic resistance in China and its environment, *Environment International*. 110 (2018) 160–172.
- [41] X. Liu, J.C. Steele, X.-Z. Meng, Usage, residue, and human health risk of antibiotics in Chinese aquaculture: A review, *Environmental Pollution*. 223 (2017) 161–169. <https://doi.org/10.1016/j.envpol.2017.01.003>.
- [42] E.Y. Klein, T.P.V. Boeckel, E.M. Martinez, S. Pant, S. Gandra, S.A. Levin, H. Goossens, R. Laxminarayan, Global increase and geographic convergence in antibiotic consumption between 2000 and 2015, *PNAS*. 115 (2018) E3463–E3470. <https://doi.org/10.1073/pnas.1717295115>.
- [43] Y.-G. Zhu, T.A. Johnson, J.-Q. Su, M. Qiao, G.-X. Guo, R.D. Stedtfeld, S.A. Hashsham, J.M. Tiedje, Diverse and abundant antibiotic resistance genes in Chinese swine farms, *PNAS*. 110 (2013) 3435–3440. <https://doi.org/10.1073/pnas.1222743110>.
- [44] M. Hvistendahl, China Takes Aim at Rampant Antibiotic Resistance, *Science*. 336 (2012) 795–795. <https://doi.org/10.1126/science.336.6083.795>.

- [45] T. Kokulnathan, S.-M. Chen, Robust and selective electrochemical detection of antibiotic residues: The case of integrated lutetium vanadate/graphene sheets architectures, *Journal of Hazardous Materials*. 384 (2020) 121304. <https://doi.org/10.1016/j.jhazmat.2019.121304>.
- [46] Q.-Q. Zhang, G.-G. Ying, C.-G. Pan, Y.-S. Liu, J.-L. Zhao, Comprehensive Evaluation of Antibiotics Emission and Fate in the River Basins of China: Source Analysis, Multimedia Modeling, and Linkage to Bacterial Resistance, *Environ. Sci. Technol.* 49 (2015) 6772–6782. <https://doi.org/10.1021/acs.est.5b00729>.
- [47] J. Muhammad, S. Khan, J.Q. Su, A.E.-L. Hesham, A. Ditta, J. Nawab, A. Ali, Antibiotics in poultry manure and their associated health issues: a systematic review, *Journal of Soils and Sediments*. 20 (2020) 486–497.
- [48] Y.-J. Lee, S.-E. Lee, D.S. Lee, Y.-H. Kim, Risk assessment of human antibiotics in Korean aquatic environment, *Environmental Toxicology and Pharmacology*. 26 (2008) 216–221.
- [49] S. Al-Maadheed, I. Goktepe, A.B.A. Latiff, B. Shomar, Antibiotics in hospital effluent and domestic wastewater treatment plants in Doha, Qatar, *Journal of Water Process Engineering*. 28 (2019) 60–68.
- [50] A.N. Ngigi, M.M. Magu, B.M. Muendo, Occurrence of antibiotics residues in hospital wastewater, wastewater treatment plant, and in surface water in Nairobi County, Kenya, *Environ Monit Assess.* 192 (2019) 18. <https://doi.org/10.1007/s10661-019-7952-8>.
- [51] D.J. Larsson, C. de Pedro, N. Paxeus, Effluent from drug manufactures contains extremely high levels of pharmaceuticals, *Journal of Hazardous Materials*. 148 (2007) 751–755.

- [52] O. Cardoso, J.-M. Porcher, W. Sanchez, Factory-discharged pharmaceuticals could be a relevant source of aquatic environment contamination: review of evidence and need for knowledge, *Chemosphere*. 115 (2014) 20–30.
- [53] C. Bouki, D. Venieri, E. Diamadopoulos, Detection and fate of antibiotic resistant bacteria in wastewater treatment plants: A review, *Ecotoxicology and Environmental Safety*. 91 (2013) 1–9. <https://doi.org/10.1016/j.ecoenv.2013.01.016>.
- [54] Y. Chen, W. Shen, B. Wang, X. Zhao, L. Su, M. Kong, H. Li, S. Zhang, J. Li, Occurrence and fate of antibiotics, antimicrobial resistance determinants and potential human pathogens in a wastewater treatment plant and their effects on receiving waters in Nanjing, China, *Ecotoxicology and Environmental Safety*. 206 (2020) 111371.
- [55] K.D. Brown, J. Kulis, B. Thomson, T.H. Chapman, D.B. Mawhinney, Occurrence of antibiotics in hospital, residential, and dairy effluent, municipal wastewater, and the Rio Grande in New Mexico, *Science of The Total Environment*. 366 (2006) 772–783. <https://doi.org/10.1016/j.scitotenv.2005.10.007>.
- [56] E. Aubertheau, T. Stalder, L. Mondamert, M.-C. Ploy, C. Dagot, J. Labanowski, Impact of wastewater treatment plant discharge on the contamination of river biofilms by pharmaceuticals and antibiotic resistance, *Science of The Total Environment*. 579 (2017) 1387–1398. <https://doi.org/10.1016/j.scitotenv.2016.11.136>.
- [57] X.-S. Miao, F. Bishay, M. Chen, C.D. Metcalfe, Occurrence of Antimicrobials in the Final Effluents of Wastewater Treatment Plants in Canada, *Environ. Sci. Technol.* 38 (2004) 3533–3541. <https://doi.org/10.1021/es030653q>.

- [58] M. Gonzalez Ronquillo, J.C. Angeles Hernandez, Antibiotic and synthetic growth promoters in animal diets: Review of impact and analytical methods, *Food Control*. 72 (2017) 255–267. <https://doi.org/10.1016/j.foodcont.2016.03.001>.
- [59] Z. Chen, X. Jiang, Microbiological Safety of Chicken Litter or Chicken Litter-Based Organic Fertilizers: A Review, *Agriculture*. 4 (2014) 1–29. <https://doi.org/10.3390/agriculture4010001>.
- [60] S. Choi, W. Sim, D. Jang, Y. Yoon, J. Ryu, J. Oh, J.-S. Woo, Y.M. Kim, Y. Lee, Antibiotics in coastal aquaculture waters: Occurrence and elimination efficiency in oxidative water treatment processes, *Journal of Hazardous Materials*. 396 (2020) 122585.
- [61] S.M. Aly, A. Albutti, Antimicrobials use in aquaculture and their public health impact, *Journal of Aquaculture Research & Development*. 5 (2014) 1.
- [62] N. Kemper, Veterinary antibiotics in the aquatic and terrestrial environment, *Ecological Indicators*. 8 (2008) 1–13. <https://doi.org/10.1016/j.ecolind.2007.06.002>.
- [63] R.J. Carman, M.A. Simon, H.E. Petzold, R.F. Wimmer, M.R. Batra, A.H. Fernández, M.A. Miller, M. Bartholomew, Antibiotics in the human food chain: Establishing no effect levels of tetracycline, neomycin, and erythromycin using a chemostat model of the human colonic microflora, *Regulatory Toxicology and Pharmacology*. 43 (2005) 168–180. <https://doi.org/10.1016/j.yrtph.2005.06.005>.
- [64] M. Arshad, R. Zafar, Chapter 9 - Antibiotics, AMRs, and ARGs: fate in the environment, in: M.Z. Hashmi (Ed.), *Antibiotics and Antimicrobial Resistance Genes in the Environment*, Elsevier, 2020: pp. 138–154. <https://doi.org/10.1016/B978-0-12-818882-8.00009-7>.

- [65] S. Liu, T.-G. Bekele, H. Zhao, X. Cai, J. Chen, Bioaccumulation and tissue distribution of antibiotics in wild marine fish from Laizhou Bay, North China, *Science of The Total Environment*. 631–632 (2018) 1398–1405. <https://doi.org/10.1016/j.scitotenv.2018.03.139>.
- [66] B.H. Schafhauser, L.A. Kristofco, C.M.R. de Oliveira, B.W. Brooks, Global review and analysis of erythromycin in the environment: Occurrence, bioaccumulation and antibiotic resistance hazards, *Environmental Pollution*. 238 (2018) 440–451. <https://doi.org/10.1016/j.envpol.2018.03.052>.
- [67] H. Yoneyama, R. Katsumata, Antibiotic Resistance in Bacteria and Its Future for Novel Antibiotic Development, *Bioscience, Biotechnology, and Biochemistry*. 70 (2006) 1060–1075. <https://doi.org/10.1271/bbb.70.1060>.
- [68] R.-N. Wang, Y. Zhang, Z.-H. Cao, X.-Y. Wang, B. Ma, W.-B. Wu, N. Hu, Z.-Y. Huo, Q.-B. Yuan, Occurrence of super antibiotic resistance genes in the downstream of the Yangtze River in China: Prevalence and antibiotic resistance profiles, *Science of The Total Environment*. 651 (2019) 1946–1957. <https://doi.org/10.1016/j.scitotenv.2018.10.111>.
- [69] J. Lach, L. Stępnia, A. Ociepa-Kubicka, Antibiotics in the Environment as one of the Barriers to Sustainable Development, *Problemy Ekorozwoju*. Vol. 13 (2018). <http://yadda.icm.edu.pl/yadda/element/bwmeta1.element.baztech-1a9a2f02-e394-4049-939c-69c4d561fe7c> (accessed October 13, 2021).
- [70] W. Yang, Z. Tang, F. Zhou, W. Zhang, L. Song, Toxicity studies of tetracycline on *Microcystis aeruginosa* and *Selenastrum capricornutum*, *Environmental Toxicology and Pharmacology*. 35 (2013) 320–324. <https://doi.org/10.1016/j.etap.2013.01.006>.

- [71] W.H. Glaze, Drinking-water treatment with ozone, *Environmental Science & Technology*. 21 (1987) 224–230.
- [72] W.H. Glaze, J.-W. Kang, D.H. Chapin, The chemistry of water treatment processes involving ozone, hydrogen peroxide and ultraviolet radiation, (1987).
- [73] W.R. Haag, J. Hoigné, Photo-sensitized oxidation in natural water via •OH radicals, *Chemosphere*. 14 (1985) 1659–1671. [https://doi.org/10.1016/0045-6535\(85\)90107-9](https://doi.org/10.1016/0045-6535(85)90107-9).
- [74] T.A. Kurniawan, W. Lo, G.Y.S. Chan, Radicals-catalyzed oxidation reactions for degradation of recalcitrant compounds from landfill leachate, *Chemical Engineering Journal*. 125 (2006) 35–57. <https://doi.org/10.1016/j.cej.2006.07.006>.
- [75] J. Peller, O. Wiest, P.V. Kamat, Sonolysis of 2,4-Dichlorophenoxyacetic Acid in Aqueous Solutions. Evidence for •OH-Radical-Mediated Degradation, *J. Phys. Chem. A*. 105 (2001) 3176–3181. <https://doi.org/10.1021/jp003478y>.
- [76] S. Zhu, B. Dong, Y. Yu, L. Bu, J. Deng, S. Zhou, Heterogeneous catalysis of ozone using ordered mesoporous Fe₃O₄ for degradation of atrazine, *Chemical Engineering Journal*. 328 (2017) 527–535. <https://doi.org/10.1016/j.cej.2017.07.083>.
- [77] S.A. Snyder, E.C. Wert, D.J. Rexing, R.E. Zegers, D.D. Drury, Ozone Oxidation of Endocrine Disruptors and Pharmaceuticals in Surface Water and Wastewater, *Ozone: Science & Engineering*. 28 (2006) 445–460. <https://doi.org/10.1080/01919510601039726>.
- [78] Y. Liu, Y. Zhao, J. Wang, Fenton/Fenton-like processes with in-situ production of hydrogen peroxide/hydroxyl radical for degradation of emerging contaminants: advances and prospects, *Journal of Hazardous Materials*. 404 (2021) 124191.

- [79] B.M. Esteves, C.S. Rodrigues, F.J. Maldonado-Hódar, L.M. Madeira, Treatment of high-strength olive mill wastewater by combined Fenton-like oxidation and coagulation/flocculation, *Journal of Environmental Chemical Engineering*. 7 (2019) 103252.
- [80] C.A. Martínez-Huitle, M. Panizza, Electrochemical oxidation of organic pollutants for wastewater treatment, *Current Opinion in Electrochemistry*. 11 (2018) 62–71. <https://doi.org/10.1016/j.coelec.2018.07.010>.
- [81] J.J. Rueda Márquez, I. Levchuk, M. Sillanpää, Application of Catalytic Wet Peroxide Oxidation for Industrial and Urban Wastewater Treatment: A Review, *Catalysts*. 8 (2018) 673. <https://doi.org/10.3390/catal8120673>.
- [82] B. Xing, H. Chen, X. Zhang, Efficient degradation of organic phosphorus in glyphosate wastewater by catalytic wet oxidation using modified activated carbon as a catalyst, *Environmental Technology*. 39 (2018) 749–758. <https://doi.org/10.1080/09593330.2017.1310935>.
- [83] Y. Zhang, C. Yang, Y. Li, Y. Huang, J. Zhang, Y. Zhang, Q. Li, Ultrasonic extraction and oxidation characteristics of functional groups during coal spontaneous combustion, *Fuel*. 242 (2019) 287–294. <https://doi.org/10.1016/j.fuel.2019.01.043>.
- [84] Y. Wang, H. Li, P. Yi, H. Zhang, Degradation of clofibric acid by UV, O₃ and UV/O₃ processes: Performance comparison and degradation pathways, *Journal of Hazardous Materials*. 379 (2019) 120771.

- [85] W. Yao, S.W.U. Rehman, H. Wang, H. Yang, G. Yu, Y. Wang, Pilot-scale evaluation of micropollutant abatements by conventional ozonation, UV/O₃, and an electro-peroxone process, *Water Research*. 138 (2018) 106–117.
- [86] Y.-M. Lee, G. Lee, K.-D. Zoh, Benzophenone-3 degradation via UV/H₂O₂ and UV/persulfate reactions, *Journal of Hazardous Materials*. 403 (2021) 123591. <https://doi.org/10.1016/j.jhazmat.2020.123591>.
- [87] W. Zhang, S. Zhou, J. Sun, X. Meng, J. Luo, D. Zhou, J. Crittenden, Impact of Chloride Ions on UV/H₂O₂ and UV/Persulfate Advanced Oxidation Processes, *Environ. Sci. Technol*. 52 (2018) 7380–7389. <https://doi.org/10.1021/acs.est.8b01662>.
- [88] M.R. Al-Mamun, S. Kader, M.S. Islam, M.Z.H. Khan, Photocatalytic activity improvement and application of UV-TiO₂ photocatalysis in textile wastewater treatment: A review, *Journal of Environmental Chemical Engineering*. 7 (2019) 103248. <https://doi.org/10.1016/j.jece.2019.103248>.
- [89] C.H. Wu, C.Y. Kuo, C.D. Dong, C.W. Chen, Y.L. Lin, Removal of sulfonamides from wastewater in the UV/TiO₂ system: effects of pH and salinity on photodegradation and mineralization, *Water Science and Technology*. 79 (2019) 349–355. <https://doi.org/10.2166/wst.2019.053>.
- [90] Y. Ahmed, J. Lu, Z. Yuan, P.L. Bond, J. Guo, Efficient inactivation of antibiotic resistant bacteria and antibiotic resistance genes by photo-Fenton process under visible LED light and neutral pH, *Water Research*. 179 (2020) 115878.

- [91] C.-H. Han, H.-D. Park, S.-B. Kim, V. Yargeau, J.-W. Choi, S.-H. Lee, J.-A. Park, Oxidation of tetracycline and oxytetracycline for the photo-Fenton process: Their transformation products and toxicity assessment, *Water Research*. 172 (2020) 115514.
- [92] R. Mosteo, A.V. Lopez, D. Muzard, N. Benitez, S. Giannakis, C. Pulgarin, Visible light plays a significant role during bacterial inactivation by the photo-fenton process, even at sub-critical light intensities, *Water Research*. 174 (2020) 115636.
- [93] L. Tang, Y. Liu, J. Wang, G. Zeng, Y. Deng, H. Dong, H. Feng, J. Wang, B. Peng, Enhanced activation process of persulfate by mesoporous carbon for degradation of aqueous organic pollutants: Electron transfer mechanism, *Applied Catalysis B: Environmental*. 231 (2018) 1–10. <https://doi.org/10.1016/j.apcatb.2018.02.059>.
- [94] F. Wang, H. Fu, F.-X. Wang, X.-W. Zhang, P. Wang, C. Zhao, C.-C. Wang, Enhanced catalytic sulfamethoxazole degradation via peroxymonosulfate activation over amorphous CoS_x@ SiO₂ nanocages derived from ZIF-67, *Journal of Hazardous Materials*. 423 (2022) 126998.
- [95] N. Liu, N. Lu, H. Yu, S. Chen, X. Quan, Enhanced degradation of organic water pollutants by photocatalytic in-situ activation of sulfate based on Z-scheme g-C₃N₄/BiPO₄, *Chemical Engineering Journal*. 428 (2022) 132116.
- [96] O.K. Nayna, S.M. Tareq, 13 - Application of Semiconductor Nanoparticles for Removal of Organic Pollutants or Dyes From Wastewater, in: A. Ahsan, A.F. Ismail (Eds.), *Nanotechnology in Water and Wastewater Treatment*, Elsevier, 2019: pp. 267–290. <https://doi.org/10.1016/B978-0-12-813902-8.00013-7>.

- [97] M.B. Tahir, T. Iqbal, M. Rafique, M.S. Rafique, T. Nawaz, M. Sagir, Chapter 5 - Nanomaterials for photocatalysis, in: M.B. Tahir, M. Rafique, M.S. Rafique (Eds.), *Nanotechnology and Photocatalysis for Environmental Applications*, Elsevier, 2020: pp. 65–76. <https://doi.org/10.1016/B978-0-12-821192-2.00005-X>.
- [98] K. Hou, Z. Pi, F. Yao, B. Wu, L. He, X. Li, D. Wang, H. Dong, Q. Yang, A critical review on the mechanisms of persulfate activation by iron-based materials: Clarifying some ambiguity and controversies, *Chemical Engineering Journal*. 407 (2021) 127078.
- [99] H. Luo, Y. Zeng, D. He, X. Pan, Application of iron-based materials in heterogeneous advanced oxidation processes for wastewater treatment: A review, *Chemical Engineering Journal*. 407 (2021) 127191.
- [100] G. Vilardi, J.M. Ochando-Pulido, M. Stoller, N. Verdone, L. Di Palma, Fenton oxidation and chromium recovery from tannery wastewater by means of iron-based coated biomass as heterogeneous catalyst in fixed-bed columns, *Chemical Engineering Journal*. 351 (2018) 1–11. <https://doi.org/10.1016/j.cej.2018.06.095>.
- [101] Y. Wu, Application of Fe(III)-EDDS complex in advanced oxidation processes : 4-ter-butylphenol degradation, These de doctorat, Clermont-Ferrand 2, 2014. <http://www.theses.fr/2014CLF22455> (accessed October 14, 2021).
- [102] K. Barbusiński, Henry John Horstman Fenton - short biography and brief history of Fenton reagent discovery, *Chemistry-Didactics-Ecology-Metrology*. R. 14, NR 1-2 (2009). <http://yadda.icm.edu.pl/yadda/element/bwmeta1.element.baztech-e7e48cd5-3aac-423f-a343-d0d8ded71b8d> (accessed October 14, 2021).

- [103] H. Fallmann, T. Krutzler, R. Bauer, S. Malato, J. Blanco, Applicability of the Photo-Fenton method for treating water containing pesticides, *Catalysis Today*. 54 (1999) 309–319.
- [104] L. Fu, S.-J. You, G. Zhang, F.-L. Yang, X. Fang, Degradation of azo dyes using in-situ Fenton reaction incorporated into H₂O₂-producing microbial fuel cell, *Chemical Engineering Journal*. 160 (2010) 164–169. <https://doi.org/10.1016/j.cej.2010.03.032>.
- [105] P.L. Huston, J.J. Pignatello, Degradation of selected pesticide active ingredients and commercial formulations in water by the photo-assisted Fenton reaction, *Water Research*. 33 (1999) 1238–1246.
- [106] B. Jain, A.K. Singh, H. Kim, E. Lichtfouse, V.K. Sharma, Treatment of organic pollutants by homogeneous and heterogeneous Fenton reaction processes, *Environmental Chemistry Letters*. 16 (2018) 947–967.
- [107] T. Mackul'ak, K. Nagyová, M. Faberová, R. Grabic, O. Koba, M. Gál, L. Birošová, Utilization of Fenton-like reaction for antibiotics and resistant bacteria elimination in different parts of WWTP, *Environmental Toxicology and Pharmacology*. 40 (2015) 492–497.
- [108] H.-J. Benkelberg, P. Warneck, Photodecomposition of iron (III) hydroxo and sulfato complexes in aqueous solution: wavelength dependence of OH and SO⁴⁻ quantum yields, *The Journal of Physical Chemistry*. 99 (1995) 5214–5221.
- [109] C. Lee, J. Yoon, Temperature dependence of hydroxyl radical formation in the hv/Fe³⁺/H₂O₂ and Fe³⁺/H₂O₂ systems, *Chemosphere*. 56 (2004) 923–934. <https://doi.org/10.1016/j.chemosphere.2004.04.047>.

- [110] L.J. Thénard, Observations sur les combinaisons nouvelle entre l'oxygen et divers acides, *Ann. Chim. Phys.* 8 (1818) 306–312.
- [111] J. Radjenovic, M.J. Farré, W. Gernjak, Effect of UV and UV/H₂O₂ in the presence of chloramines on NDMA formation potential of tramadol, *Environmental Science & Technology.* 46 (2012) 8356–8364.
- [112] Y. Pi, J. Schumacher, M. Jekel, Decomposition of aqueous ozone in the presence of aromatic organic solutes, *Water Research.* 39 (2005) 83–88.
<https://doi.org/10.1016/j.watres.2004.09.004>.
- [113] H. Tomiyasu, H. Fukutomi, G. Gordon, Kinetics and mechanism of ozone decomposition in basic aqueous solution, *Inorg. Chem.* 24 (1985) 2962–2966.
<https://doi.org/10.1021/ic00213a018>.
- [114] V. Kitsiou, N. Filippidis, D. Mantzavinos, I. Poullos, Heterogeneous and homogeneous photocatalytic degradation of the insecticide imidacloprid in aqueous solutions, *Applied Catalysis B: Environmental.* 86 (2009) 27–35.
<https://doi.org/10.1016/j.apcatb.2008.07.018>.
- [115] S.R. Pouran, A. Bayrami, M.S. Shafeeyan, A.A.A. Raman, W.M.A.W. Daud, A comparative study on a cationic dye removal through homogeneous and heterogeneous Fenton oxidation systems, *Acta Chimica Slovenica.* 65 (2018) 166–171.
- [116] I.I. Moiseev, *Catalysis: 2000 Ad1, Kinetics and Catalysis.* 42 (2001) 1–22.
- [117] R.A. Sheldon, I.W. Arends, G.-J. Ten Brink, A. Dijksman, Green, catalytic oxidations of alcohols, *Accounts of Chemical Research.* 35 (2002) 774–781.

- [118] S. Kim, Y.F. Tsang, E.E. Kwon, K.-Y.A. Lin, J. Lee, Recently developed methods to enhance stability of heterogeneous catalysts for conversion of biomass-derived feedstocks, *Korean Journal of Chemical Engineering*. 36 (2019) 1–11.
- [119] Y. Shiraishi, H. Sakamoto, K. Fujiwara, S. Ichikawa, T. Hirai, Selective Photocatalytic Oxidation of Aniline to Nitrosobenzene by Pt Nanoparticles Supported on TiO₂ under Visible Light Irradiation, *ACS Catal.* 4 (2014) 2418–2425. <https://doi.org/10.1021/cs500447n>.
- [120] S. Fountoulaki, P.L. Gkizis, T.S. Symeonidis, E. Kaminioti, A. Karina, I. Tamiolakis, G.S. Armatas, I.N. Lykakis, Titania-Supported Gold Nanoparticles Catalyze the Selective Oxidation of Amines into Nitroso Compounds in the Presence of Hydrogen Peroxide, *Advanced Synthesis & Catalysis*. 358 (2016) 1500–1508. <https://doi.org/10.1002/adsc.201500957>.
- [121] K. Maeda, Photocatalytic water splitting using semiconductor particles: History and recent developments, *Journal of Photochemistry and Photobiology C: Photochemistry Reviews*. 12 (2011) 237–268. <https://doi.org/10.1016/j.jphotochemrev.2011.07.001>.
- [122] J.S. Jang, H.G. Kim, J.S. Lee, Heterojunction semiconductors: A strategy to develop efficient photocatalytic materials for visible light water splitting, *Catalysis Today*. 185 (2012) 270–277.
- [123] A.-W. Xu, Y. Gao, H.-Q. Liu, The preparation, characterization, and their photocatalytic activities of rare-earth-doped TiO₂ nanoparticles, *Journal of Catalysis*. 207 (2002) 151–157.

- [124] M.T. Thein, S.-Y. Pung, A. Aziz, M. Itoh, The role of ammonia hydroxide in the formation of ZnO hexagonal nanodisks using sol–gel technique and their photocatalytic study, *Journal of Experimental Nanoscience*. 10 (2015) 1068–1081. <https://doi.org/10.1080/17458080.2014.953609>.
- [125] R. Qian, H. Zong, J. Schneider, G. Zhou, T. Zhao, Y. Li, J. Yang, D.W. Bahnemann, J.H. Pan, Charge carrier trapping, recombination and transfer during TiO₂ photocatalysis: An overview, *Catalysis Today*. 335 (2019) 78–90. <https://doi.org/10.1016/j.cattod.2018.10.053>.
- [126] A. Kumar, A Review on the Factors Affecting the Photocatalytic Degradation of Hazardous Materials, *Material Science & Engineering International Journal*. 1 (2017). <https://doi.org/10.15406/mseij.2017.01.00018>.
- [127] A. Kutuzova, T. Dontsova, W. Kwapinski, Application of TiO₂-Based Photocatalysts to Antibiotics Degradation: Cases of Sulfamethoxazole, Trimethoprim and Ciprofloxacin, *Catalysts*. 11 (2021) 728. <https://doi.org/10.3390/catal11060728>.
- [128] X. Chen, Y. Zhou, V.A. Roy, S.-T. Han, Evolutionary metal oxide clusters for novel applications: toward high-density data storage in nonvolatile memories, *Advanced Materials*. 30 (2018) 1703950.
- [129] J.J. Borrás-Almenar, E. Coronado, A. Müller, M. Pope, *Polyoxometalate Molecular Science*, Springer Science & Business Media, 2003.
- [130] J. J. Berzelius, The preparation of phosphomolybdate ion [PMo₁₂O₄₀]³⁻, *Ann. Phys. Chem.* 82 (1826) 369–392.

- [131] J.-C.G. de Marignac, Recherches sur les acides silicotungstiques et note sur la constitution de l'acide tungstique, Gauthier-Villars, 1864.
- [132] C.W. Blomstrand, Zur Kenntnis der Doppelsäuren des siebenatomigen Jobs, Zeitschrift Für Anorganische Chemie. 1 (1892) 10–50. <https://doi.org/10.1002/zaac.18920010104>.
- [133] W.H. Baur, One hundred years of inorganic crystal chemistry – a personal view, Crystallography Reviews. 20 (2014) 64–116. <https://doi.org/10.1080/0889311X.2013.879648>.
- [134] Q. Chen, C. Shen, L. He, Recent advances of polyoxometalate-catalyzed selective oxidation based on structural classification, Acta Crystallogr C Struct Chem. 74 (2018) 1182–1201. <https://doi.org/10.1107/S2053229618010902>.
- [135] A.-E. Stamate, O.D. Pavel, R. Zavoianu, I.-C. Marcu, Highlights on the Catalytic Properties of Polyoxometalate-Intercalated Layered Double Hydroxides: A Review, Catalysts. 10 (2020) 57. <https://doi.org/10.3390/catal10010057>.
- [136] N. Joo, NEW FUNCTIONALIZED POLYOXOMETALATES (POMs) FOR MOLECULAR MEMORY DEVICES COMPATIBLE WITH A CMOS PROCESSING, phdthesis, Université Joseph-Fourier - Grenoble I, 2010. <https://tel.archives-ouvertes.fr/tel-00542657> (accessed June 11, 2021).
- [137] L. Pauling, THE MOLECULAR STRUCTURE OF THE TUNGSTOSILICATES AND RELATED COMPOUNDS, J. Am. Chem. Soc. 51 (1929) 2868–2880. <https://doi.org/10.1021/ja01385a002>.

- [138] J.F. Keggin, Structure of the Molecule of 12-Phosphotungstic Acid, *Nature*. 131 (1933) 908–909. <https://doi.org/10.1038/131908b0>.
- [139] B. Dawson, The structure of the 9(18)-heteropoly anion in potassium 9(18)-tungstophosphate, $K_6(P_2W_{18}O_{62}) \cdot 14H_2O$, *Acta Cryst.* 6 (1953) 113–126. <https://doi.org/10.1107/S0365110X53000466>.
- [140] L. Vilà-Nadal, S. Romo, X. López, J.M. Poblet, Structural and Electronic Features of Wells-Dawson Polyoxometalates, in: C. Hill, D.G. Musaev (Eds.), *Complexity in Chemistry and Beyond: Interplay Theory and Experiment*, Springer Netherlands, Dordrecht, 2012: pp. 171–183. https://doi.org/10.1007/978-94-007-5548-2_10.
- [141] T. Ruther, W.R. Jackson, A.M. Bond, Dawson-type heteropoloxometalates $[R_4N]_4[S_2M_{18}O_{62}]$ (M = W, Mo) as catalysts for the homogeneous phase H_2O_2 oxidation of organic substrates, *Australian Journal of Chemistry: An International Journal for Chemical Science*. 55 (2002) 691–694. <https://doi.org/10.1071/CH02141>.
- [142] A. Bijelic, A. Rompel, Polyoxometalates: more than a phasing tool in protein crystallography, *ChemTexts*. 4 (2018) 10. <https://doi.org/10.1007/s40828-018-0064-1>.
- [143] M.H. Alizadeh, A.R. Salimi, Density functional theory and Hartree–Fock studies: Geometry, vibrational frequencies and electronic properties of Anderson-type heteropolyanion, $[XM_6O_{24}]^{n-}$ (X= TeVI, IVII and M= Mo, W) and $[SbVW_6O_{24}]^{7-}$, *Spectrochimica Acta Part A: Molecular and Biomolecular Spectroscopy*. 65 (2006) 1104–1111.

- [144] D.D. Dexter, J.V. Silverton, A new structural type for heteropoly anions. The crystal structure of $(\text{NH}_4)_2\text{H}_6(\text{CeMo}_{12}\text{O}_{42}) \cdot 12\text{H}_2\text{O}$, *J. Am. Chem. Soc.* 90 (1968) 3589–3590. <https://doi.org/10.1021/ja01015a067>.
- [145] R. Dehghani, S. Aber, F. Mahdizadeh, Polyoxometalates and Their Composites as Photocatalysts for Organic Pollutants Degradation in Aqueous Media—A Review, *CLEAN - Soil, Air, Water.* 46 (2018). <https://doi.org/10.1002/clen.201800413>.
- [146] C.L. Hill, C.M. Prosser-McCartha, Photocatalytic and photoredox properties of polyoxometalate systems, *Photosensitization and Photocatalysis Using Inorganic and Organometallic Compounds.* (1993) 307–330.
- [147] B. Keita, T. Liu, L. Nadjo, Synthesis of remarkably stabilized metal nanostructures using polyoxometalates, *Journal of Materials Chemistry.* 19 (2009) 19–33. <https://doi.org/10.1039/B813303D>.
- [148] A. Dolbecq, P. Mialane, B. Keita, L. Nadjo, Polyoxometalate-based materials for efficient solar and visible light harvesting: application to the photocatalytic degradation of azo dyes, *J. Mater. Chem.* 22 (2012) 24509–24521. <https://doi.org/10.1039/C2JM33246A>.
- [149] Y. Nosaka, T. Takei, N. Fujii, Photoinduced reduction of $\text{W}_{10}\text{O}_{32}^{4-}$ by organic compounds in aqueous solution, *Journal of Photochemistry and Photobiology A: Chemistry.* 92 (1995) 173–179. [https://doi.org/10.1016/1010-6030\(95\)04125-6](https://doi.org/10.1016/1010-6030(95)04125-6).
- [150] J.J. Walsh, Association of the Dawson-type polyoxometalates with photoactive transition metal monomers and polymers., PhD Thesis, Dublin City University, 2011.

- [151] J.M. Cameron, S. Fujimoto, R.-J. Wei, G.N. Newton, H. Oshio, Post-functionalization of a photoactive hybrid polyoxotungstate, *Dalton Trans.* 47 (2018) 10590–10594. <https://doi.org/10.1039/C8DT01253A>.
- [152] L. Zhang, Q. Wang, Y. Qi, L. Li, S. Wang, X. Wang, An ultrasensitive sensor based on polyoxometalate and zirconium dioxide nanocomposites hybrids material for simultaneous detection of toxic clenbuterol and ractopamine, *Sensors and Actuators B: Chemical*. 288 (2019) 347–355.
- [153] Z. Kang, C.H.A. Tsang, Z. Zhang, M. Zhang, N. Wong, J.A. Zapien, Y. Shan, S.-T. Lee, A Polyoxometalate-Assisted Electrochemical Method for Silicon Nanostructures Preparation: From Quantum Dots to Nanowires, *J. Am. Chem. Soc.* 129 (2007) 5326–5327. <https://doi.org/10.1021/ja068894w>.
- [154] X. Huang, X. Liu, Morphology control of highly efficient visible-light driven carbon-doped POM photocatalysts, *Applied Surface Science*. 505 (2020) 144527.
- [155] T.J. Wilke, M.A. Barteau, Cation exchange effects on methanol oxidation and dehydration by supported polyoxometalates, *Journal of Catalysis*. 371 (2019) 357–367. <https://doi.org/10.1016/j.jcat.2019.02.006>.
- [156] Y. Zhou, G. Chen, Z. Long, J. Wang, Recent advances in polyoxometalate-based heterogeneous catalytic materials for liquid-phase organic transformations, *RSC Advances*. 4 (2014) 42092–42113. <https://doi.org/10.1039/C4RA05175K>.
- [157] S.-S. Wang, G.-Y. Yang, Recent advances in polyoxometalate-catalyzed reactions, *Chemical Reviews*. 115 (2015) 4893–4962.

- [158] J.K. Kim, J.H. Choi, J.H. Song, J. Yi, I.K. Song, Etherification of n-butanol to di-n-butyl ether over $H_nXW_{12}O_{40}$ (XCo^{2+} , B^{3+} , Si^{4+} , and P^{5+}) Keggin heteropolyacid catalysts, *Catalysis Communications*. 27 (2012) 5–8. <https://doi.org/10.1016/j.catcom.2012.06.014>.
- [159] Isopoly and heteropoly compounds: A general chemistry laboratory experiment | *Journal of Chemical Education*, (n.d.). https://pubs.acs.org/doi/abs/10.1021/ed047p212?casa_token=PExK2spkw5MAAAA:pJbq7rCYTur0bgeQucmCoBx_AxXLEiLnvo9ey95LsdR-og3EGavTg-tuyqxH26j2T7HTH44j12lbOw (accessed October 17, 2021).
- [160] D. Ravelli, S. Protti, M. Fagnoni, Decatungstate Anion for Photocatalyzed “Window Ledge” Reactions, *Acc. Chem. Res.* 49 (2016) 2232–2242. <https://doi.org/10.1021/acs.accounts.6b00339>.
- [161] P. Xiao, J. Zhang, F. Dumur, M.-A. Tehfe, F. Morlet-Savary, B. Graff, D. Gigmes, J. Fouassier, J. Lalevée, Visible light sensitive photoinitiating systems: Recent progress in cationic and radical photopolymerization reactions under soft conditions, *Undefined*. (2015). </paper/Visible-light-sensitive-photoinitiating-systems%3A-in-Xiao-Zhang/f84eb96e96e6eba19ad314d53ed6571bc83f1f68> (accessed May 27, 2021).
- [162] L.P. Ermolenko, J.A. Delaire, C. Giannotti, Laser flash photolysis study of the mechanism of photooxidation of alkanes catalysed by decatungstate anion, *Journal of the Chemical Society, Perkin Transactions 2*. 0 (1997) 25–30. <https://doi.org/10.1039/A604691F>.
- [163] D.C. Duncan, T.L. Netzel, C.L. Hill, Early-Time Dynamics and Reactivity of Polyoxometalate Excited States. Identification of a Short-Lived LMCT Excited State and

- a Reactive Long-Lived Charge-Transfer Intermediate following Picosecond Flash Excitation of $[W_{10}O_{32}]^{4-}$ in Acetonitrile, *Inorg. Chem.* 34 (1995) 4640–4646. <https://doi.org/10.1021/ic00122a021>.
- [164] I. Texier, J.A. Delaire, C. Giannotti, Reactivity of the charge transfer excited state of sodium decatungstate at the nanosecond time scale, *Phys. Chem. Chem. Phys.* 2 (2000) 1205–1212. <https://doi.org/10.1039/A908588B>.
- [165] C. Tanielian, K. Duffy, A. Jones, Kinetic and Mechanistic Aspects of Photocatalysis by Polyoxotungstates: A Laser Flash Photolysis, Pulse Radiolysis, and Continuous Photolysis Study, *J. Phys. Chem. B.* 101 (1997) 4276–4282. <https://doi.org/10.1021/jp9704751>.
- [166] A. Molinari, E. Sarti, N. Marchetti, L. Pasti, Degradation of emerging concern contaminants in water by heterogeneous photocatalysis with $Na_4W_{10}O_{32}$, *Applied Catalysis B: Environmental.* 203 (2017) 9–17. <https://doi.org/10.1016/j.apcatb.2016.09.031>.
- [167] X. Yang, J. Yu, Y. Zhang, Y. Peng, Z. Li, C. Feng, Z. Sun, X. Yu, J. Cheng, Y. Wang, Visible-near-infrared-responsive $g-C_3N_4H_x^+$ reduced decatungstate with excellent performance for photocatalytic removal of petroleum hydrocarbon, *Journal of Hazardous Materials.* 381 (2020) 120994. <https://doi.org/10.1016/j.jhazmat.2019.120994>.
- [168] S. Wang, S. Xing, Z. Shi, J. He, Q. Han, M. Li, Electrostatic polypyridine–ruthenium(II)–decatungstate dyads: structures, characterizations and photodegradation of dye, *RSC Advances.* 7 (2017) 18024–18031. <https://doi.org/10.1039/C7RA01342F>.

- [169] X. Yang, F. Qian, Y. Wang, M. Li, J. Lu, Y. Li, M. Bao, Constructing a novel ternary composite ($C_{16}H_{33}(CH_3)_3N)_4W_{10}O_{32}/g-C_3N_4/rGO$ with enhanced visible-light-driven photocatalytic activity for degradation of dyes and phenol, *Applied Catalysis B: Environmental*. 200 (2017) 283–296. <https://doi.org/10.1016/j.apcatb.2016.07.024>.
- [170] E.S. Da Silva, V. Prevot, C. Forano, P. Wong-Wah-Chung, H.D. Burrows, M. Sarakha, Heterogeneous photocatalytic degradation of pesticides using decatungstate intercalated macroporous layered double hydroxides, *Environ Sci Pollut Res*. 21 (2014) 11218–11227. <https://doi.org/10.1007/s11356-014-2971-z>.
- [171] A. Allaoui, M.A. Malouki, P. Wong-Wah-Chung, Efficient degradation of methabenzthiazuron photoinduced by decatungstate anion in water: Kinetics and mechanistic studies, *Chemosphere*. 85 (2011) 558–564. <https://doi.org/10.1016/j.chemosphere.2011.06.071>.
- [172] L. Pasti, E. Sarti, A. Martucci, N. Marchetti, C. Stevanin, A. Molinari, An advanced oxidation process by photoexcited heterogeneous sodium decatungstate for the degradation of drugs present in aqueous environment, *Applied Catalysis B: Environmental*. 239 (2018) 345–351. <https://doi.org/10.1016/j.apcatb.2018.08.015>.
- [173] B. Yang, Z. Fu, A. Su, J. She, M. Chen, S. Tang, W. Hu, C. Zhang, Y. Liu, Influence of tetraalkylammonium cations on quality of decatungstate and its photocatalytic property in visible light-triggered selective oxidation of organic compounds by dioxygens, *Applied Catalysis B: Environmental*. 242 (2019) 249–257. <https://doi.org/10.1016/j.apcatb.2018.09.099>.

- [174] P. Xie, C. Xue, J. Luo, S. Shi, D. Du, Decatungstate-mediated solar photooxidative cleavage of C=C bonds using air as an oxidant in water, *Green Chem.* 23 (2021) 5936–5943. <https://doi.org/10.1039/D1GC01234G>.
- [175] B. Yang, W. Hu, F. Wan, C. Zhang, Z. Fu, A. Su, M. Chen, Y. Liu, Adjusting effect of additives on decatungstate-photocatalyzed HMF oxidation with molecular oxygen under visible light illumination, *Chemical Engineering Journal.* 396 (2020) 125345. <https://doi.org/10.1016/j.cej.2020.125345>.
- [176] G. Laudadio, S. Govaerts, Y. Wang, D. Ravelli, H.F. Koolman, M. Fagnoni, S.W. Djuric, T. Noël, Selective C(sp³)-H Aerobic Oxidation Enabled by Decatungstate Photocatalysis in Flow, *Angewandte Chemie.* 130 (2018) 4142–4146. <https://doi.org/10.1002/ange.201800818>.
- [177] D. Ravelli, M. Fagnoni, T. Fukuyama, T. Nishikawa, I. Ryu, Site-Selective C–H Functionalization by Decatungstate Anion Photocatalysis: Synergistic Control by Polar and Steric Effects Expands the Reaction Scope, *ACS Catal.* 8 (2018) 701–713. <https://doi.org/10.1021/acscatal.7b03354>.

Chapter 3: Methods and Materials

3.1. Chemical reagents

3.1.1. Commercial reagents

All the commercial reagents used in the experiments were presented in the **Table 3-1**. All reagents were used without further purification. Water was purified using a reverse osmosis RIOS 5 and Synergy (Millipore) device (resistivity 18 M Ω cm, DOC < 0.1 mg L⁻¹).

3.1.2. Synthetic reagents

3.1.2.1. Synthesis of sodium decatungstate (NaDT)

The preparation of sodium decatungstate refers to the previous study available [1]. The boiling sodium tungstate solution (50 g of Na₂WO₄·2H₂O dissolved in 300 mL of ultrapure water) was mixed with 1.0 M boiling hydrochloric acid (300 mL) in a beaker, refluxed for 20 seconds to form a green solution. It was followed by adding 150 g of solid sodium chloride, stirring until the solution has been re-boiled and keeping for 20 seconds, then rapidly putting into the ice-water bath. This suspension solution was maintained in a freezer (-18°C) overnight. The next day, this suspension solution of NaCl and crude Na₄W₁₀O₃₂ was filtered and the solid was dissolved into 150 mL of acetonitrile solution. The acetonitrile solution was refluxed for 5 min at 79°C and filtered to remove the insoluble NaCl after cooling at ambient temperature. The acetonitrile solution was gently evaporated in hot-water bath (79°C) to obtain the yellow-green catalyst.

Table 3-1. The reagents used in the experiment

Reagent	Purity	Company
Sodium tungstate ($\text{Na}_2\text{WO}_4 \cdot 2\text{H}_2\text{O}$)	99.0%	Sigma Aldrich
Hydrogen peroxide (H_2O_2)	30%	Sigma Aldrich
Sulfasalazine (SSZ)	98.0-101.5%	Sigma Aldrich
Sulfapyridine (SPD)	99.0%	Sigma Aldrich
Terephthalic acid	98%	Sigma Aldrich
Sodium chloride (NaCl)	99.0%	Sigma Aldrich
Hydrochloric acid (HCl)	37%	Sigma Aldrich
Perchloric acid (HClO_4)	70-72%	Sigma Aldrich
Sodium hydroxide (NaOH)	97%	Sigma Aldrich
Phosphoric acid	85-88 wt. % in H_2O	Honeywell
Methanol	HPLC, 99.9%	Sigma Aldrich
Acetonitrile	HPLC, 99.9%	Sigma Aldrich
Ethanol	96%	Carlo Erba
Lithium perchlorate	Battery grade, 99.99%	Sigma Aldrich
Tetra-n-butylammonium bromide	98%	Sigma Aldrich
2-propanol	HPLC, 99.9%	Sigma Aldrich
Dichloromethane	HPLC, 99.8%	Sigma Aldrich
Nifion solution	5%	Sigma Aldrich
Deuterium water (D_2O)	99.9 atom % D	Sigma Aldrich
3-(Trimethylsilyl) propionic acid- d_4 sodium salt (TSP d_4)	98 atom % D	Sigma Aldrich
Trifluoroacetic acid (TFA)	HPLC, 99.0%	Sigma Aldrich
pH standerd buffer	pH = 4.01, 7.01, 10.01	Merck, Hanna
2-Hydroxyterephthalic acid	97%	Sigma Aldrich
Terephthalic acid	98%	Sigma Aldrich
Lithium Hydroxide (LiOH)	98%	Sigma Aldrich

3.1.2.2. Synthesis of tetra-n-butylammonium decatungstate (TBADT)

The preparation of tetra-n-butylammonium decatungstate (TBADT) refers to the previous study available [2]. To a boiling sodium tungstate solution (8 g of $\text{Na}_2\text{WO}_4 \cdot 2\text{H}_2\text{O}$ dissolved in 100 mL of ultrapure water) was added 16.75 mL boiling hydrochloric acid (3.0 M). The temperature was maintained at 95 °C for 5 min till the change of the solution color to green. Then, the addition of an aqueous solution (95 °C) of tetra-n-butylammonium bromide (TBABr 6.4 g/10 mL) leads to the immediate formation of a white precipitate. The mixture was kept under stirring at a temperature of 95 °C. This suspension solution was then filtered after cooling at ambient temperature. The solid was dissolved into dichloromethane and filtered with the aim to remove the insoluble particles. Finally, the obtained dichloromethane solution was gently evaporated at 38 °C to obtain the yellow-green catalyst.

3.1.2.3. Synthesis of magnetite

Magnetite was prepared by following the procedure reported in the literature [3]. A mixture of 27.03 g $\text{FeCl}_3 \cdot 6\text{H}_2\text{O}$ and 19.88 g $\text{FeCl}_2 \cdot 4\text{H}_2\text{O}$ in 800 mL Milli-Q water was constantly stirred under nitrogen atmosphere. The pH was adjusted by NaOH aqueous solution to 9–10 and the solution volume was adjusted to 1.0 L with Milli-Q water. Then, the reaction vessel was kept in the dark for 48 h at 60 °C. After centrifugation, the solid was washed with Milli-Q water until the water conductivity after washing was less than $2.0 \mu\text{S cm}^{-1}$, and then dried.

3.1.2.4. Synthesis of magnetite-TBADT (M-T) complex

The complex magnetite-TBADT (M-T) was prepared by the following procedure. A mixture of 1.0 g tetra-n-butylammonium decatungstate (TBADT) and 2.0 g magnetite was vigorously stirred in 10.0 mL acetonitrile solution. The reaction vessel was then kept in the dark for 24 hours at ambient temperature. After centrifugation the solid was washed with Milli-Q water three times and then dried in the oven at 50 °C. The different ratios of magnetite/TBADT (20/1, 10/1, 5/1, 2/1) were prepared using similar process with the same amount of magnetite and so different amount of TBADT.

3.2. Laboratory equipments

3.2.1. Irradiation reactor

Irradiation reactor I

Irradiation experiments (320 - 420 nm) were carried out in a stainless-steel cylindrical reactor. Six high pressure mercury tubes (Philips HPW, 15 W, emission centered at 365 nm) were located evenly on the edge of the cylinder with a fan placed on the bottom of the cylinder to cool the irradiation system. The reactor, a Pyrex tube (2 cm diameter), was placed at the center of the cylinder (**Fig. 3-1**).

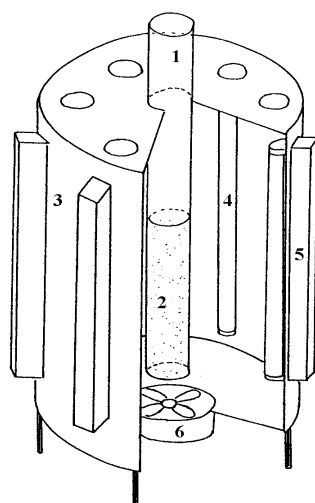


Fig. 3-1. The irradiation reactor I setup. 1) Pyrex tube; 2) sample; 3) Cylindrical reactor; 4) High pressure mercury tubes (Philips HPW, 15W, emission centered at 365 nm); 5) power supply; 6) air cooling fan.

The light sources are Philips HPW, 15W tubes. The shape of the emission spectrum of the tubes was obtained by the optical fiber (Ocean optics SD 2000), the emission is mainly between 320 and 420 nm (**Fig. 3-2**).

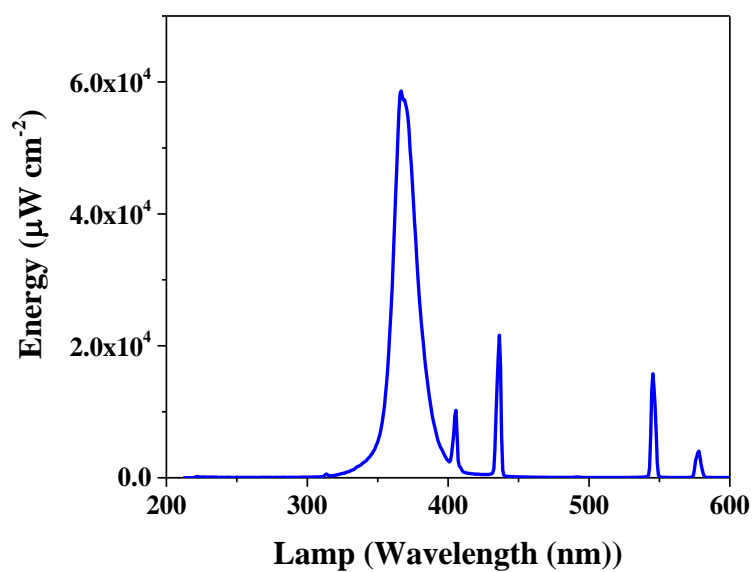


Fig. 3-2. Emission spectrum of the Philips HPW, 15W tube

Irradiation reactor II

The irradiation device is a reflective enclosure built on a circular base. The reactor and the water circulation system are placed in the center of the enclosure and three lamps are arranged around the reactor. In addition, the device is equipped with a magnetic stirrer which allows us to have a good homogenization of the solutions during the irradiation (**Fig. 3-3**).

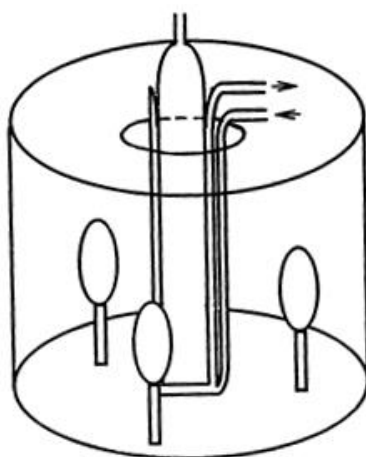


Fig. 3-3. The 365 nm irradiation setup

The light sources are MAZDA MAW 125W lamps; they are medium-pressure mercury vapor lamps whose emission, filtered by a black globe, is mainly at 365 nm (**Fig. 3-4**).

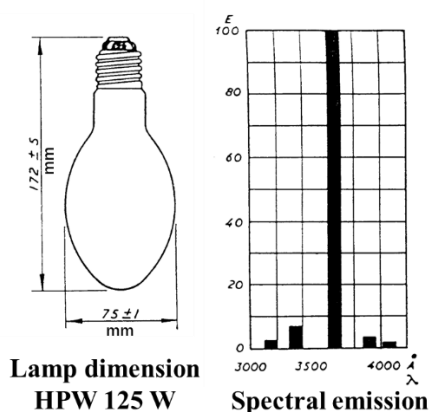


Fig. 3-4. Emission spectrum of the MAZDA MAW 125 W lamp

3.2.2. Analytical instruments

All the instruments used in the experiments were shown in the **Table 3-2**.

Table 3-2. The table of analytical instrument performing in the experiment.

Instrument	Model
UV–Vis absorption spectroscopy	Varian Cary 300
High Performance Liquid Chromatography (HPLC)	Shimadzu NEXERA XR HPL
UHPLC-HRMs	THERMO SCIENTIFIC UHPLC (Ultimate 3000) with U3000 detector (PDA)) HRMS (Q-Exactive)
Total organic carbon (TOC) analyzer	Shimadzu TOC 5050A
Nuclear Magnetic Resonance spectrometer (NMR)	Bruker Advance III 500 MHz Ultrashield™ plus spectrometer
Electrochemical potentiostat	Autolab PGSTAT204
Transmission Electron Microscope (TEM)	TEM, Hitachi H-7650
Scanning Electron Microscope (SEM)	JEOL JSM-6490LV
X-ray photoelectron spectroscopy (XPS)	OMICRON EA125, Germany
FT-IR spectrometer	Thermo-Nicolet 380
X-Ray diffraction spectrometer (XRD)	Siemens Model D500

3.2.3. Other equipments

Table 3-3 The table of other instruments using in the experiment

Instrument	Model
pH meter	Fiveeasy™ Plus
Preparative HPLC	Varian Prep Star 218
Balance	Mettler Toledo-Newclassic FM
Oven	Memment UM 400
Magnetic stirrer	IKA® R010
Centrifuge	Sigma, Fisher Bioblock Scientific 1-6
Rotary evaporator	Heidolph WB 200

3.3. Preparation of solution

All the solutions were prepared with Milli-Q ultrapure water

(1) Sulfapyridine (SPD) stock solution

18.697 mg SPD were diluted in 500 mL of Milli-Q water and the magnetic stirring was used for several hours to make SPD completely dissolved in water ($[\text{SPD}]_{\text{stock}} = 150 \mu\text{M}$). This SPD stock solution was stored avoid light. The solution of SPD used in all experiments was diluted from this SPD stock solution. **Fig. 3-5** shows the molecular formula of SPD.

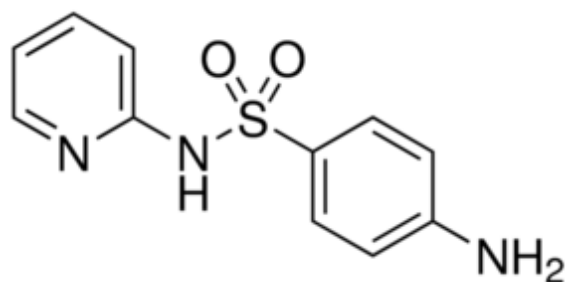


Fig. 3-5. The molecular formula of SPD

(2) Sulfasalazine (SSZ) stock solution

29.873 mg SSZ were diluted in 500 mL of Milli-Q water and the magnetic stirring was used for several hours to make SSZ completely dissolved in water ($[SSZ]_{\text{stock}} = 150 \mu\text{M}$). This SSZ stock solution was stored avoid light. The solution of SSZ used in all experiments was diluted from this SSZ stock solution. **Fig. 3-6** shows the molecular formula of SSZ.

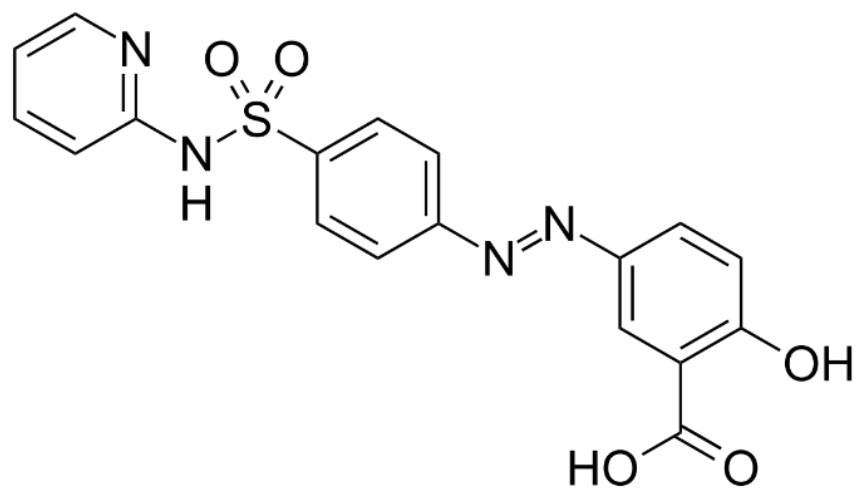


Fig. 3-6. The molecular formula of SSZ

(3) Terephthalic acid (TA) stock solution

16.613 mg TA were diluted in 500 mL of Milli-Q water and the magnetic stirring was used for several hours to make TA completely dissolved in water ($[TA]_{\text{stock}} = 200 \mu\text{M}$). This TA stock solution was stored avoid light. The solution of TA used in all experiments was diluted from this TA stock solution.

(4) 2-hydroxyterephthalic acid (TAOH) stock solution

18.213 mg TAOH were diluted in 500 mL of Milli-Q water and the magnetic stirring was used for several hours to make TAOH completely dissolved in water ($[TAOH]_{\text{stock}} = 200 \mu\text{M}$). This TAOH stock solution was stored avoid light. The solution of TAOH used in all experiments was diluted from this TAOH stock solution.

(5) H₂O₂ stock solution

10 mL H₂O₂ (30% wt, $\rho = 1.11 \text{ g cm}^{-3}$) were diluted in 100 mL of Milli-Q water. The concentration of H₂O₂ stock solution is about 1~2 M. The H₂O₂ stock solution was stored in the fridge. H₂O₂ will be diluted and its accurate concentration will be determined before being used.

(6) K₂S₂O₈ stock solution

11.905 g K₂S₂O₈ were diluted in 100 mL of Milli-Q water and then stored in the fridge. The concentration of K₂S₂O₈ stock solution is 0.5 M.

(7) LiClO₄ electrolyte solution

The electrolyte solution used in cyclic voltammetry experiments is 0.1 M of LiClO_4 solution. 8.022g LiClO_4 were diluted in 500 ml of Milli-Q water and then stored in the fridge. The pH of LiClO_4 electrolyte solution was adjusted by adding the negligible volume of 1 M of HClO_4 and LiOH solutions.

(8) HClO_4 solution

6.04 mL HClO_4 (70% wt, $\rho = 1.664 \text{ g cm}^{-3}$) were diluted in 100 mL of Milli-Q water. The concentration of HClO_4 solution is about 1 M, which is mainly used to adjust the initial pH of the reaction solution. The HClO_4 solution was stored in the fridge.

(9) NaOH solution

4.0 g NaOH were diluted in 100 mL of Milli-Q water and then stored in the fridge. NaOH stock solution is 1.0 M. NaOH solution is mainly used to adjust the initial pH of the reaction solution.

(10) LiOH solution

2.395 g LiOH were diluted in 100 mL of Milli-Q water and then stored in the fridge. LiOH solution (1.0 M) is mainly used to adjust the initial pH of electrolyte solution when we are performing cyclic voltammetry experiments.

3.4. Characterization

3.4.1. Purity of catalyst testing

➤ **UV-Visible absorption spectroscopy**

UV-visible absorption spectroscopy can be used as a method to identify and determine purity of the catalyst in solution. According to the Beer-Lamber law, the molar absorption coefficient (ϵ) can be obtained when the absorbance, concentration of catalyst and length of the optical path are known. In this thesis, the UV-Visible absorption spectroscopy was used to determine the purity of decatungstate via the absorbance of the characteristic peaks and comparisons of the molar absorption coefficient at this wavelength with previous studies.

The UV spectra of the solution were recorded with a Varian Cary 300 UV-visible spectrophotometer. The detection wavelength range is 200 - 800 nm with the precision of wavelength at 1.0 nm. The scanning time is 1.0 min.

3.4.2. Phase analysis

➤ **XRD spectroscopy**

X-ray diffraction (XRD) technique is an essential method in the field of material synthesis to identify and study the crystal structure of the sample [4]. Therefore, X-ray diffraction patterns of the synthesized samples were collected using a Siemens Model D500 X-ray diffractometer with a diffracted beam monochromator Cu $K\alpha$ source (40 kV - 40 mA). Patterns were recorded over the form $2\theta = 5$ to 70° , in steps of 0.08° with a count time of 4 seconds.

➤ FTIR spectroscopy

Fourier transform infrared (FTIR) spectroscopy is probably the most widely used spectroscopic techniques due to its versatility in determining composition, conformation, crystallinity. The FTIR spectra of the synthesis samples were recorded on a Fourier infrared absorption spectrometer (Thermo-Nicolet 380) with an advanced diamond ATR accessory (Specac-Golden Gate). Detection of the scan range is $560 - 4000 \text{ cm}^{-1}$, with a resolution of 4 cm^{-1} .

➤ XPS

X-ray Photoelectron Spectroscopy (XPS) is a surface chemical analysis technology that can be used to analyze the surface chemistry of metal materials in a specific state or after some processing [5]. In this thesis, XPS studies were performed on a Physical Electronics/PHI 5300 X-ray photoelectron spectrometer with a hemispherical analyzer and a single-channel detector that was operated at 300 W (15 kV and 20 mA). Mg $K\alpha$ radiation (1253.6 eV) and pass energies of 89.45 eV for survey scans and 17.9 eV for high-resolution scans were used.

3.4.3. Morphological and size

➤ TEM

The morphology and the size of the prepared samples were analyzed by transmission electron microscopy (TEM, Hitachi H-7650) at 80 kV acceleration voltage with magnifications

up to 200 000 times. The samples investigated by TEM were suspended in ethanol and dropped onto a 400-mesh holey carbon-coated copper grid and dried at room temperature in air.

➤ SEM-EDS

With the objective to check whether TBADT is uniformly covered on the surface of nano-magnetite, SEM-EDS element mapping experiment was used to visually study the distribution of elements recording on Scanning Electron Microscope (JEOL JSM-6490LV).

➤ BET

Nitrogen physisorption (the BET method) was performed to determine the specific surface area of the particles using a Quantachrome Nova 3000e Surface Area Analyzer. Before nitrogen adsorption, the sample needs to be degassed at 150 °C for 8 hours.

3.5. Experimental methods

3.5.1. Photodegradation in presence of decatungstate (NaDT) and H₂O₂

3.5.1.1. Photoreaction in the presence of sodium decatungstate (NaDT)

The reaction solution was a mixture of decatungstate and sulfapyridine (SPD) or sulfasalazine (SSZ). The irradiation (with irradiation reactor **I**) started since the solution was poured into the reactor. 0.5 mL solution was taken for the HPLC analysis at fixed time intervals.

3.5.1.2. Photoreaction in the presence of sodium decatungstate (NaDT) and H₂O₂

The reaction solution was a mixture of decatungstate (NaDT), H₂O₂ and sulfapyridine (SPD) or sulfasalazine (SSZ). The irradiation started since the negligible volume of H₂O₂ stock solution was added into the reactor. 0.5 mL solution was taken for the HPLC analysis at fixed time intervals. In this experiment, different parameter like initial pH, NaDT concentration, H₂O₂ concentration, SPD or SSZ concentration were investigated.

3.5.1.3. Hydroxyl radical trap experiment

The reaction solution was a mixture of decatungstate (NaDT), H₂O₂ and Terephthalic acid (TA). The irradiation started since the negligible volume of H₂O₂ stock solution was added into the reactor. 0.5 mL solution was taken the HPLC analysis at fixed time intervals.

3.5.2. Photodegradation in presence of decatungstate (NaDT) and S₂O₈²⁻

3.5.2.1. Photoreaction in the presence of decatungstate (NaDT)

The reaction solution was a mixture of decatungstate and sulfapyridine (SPD) or sulfasalazine (SSZ). The irradiation (with irradiation reactor II) started since the solution was poured into the reactor. 0.5 mL solution was taken for the HPLC analysis at fixed time intervals.

3.5.2.2. Photoreaction in the presence of decatungstate (NaDT) and $K_2S_2O_8$

The reaction solution was a mixture of decatungstate (NaDT), $K_2S_2O_8$ and sulfapyridine (SPD). The irradiation started since the negligible volume of H_2O_2 stock solution was added into the reactor. 0.5 mL solution was taken for the HPLC analysis at fixed time intervals.

3.5.3. Selective sulfapyridine oxidation via decatungstate/magnetite/ H_2O_2 system.

3.5.3.1. Selective oxidation batch experiment

➤ NaDT/ Fe_3O_4 / H_2O_2 system

The selective oxidation of SPD and the formation yield of its corresponding nitroso compound were performed in a batch experiment at room temperature (25°C). 5.0 mg Sodium decatungstate (NaDT) and 13.2 mg magnetite was added into 50 mL of the sulfapyridine (SPD) solution (30 μ M). The concentration of decatungstate was then equal to 41 μ M and the amount of magnetite was 0.264 g L^{-1} . The pH of solution was adjusted to 3.0 ± 0.05 using perchloric acid and sodium hydroxide (0.1 M). Hydrogen peroxide was added using a concentrated solution, and so with negligible volume, prior to starting the reaction using the magnetic stirrer at 1100 rpm min^{-1} in order to disperse magnetite particles. Then, aliquots of the mixture were taken at different time intervals and were immediately filtrated using PTFE filters of 0.2 μ m (CHROMAFIL[®] Xtra RC-20/25, 25 mm, Macherey-Nagel).

The effect of pH (2.5, 3.0, 4.1, 4.9 and 6.9), of H_2O_2 (1, 5, 10 and 20 mM) and NaDT (20, 41, 82, 164 and 246 μ M) concentrations and of the amount of magnetite (0.1, 0.2, 0.264, 0.4, 0.8 and 1.5 g L^{-1}) were also investigated.

➤ M-T/H₂O₂ system

The conversion of SPD and the formation yield of its corresponding nitroso compound were performed in batch experiments at room temperature (roughly 25°C). 20 mg M-T complex was added into 50 mL of SPD solution (30 μM). The pH of solution was adjusted to 3.0 ± 0.05 using perchloric acid and sodium hydroxide (0.1 M). Hydrogen peroxide was added using a concentrated solution, and so with negligible volume, prior to starting the reaction using the magnetic stirrer at 1100 rpm min⁻¹ in order to disperse magnetite particles. Then, aliquots of the mixture were taken at different time intervals and were immediately filtrated using PTFE filters of 0.2 μm (CHROMAFIL[®] Xtra RC-20/25, 25 mm, Macherey-Nagel).

The effect of ratio of magnetite/TBADT (20/1, 10/1, 5/1 and 2/1), pH (1.9, 2.5, 3.0, 4.0, 4.6, 5.2 and 7.2), of H₂O₂ concentration (1, 5, 10, 20, 30, 40 and 50 mM) and M-T amount (0.1, 0.2, 0.4 and 0.8 g L⁻¹)

3.5.3.2 Cyclic Voltammetry (CV) experiments

Cyclic voltammetry (CV) is a powerful and popular electrochemical technique commonly employed to investigate the reduction and oxidation processes of molecular species [6]. CV is also essential to study electron transfer-initiated chemical reactions which includes catalysis [6]. In order to clarify the mechanism of the selective oxidation of sulfapyridine under the novel ternary NaDT/magnetite/H₂O₂ or M-T/H₂O₂ system, cyclic voltammetry (CV) experiments were carried out with a potentiostat Autolab PGSTAT204 controlled by the NOVA software (Metrohm) equipped with a three-electrodes system. An Ag-AgCl electrode was used as the reference electrode and a platinum wire as the auxiliary electrode. The working electrode was

a pyrolytic graphite electrode (PGE, $A = 0.07 \text{ cm}^2$). Before its use, the electrode surface was polished with $1 \mu\text{m}$ diamond paste and washed with acetone and then it was polished again with $0.04 \mu\text{m}$ alumina slurry to be finally rinsed with ethanol and water.

➤ **NaDT/magnetite/H₂O₂ system**

The CV experiments were carried out under inert atmosphere (under Ar) in a 0.1 M LiClO_4 electrolyte solution (at pH 2.6) using a bare PGE or a PGE modified with a magnetite coating (M-PGE). The M-PGE was prepared using a solvent casting modified reference method [7]. A suspension was prepared with 2.0 mg of magnetite dispersed in 1.0 mL ethanol by sonication for approximately 15 minutes. Then $10 \mu\text{L}$ of nafion solution (5%, Sigma Aldrich) was added in the 1.0 mL magnetite suspension followed by sonication for 15 more minutes. $10 \mu\text{L}$ of the slurry was deposited onto the polished PGE then air dried for 10 minutes.

Cyclic voltammograms were recorded at a scan rate (v) of 10 mV s^{-1} in a 0.1 M LiClO_4 (at pH 2.6) containing 1 mM sodium decatungstate in presence of different concentrations of H_2O_2 ($0, 1, 2, 5 \text{ mM}$) with a PGE electrode. The effect of different scan rates ($10, 20, 40, 60, 80, 100, 110, 120, 140, 160, 180$ and 200 mV s^{-1}) and different pH ($2.6, 3.0, 3.5, 4.0, 5.0$ and 6.9) were also investigated.

In order to prove that the magnetite could highly improve the oxidation potential of NaDT/H₂O₂ system, it was immobilized on the surface of the pyrolytic graphite electrode (0.07 cm^2 PGE) to perform the CVs experiments. Cyclic voltammograms were recorded in a LiClO_4 solution (pH 2.60, 0.1 M) with M-PGE to get the M-PGE baseline, then CVs experiments were performed in a 1 mM LiClO_4 solution (pH 2.6, 1 mM) in the presence of NaDT or/and H_2O_2 .

➤ M-T/H₂O₂ system

The working electrodes were a pyrolytic graphite electrode (PGE, A = 0.07 cm²) modified with a TBADT coating (T-PGE), with a magnetite coating (M-PGE), and with a mixed magnetite and TBADT coating (M-T-PGE) prepared by adapted solvent casting methods [7].

To prepare the T-PGE, a TBADT solution was prepared with 40 mg of TBADT diluted in 1.0 mL acetonitrile by sonication for 2 minutes. The 10 μL TBADT solution was deposited onto the polished PGE then air dried for 120 min. For M-PGE, a suspension was prepared with 80 mg of magnetite dispersed in 1.0 mL ethanol by sonication for approximately 30 minutes. Then 10 μL nafion solution (5%, Sigma Aldrich) was added in the 1.0 mL magnetite suspension followed by sonication for 15 more minutes. 10 μL of the slurry was deposited onto the polished PGE then air dried for 120 minutes. Finally, for the M-T-PGE, a suspension was prepared in a centrifuge tube with 40.0 mg of TBADT and 80.0 mg of magnetite (TBADT/M = 1/2) dispersed in 1.0 mL acetonitrile for 24 hours on a rotating reactor (45 rpm min⁻¹) at ambient temperature. After centrifugation the solid was washed with acetonitrile and Milli-Q water for three times and then dry in the oven at 50 °C. After getting the M-TBADT mixture, 1 mg was added in 1 mL ethanol in this centrifuge tube with sonication for approximately 30 min. Then 10 μL of nafion solution (5%, Sigma Aldrich) was added in the 1.0 mL M-TBADT suspension followed by sonication for 30 min more. 10 μL of the slurry was deposited onto the polished PGE then air dried for 120 minutes.

Cyclic voltammograms were recorded under inert atmosphere (Ar) at a scan rate (ν) of 10 mV s⁻¹ in a 0.1 M LiClO₄ (at pH 3.5) in presence or absence of H₂O₂ (5 mM) with a T-PGE, M-TBADT or M-T-PGE electrode, respectively. The CVs shown correspond to the 10th cycle.

Recycle of M-TBADT-PGE electrode was also performed in the same parameters, each time with fresh LiClO₄ electrolyte solution.

3.6. Analytical Methods

3.6.1. High Performance Liquid Chromatography (HPLC) Method

The concentration of organic compounds in the aqueous solution were determined by HPLC (Shimadzu NEXERA XR HPL) equipped with a photodiode array detector (SPD-M20A), two pumps (LC-20D) and an autosampler (SIL-30AC).

(1) Sulfapyridine (SPD)

The column was a Macherey Nagel EC 150/2 NUCLEODUR C18ec (150 mm × 2 mm, 2 μm particle size). The analyses were performed using acetonitrile (ACN) as mobile phase and water with 0.5 % of phosphoric acid at a flow rate of 0.40 mL min⁻¹. The elution was performed using the following gradient: shown in **Table 3-4**.

The injection volume was 15 μL and the temperature of column was 30 °C. In this condition, the retention time of SPD was 3.40 min. The calibration curve of SPD is shown in **Fig. 3-7**.

Table 3-4. HPLC conditions for Analyzing of SPD

Time (min)	Acetonitrile (ACN)	Water (0.5 % of phosphoric acid)
0.0	5%	95%
2.5	5%	95%
7.0	40%	60%
8.5	95%	5%
9.5	95%	5%
10.0	5%	95%
19.0	5%	95%
19.0	stop	

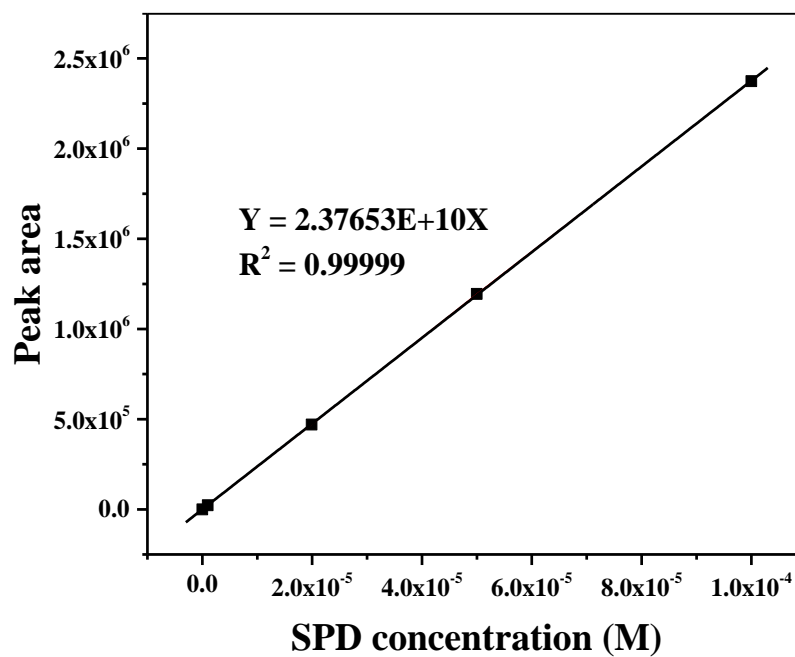


Fig. 3-7. The Calibration curve of SPD

(2) Sulfasalazine (SSZ)

The column was a Macherey Nagel EC 150/2 NUCLEODUR C18ec (150 mm × 2 mm, 2 μm particle size), The analyses were performed using methanol as mobile phase and water with 0.5 % of phosphoric acid at a flow rate of 0.20 mL min⁻¹. The elution was performed using the following gradient: shown in **Table 3-5**.

Table 3-5. HPLC conditions for Analyzing of SSZ

Time (min)	Methanol	Water (0.5 % of phosphoric acid)
0.0	40%	60%
2.5	40%	60%
20.0	95%	5%
25.0	95%	5%
25.1	40%	60%
45.0	40%	60%
45.0	stop	

The injection volume was 15 μL and the temperature of column was 30 °C. In this condition, the retention time of SSZ was 21.74 min. The calibration curve of SSZ is shown in **Fig. 3-8**.

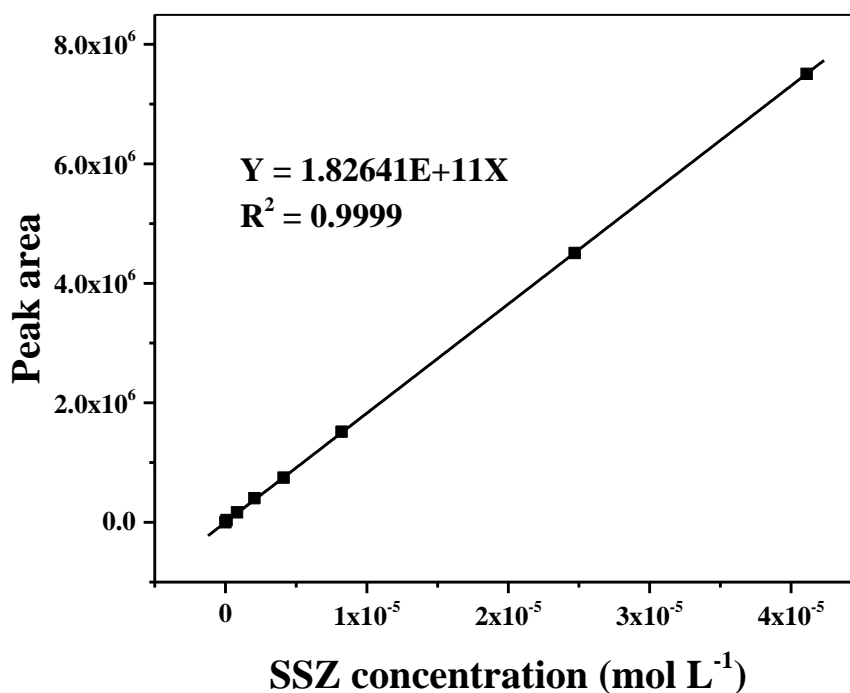


Fig. 3-8. The Calibration curve of SSZ

(3) 2-Hydroxyterephthalic acid (TAOH)

The concentration of TAOH was detected by HPLC with a fluorescence detector ($\lambda_{\text{exc}} = 315 \text{ nm}$; $\lambda_{\text{em}} = 433 \text{ nm}$) [8]. The column was a ZORBAX Rx-C8 (250 mm \times 4.6 mm, 5 μm particle size). The analyses were performed using methanol as mobile phase and water with 0.5 % of phosphoric acid at a flow rate of 1.00 mL min⁻¹. The elution was performed using isocratic mode at 75/25% at 30 °C. The calibration curve of TAOH is shown in **Fig. 3-9**.

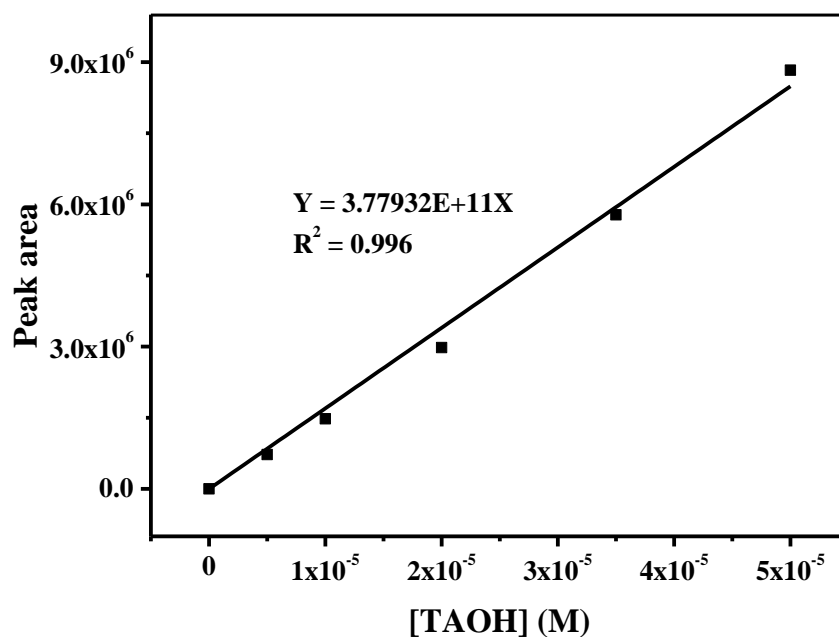
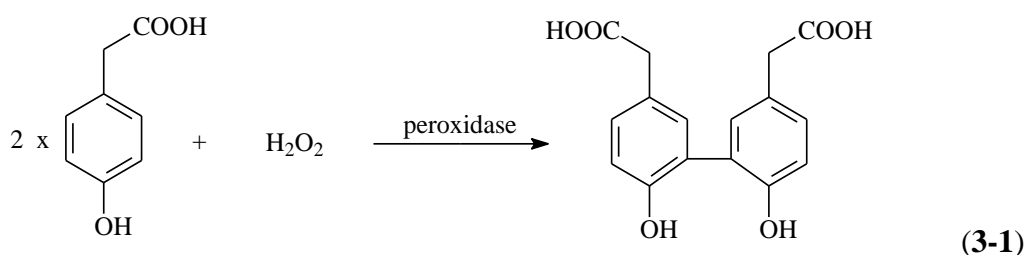


Fig. 3-9. The Calibration curve of TAOH

3.6.2. Determination of H₂O₂ concentration

(1) Determination of H₂O₂ by spectrofluorometric method

The concentration of H₂O₂ was determined according to the spectrofluorometric method described by Miller that uses the dimerization of the 4-hydroxyphenylacetic acid (HPAA) in presence of horseradish peroxidase [9,10]. The resulting dimer is a highly fluorescent compound whose formation is directly proportional to the concentration of H₂O₂ present in solution, which is usually expressed by the equation (3-1).



The excitation wavelength of p-hydroxyphenyl acetic acid dimer was 320 nm and the emission wavelength of the fluorescence was 400 nm [11]. Therefore, the H₂O₂ concentration could be calculated by detecting the concentration of the p-hydroxyphenyl acetic acid dimer.

(2) Determination of H₂O₂ by UV-Vis spectrometer

According to the literature, the concentration of hydrogen peroxide solution can be determined by UV-Vis spectrophotometer. H₂O₂ has ultraviolet absorption in the 200-300 nm spectral range. According to Beer Lambert's law, the absorbance is proportional to the concentration of hydrogen peroxide and length of the light path through the sample at a specific absorption wavelength. Knowing the absorbance, length of the light path and the H₂O₂ concentration, the molar absorption coefficient of H₂O₂ can be calculated at a specific wavelength. The calibration curve of H₂O₂ at 240 nm (optical pass length = 1 cm) was shown in Fig. 3-10.

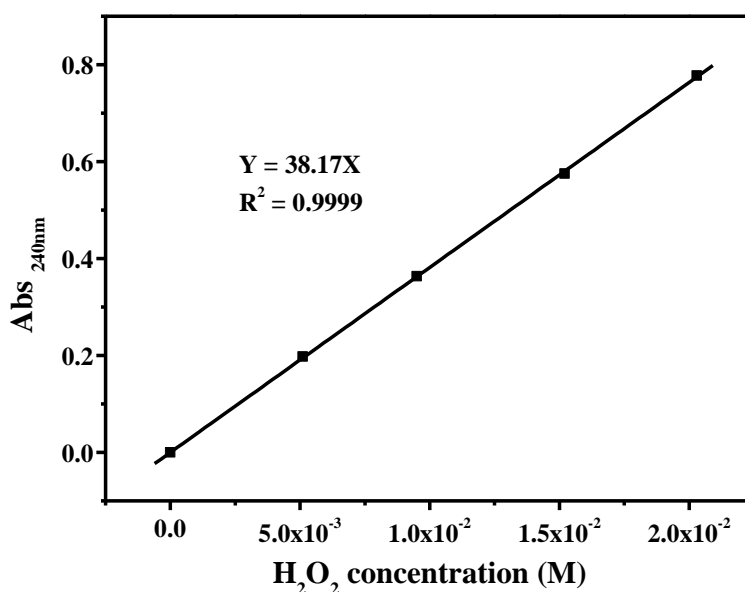


Fig. 3-10. The Calibration curve of H₂O₂

3.6.4. Quantification of nitroso-sulfapyridine (N-SPD) by NMR

For the quantification of nitroso-sulfapyridine (N-SPD), NMR spectroscopy was used. 100 μL at 5 mM of 3-(Trimethylsilyl) propionic acid- d_4 sodium salt (TSP d_4) in D_2O solution as a reference was added in 900 μL concentrated pure N-SPD solution. NMR data were obtained with a Bruker Avance III 500 MHz UltrashieldTM plus spectrometer (equipped with 5 mm TCI-13C-15N-2H Prodigy Cryoprobe). All spectra were recorded in 600 μL of H_2O (10% D_2O). Chemical shifts (δ) are expressed in ppm relative to residual peak 4.79 (ppm) of water. TopSpin 4.1.1 Software is used to analyze experimental data.

The concentration of nitroso-sulfapyridine was calculated as follows equation (3-2):

$$[\text{N-SPD}] = \frac{9A_0 \times [\text{TSPd}_4]}{b \times A_{\text{ref}}} \times 1.1 \quad (3-2)$$

Where [N-SPD] is the concentration of nitroso-sulfapyridine, A_0 is the area of nitroso-sulfapyridine resonance in the ^1H NMR spectrum, [TSP d_4] is the concentration of the reference, A_{ref} is the area of reference resonance in the ^1H NMR spectrum, b is the number of protons of N-SPD in the signal integrated, and 9 is the number of protons resonating of TSP d_4 at 0 ppm. The 1.1 factor came from dilution of TSP d_4 .

3.6.5. HPLC-MS

The identification of all the byproducts was performed using high resolution mass spectrometry (HRMS) constituted of an Orbitrap QExactive (ThermoScientific) coupled to an ultra-high performance liquid chromatography (UHPLC) instrument Ultimate 3000 RSLC (ThermoScientific). The resolution of the instrument was 35000. Analyses were carried out in

both negative and positive electrospray modes (ESI⁺ and ESI⁻). The ESI voltage was 3.2 kV for the positive mode and -3.0 kV for the negative one. The chromatographic separation was performed using a Kinetex EVO C18 (100 mm x 2.1 mm; 1.7 μm (Phenomenex)). The analyses were performed using acetonitrile (ACN) as mobile phase and acidified water with 0.1 % of formic acid at a flow rate of 0.45 mL min⁻¹. The elution was performed using the following gradient shown in **Table 3-6**. The injection volume was between 5 and 15 μL. Xcalibur Software is used to analyze experimental data

The high resolving power of the orbitrap allows the identification of unknown compounds by providing their exact molecular formula. The molecular structure was often identified by calculating the number of double bonds using the equation (3-3):

$$\text{DoU} = \frac{2C+2+N-X-H}{2} \quad (3-3)$$

Where DoU is the Degree of Unsaturation, C is the number of carbon atoms, N is the number of nitrogen atoms, X is the number of halogens atoms (F, Cl, Br, I), and H is the number of hydrogen atoms contained in the molecular formula.

3.6.6. Determination of Total organic carbon (TOC)

Total carbon (TC) includes both inorganic carbon (IC) and total organic carbon (TOC). TOC is often not available through direct testing. To calculate TOC, you can subtract the total amount of inorganic carbon from total carbon found, which is usually expressed by the equation (3-4):

$$\text{TOC} = \text{TC} - \text{IC} \quad (3-4)$$

Table 3-6. UHPLC-MS conditions for Analyzing of SPD and SSZ

Time (min)	Acetonitrile (ACN)	Water (0.5 % of phosphoric acid)
0.0	5%	95%
7.5	99%	1%
8.5	99%	1%
9.0	5%	95%
11.0	5%	95%
11.0	stop	

The concentration of the total organic carbon (TOC) in the aqueous solution was evaluated with a Shimadzu TOC 5050A analyzer equipped with an OCT-L 8-port auto-sample. For inorganic carbon (IC) measurement, sample solution is automatically acidified with HCl in order to convert carbonate and bicarbonate anions into CO₂ that is then purged using clean compressed air and measured in a NDIR detector. For total carbon (TC), the sample solution is directly sent to a high temperature furnace (680 °C) where, in presence of platinum catalyst, both organic and inorganic carbon are converted to CO₂ that is measured in the same NDIR detector. The total organic carbon (TOC) is therefore obtained by subtracting the concentration of IC from the concentration of TC measured independently.

The calibration for total carbon was performed with potassium hydrogen phthalate in the range 0-10 mg L⁻¹ of carbon. External calibration for inorganic carbon was performed with a standard mixed solution of sodium carbonate and sodium bicarbonate in the range 0-4 mg L⁻¹. The TOC value was the average of three individual injections, each with an injection volume of 50 µL. The calibration curve of TC and IC were shown in **Fig. 3-11**.

3.6.7. pH measurement

The pH value of the solution was adjusted with HClO₄ or NaOH. pH values of the solutions were measured using a Fiveeasy™ Plus pH meter. The pH meter needs to be calibrated at three points at pH = 4.01, 7.01 and 10.01 with standard pH buffers before use.

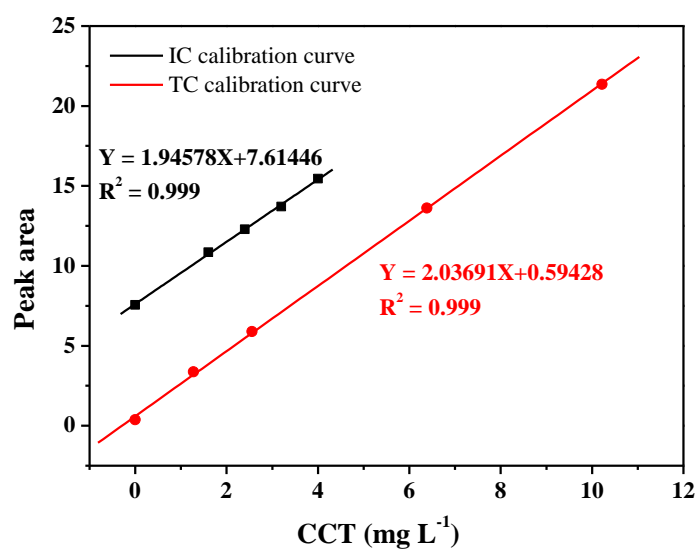


Fig. 3-11. The Calibration curves of TC and IC

References

- [1] R.F. Renneke, M. Pasquali, C.L. Hill, Polyoxometalate systems for the catalytic selective production of nonthermodynamic alkenes from alkanes. Nature of excited-state deactivation processes and control of subsequent thermal processes in polyoxometalate photoredox chemistry, *J. Am. Chem. Soc.* 112 (1990) 6585–6594. <https://doi.org/10.1021/ja00174a020>.
- [2] H. Li, X. Jiang, W. Zhu, J. Lu, H. Shu, Y. Yan, Deep Oxidative Desulfurization of Fuel Oils Catalyzed by Decatungstates in the Ionic Liquid of [Bmim]PF₆, *Ind. Eng. Chem. Res.* 48 (2009) 9034–9039. <https://doi.org/10.1021/ie900754f>.
- [3] W. Huang, M. Luo, C. Wei, Y. Wang, K. Hanna, G. Mailhot, Enhanced heterogeneous photo-Fenton process modified by magnetite and EDDS: BPA degradation, *Environmental Science and Pollution Research.* 24 (2017) 10421–10429. <https://doi.org/10.1007/s11356-017-8728-8>.
- [4] A. Chauhan, Powder XRD Technique and its Applications in Science and Technology, *J Anal Bioanal Tech.* 5 (2014). <https://doi.org/10.4172/2155-9872.1000212>.
- [5] A.M. Venezia, X-ray photoelectron spectroscopy (XPS) for catalysts characterization, *Catalysis Today.* 77 (2003) 359–370. [https://doi.org/10.1016/S0920-5861\(02\)00380-2](https://doi.org/10.1016/S0920-5861(02)00380-2).
- [6] N. Elgrishi, K.J. Rountree, B.D. McCarthy, E.S. Rountree, T.T. Eisenhart, J.L. Dempsey, A Practical Beginner's Guide to Cyclic Voltammetry, *J. Chem. Educ.* 95 (2018) 197–206. <https://doi.org/10.1021/acs.jchemed.7b00361>.
- [7] H. Liu, Q. Chen, X. Cheng, Y. Wang, Y. Zhang, G. Fan, Sustainable and scalable in-situ fabrication of Au nanoparticles and Fe₃O₄ hybrids as highly efficient electrocatalysts for

- the enzyme-free sensing of H₂O₂ in neutral and basic solutions, *Sensors and Actuators B: Chemical*. 314 (2020) 128067. <https://doi.org/10.1016/j.snb.2020.128067>.
- [8] W. Huang, M. Brigante, F. Wu, K. Hanna, G. Mailhot, Effect of Ethylenediamine-N,N'-disuccinic acid on Fenton and photo-Fenton processes using goethite as an iron source: optimization of parameters for Bisphenol A degradation., *Environmental Science and Pollution Research International*. 20 (2012). <https://doi.org/10.1007/s11356-012-1042-6>.
- [9] A.L. Lazrus, G.L. Kok, S.N. Gitlin, J.A. Lind, S.E. McLaren, Automated fluorimetric method for hydrogen peroxide in atmospheric precipitation, *Anal. Chem.* 57 (1985) 917–922. <https://doi.org/10.1021/ac00281a031>.
- [10] G.G. Guilbault, P.J. Brignac, Mark. Juneau, Substrates for the fluorometric determination of oxidative enzymes, *Anal. Chem.* 40 (1968) 1256–1263. <https://doi.org/10.1021/ac60264a027>.
- [11] G.L. Kok, K. Thompson, A.L. Lazrus, S.E. McLaren, Derivatization technique for the determination of peroxides in precipitation, *Analytical Chemistry*. 58 (1986) 1192–1194.

Chapter 4: Results and Discussion

Manuscript 1

Enhancement of the photocatalytic activity of Decatungstate, $W_{10}O_{32}^{4-}$, for the oxidation of sulfasalazine/sulfapyridine in the presence of hydrogen peroxide

P. Cheng¹, Yajie Wang², M. Sarakha^{1*}, G. Mailhot¹

¹Université Clermont Auvergne, CNRS, Sigma Clermont, Institut de Chimie de Clermont Ferrand (ICCF) UMR 6296, BP 80026, F-63171, Aubière cedex, France.

²School of Eco-Environmental Engineering, Guizhou Minzu University, Guiyang 550025, China

* Corresponding author, E-mail address: Mohamed.Sarakha@uca.fr.

Abstract

The degradations of sulfasalazine and also sulfapyridine have been investigated by using the sodium decatungstate $\text{Na}_4\text{W}_{10}\text{O}_{32}$ as a photocatalyst in the presence of hydrogen peroxide as a sacrificial agent. The selective irradiation of decatungstate, $\text{W}_{10}\text{O}_{32}^{4-}$, in the presence of the pollutants at 365 nm and at pH = 4.0 leads to the reduction of hydrogen peroxide via a Fenton like reaction involving the reduced species, $\text{W}_{10}\text{O}_{32}^{5-}$. Such process represents an efficient way for the formation of the highly reactive species, namely the hydroxyl radicals. The process appears then to be highly efficient for the oxidation of the pollutants sulfasalazine and sulfapyridine. Under our experimental conditions, the process was optimized in terms of concentrations of the photocatalyst, hydrogen peroxide and pollutant concentrations and also in term of pH. For both pollutants, the analysis of the generated by-products, using HPLC/MS, shows that the degradation proceeds primarily through three and common chemical processes: i) hydroxylation ii) desulfurization and iii) scission at the azo group $-\text{N}=\text{N}-$. The attack of the hydroxyl radical is clearly the main species for the degradation processes. As clearly demonstrated by the TOC experiments, the combination of $\text{W}_{10}\text{O}_{32}^{4-}/\text{H}_2\text{O}_2/h\nu$ system permitted a total mineralization of the solution indicating its high efficiency for the potential application of water depollution.

Keywords: Decatungstate, Photocatalysis, Fenton-like reaction, Antibiotics, Mineralization

1. Introduction

Nowadays, the emergence of antibiotics in the environment and their potential hazards have attracted more and more attention [1–3]. Most antibiotics are not completely absorbed by the body, and an average of more than 50-90% of the antibiotics are excreted in the form of protoplasts or metabolites, which have been widely detected in surface water, groundwater, sewage treatment plant effluent, drinking water and soil sediments [4]. For example, antibiotics such as ofloxacin at 306 ng L^{-1} , lincomycin at 249 ng L^{-1} and spiramycin at 74 ng L^{-1} and trace amounts of amoxicillin and penicillin were detected in the Lambro and Po rivers in Italy at significant concentrations [5]. The presence of antibiotics into the environment not only has adverse effects on the ecosystem, such as the emergence of resistant pathogens and toxicity to aquatic organisms, but also can enter the human body through the enrichment of food chain, leading to a serious threat to human health such as causing vomiting or diabetes mellitus [6,7]. The common occurrence of abusing of antibiotics is easily found especially in aquaculture field in some Asian countries like China and India. China has been one of the largest producers and users of the antibiotics in the world, approximately 162 000 tons of antibiotics were used in 2013. Aquaculture consumption accounted for about 52% of the total antibiotics [8]. Therefore, the treatment of antibiotics in the environment is particularly important.

The biological, adsorption and chemical oxidation methods, etc. were applied in treating the antibiotics present in wastewater. For example, Xiong et al. combined amino-functionalized Metal-organic framework (MOFs, MIL-53(Fe)) with multi-walled carbon nanotubes (MWCNT) to synthesize a novel adsorbent composite which was used to adsorb tetracycline hydrochloride (TCN) and chlortetracycline hydrochloride (CTC) [9]. While antibiotics are composed by

various functional groups and substituents, the structure is very different, which makes the adsorption behavior on adsorbents different for distinct antibiotics and so the efficiency of the treatment will be strongly chemical structure dependent.

Advanced oxidation processes (AOPs), also known as deep oxidation technology, are characterized by the generation of reactive species (reactive oxygen species “ROS”), such as hydroxyl radicals (HO^\bullet), sulfate radicals ($\text{SO}_4^{\bullet-}$), with strong oxidizing power [10]. The organic substances which are difficult to degrade, can be oxidized into a low-toxic or non-toxic small molecule substance, and very often more readily (bio-)degradable, [4,11–15]. Due to its green environmentally friendly sustainable properties, the photocatalytic oxidation became one of the best promising techniques in treating organic wastewater. Many researchers develop important energy in the synthesis of new photocatalysts or the modification of already prepared photocatalyst with the aim to improve the efficiency of organic pollutants degradation.

The decatungstate anion ($\text{W}_{10}\text{O}_{32}^{4-}$) was shown to be one of the most photo-chemically active polyoxometalates, which catching the interesting of thousands of researchers over the past 30 years [16]. It is worth noting that $\text{W}_{10}\text{O}_{32}^{4-}$ absorbs in the UV with a maximum at 320 nm and its absorption spectrum presents a useful overlap with the solar emission spectrum. Illumination of $\text{W}_{10}\text{O}_{32}^{4-}$, within the range 300 - 400 nm, leads to the formation of an oxygen-to-metal charge transfer excited state $\text{W}_{10}\text{O}_{32}^{4-*}$ that decays in less than 30 ps to an extremely reactive non-emissive transient, which has been referred to as wO [17]. This latter species is able to oxidize organic compounds through electron transfer or/and hydrogen abstraction owing to the presence of an electron-deficient oxygen center. In decatungstate system, the reactive species has a lifetime τ_{wO} of 65 ± 5 ns in the case of sodium decatungstate and its formation

quantum yield Φ_{wO} is 0.57 [17]. Such reaction between wO and appropriate hydrogen or/and electron donor leads to the formation of the one electron reduced form of decatungstate $W_{10}O_{32}^{5-}$ that absorbs in the visible region with a maximum at 778 nm. The reduction of molecular oxygen to superoxide anion by such species is an efficient process for the regeneration of the starting catalyst, $W_{10}O_{32}^{4-}$. In previous studies, the decatungstate ($W_{10}O_{32}^{4-}$) was used as an efficient and optimistic tool in organic synthesis, which can functionalize some organic compounds such as alkanes, alkenes, alcohols, aldehydes and sulfides in organic and aqueous media via free radical carbon-centered intermediates [18]. On the other hand, the decatungstate was also deeply studied for water depollution. Allaoui et al. studied the photodegradation of 2-mercaptobenzothiazole (MBT) and illustrated that the photodegradation rate of MBT clearly increased in the presence of decatungstate ($W_{10}O_{32}^{4-}$) by a factor of six when compared with the direct photolysis; and oxygen appeared to be the key species for catalyst regeneration [19].

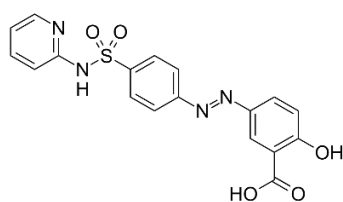
In the present work, we choose the soluble sodium decatungstate ($Na_4W_{10}O_{32}$) as a photocatalyst to degrade the sulfonamides antibiotics (sulfasalazine and sulfapyridine). Moreover, and in this homogeneous system, we added hydrogen peroxide as a supplementary oxidant (with oxygen) in order to oxidize the reduced species of decatungstate ($W_{10}O_{32}^{5-}$) permitting the efficient regeneration of the starting $W_{10}O_{32}^{4-}$. This additional process permits the formation of the highly reactive species, namely hydroxyl radicals. Our purpose was to evaluate the photodegradation of sulfasalazine (SSZ) and sulfapyridine (SPD) through the determination of kinetics, the initial rate constants and the yields of SSZ and SPD degradation. In addition, with the photoproduct's identification, the mechanistic pathways involved in the

degradation will be proposed with the aim to have a better insight into the SSZ and SPD degradation scheme.

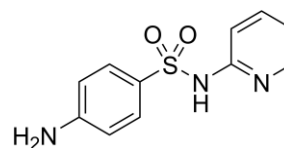
2. Materials and Methods

2.1. Materials

Sulfasalazine (SSZ) (99.8%), Sulfapyridine (SPD) ($\geq 99\%$), sodium tungstate ($\text{Na}_2\text{WO}_4 \cdot 2\text{H}_2\text{O}$), sodium chloride (NaCl), hydrochloric acid (HCl), hydrogen peroxide (H_2O_2), perchloric acid (HClO_4), and sodium hydroxide (NaOH) were purchased from Sigma Aldrich and used as received. Water was purified using a reverse osmosis RIOS 5 and Synergy (Millipore) device (resistivity $18 \text{ M}\Omega \cdot \text{cm}$, $\text{DOC} < 0.1 \text{ mg} \cdot \text{L}^{-1}$).



SSZ



SPD

2.2. Preparation and characterization of sodium decatungstate

The preparation of sodium decatungstate refers to the previous studies available [20]. The boiling sodium tungstate solution (50 g of $\text{Na}_2\text{WO}_4 \cdot 2\text{H}_2\text{O}$ dissolved in 300 mL of ultrapure water) was mixed with 1.0 M boiling hydrochloric acid (300 mL) in a beaker, refluxed for 20 seconds to form a green solution. It was followed by adding 150 g of solid sodium chloride, stirring until the solution has been re-boiled and keeping for 20 seconds, then rapidly putting into the ice-water bath. This suspension solution was maintained in a freezer (-18°C) overnight.

The next day, this suspension solution of NaCl and crude $\text{Na}_4\text{W}_{10}\text{O}_{32}$ was filtered and the solid was dissolved into 150 mL of acetonitrile solution. The acetonitrile solution was refluxed for 5 min at 79°C and filtered to remove the insoluble NaCl after cooling at ambient temperature. The acetonitrile solution was gently evaporated in hot-water bath (79°C) to obtain the yellow-green catalyst.

The UV-Vis absorption spectra were obtained using a Varian Cary 300 UV-visible spectrophotometer. The infrared absorption spectra were obtained by Fourier infrared absorption spectrometer, operated by potassium bromide pressed-disk technique (98% KBr).

2.3. Irradiation experiments and photoreactor

Irradiation experiments (365 nm) were carried out in a stainless-steel cylindrical reactor. Six high pressure mercury lamps (Philips HPW, 15W, emission centered at 365 nm) was located evenly on the edge of the cylinder with a fan placed on the bottom of the cylinder to cool the irradiation system. The reactor, a Pyrex tube (2 cm diameter), was placed at the center of the cylinder (**Fig. S1**).

The degradation of SSZ and SPD was performed in a batch experiment. The 5.0×10^{-5} M solution of SSZ and SPD was prepared and 10.0 mg soluble decatungstate was added into the 100 mL of SSZ or SPD solution, the concentration of decatungstate was then evaluated to 4.0×10^{-5} M. Hydrogen peroxide was added using a concentrated solution, and so with negligible volume, prior to irradiation using the photo-reactor system. The pH of solution was adjusted to 4.0 ± 0.05 using perchloric acid and sodium hydroxide (0.1 M). Aliquots were taken at different interval times of 0, 2, 5, 10, 15, 20, 25 min at ambient temperature.

The effect of initial pH was studied at 23 °C using a similar procedure, 10 mg decatungstate (4.0×10^{-5} M) were mixed with 100 mL 5.0×10^{-5} M solution of SSZ or SPD at different initial pH of 3, 4, 5 and 6. The solution pHs were adjusted by adding small negligible volume of perchloric acid and/or sodium hydroxide (0.1 M).

The effect of the concentration of H_2O_2 (from 10^{-5} to 10^{-2} M), SSZ and SPD (5.0×10^{-6} , 10^{-5} , 2.0×10^{-5} , 5.0×10^{-5} and 1.0×10^{-4} M) and decatungstate (2.0×10^{-5} , 4.0×10^{-5} , 7.0×10^{-5} , 1.0×10^{-4} and 2.0×10^{-4} M) were also investigated.

2.4. HPLC Analysis

The concentrations of SSZ and SPD were evaluated by HPLC (Shimadzu NEXERA XR HPL) equipped with a photodiode array detector and an auto sampler. The column was a Macherey Nagel EC 150/2 NUCLEODUR C18ec (150 mm \times 2 mm, 2 μm particle size)

The analysis of SSZ was performed using methanol (MeOH, solvent B) as mobile phase and water with 0.5 % phosphoric acid (solvent A) at a flow rate of 0.20 mL min^{-1} . The elution was performed using the following gradient: 40 % of B for 5min, linear increase of B to 95 % in 15 min, 95 % of B for 5 min and decrease of B to 40 % in 0.1 min. For SPD, the analyses were performed using acetonitrile (ACN, solvent C) as mobile phase and water with 0.5 % of phosphoric acid at a flow rate of 0.40 mL min^{-1} . The elution was performed using the following gradient: 5 % of C for 2.5 min, linear increase of C to 40 % in 4.5 min, then increase of C to 95 % in 1.5 min, 95 % of C for 1 min and decrease of C to 5 % in 0.5 min.

The identification of degradation products was performed using high resolution mass spectrometry (HRMS) constituted of an Orbitrap Q-Exactive (ThermoScientific) coupled to an

ultra-high performance liquid chromatography (UHPLC) instrument Ultimate 3000 RSLC (ThermoScientific). Analyses were carried out in both negative and positive electrospray modes (ESI⁺ and ESI⁻). SSZ, SPD and the degradation products were separated using the same elution gradient as previously indicated. The column was a Kinetec EVO C18 Phenomenex (100 mm × 2.1 mm, particle size of 1.7 μm) and the flow rate was set at 0.45 mL·min⁻¹.

2.5. TOC Analysis

The concentration of the total organic carbon (TOC) in the aqueous solution was followed on a Shimadzu TOC 5050A analyzer. The TOC value was the average of three individual injections.

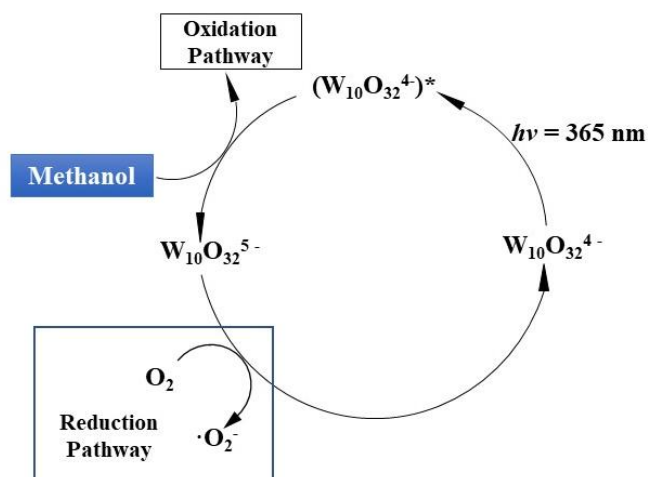
3. Results

3.1. Characterization and photochemistry behavior of the photocatalyst

The UV-visible spectrum of the synthesized photocatalyst decatungstate, W₁₀O₃₂⁴⁻ (NaDT), is given in **Fig. 1**. It shows an absorption band with a defined maximum at 321 nm and a molar absorption coefficient of 12365 M⁻¹ cm⁻¹ in perfect agreement with the published literature data [20]. The UV absorption extends up to 400 nm indicating an important and interesting overlap with the emission spectrum of solar light. In addition to the UV visible spectrum, the characterization of the decatungstate was also performed by employing the Fourier transformed IR. In **Fig. S2**, the strong broad band centered at around 3500 cm⁻¹ and the peak at around 1600 cm⁻¹ are attributed to the O–H stretching vibrations and to the bending modes of water molecules. This implied that the hydrophilicity of the substrate will improve

the photocatalysis activity as suggested by H-Y. He [21,22]. The main vibration bands of decatungstate ($W_{10}O_{32}^{4-}$) are observed at 1006 cm^{-1} corresponding to the stretching vibration of the W=O bond, and at 962, 915, 796, 667, 586, 431 cm^{-1} due to the deformation of W-O-W bonds [17,23,24]. Moreover, and as largely reported in the literature [16,25,26], the excitation of the mixture decatungstate and methanol (used as a sacrificial agent since it acts as an electron or/and hydrogen donor) permits in deoxygenated conditions the formation of a blue component that presents two well defined bands with maximums at 360 and 780 nm (**Fig. S3**) with roughly similar molar absorption coefficients ($6.7\text{-}6.9 \times 10^3\text{ M}^{-1}\text{ cm}^{-1}$ at 360 nm and $9.5\text{-}11 \times 10^3\text{ M}^{-1}\text{ cm}^{-1}$ at 780 nm). Such absorptions are owing to the formation of the reduced species of decatungstate, namely $W_{10}O_{32}^{5-}$ that disappears rapidly by bubbling oxygen through an electron transfer process leading to the formation of superoxide anion radical $O_2^{\bullet-}$ with the simultaneous regeneration of the starting photocatalyst decatungstate [27] (**Scheme 1**). Such interesting behavior was used within the present work to enhance the ability of the photocatalyst to decontaminate polluted waters by producing reactive oxygen species (ROS) that are highly oxidant such as hydroxyl radical. The formation of this latter species was reached by introducing hydrogen peroxide as a sacrificial reactant.

The efficiency of the photocatalytic cycle was studied and optimized by studying sulfonamides antibiotics sulfasalazine (SSZ) and sulfapyridine (SPD) degradations.



Scheme 1. Photocatalytic cycle of decatungstate upon UV excitation in the presence of methanol showing oxidation and reduction processes

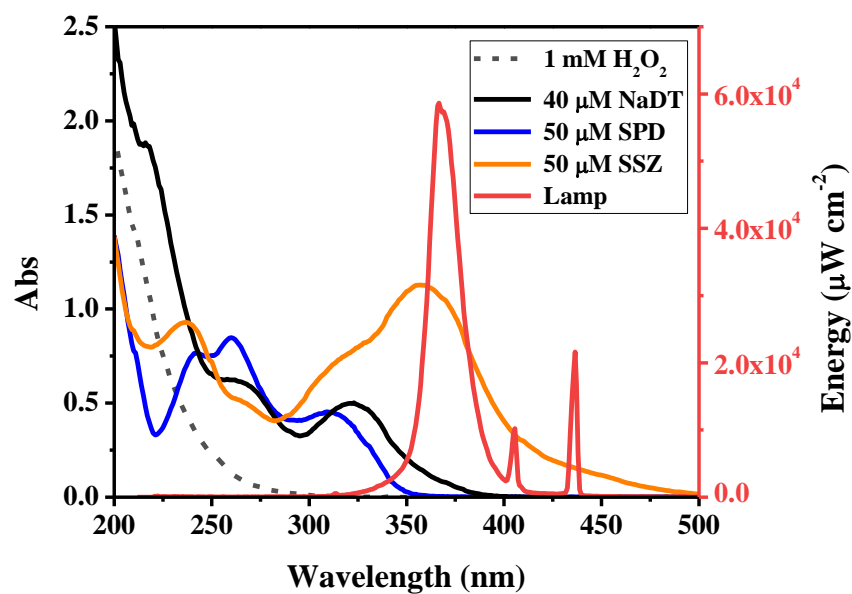


Fig. 1. Emission spectrum of lamps used in the reactor and UV-visible absorption spectra of SSZ, SPD and decatungstate (NaDT)

3.2. photodegradation of SSZ and SPD by NaDT, H₂O₂ or NaDT/H₂O₂ systems

In order to evaluate the efficiency of the decatungstate photocatalysis process, irradiations were performed under UVA (365 nm) for different aerated solutions in the presence of SSZ in

various conditions (SSZ alone, SSZ + H₂O₂, SSZ + NaDT and SSZ + H₂O₂ + NaDT). As clearly shown in **Fig. 2A**, no degradation was noted when SSZ was alone in aqueous solution, despite its significant absorption at the excitation wavelength. This indicates the relative photochemical stability of SSZ under our experimental conditions. However, in the presence of hydrogen peroxide, a negligible degradation was observed representing 2% within 120 minutes of irradiation. In the presence of decatungstate, the conversion percentage of SSZ reached 16% demonstrating the oxidation ability of the photocatalyst decatungstate through an oxidation process (electron transfer) as shown in **Scheme 1**. The initial rate of SSZ disappearance was estimated to $1.2 \times 10^{-7} \text{ M min}^{-1}$. By addition of hydrogen peroxide in the previous system, the conversion percentage increased significantly in agreement with the fact that hydrogen peroxide interacts in the photocatalytic cycle and presents a positive and beneficial effect when it is used simultaneously with decatungstate. In this latter system, the degradation of SSZ reaches 28% after 120 minutes irradiation time with an initial rate of $1.6 \times 10^{-7} \text{ M min}^{-1}$. The benefit of hydrogen peroxide in the photocatalysis process is then effective and it was deeply studied and optimized within the present work. Similar experiments were performed with SPD showing a more pronounced degradation. This is owing to the fact that SPD does not absorb at the excitation wavelength, in contrary to SSZ, and thus no competition of the absorbed light intensity is involved (**Fig. 2B**). The initial rate of SPD degradation was estimated to $4.3 \times 10^{-7} \text{ M min}^{-1}$ and $7.0 \times 10^{-7} \text{ M min}^{-1}$ in the presence of decatungstate and decatungstate/H₂O₂ respectively.

The involvement of hydrogen peroxide in the photocatalytic system was also studied by analyzing its reactivity with the reduced species of decatungstate, namely W₁₀O₃₂⁵⁻. As shown

in **Scheme 1**, the latter species was selectively formed by irradiation of decatungstate ($40 \mu\text{M}$) in the presence of 1 % of methanol in deaerated solution. $\text{W}_{10}\text{O}_{32}^{5-}$ immediately disappears when hydrogen peroxide is added to the solution with the regeneration of the $\text{W}_{10}\text{O}_{32}^{4-}$. It is then clear that H_2O_2 is efficiently reduced by $\text{W}_{10}\text{O}_{32}^{5-}$ owing, very likely, to the following Fenton like process (Equation 1).



Equation 1. Fenton like reaction between $\text{W}_{10}\text{O}_{32}^{5-}$ and H_2O_2

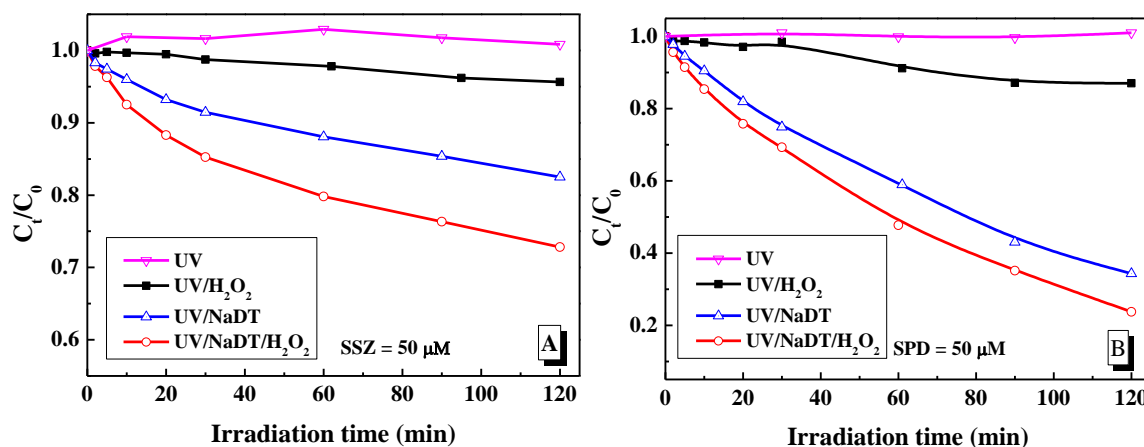
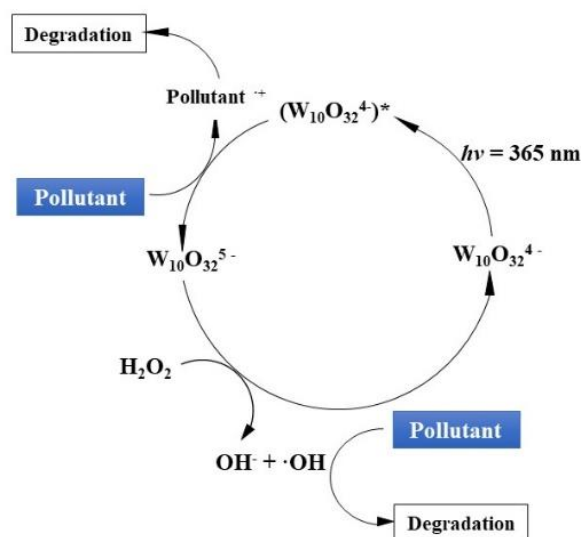


Fig. 2. Degradation kinetics of (A) SSZ and (B) SPD in the different systems. $[\text{SSZ}] = [\text{SPD}] = 50 \mu\text{M}$; $[\text{H}_2\text{O}_2] = 1 \text{ mM}$; $[\text{NaDT}] = 40 \mu\text{M}$; $\text{pH} = 4.0$

The effective formation of hydroxyl radical as a reactive oxygen species (ROS) was demonstrated by employing a probe such as terephthalic acid. As largely reported in the literature, the reactivity of this non fluorescent substrate with hydroxyl radical leads to the formation of a highly fluorescent hydroxyterephthalic acid [28]. As clearly shown in **Fig. 3**, the excitation of aerated aqueous solution of decatungstate (NaDT) in the presence of terephthalic acid (TA) and hydrogen peroxide (H_2O_2) at $\text{pH} = 4.0$ leads to a rapid and efficient formation of

hydroxyterephthalic acid (TAOH) from the early stages of the irradiation. This demonstrates the involvement of an additional pathway for the formation of the reactive oxygen species, namely the hydroxyl radical. The absence of the blue color following irradiation is clear evidence for involvement of the reduced species of decatungstate ($W_{10}O_{32}^{5-}$) for the formation of this ROS species. The smaller amount of hydroxyl radical in the absence of hydrogen peroxide could be due to the disproportionation process of hydroperoxide radical and/or superoxide anion radical ($HO_2^*/O_2^{\bullet-}$) to form H_2O_2 [29]. It is then clear from these results that the amount of hydroxyl radical mainly originates from the reactivity of $W_{10}O_{32}^{5-}$ and hydrogen peroxide permitting the implication of a supplementary pathway for the degradation of the pollutants: first through the oxidation by the excited state of decatungstate via an electron transfer or/and hydrogen transfer processes and then through the oxidation by the hydroxyl radical generated via the Fenton like process (**Scheme 2**). It should be pointed out that the latter reaction is in competition with the reactivity of $W_{10}O_{32}^{5-}$ with oxygen.



Scheme 2. Photocatalytic cycle of decatungstate in the presence of H_2O_2 showing the two ways for the organic pollutant degradation.

In the following parts of the paper, the optimization of the experimental conditions was studied by analyzing the effect of various parameters such as: concentrations of decatungstate; hydrogen peroxide and organic pollutant and the initial pH of the solution. These parameters represent fundamental parameters for the photocatalysis to be effective since i) decatungstate is the absorbing species and thus its optimum concentration will ensure high concentration of the excited state without the negative inner filter effect ii) hydrogen peroxide efficiently contributes in the system to the formation of hydroxyl radicals. The latter species react simultaneously with the pollutant and hydrogen peroxide via competitive reactions and iii) the stability of the photocatalyst depends on the solution pH.

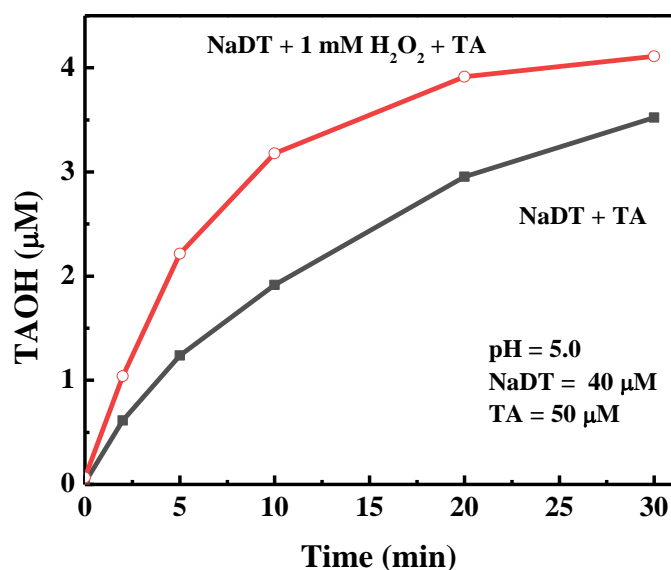


Fig. 3. Formation of Hydroxyterephthalic acid by excitation of decatungstate (40 μM) at 365 nm in the presence of H_2O_2

3.3. Effect of different amount of decatungstate

In order to study the effect of decatungstate concentration on the removal of the pollutants SSZ and SPD, the experiments were performed at pH= 4.0. As clearly shown in **Fig. 4A** and

4B, the degradation rates of SSZ and SPD increase by increasing the concentration of the photocatalyst decatungstate. This effect is without any doubt due to the increase of the light absorption by decatungstate at higher concentration. However, under our experimental conditions the degradation rate rapidly levelled off when decatungstate concentration reaches 50 μM , as shown in **Fig. 4C**. This is more probably owing to the inner filter effect. Thus, the concentration close to 40 μM was chosen as the optimal concentration of the photocatalyst for the following experiments.

3.4. Effect of different concentrations of H_2O_2

Table 1 gathers the initial degradation rate obtained for both pollutants by excitation of decatungstate (40 μM) in the presence of various hydrogen peroxide concentrations. In the absence of H_2O_2 and at lower concentration of H_2O_2 (1 mM), the disappearance initial rate is found roughly 4 times higher for SPD than for SSZ due to the absorption of light by SSZ. At higher concentrations of H_2O_2 (10 to 100 mM), the disappearance initial rate of SPD is always higher than that of SSZ but by a factor of about 1.5. In addition to the electron transfer between SSZ or SPD and $\text{W}_{10}\text{O}_{32}^{4-}$ excited state, a second pathway is involved when hydrogen peroxide is added to the system via the production of hydroxyl radicals as demonstrated above. As clearly shown in **Table 1**, this reaction is effective despite the presence of dissolved molecular oxygen at a concentration of 2.6×10^{-4} M [30,31]. Moreover, the initial disappearance rate increases when hydrogen peroxide concentration increases. One should also note, that under our experimental conditions and at high concentrations, the direct light absorption by hydrogen peroxide also participate in the generation of hydroxyl radical and thus to the degradation of

the pollutant through the homolytic scission of O-O bond [32,33]. It should be noted that at high concentration of hydrogen peroxide, the consumption of hydroxyl radical could be observed by H₂O₂ itself which is detrimental under our experimental conditions [34,35].

Table 1. SSZ and SPD initial degradation rates as a function of H₂O₂ concentration

[H ₂ O ₂] mM	Initial rate of SSZ disappearance (M min ⁻¹)		Initial rate of SPD Disappearance (M min ⁻¹)	
	Without decatungstate	With decatungstate	Without decatungstate	With decatungstate
	0	No degradation	1.2×10 ⁻⁷	No degradation
1	0.1×10 ⁻⁷	1.6×10 ⁻⁷	0.6×10 ⁻⁷	7.0×10 ⁻⁷
10	1.1×10 ⁻⁷	6.1×10 ⁻⁷	4.2×10 ⁻⁷	10.9×10 ⁻⁷
50	5.0×10 ⁻⁷	14.0×10 ⁻⁷	13.7×10 ⁻⁷	21.9×10 ⁻⁷
100	7.2×10 ⁻⁷	21.5×10 ⁻⁷	21.3×10 ⁻⁷	33.9×10 ⁻⁷

[NaDT] = 40 μM; [SSZ] = [SPD] = 50 μM; pH = 4.0

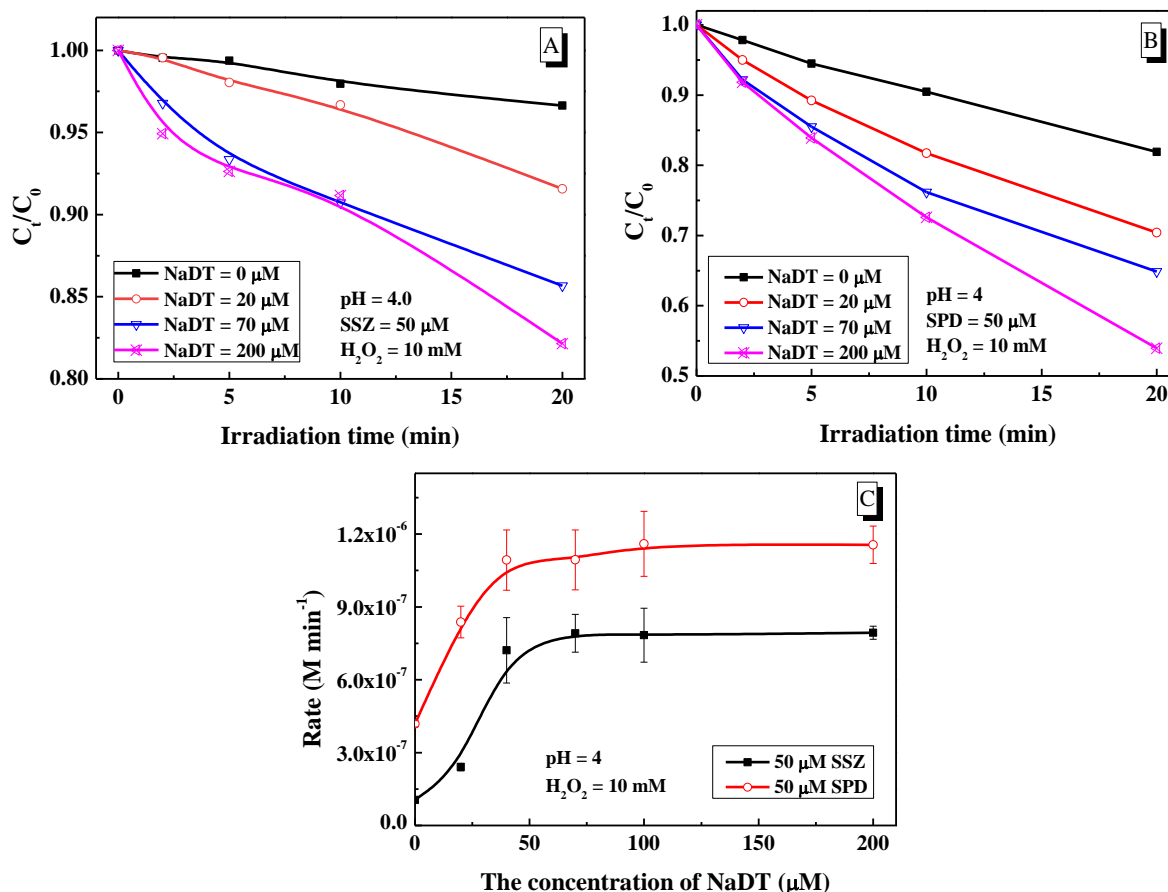


Fig. 4. Effect of decatungstate concentration on SSZ (A) and SPD (B) removal in the presence of H₂O₂. [SSZ] = [SPD] = 50 μM ; [H₂O₂] = 10 mM, pH = 4.0.

3.5. Effect of different SSZ and SPD concentrations

With the aim to use the photocatalyst decatungstate for various pollutants that have different chemical structures and also different light absorption profiles, we undertook the effect of the concentration of both pollutants, SSZ and SPD, on the efficiency of the photocatalytic process. We can note that SPD does not absorb at the excitation wavelengths, namely at 365 nm, while SSZ shows significant absorbance with a molar absorption coefficient $\epsilon_{365 \text{ nm}} = 21850.4 \text{ M}^{-1} \text{ cm}^{-1}$. The experiments were performed by using decatungstate at the concentration of 40.0 μM in the presence of H₂O₂ 10 mM with various concentrations of the pollutants within

the range 5.0 to 100 μM at $\text{pH} = 4.0$. As shown in **Fig. 5**, the initial disappearance rate of SPD increased by increasing its initial concentration. This clearly shows that under our experimental conditions, hydroxyl radical is involved in the oxidation of SPD but it is also trapped by hydrogen peroxide as largely reported in the literature with a rate constant of $3.0 \times 10^7 \text{ M}^{-1} \text{ s}^{-1}$ [34,35]. Such reaction is detrimental since it participates to the decrease of the stationary concentration of the reactive species: hydroxyl radical. So, the use of relatively high concentrations of SPD will be in favor of its degradation.

In the case of SSZ, the initial rate first increases within the concentration range 5.0 to 20.0 μM and then decreases at higher concentrations. Such decrease of the initial rate is mainly owing to the competition in the absorption of light intensity involving the photocatalyst decatungstate and SSZ. Such effect is detrimental to the photocatalysis effect and leads to the decrease of the concentration/formation of reactive excited state of decatungstate, namely, $\text{W}_{10}\text{O}_{32}^{4-*}$.

3.6. Effect of different initial pH

The initial pH of the solution is a crucial parameter for the photocatalysis processes owing to the stability of decatungstate and/or the various forms of the pollutants when a protonation-deprotonation process is present (**Fig. S4**). Thus, we studied the optimum pH under our experimental conditions. For both substrates, SSZ and SPD at a concentration of 50.0 μM , the excitation of decatungstate (40 μM) at 365 nm in the presence of 1.0 mM H_2O_2 permitted the degradation of the pollutants with a rate that decreases when the pH of the solution increases. The initial rates of SSZ were estimated to $2.1 \times 10^{-7} \text{ M min}^{-1}$ and $1.1 \times 10^{-7} \text{ M min}^{-1}$ at $\text{pH} = 3.0$

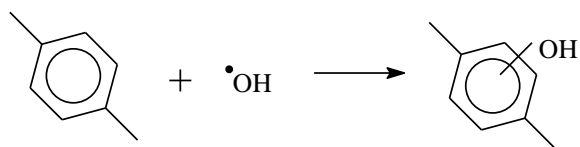
and 6.0 respectively and the initial rates of SPD were estimated to $7.4 \times 10^{-7} \text{ M min}^{-1}$ and $5.5 \times 10^{-7} \text{ M min}^{-1}$ at pH = 3.0 and 6.0 respectively. This effect is more likely due to the fact that decatungstate is relatively instable at high pH values as largely reported in the literature [29,36].

3.7. Elucidation of the initial products and degradation pathways for the pollutant disappearance

The elucidation of the generated byproducts was performed by employing HPLC/MS technique. The results are gathered in **Table 2** for both substrates: SSZ and SPD. They were obtained for irradiated samples that show roughly 30% conversion corresponding under our experimental conditions to 120 min of irradiation time. The suggested structures were based on the elemental compositions that were obtained from the obtained accurate masses. Some of them are clearly primary products while others originate from secondary reactions.

The analysis of the chemical structures of the products leads us to the conclusion that in the early stages of the irradiation mainly three and common chemical processes are involved for both pollutants: i) hydroxylation ii) desulfurization and iii) scission at the azo group $-\text{N}=\text{N}-$.

The hydroxylation process is a clear evidence of the reactivity of the hydroxyl radical with the used pollutants via an electron transfer process with the aromatic groups as largely reported in the literature [37–39] leading finally to the addition of the hydroxyl group to the substrate (**scheme 3**).



Scheme 3. Process of the reactivity of the hydroxyl radical with the benzene ring via an electron transfer process

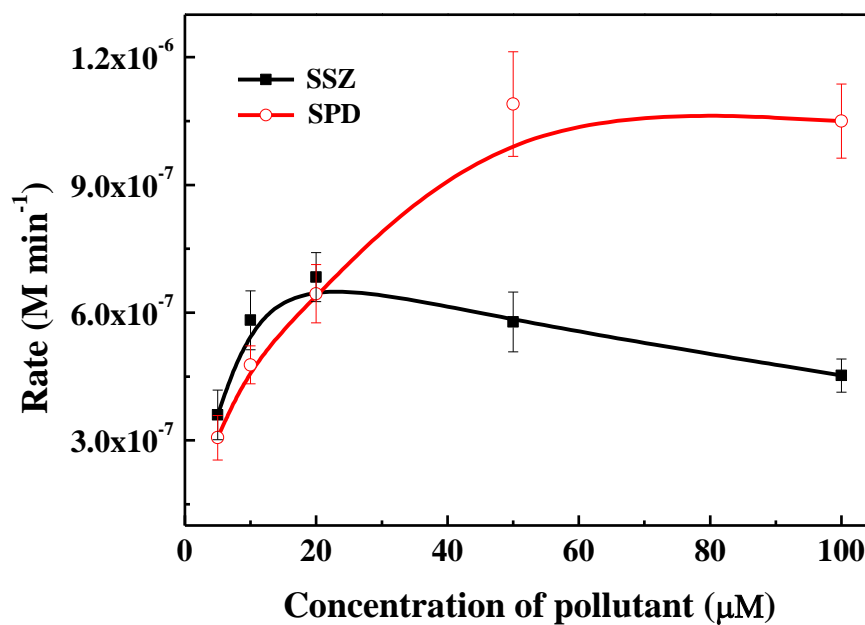
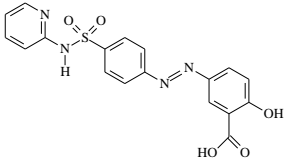
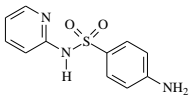
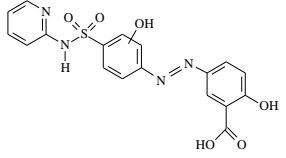
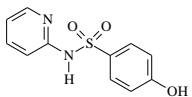
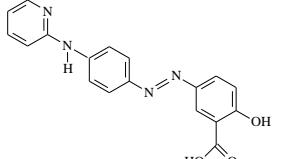
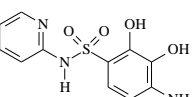
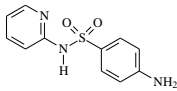
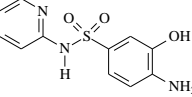
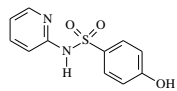
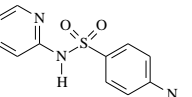
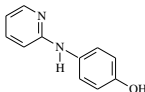
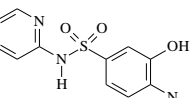
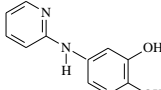
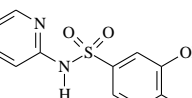
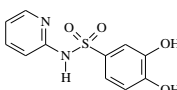
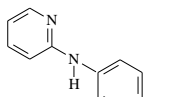
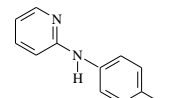
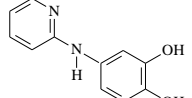


Fig. 5. Initial degradation rates of SSZ and SPD as a function of their initial concentrations.

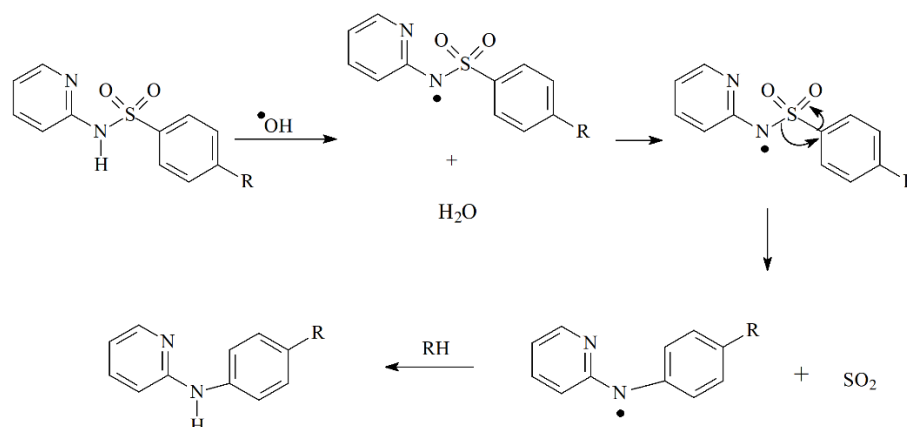
$[\text{H}_2\text{O}_2] = 10 \text{ mM}$; $[\text{NaDT}] = 40 \mu\text{M}$; $\text{pH} = 4.0$

Table 2. MS analysis of SPD and SSZ by-products and suggested structures.

SSZ			SPD		
m/z	Elemental composition	Suggested structure	m/z	Elemental composition	Suggested structure
398	C ₁₈ H ₁₄ N ₄ O ₅ S		249	C ₁₁ H ₁₁ N ₃ O ₂ S	
414	C ₁₈ H ₁₄ N ₄ O ₆ S		250	C ₁₁ H ₁₀ N ₂ O ₃ S	
334	C ₁₈ H ₁₄ N ₄ O ₃		281	C ₁₁ H ₁₁ N ₃ O ₄ S	
249	C ₁₁ H ₁₁ N ₃ O ₂ S		265	C ₁₁ H ₁₁ N ₃ O ₃ S	
250	C ₁₁ H ₁₀ N ₂ O ₃ S		263	C ₁₁ H ₉ N ₃ O ₃ S	
186	C ₁₁ H ₁₀ N ₂ O		279	C ₁₁ H ₉ N ₃ O ₄ S	
202	C ₁₁ H ₁₀ N ₂ O ₂		266	C ₁₁ H ₁₀ N ₂ O ₄ S	
266	C ₁₁ H ₁₀ N ₂ O ₄ S		185	C ₁₁ H ₁₁ N ₃	
			186	C ₁₁ H ₁₀ N ₂ O	
			202	C ₁₁ H ₁₀ N ₂ O ₂	

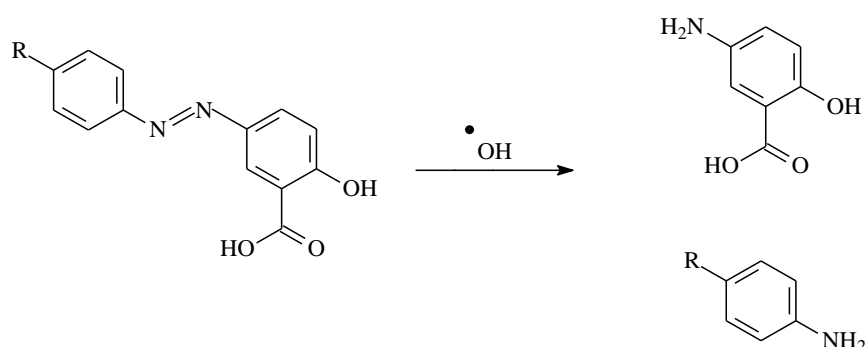
[NaDT] = 40 μM; [H₂O₂] = 10 mM; [SSZ] = [SPD] = 50 μM; pH = 4.0

The desulfurization reaction is a reaction that is more likely triggered by the attack of the hydroxyl radical on the adjacent amine group via an electron or/and a hydrogen abstraction process followed by an intramolecular rearrangement as shown in the following **scheme 4** [40].



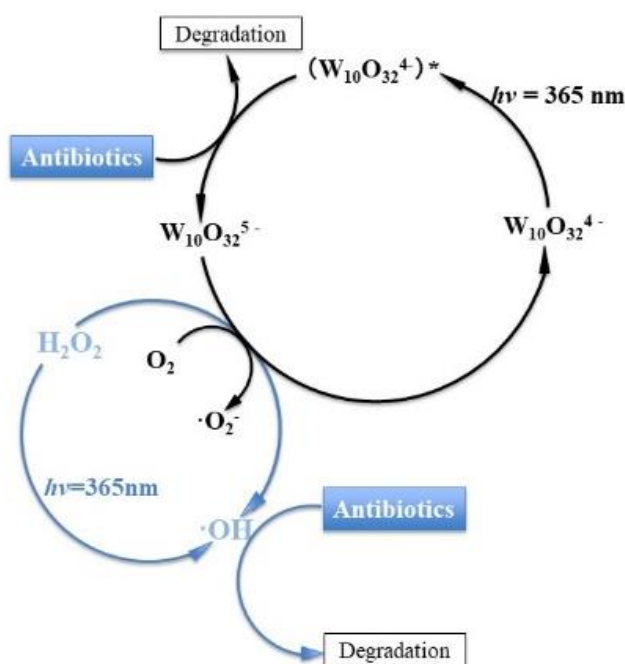
Scheme 4. The process of the desulfurization via an electron or/and a hydrogen abstraction process

The third process is a scission at the azo group $-N=N-$ that is more likely triggered by the attack of the hydroxyl radical on the nitrogen sites leading to the formation of the two amine products as shown in the following **scheme 5** [41].



Scheme 5. Process of the azo group $-N=N-$ scission via an attack of hydroxyl radical

The photocatalytic process; involving decatungstate and H_2O_2 is given in **Scheme 6**. $\text{W}_{10}\text{O}_{32}^{4-}$ could be excited upon UVA (365 nm) irradiation to form the excited state $\text{W}_{10}\text{O}_{32}^{4-*}$ which leads, via an electron transfer process with the pollutant, to the formation of the reduced form of decatungstate namely $\text{W}_{10}\text{O}_{32}^{5-}$ and the radical cation of the pollutant. This process provides one of the degradation pathways. The regeneration of the photocatalyst can operate in the presence of H_2O_2 and oxygen, following the formation of the hydroxyl radicals and superoxide anion radicals respectively. The former free radical is highly and efficiently involved in the oxidation of SPD and SSZ. And this represents the second pathway of organic pollutant degradation.



Scheme 6. Photocatalytic cycle of decatungstate/ H_2O_2 system showing the two ways for the degradation of the organic pollutant and the production of hydroxyl radicals via Fenton like reaction between $\text{W}_{10}\text{O}_{32}^{5-}$ and H_2O_2 .

3.8. Total organic carbon analysis

In order to confirm the efficient degradation of the pollutants and also of their metabolites up to the mineralization of the solution, we followed the total organic carbon (TOC) under light excitation. We followed the evolution of TOC in a solution of SPD or/and SSZ under similar conditions ($[\text{NaDT}] = 40.0 \mu\text{M}$, $[\text{H}_2\text{O}_2] = 10.0 \text{ mM}$, $\text{pH} = 4.0$). In this case, after 24 h of irradiation, 90% of the initial organic carbon (SSZ alone) has been transformed into CO_2 (Fig. 6). After 48h of irradiation, 75% of the initial organic carbon (SPD alone, SPD and SSZ) has been converted into CO_2 (Fig. 6). Such observations confirm that the decatungstate/ H_2O_2 system could be used in order to completely achieve the removal of SPD or/and SSZ and their byproducts from water. Moreover, they suggest that decatungstate/ H_2O_2 system could be applied to treat multiple pollutants in water under the optimized experimental conditions.

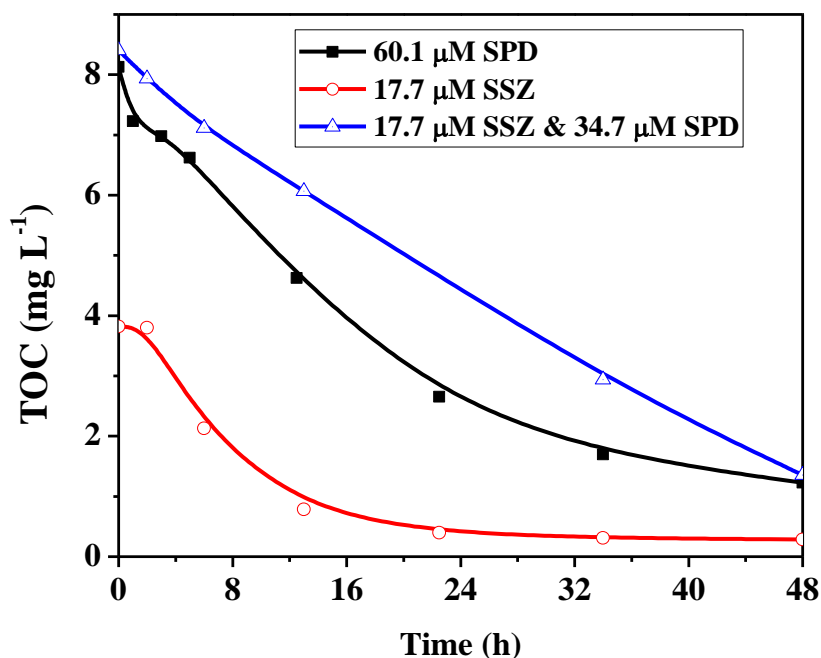


Fig. 6. Evolution of TOC in a SSZ or/and SPD solution in decatungstate/ H_2O_2 system

$[\text{H}_2\text{O}_2] = 10 \text{ mM}$; $[\text{NaDT}] = 40 \mu\text{M}$; $\text{pH} = 4.0$

4. Conclusion

The combination of $W_{10}O_{32}^{4-}/H_2O_2/h\nu$ at pH=4.0 permitted an efficient degradation of the pollutants (sulfasalazine and sulfapyridine). The process involves two ways of reaction for the oxidation of the organic compounds i) an electron transfer reaction with the excited state of decatungstate and ii) also the hydroxyl radical reactivity. HO^\bullet is formed from the Fenton like reaction with the reduced species of decatungstate, $W_{10}O_{32}^{5-}$ and H_2O_2 . The latter process represents under our experimental conditions the main process for the disappearance of the pollutants and it is also a way for the regeneration of starting catalyst, decatungstate. The main primary reactions were found to be hydroxylation, desulfurization and scission at the azo group $-N=N-$ moiety. For prolonged irradiations, the mineralization of the solution was observed which highlights the point that the conjunction of $W_{10}O_{32}^{4-}/H_2O_2$ and light represent an interesting AOP's system for water depollution. Indeed, the two possible pathways for the oxidation of organic compounds in this system are important asset for treating polluted waters leading us to the conclusion that this system could be considered in the future as a promising process for the decontamination of water. As a perspective of this work, the immobilization of the photocatalyst decatungstate on solid supports will be a goal in order to recycle the photocatalyst after treatment.

Acknowledgements

Peng CHENG thanks the Chinese scholarship council for its financial support and thanks professor Marcello Brigante, engineer Guillaume Voyard and PhD student Yara Arbid for their help in some of the experiments.

References

- [1] R. Laxminarayan, A. Duse, C. Wattal, A.K. Zaidi, H.F. Wertheim, N. Sumpradit, E. Vlieghe, G.L. Hara, I.M. Gould, H. Goossens, Antibiotic resistance—the need for global solutions, *The Lancet Infectious Diseases*. 13 (2013) 1057–1098.
- [2] C. Ding, J. He, Effect of antibiotics in the environment on microbial populations, *Appl Microbiol Biotechnol*. 87 (2010) 925–941. <https://doi.org/10.1007/s00253-010-2649-5>.
- [3] M. Qiao, G.-G. Ying, A.C. Singer, Y.-G. Zhu, Review of antibiotic resistance in China and its environment, *Environment International*. 110 (2018) 160–172.
- [4] L.V. de S. Santos, A.M. Meireles, L.C. Lange, Degradation of antibiotics norfloxacin by Fenton, UV and UV/H₂O₂, *Journal of Environmental Management*. 154 (2015) 8–12. <https://doi.org/10.1016/j.jenvman.2015.02.021>.
- [5] D. Calamari, E. Zuccato, S. Castiglioni, R. Bagnati, R. Fanelli, Strategic Survey of Therapeutic Drugs in the Rivers Po and Lambro in Northern Italy, *Environ. Sci. Technol*. 37 (2003) 1241–1248. <https://doi.org/10.1021/es020158e>.
- [6] B.A. Cunha, ANTIBIOTIC SIDE EFFECTS, *Medical Clinics of North America*. 85 (2001) 149–185. [https://doi.org/10.1016/S0025-7125\(05\)70309-6](https://doi.org/10.1016/S0025-7125(05)70309-6).
- [7] A. Sola, Abuse of Antibiotics in Perinatology: Negative Impact for Health and the Economy, *NeoReviews*. 21 (2020) e559–e570. <https://doi.org/10.1542/neo.21-8-e559>.
- [8] Q.-Q. Zhang, G.-G. Ying, C.-G. Pan, Y.-S. Liu, J.-L. Zhao, Comprehensive Evaluation of Antibiotics Emission and Fate in the River Basins of China: Source Analysis, Multimedia Modeling, and Linkage to Bacterial Resistance, *Environ. Sci. Technol*. 49 (2015) 6772–6782. <https://doi.org/10.1021/acs.est.5b00729>.

- [9] W. Xiong, Z. Zeng, X. Li, G. Zeng, R. Xiao, Z. Yang, Y. Zhou, C. Zhang, M. Cheng, L. Hu, Multi-walled carbon nanotube/amino-functionalized MIL-53 (Fe) composites: remarkable adsorptive removal of antibiotics from aqueous solutions, *Chemosphere*. 210 (2018) 1061–1069.
- [10] T. Oppenländer, Photochemical purification of water and air: advanced oxidation processes (AOPs)-principles, reaction mechanisms, reactor concepts, John Wiley & Sons, 2007.
- [11] L. Hu, P. Wang, T. Shen, Q. Wang, X. Wang, P. Xu, Q. Zheng, G. Zhang, The application of microwaves in sulfate radical-based advanced oxidation processes for environmental remediation: A review, *Science of The Total Environment*. 722 (2020) 137831. <https://doi.org/10.1016/j.scitotenv.2020.137831>.
- [12] J. Deng, Y. Shao, N. Gao, Y. Deng, S. Zhou, X. Hu, Thermally activated persulfate (TAP) oxidation of antiepileptic drug carbamazepine in water, *Chemical Engineering Journal*. 228 (2013) 765–771.
- [13] F. Sopaj, N. Oturan, J. Pinson, F.I. Podvorica, M.A. Oturan, Effect of cathode material on electro-Fenton process efficiency for electrocatalytic mineralization of the antibiotic sulfamethazine, *Chemical Engineering Journal*. 384 (2020) 123249. <https://doi.org/10.1016/j.cej.2019.123249>.
- [14] L. Hou, H. Zhang, X. Xue, Ultrasound enhanced heterogeneous activation of peroxydisulfate by magnetite catalyst for the degradation of tetracycline in water, *Separation and Purification Technology*. 84 (2012) 147–152. <https://doi.org/10.1016/j.seppur.2011.06.023>.

- [15] M. Xing, W. Xu, C. Dong, Y. Bai, J. Zeng, Y. Zhou, J. Zhang, Y. Yin, Metal Sulfides as Excellent Co-catalysts for H₂O₂ Decomposition in Advanced Oxidation Processes, *Chem.* 4 (2018) 1359–1372. <https://doi.org/10.1016/j.chempr.2018.03.002>.
- [16] G. Laudadio, Y. Deng, K. van der Wal, D. Ravelli, M. Nuño, M. Fagnoni, D. Guthrie, Y. Sun, T. Noël, C(sp³)-H functionalizations of light hydrocarbons using decatungstate photocatalysis in flow, *Science*. 369 (2020) 92–96. <https://doi.org/10.1126/science.abb4688>.
- [17] I. Texier, J.A. Delaire, C. Giannotti, Reactivity of the charge transfer excited state of sodium decatungstate at the nanosecond time scale, *Phys. Chem. Chem. Phys.* 2 (2000) 1205–1212. <https://doi.org/10.1039/A908588B>.
- [18] M. D. Tzirakis, I. N. Lykakis, M. Orfanopoulos, Decatungstate as an efficient photocatalyst in organic chemistry, *Chemical Society Reviews*. 38 (2009) 2609–2621. <https://doi.org/10.1039/B812100C>.
- [19] A. Allaoui, M.A. Malouki, P. Wong-Wah-Chung, Homogeneous photodegradation study of 2-mercaptobenzothiazole photocatalysed by sodium decatungstate salts: Kinetics and mechanistic pathways, *Journal of Photochemistry and Photobiology A: Chemistry*. 212 (2010) 153–160. <https://doi.org/10.1016/j.jphotochem.2010.04.010>.
- [20] D.C. Duncan, T.L. Netzel, C.L. Hill, Early-Time Dynamics and Reactivity of Polyoxometalate Excited States. Identification of a Short-Lived LMCT Excited State and a Reactive Long-Lived Charge-Transfer Intermediate following Picosecond Flash Excitation of [W₁₀O₃₂]⁴⁻ in Acetonitrile, *Inorg. Chem.* 34 (1995) 4640–4646. <https://doi.org/10.1021/ic00122a021>.

- [21] H.-Y. He, J. Lu, Highly photocatalytic activities of magnetically separable reduced graphene oxide-CoFe₂O₄ hybrid nanostructures in dye photodegradation, *Separation and Purification Technology*. 172 (2017) 374–381. <https://doi.org/10.1016/j.seppur.2016.08.040>.
- [22] H.-Y. He, Z. He, Q. Shen, Efficient hydrogen evolution catalytic activity of graphene/metallic MoS₂ nanosheet heterostructures synthesized by a one-step hydrothermal process, *International Journal of Hydrogen Energy*. 43 (2018) 21835–21843.
- [23] M. Bonchio, M. Carraro, M. Gardan, G. Scorrano, E. Drioli, E. Fontananova, Hybrid photocatalytic membranes embedding decatungstate for heterogeneous photooxygenation, *Top Catal.* 40 (2006) 133–140. <https://doi.org/10.1007/s11244-006-0115-5>.
- [24] Y. Guo, C. Hu, X. Wang, Y. Wang, E. Wang, Y. Zou, H. Ding, S. Feng, Microporous Decatungstates: Synthesis and Photochemical Behavior, *Chem. Mater.* 13 (2001) 4058–4064. <https://doi.org/10.1021/cm010211i>.
- [25] Y. Nosaka, T. Takei, N. Fujii, Photoinduced reduction of W₁₀O₃₂⁴⁻ by organic compounds in aqueous solution, *Journal of Photochemistry and Photobiology A: Chemistry*. 92 (1995) 173–179. [https://doi.org/10.1016/1010-6030\(95\)04125-6](https://doi.org/10.1016/1010-6030(95)04125-6).
- [26] C. Tanielian, R. Seghrouchni, C. Schweitzer, Decatungstate Photocatalyzed Electron-Transfer Reactions of Alkenes. Interception of the Geminate Radical Ion Pair by Oxygen, *J. Phys. Chem. A*. 107 (2003) 1102–1111. <https://doi.org/10.1021/jp0217031>.
- [27] S. Rafqah, P.W.-W. Chung, C. Forano, M. Sarakha, Photocatalytic degradation of metsulfuron methyl in aqueous solution by decatungstate anions, *Journal of*

- Photochemistry and Photobiology A: Chemistry. 199 (2008) 297–302.
<https://doi.org/10.1016/j.jphotochem.2008.06.012>.
- [28] T. Charbouillot, M. Brigante, G. Mailhot, P.R. Maddigapu, C. Minero, D. Vione, Performance and selectivity of the terephthalic acid probe for OH as a function of temperature, pH and composition of atmospherically relevant aqueous media, *Journal of Photochemistry and Photobiology A: Chemistry*. 222 (2011) 70–76.
<https://doi.org/10.1016/j.jphotochem.2011.05.003>.
- [29] B.H. Bielski, Reevaluation of the spectral and kinetic properties of HO₂ and O₂-free radicals, *Photochemistry and Photobiology*. 28 (1978) 645–649.
- [30] L. Wu, X. Zhang, H. Ju, Amperometric glucose sensor based on catalytic reduction of dissolved oxygen at soluble carbon nanofiber, *Biosensors and Bioelectronics*. 23 (2007) 479–484. <https://doi.org/10.1016/j.bios.2007.06.009>.
- [31] H. Ju, C. Shen, Electrocatalytic reduction and determination of dissolved oxygen at a poly (nile blue) modified electrode, *Electroanalysis*. 13 (2001) 789–793.
- [32] Y.-S. Shen, Y. Ku, K.-C. Lee, The effect of light absorbance on the decomposition of chlorophenols by ultraviolet radiation and UV/H₂O₂ processes, *Water Research*. 29 (1995) 907–914.
- [33] G.S. Wang, C.-H. Liao, H.-W. Chen, H.C. Yang, Characteristics of natural organic matter degradation in water by UV/H₂O₂ treatment, *Environmental Technology*. 27 (2006) 277–287.

- [34] H. Christensen, K. Sehested, H. Corfitzen, Reactions of hydroxyl radicals with hydrogen peroxide at ambient and elevated temperatures, *J. Phys. Chem.* 86 (1982) 1588–1590. <https://doi.org/10.1021/j100206a023>.
- [35] M.S. Alam, M. Kelm, B.S.M. Rao, E. Janata, Reaction of H with H₂O₂ as observed by optical absorption of perhydroxyl radicals or aliphatic alcohol radicals and of OH with H₂O₂. A pulse radiolysis study, *Radiation Physics and Chemistry.* 71 (2004) 1087–1093. <https://doi.org/10.1016/j.radphyschem.2003.11.007>.
- [36] E. Papaconstantinou, A. Hiskia, A. Troupis, Photocatalytic processes with tungsten oxygen anion clusters, *Frontiers in Bioscience : A Journal and Virtual Library.* 8 (2003) 813–25. <https://doi.org/10.2741/1156>.
- [37] A. Broo, S. Larsson, Electron transfer in azurin and the role of aromatic side groups of the protein, *J. Phys. Chem.* 95 (1991) 4925–4928. <https://doi.org/10.1021/j100166a002>.
- [38] J.O. Howell, J.M. Goncalves, C. Amatore, L. Klasinc, R.M. Wightman, J.K. Kochi, Electron transfer from aromatic hydrocarbons and their π -complexes with metals. Comparison of the standard oxidation potentials and vertical ionization potentials, *J. Am. Chem. Soc.* 106 (1984) 3968–3976. <https://doi.org/10.1021/ja00326a014>.
- [39] B. Krimmel, F. Swoboda, S. Solar, G. Reznicek, OH-radical induced degradation of hydroxybenzoic-and hydroxycinnamic acids and formation of aromatic products—A gamma radiolysis study, *Radiation Physics and Chemistry.* 79 (2010) 1247–1254.
- [40] Y. Zhang, X. Xie, W. Huang, S. Huang, Degradation of aniline by Fe²⁺-activated persulfate oxidation at ambient temperature, *Journal of Central South University.* 20 (2013) 1010–1014.

- [41] A. Rehorek, M. Tauber, G. Gübitz, Application of power ultrasound for azo dye degradation, *Ultrasonics Sonochemistry*. 11 (2004) 177–182.
<https://doi.org/10.1016/j.ultsonch.2004.01.030>.

Supporting Information

Enhancement of the photocatalytic activity of Decatungstate, $W_{10}O_{32}^{4-}$, for the oxidation of sulfasalazine/sulfapyridine in the presence of hydrogen peroxide

P. Cheng¹, Yajie Wang², M. Sarakha^{1*}, G. Mailhot¹

¹Université Clermont Auvergne, CNRS, Sigma Clermont, Institut de Chimie de Clermont Ferrand (ICCF) UMR 6296, BP 80026, F-63171, Aubière cedex, France.

²School of Eco-Environmental Engineering, Guizhou Minzu University, Guiyang 550025, China

* Corresponding author, E-mail address: Mohamed.Sarakha@uca.fr.

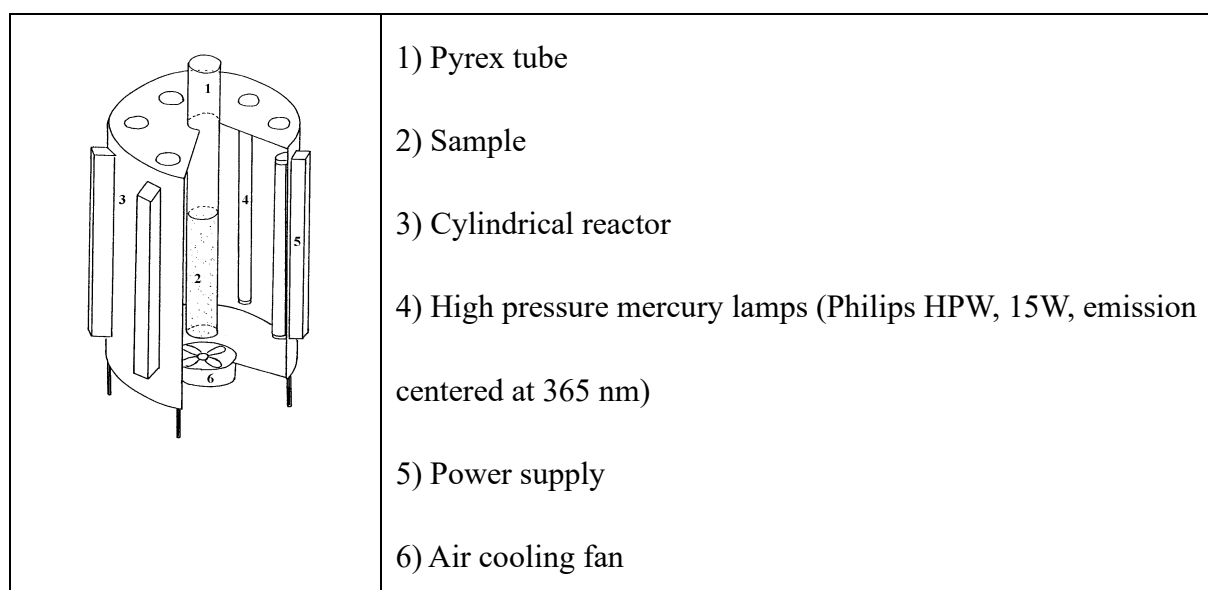


Fig. S1. The 365 nm irradiation setup

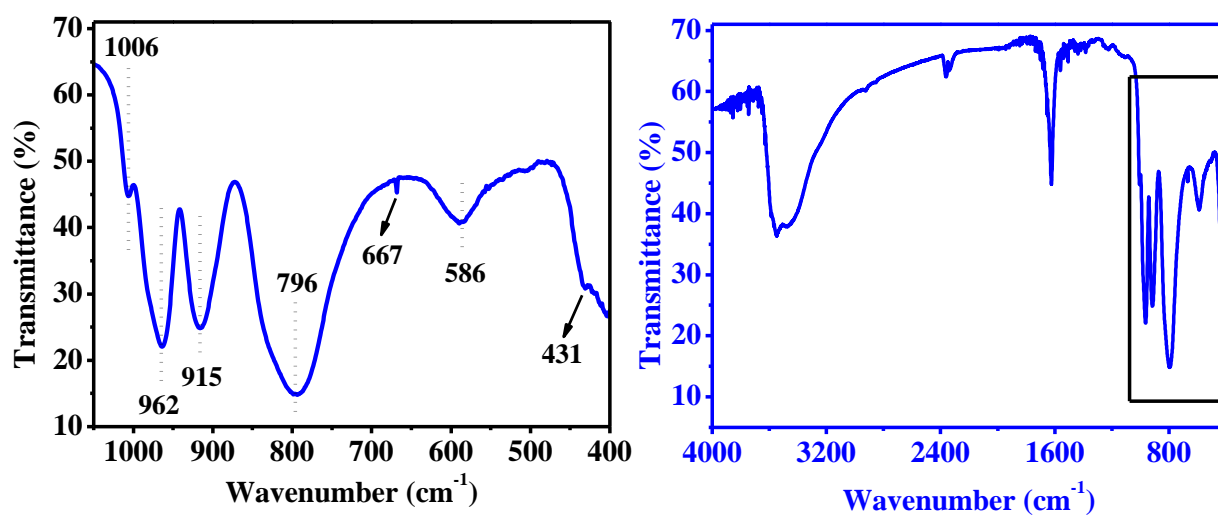


Fig. S2. The infrared spectrum of the decatungstate

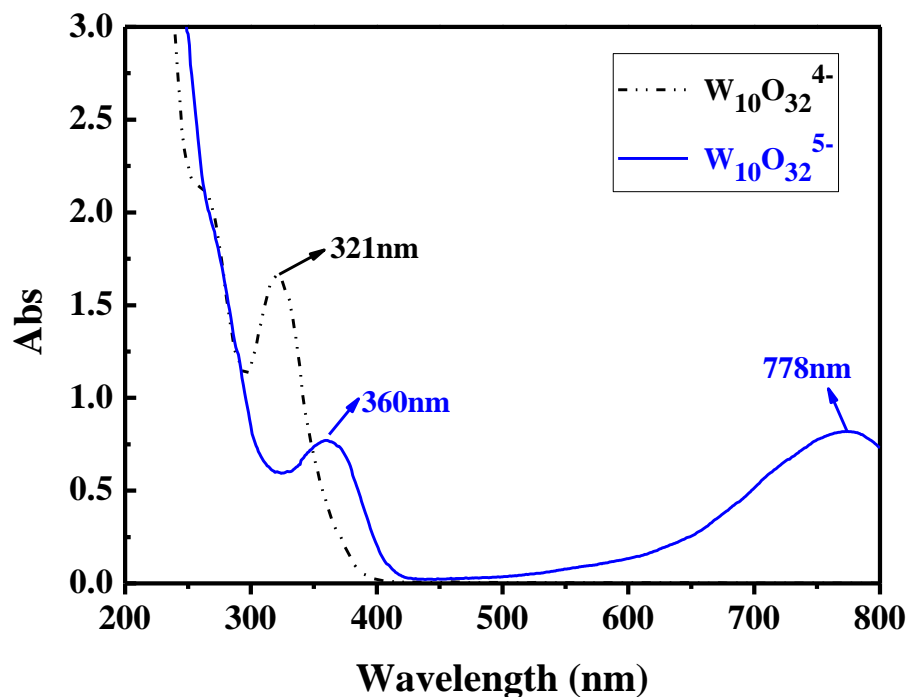


Fig. S3. The UV-Vis spectra of decatungstate and its reduced specie

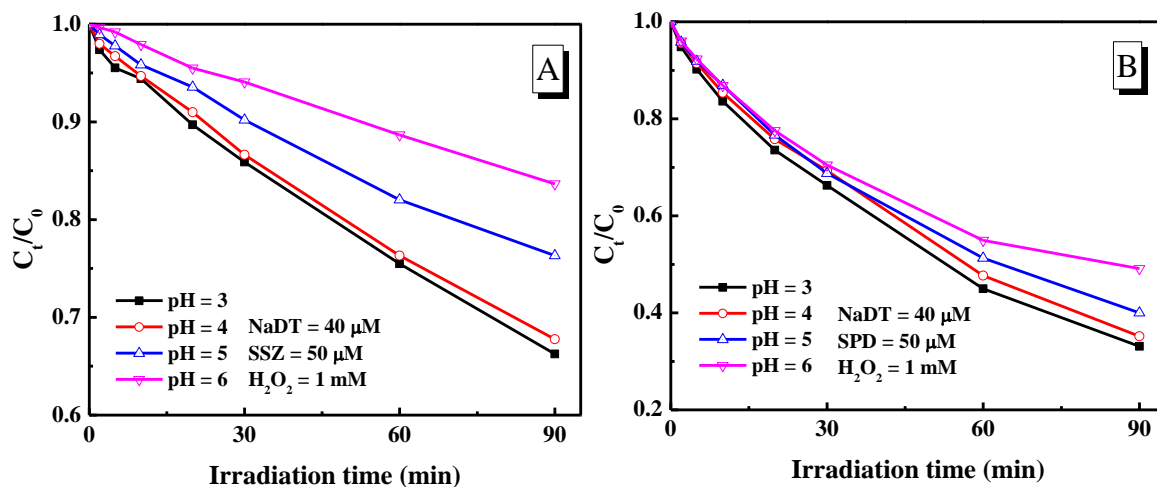


Fig. S4. The effect of different pH on pollutants removal

Manuscript 2

Decatungstate photocatalyst: simultaneous reduction of persulfate and oxidation of organic pollutants

1. Introduction

In recent years, due to the frequent detection of drugs, especially antibiotic drugs, in the secondary effluent of sewage treatment plants, they have attracted great attention [1–3]. Such substances have huge risks to human health and the water environment and ecosystem [4,5].

Advanced oxidation process (AOPs) is one of the most effective methods to treat this type of wastewater [6]. Moreover, photo-catalysis is the most commonly used method to treat organic wastewater among the AOPs [7]. Catalysts are most important in photocatalytic systems, which can significantly influence the performance of photo-catalysis.

The decatungstate or NaDT ($W_{10}O_{32}^{4-}$) photoexcitation performance has attracted the attention of many researchers [8,9]. Illumination of $W_{10}O_{32}^{4-}$ under UV light (ranged from 300 to 400 nm), leads to the formation of excited state of decatungstate ($W_{10}O_{32}^{4-*}$) that has a ligand-to-metal charge (LMCT) character. $W_{10}O_{32}^{4-*}$ can decay to an extremely reactive non-emissive transient (a dark state tagged wO), which has a lifetime τ_{wO} of 65 ± 5 ns in the case of sodium decatungstate and its formation quantum yield Φ_{wO} is 0.57 [10]. The reaction between wO and appropriate hydrogen or/and electron donor leads to the formation of the one electron reduced form of decatungstate ($W_{10}O_{32}^{5-}$) that absorbs in the visible region with a maximum at 778 nm. The reduction of molecular oxygen to superoxide anion by such species is an efficient process for the regeneration of the starting catalyst, $W_{10}O_{32}^{4-}$ [11].

Persulfate (PS) is a strong oxidant and is widely used in the treatment of organic pollutants [12]. The persulfate-based advanced oxidation processes (PS-AOPs) have been rapidly developed, because the reactive oxygen species (ROS), such as sulfate radicals ($SO_4^{\cdot-}$),

generated in the PS activation processes have strong oxidizing ability to efficiently degrade organic pollutants [13].

In this study, we used NaDT as a catalyst to degrade one antibiotic sulfapyridine (SPD). In order to improve the efficiency of degradation, PS was selected as an oxidant, the combination of NaDT and PS was applied to treat pollution by this antibiotic SPD.

2. Materials and Methods

2.1. Materials

Sulfapyridine (SPD) ($\geq 99\%$), sodium tungstate ($\text{Na}_2\text{WO}_4 \cdot 2\text{H}_2\text{O}$), sodium chloride (NaCl), hydrochloric acid (HCl), Potassium persulfate ($\text{K}_2\text{S}_2\text{O}_8$ 99.99%), perchloric acid (HClO_4), and sodium hydroxide (NaOH) were purchased from Sigma Aldrich and used as received. Water (Milli-Q) was purified using a reverse osmosis RIOS 5 and Synergy (Millipore) device (resistivity $18\text{ M}\Omega\text{ cm}$, $\text{DOC} < 0.1\text{ mg L}^{-1}$).

2.2. Preparation of sodium decatungstate (NaDT)

The synthesis of sodium decatungstate ($\text{Na}_4\text{W}_{10}\text{O}_{32}$) was performed according to our previous study [14]. The boiling sodium tungstate solution (50 g of $\text{Na}_2\text{WO}_4 \cdot 2\text{H}_2\text{O}$ dissolved in 300 mL of ultrapure water) was mixed with 1.0 M boiling hydrochloric acid (300 mL) in a beaker, refluxed for 20 seconds to form a green solution. It was followed by adding 150 g of solid sodium chloride, stirring until the solution is re-boiled and keeping for 20 seconds, then rapidly transferred into the ice-water bath. This suspension solution was maintained in a freezer ($-18\text{ }^\circ\text{C}$) overnight. The day after, the suspension solution of NaCl and crude $\text{Na}_4\text{W}_{10}\text{O}_{32}$ was

filtered and the solid was dissolved into 150 mL of acetonitrile solution. The latter solution was refluxed for 5 minutes at 79 °C and filtered in order to remove the insoluble NaCl after cooling at ambient temperature. The acetonitrile solution was gently evaporated in hot-water bath (79 °C) to obtain the catalyst NaDT with a yellow-green color.

2.3. Irradiation experiments and photoreactor

Irradiation experiments (365 nm) were carried out in a reflective enclosure based on a circular form. The reactor and the water circulation system are placed in the center of the enclosure and three lamps are arranged around the reactor. In addition, the device is equipped with a magnetic stirrer which allows us to have a good homogenization of the solutions during the irradiation (**Fig. 1**).

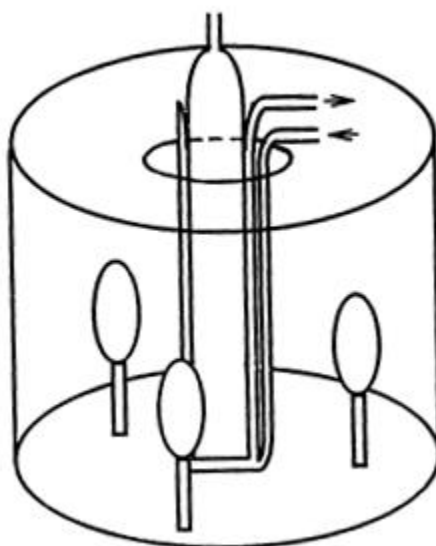


Fig. 1. Scheme of the 365 nm irradiation setup

The light sources are MAZDA MAW 125W lamps; they are medium-pressure mercury vapor lamps whose emission, filtered by a black globe, is mainly at 365 nm (**Fig. 2**).

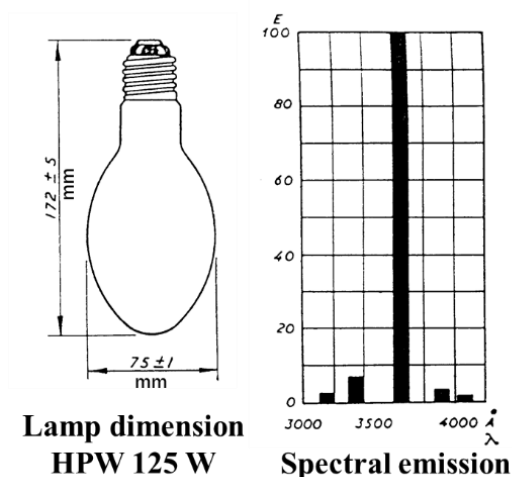


Fig. 2. Emission spectrum of the MAZDA MAW 125 W lamp.

➤ **The Preparation of reduced forms of decatungstate ($\text{NaDT}^{1-}/\text{NaDT}^{2-}$)**

Irradiation ($\lambda = 365 \text{ nm}$) of oxygen-free aqueous solution of decatungstate (NaDT) in presence of methanol results in the formation of blue reduced species. 23.8 mg NaDT was added into the 50 mL of aqueous solution with methanol (124 mM). 3.0 mL of this solution was added into the spectrophotometer cell, and the solution was bubbled with nitrogen (N_2) for 30 min. Then the cell was sealed with a rubber stopper and wrapped with paraffin film to ensure that the air cannot enter into the cell. The cell was put under irradiation and the UV-Vis spectra of the solution was recorded at different irradiation time.

➤ **Reaction between Persulfate and reduced decatungstate ($\text{NaDT}^{1-}/\text{NaDT}^{2-}$)**

The concentrated Persulfate solution (30 mM) was added into prepared reduced decatungstate ($\text{NaDT}^{1-}/\text{NaDT}^{2-}$) solution (Oxygen free) with a negligible volume. The oxygen free water was used as a control. The kinetic of the absorbance was recorded with the UV-Vis spectrophotometer (Varian Cary 300)

➤ **Degradation of SPD under UVA light**

The degradation of SPD was performed in a batch experiment. The 30 μM solution of SPD was prepared and 18.3 mg soluble decatungstate (NaDT) was added into the 25 mL of SPD solution, the concentration of NaDT was then evaluated to 0.3 mM. Potassium persulfate was added using a concentrated solution, and so with negligible volume, prior to irradiation using the photo-reactor system. The pH of solution was adjusted to 3.0 ± 0.05 using perchloric acid and sodium hydroxide (0.1 M). Aliquots were taken at different interval times of 0, 2.5, 5, 10, 15, 20, 30 min at ambient temperature.

3. Results and Discussions

3.1. Photoreduction of $\text{W}^{10}\text{O}_{32}^{4-}$

As we know the soluble decatungstate (NaDT) is an efficient photocatalyst, which can form NaDT reduced species, which have blue color and can oxidize organic compounds. Details of the photoredox chemistry of $\text{W}^{10}\text{O}_{32}^{4-}$ have been published in a series of Nozaka et al.'s studies [15]. Irradiation ($\lambda = 365 \text{ nm}$) of oxygen-free aqueous solution of decatungstate in presence of methanol results in the formation of blue reduced species. In **Fig. 3**, UV-visible spectra of NaDT are presented. They show a peak at 321 nm which is due to the vibration of the W-O band of decatungstate ($\text{W}_{10}\text{O}_{32}^{4-}$). The molar absorption coefficients (ϵ) at 321 and 360 nm of NaDT are calculated from the spectra in **Fig. 3** and are gathered in **Table 1**.

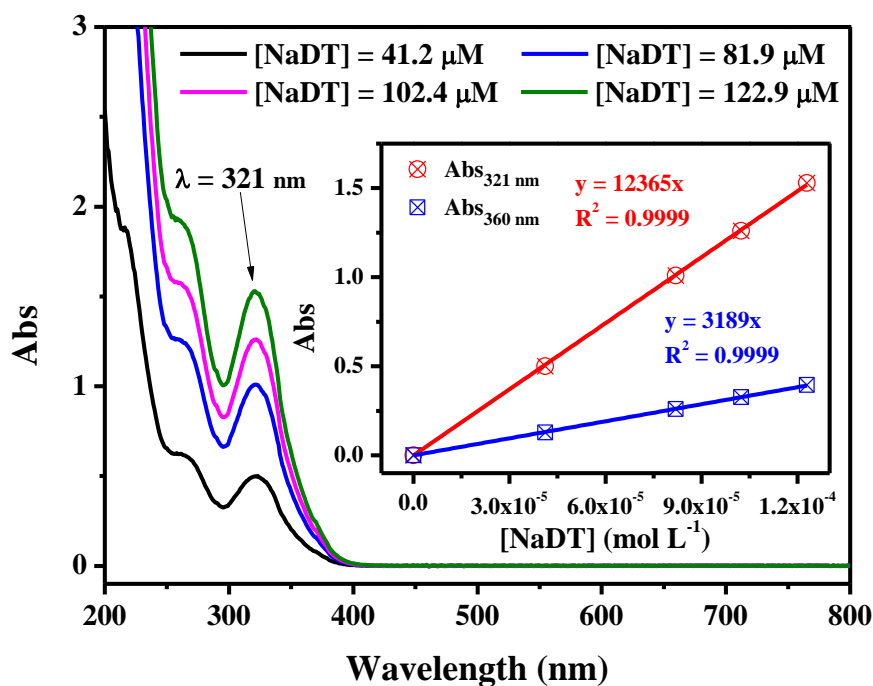


Fig. 3. UV-Visible absorption spectra of NaDT at different concentrations. Insert shows the calibration curves of NaDT at 321 and 360 nm to calculate the molar adsorption coefficient

(ϵ).

Fig. 4. shows the change in the absorption spectra of NaDT in presence of 124 mM of methanol (MeOH) at different irradiation times and in the absence of oxygen. A decrease of the absorption at 321 nm can be observed under ultraviolet irradiation in the presence of methanol. The characteristic peaks at 360, 635 and 775 nm appear simultaneously, which are due the formation of the reduced decatungstate (peaks at 360 and 775 nm are attributed to NaDT^{1-} ($\text{W}_{10}\text{O}_{32}^{5-}$) while peak at 635 nm is attributed to NaDT^{2-} ($\text{W}_{10}\text{O}_{32}^{6-}$)) [15]. Hence the molar absorption coefficient (ϵ) at 360 nm can be used to estimate the concentration of NaDT^{1-} . In order to calculate the concentrations of the two reduced species and due to peaks overlap at 630 and 775 nm, the molar absorption coefficient (ϵ) at each wavelength must be known. The initial increase in absorbance at 635 and 775 nm concomitant with the decrease in absorbance at 321

nm allows to calculate the ϵ of NaDT^{1-} . The value of ϵ at these wavelengths for NaDT^{2-} was calculated as an average value from the spectra obtained after sufficient irradiation of NaDT in the presence of methanol. In **Table 1**, the values of ϵ thus obtained are shown with the reported values from the literature for NaDT, NaDT^{1-} and NaDT^{2-} . Our values are similar with the previous studies.

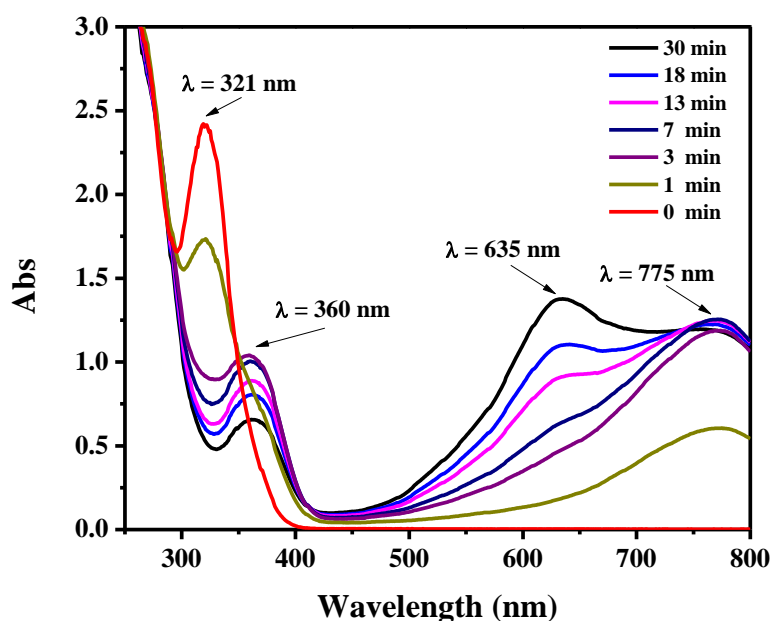


Fig. 4. UV-Vis spectra of sodium decatungstate ($\text{W}_{10}\text{O}_{32}^{4-}$) in aqueous solution under irradiation at $\lambda = 365$ nm in the presence of methanol and in deoxygenated solution. $[\text{NaDT}] = 195 \mu\text{M}$, $[\text{MeOH}] = 124$ mM.

By using the two pairs of ϵ values for NaDT^{1-} and NaDT^{2-} at 635 and 775 nm, the concentration of both reduced species was calculated at each irradiation time. For the reaction with methanol, NaDT decreases at an initial rate of $4.1 \times 10^{-5} \text{ M s}^{-1}$. At the meantime, NaDT^{1-} is formed at an initial rate of $3.8 \times 10^{-5} \text{ M s}^{-1}$ and reach a maximum value of 103 μM after 10 min of irradiation. NaDT^{2-} increases at a rate of $6.7 \times 10^{-6} \text{ M s}^{-1}$ and reaches 87 μM after 30 min as

shown in **Fig. 5**. After 30 min, the yields of NaDT^{1-} and NaDT^{2-} were calculated to be 43% and 57% respectively. These results illustrate that the conversion between NaDT and reduced decatungstate ($\text{NaDT}^{1-}/\text{NaDT}^{2-}$) can be expressed with the following equations:

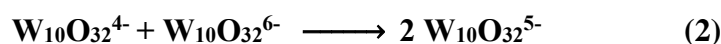
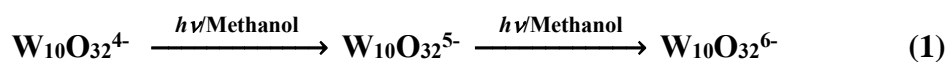


Table 1. Molar absorption coefficients of decatungstate (NaDT) and reduced species (NaDT^{1-} and NaDT^{2-})

Species	ϵ ($10^3 \text{ M}^{-1} \text{ cm}^{-1}$)			
	321 nm	360 nm	635 nm	775 nm
NaDT ($\text{W}_{10}\text{O}_{32}^{4-}$)	12.365	3.189		
	13.2 ^a (320 nm)	3.3 ^a		
	13.0 ^b			
NaDT¹⁻ ($\text{W}_{10}\text{O}_{32}^{5-}$)		7.921	2.654	10.772
		6.9 ^a	2.4 ^a (630 nm)	9.5 ^a (780 nm)
		6.7 ^c		9.8 ^b
NaDT²⁻ ($\text{W}_{10}\text{O}_{32}^{6-}$)			13.529	5.058
			12.9 ^a (630 nm)	5.9 ^a (780 nm)
			14.0 ^c	

^a, ^b and ^c are from Ref. [15], [16] and [17], respectively.

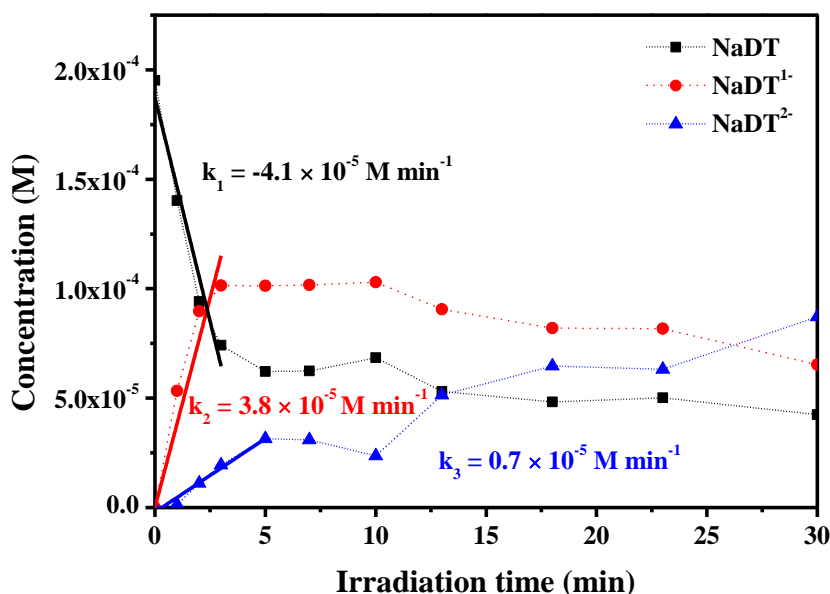


Fig. 5. Kinetics of NaDT, NaDT¹⁻ and NaDT²⁻ concentration in aqueous solution in the presence of methanol without oxygen and under irradiation at 365 nm

3.2. Reaction between reduced decatungstate and persulfate (S₂O₈²⁻)

As we know the persulfate (PS) is one of strongest oxidant commonly used for the water treatment in advanced oxidation processes (AOPs). Theoretically, the redox reaction can occur between NaDT¹⁻/NaDT²⁻ and persulfate, and the sulfate radicals (SO₄^{•-}) can be generated when PS get the electron from reduced decatungstate species. In order to prove that the NaDT¹⁻ and NaDT²⁻ can react with the persulfate, UV-Visible spectrophotometer was used to record the kinetics of absorbance of NaDT¹⁻ and NaDT²⁻ at 775 nm when oxygen-free concentrated persulfate solution was added. Aqueous mixture of decatungstate and methanol (oxygen-free) was irradiated at 365 nm in order to prepare the NaDT¹⁻/NaDT²⁻ solution.

Fig. 6 shows the kinetics of the absorbance of NaDT¹⁻/NaDT²⁻ at 775 nm after adding persulfate solution at different concentrations. The absorbance of NaDT¹⁻/NaDT²⁻ decreases quickly when the persulfate solution was added. After about 120 seconds the absorbance

reaches a plateau value which means that all the PS was consumed. The absorbance of $\text{NaDT}^{1-}/\text{NaDT}^{2-}$ decreases from about 1.9 to 1.8, 1.6, 1.1 and 0.4 when 0, 1.5, 3.0 and 6.0 μM PS were added into the obtained blue solution, respectively. The decrease observed without PS is only due to the dilution factor. This kinetics illustrate that the reduced decatungstate ($\text{NaDT}^{1-}/\text{NaDT}^{2-}$) is reacting with PS with the regeneration the original decatungstate (NaDT) and leading to the formation of sulfate radical. The process can be expressed by the following equation:

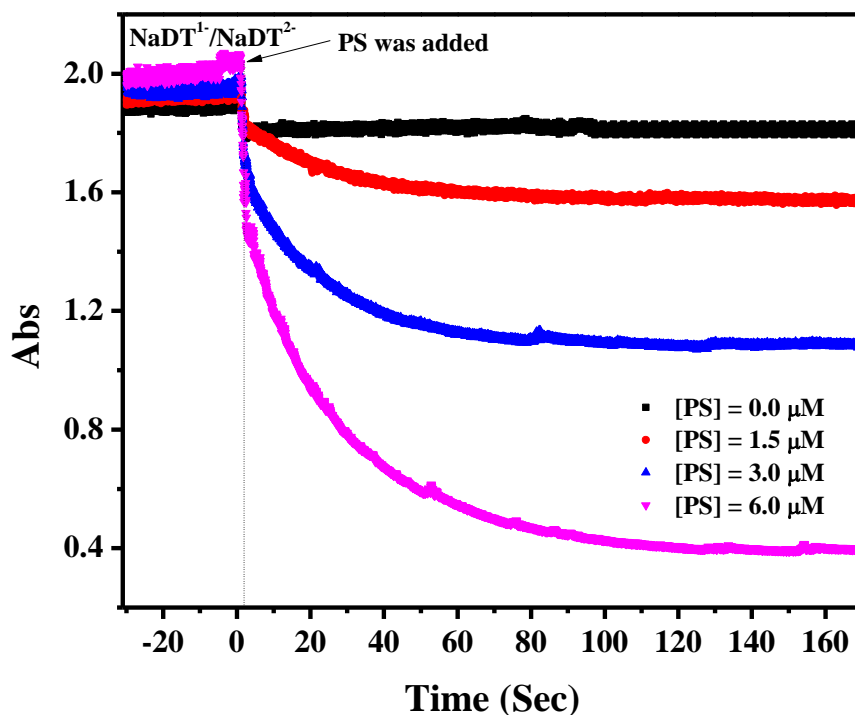


Fig. 6. Absorbance of $\text{NaDT}^{1-}/\text{NaDT}^{2-}$ at 775 nm and kinetics change of its absorbance after adding persulfate solution at different concentrations. $[\text{NaDT}] = 200 \mu\text{M}$, $[\text{MeOH}] = 124 \text{ mM}$, $\text{pH} = 3$; The experiments were performed in oxygen free solution.

3.3 Irradiation experiments

The decatungstate (NaDT) associated with persulfate (PS) was used for the degradation of organic contaminant, sulfapyridine (SPD) under UV irradiation and the efficiency was then evaluated. With this objective, aqueous solution of SPD at a concentration of $30\ \mu\text{M}$ was mixed first with NaDT (0.3 mM) and PS (2.0 mM) at $\text{pH} = 3.0$. UV light with a characteristic wavelength at 365 nm was used as irradiation source. For comparison, experiments were also performed with SPD alone, PS/SPD, NaDT/SPD under the same experimental conditions (Fig. 7).

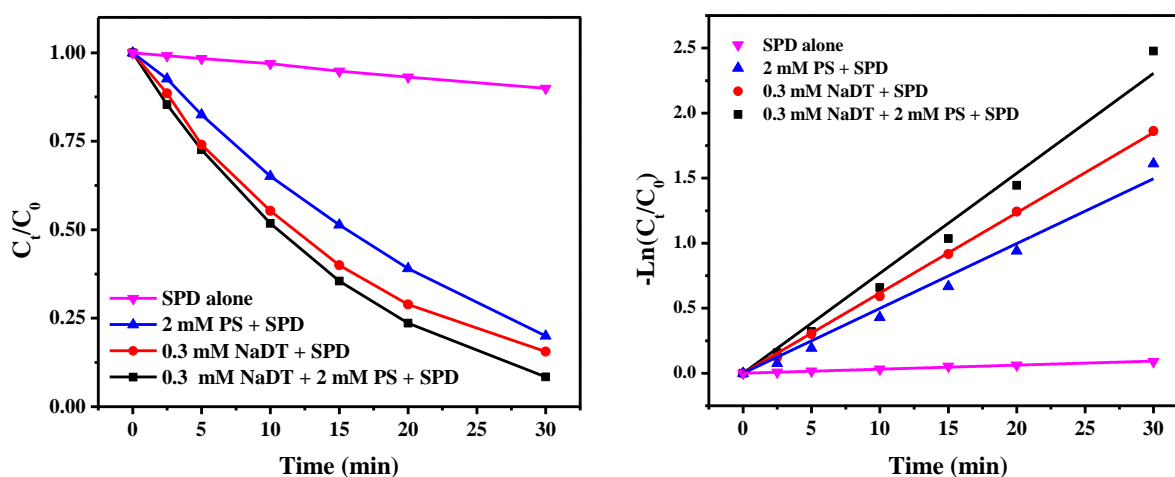


Fig. 7. Comparison of sulfapyridine degradation experiments. $[\text{SPD}] = 30\ \mu\text{M}$, $[\text{NaDT}] = 0.3\ \text{mM}$, $[\text{PS}] = 2\ \text{mM}$, $\text{pH} = 3$.

The photolysis of SPD (about 10% after 30 min of irradiation) with a pseudo order rate constant of $0.3 \times 10^{-2}\ \text{min}^{-1}$ was obtained under our experiment conditions. In the same time, the degradation was estimated to 80% with NaDT/SPD with rate constant of $5.0 \times 10^{-2}\ \text{min}^{-1}$ and 84% with PS/SPD with a rate constant of $6.2 \times 10^{-2}\ \text{min}^{-1}$. However, in NaDT/PS/SPD system, the degradation reached 92% with rate constant of $7.7 \times 10^{-2}\ \text{min}^{-1}$ which clearly demonstrates that

NaDT associated with PS can improved the degradation efficiency. However, the increase of SPD degradation in the presence of both NaDT and PS is not very strong and no synergy effect is observed. While experiments in the dark in the same conditions was also performed. **Fig. 8(a)** shows that about 14-15% of SPD degradation can be observed in presence of the PS alone or in NaDT/PS system within 22 hours, while no degradation was occurred in the presence of NaDT alone. This result is due the decomposition of PS happened in the solution, which can produce the oxygen reactive species that can degrade the organic contaminant [18].

In order to prove that the reactive species is sulfate radical ($\text{SO}_4^{\bullet-}$), methanol was added as sulfate radical trap. **Fig. 8(b)** shows that the comparison of SPD degradation with/without methanol (4 M) in NaDT/PS system in the dark. About 14 % of SPD was degraded after 22 hours in NaDT/PS system in absence of MeOH, while 7% degradation of SPD was observed in presence of MeOH, which means that 7% degradation of SPD could be attributed to $\text{SO}_4^{\bullet-}$ radicals and 7% degradation is due to another oxygen reactive species. This species could be the singlet oxygen ($^1\text{O}_2$) produced by electronic process [19].

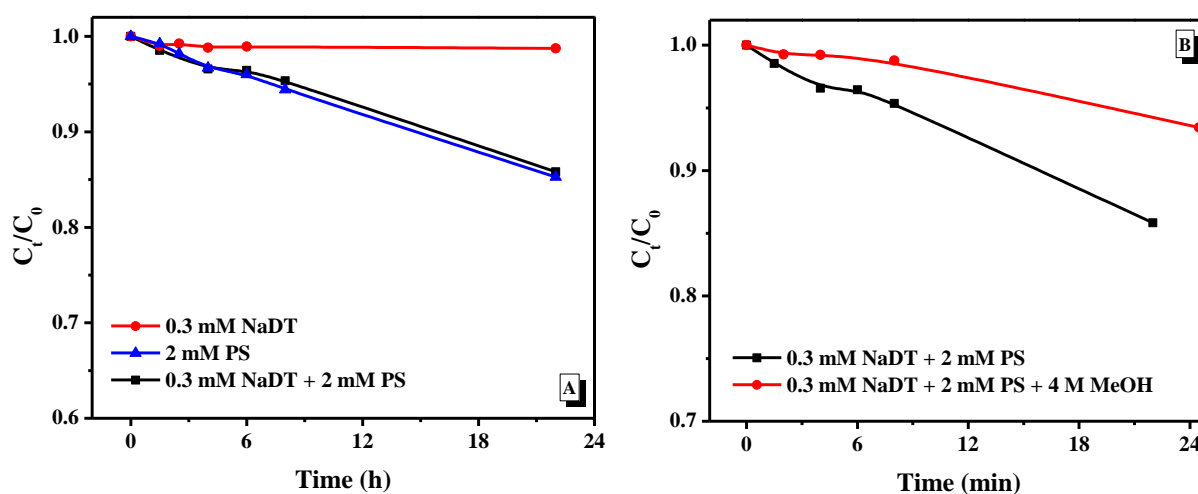


Fig. 8. Comparison of sulfapyridine degradation experiments in the dark. [SPD] = 30 μM ,

$$[\text{NaDT}] = 0.3 \text{ mM}, [\text{PS}] = 2 \text{ mM}, \text{pH} = 3.$$

3.4 Products analysis by HPLC

In order to study the degradation mechanism of SPD, the products formation in NaDT/SPD, PS/SPD and NaDT/PS/SPD systems were analysed first by High Performance Liquid Chromatography. **Fig. 9** shows the chromatogram after 90 min of irradiation in the three different systems. Comparing the chromatogram in three different systems, different main products can be observed. For the black curve represent the NaDT/PS/SPD (0.3 mM/2 mM/30 μ M) system, one main product at retention time of 7.23 min can be observed, which is not produced in the other two system. This indicates that the photo-degradation process is different in the three systems. **Fig. 10** shows the chromatogram of the NaDT/PS/SPD (0.3 mM/2 mM/30 μ M) system at different irradiation times.

The peak of the main product at a retention time of 7.23 min increases when the irradiation time increases. For example, the peak area at irradiation time equal to 90 min is much higher (about 3 times) than the peaks at irradiation time equal to 20 min (**Fig. 10**). Insert of the **Fig. 10** shows the change of the peak area of this product as function of time. The peak area increases from 0 to 60 min then reach to a plateau, then a decrease can be observed from 90-120 min. This suggests that the accumulation of the main product occurs in this system and could be due to the selective reaction.

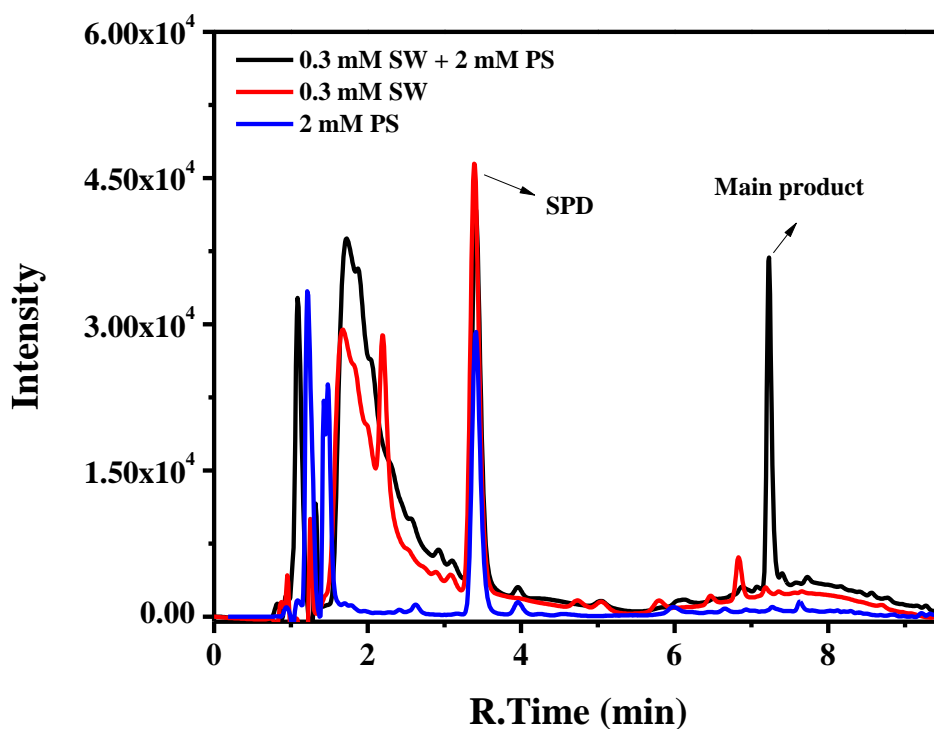


Fig. 9. Chromatogram of HPLC after 90 min of irradiation in three different systems. [SPD] = $30 \mu\text{M}$; pH = 3

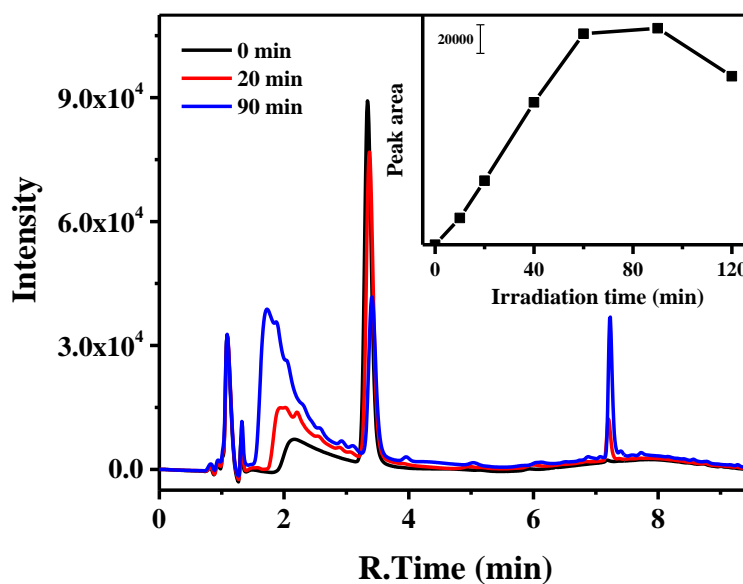


Fig. 10. Chromatogram of the NaDT/PS/SPD system at different irradiation times. Insert: Peak area of the main product (R.T. = 7.23 min) as function of irradiation time. [NaDT] = 0.3 mM; [PS] = 2 mM; [SPD] = $30 \mu\text{M}$.

4. Conclusion

This study has investigated the photochemical conversion of NaDT into its reduced species ($\text{NaDT}^{1-}/\text{NaDT}^{2-}$). The NaDT^{1-} and NaDT^{2-} are formed under irradiation in oxygen-free aqueous solution in the presence of methanol with rate of $3.8 \times 10^{-5} \text{ M min}^{-1}$ and $0.3 \times 10^{-5} \text{ M min}^{-1}$, respectively. These two reduced forms of decatungstate can be oxidized by the persulfate according to the UV-Vis spectroscopy. Photodegradation experiments indicate that the efficiency of SPD degradation increases slightly in presence of PS. This might be due to generation of sulfate radical while reducing PS.

5. Proposal

Due to the limited time during the PhD period, this part of the work is not complete, and the following work still needs to be completed after the end of the defense:

- 1) The rate constant of the reaction between PS and two reduced species of NaDT ($\text{NaDT}^{1-}/\text{NaDT}^{2-}$) need to be calculated.
- 2) The effect of different parameters, such as pH, different PS concentrations and the presence of different ions, on the degradation of SPD in NaDT/PS/SPD system will be studied.
- 3) The analysis of products in NaDT/PS/SPD system will be studied via UHPLC-MS system.
- 4) The reactive oxygen species (ROS) in NaDT/PS/SPD system will be identified with ESR technique.
- 5) The change of total carbon (TOC) in solution should to be determined.
- 6) The degradation mechanism should be investigated in more detail.

References

- [1] M. Qiao, G.-G. Ying, A.C. Singer, Y.-G. Zhu, Review of antibiotic resistance in China and its environment, *Environment International*. 110 (2018) 160–172.
- [2] V.N. Binh, N. Dang, N.T.K. Anh, L.X. Ky, P.K. Thai, Antibiotics in the aquatic environment of Vietnam: Sources, concentrations, risk and control strategy, *Chemosphere*. 197 (2018) 438–450. <https://doi.org/10.1016/j.chemosphere.2018.01.061>.
- [3] S. Li, W. Shi, W. Liu, H. Li, W. Zhang, J. Hu, Y. Ke, W. Sun, J. Ni, A duodecennial national synthesis of antibiotics in China's major rivers and seas (2005–2016), *Science of The Total Environment*. 615 (2018) 906–917. <https://doi.org/10.1016/j.scitotenv.2017.09.328>.
- [4] L. Zhou, S.M. Limbu, M. Shen, W. Zhai, F. Qiao, A. He, Z.-Y. Du, M. Zhang, Environmental concentrations of antibiotics impair zebrafish gut health, *Environmental Pollution*. 235 (2018) 245–254. <https://doi.org/10.1016/j.envpol.2017.12.073>.
- [5] E. Felis, J. Kalka, A. Sochacki, K. Kowalska, S. Bajkacz, M. Harnisz, E. Korzeniewska, Antimicrobial pharmaceuticals in the aquatic environment - occurrence and environmental implications, *European Journal of Pharmacology*. 866 (2020) 172813. <https://doi.org/10.1016/j.ejphar.2019.172813>.
- [6] J.A. Garrido-Cardenas, B. Esteban-García, A. Agüera, J.A. Sánchez-Pérez, F. Manzano-Agugliaro, Wastewater Treatment by Advanced Oxidation Process and Their Worldwide Research Trends, *International Journal of Environmental Research and Public Health*. 17 (2020) 170. <https://doi.org/10.3390/ijerph17010170>.

- [7] M. Saeed, S. Adeel, M. Muneer, A. ul Haq, Photo Catalysis: An Effective Tool for Treatment of Dyes Contaminated Wastewater, in: R.A. Bhat, K.R. Hakeem, M.A. Dervash (Eds.), *Bioremediation and Biotechnology, Vol 2: Degradation of Pesticides and Heavy Metals*, Springer International Publishing, Cham, 2020: pp. 175–187. https://doi.org/10.1007/978-3-030-40333-1_10.
- [8] G. Laudadio, Y. Deng, K. van der Wal, D. Ravelli, M. Nuño, M. Fagnoni, D. Guthrie, Y. Sun, T. Noël, C(sp³)–H functionalizations of light hydrocarbons using decatungstate photocatalysis in flow, *Science*. 369 (2020) 92–96. <https://doi.org/10.1126/science.abb4688>.
- [9] G. Laudadio, S. Govaerts, Y. Wang, D. Ravelli, H.F. Koolman, M. Fagnoni, S.W. Djuric, T. Noël, Selective C(sp³)–H Aerobic Oxidation Enabled by Decatungstate Photocatalysis in Flow, *Angewandte Chemie*. 130 (2018) 4142–4146. <https://doi.org/10.1002/ange.201800818>.
- [10] I. Texier, J.A. Delaire, C. Giannotti, Reactivity of the charge transfer excited state of sodium decatungstate at the nanosecond time scale, *Phys. Chem. Chem. Phys.* 2 (2000) 1205–1212. <https://doi.org/10.1039/A908588B>.
- [11] D. Ravelli, S. Protti, M. Fagnoni, Decatungstate Anion for Photocatalyzed “Window Ledge” Reactions, *Acc. Chem. Res.* 49 (2016) 2232–2242. <https://doi.org/10.1021/acs.accounts.6b00339>.
- [12] J. Wang, S. Wang, Activation of persulfate (PS) and peroxymonosulfate (PMS) and application for the degradation of emerging contaminants, *Chemical Engineering Journal*. 334 (2018) 1502–1517. <https://doi.org/10.1016/j.cej.2017.11.059>.

- [13] L. Tang, Y. Liu, J. Wang, G. Zeng, Y. Deng, H. Dong, H. Feng, J. Wang, B. Peng, Enhanced activation process of persulfate by mesoporous carbon for degradation of aqueous organic pollutants: Electron transfer mechanism, *Applied Catalysis B: Environmental*. 231 (2018) 1–10. <https://doi.org/10.1016/j.apcatb.2018.02.059>.
- [14] R.F. Renneke, M. Pasquali, C.L. Hill, Polyoxometalate systems for the catalytic selective production of nonthermodynamic alkenes from alkanes. Nature of excited-state deactivation processes and control of subsequent thermal processes in polyoxometalate photoredox chemistry, *J. Am. Chem. Soc.* 112 (1990) 6585–6594. <https://doi.org/10.1021/ja00174a020>.
- [15] Y. Nosaka, T. Takei, N. Fujii, Photoinduced reduction of $W_{10}O_{32}^{4-}$ by organic compounds in aqueous solution, *Journal of Photochemistry and Photobiology A: Chemistry*. 92 (1995) 173–179. [https://doi.org/10.1016/1010-6030\(95\)04125-6](https://doi.org/10.1016/1010-6030(95)04125-6).
- [16] N. Takabayashi, T. Yamase, HYDROGEN EVOLUTION FROM ALCOHOLS BY USE OF DECATUNGSTATE PHOTOCATALYST, *Nippon Kagaku Kaishi*. (1984) 264–270.
- [17] A. Chemseddine, C. Sanchez, J. Livage, J.P. Launay, M. Fournier, Electrochemical and photochemical reduction of decatungstate: a reinvestigation, *Inorg. Chem.* 23 (1984) 2609–2613. <https://doi.org/10.1021/ic00185a014>.
- [18] Y. Dou, X. Shen, J. Zou, R. Shi, T. Yan, Q. Sun, L. Wang, Green synthesis of sulfur-doped g- C_3N_4 nanosheets for enhanced removal of oxytetracycline under visible-light irradiation and reduction of its N-nitrosodimethylamine formation potential, *Journal of Chemical Technology & Biotechnology*. 96 (2021) 1580–1592. <https://doi.org/10.1002/jctb.6674>.

- [19] X. Cheng, H. Guo, Y. Zhang, X. Wu, Y. Liu, Non-photochemical production of singlet oxygen via activation of persulfate by carbon nanotubes, *Water Research*. 113 (2017) 80–88. <https://doi.org/10.1016/j.watres.2017.02.016>.

1 **Manuscript 3**

2 **Oxidation mechanism from an innovative ternary**
3 **catalytic process based on intrasystem interaction:**
4 **Decatungstate/Fe₃O₄/H₂O₂**

5 *Peng Cheng, Mohamed Sarakha, Christine Mousty, Pierre Bonnet and Gilles Mailhot**

6 Université Clermont Auvergne, CNRS, Clermont Auvergne INP, Institut de Chimie de
7 Clermont Ferrand (ICCF) UMR 6296, BP 80026, F-63171, Aubière cedex, France

8 * Corresponding author. E-mail address: Gilles.Mailhot@uca.fr.

9

10 **Abstract**

11 A process for the selective oxidation of aromatic compound into nitroso compounds based
12 on a ternary system by simply mixing decatungstate/magnetite/hydrogen peroxyde in aqueous
13 solution has been designed. This research work is focused on the efficient oxidation of
14 sulfapyridine (SPD) into nitroso-sulfapyridine (N-SPD). Sodium decatungstate ($\text{Na}_4\text{W}_{10}\text{O}_{32}$,
15 noted NaDT) and magnetite (Fe_3O_4) were well characterized via different technics, such as
16 XRD, FTIR and XPS. Comparing the oxidation efficiency in the NaDT ($41\ \mu\text{M}$)/ H_2O_2 ($5.0\ \text{mM}$)
17 binary system (rate constant = $2.97 \times 10^{-5}\ \text{min}^{-1}$), the efficiency increased in NaDT (41
18 μM)/ Fe_3O_4 ($0.264\ \text{g L}^{-1}$)/ H_2O_2 ($5.0\ \text{mM}$) ternary system by approximately 380 times (rate
19 constant = $1.13 \times 10^{-2}\ \text{min}^{-1}$). The oxidation efficiency and the selective conversion of amine
20 substrates to their nitroso-derivatives were reached up to 97% and up to 81%, respectively. The
21 effectiveness of the system is based on a complex mechanism obtained through interactions
22 between Fe_3O_4 and NaDT, confirmed by the FTIR and XPS measurements, on one side and
23 between NaDT and H_2O_2 on the other side, as clearly demonstrated in cyclic voltammetry (CV).
24 The effects of different parameters (pH, H_2O_2 , Fe_3O_4 and NaDT concentrations) are also
25 investigated. The obtained results demonstrated that the oxidation of SPD into N-SPD is
26 efficient at pH lower than 5.0 in our ternary system. The rate constant and the percentage of
27 SPD disappearance reach a plateau when concentrations of NaDT, Fe_3O_4 and H_2O_2 increased,
28 with limit concentrations approximately $40\ \mu\text{M}$, $0.8\ \text{g L}^{-1}$ and $10.0\ \text{mM}$ respectively.

29 **Keywords:** Decatungstate, Fe_3O_4 , H_2O_2 , Selective catalysis, Electron transfer

1. Introduction

Decatungstate ($W_{10}O_{32}^{4-}$), as one kind of high-valent early-transition metal-oxygen anion polyoxometalates catalyst, was widely used in organic chemistry and wastewater depollution [1]. Oxidation reactions with sodium decatungstate (NaDT) associated with hydrogen peroxide (H_2O_2) as “green” methods for organic synthesis have gained significant impetus over the past [2,3]. Franca Bigi and collaborators used silica-bound alkylammonium NaDT/ H_2O_2 as heterogeneous catalysts system for selective oxidation of sulfide compounds to the corresponding sulfoxide derivatives [3]. The process appears to be very efficient, giving methyl phenyl sulfoxide in a high yield (92%) and selectivity (95%) under optimal conditions. Gkizis, et. al prepared tetrabutylammonium decatungstate (TBADT) which supported on mesoporous TiO_2 nanoparticles working as a catalyst and using H_2O_2 as oxidant to selectively oxidize various aryl amines [2]. In contrast with TBADT/ H_2O_2 oxidation system, the TBADT/ TiO_2 / H_2O_2 ternary catalytic system was shown to be much more efficient and present a higher selectivity (the corresponding 10 kinds of nitrosoarenes were formed, with high yields (up to 99%) and selectivity (>90%)). Hence, the above study provides us a strategy to build a selective catalytic system by the combination of decatungstate with other materials.

Nitroso compounds are known to be highly valuable chemical intermediates, that were observed in the process of human metabolism [4] and widely used as powerful reagents in a variety of synthetic chemical transformations [5], such as nitroso aldol reactions [6], nitroso ene reactions [7], Diels–Alder cycloadditions [8], and couplings with amines to yield azoarenes [9]. In addition, in the last years, nitroso compounds chemistry was shown to play a pivotal role

in asymmetric catalysis [10]. Since nitroso compounds emergence over one century ago, preparing these reagents has attracted a lot of attention and large number of methods of synthesis of these compounds has been developed [11,12]. Direct substitution of hydrogen by nitroso group, oxidation of other nitrogen-containing functional groups, preparation from nitro compounds and reaction of free radicals with nitric oxide, have been shown to be among the main methods [12]. However, the preparation of nitroso compounds by oxidation of primary amines is one of the widely used method with a variety of oxidizing agents such as caro's acid [13], peracetic acid [14], molecular oxygen [15] and H_2O_2 [16,17]. Among the oxidants, H_2O_2 is the most used reagent. As it is largely reported, H_2O_2 is considered as a “green oxidant” which is easy to obtain, store and transport [18]. In addition, H_2O and O_2 represent the main reaction products, so H_2O_2 is a very environment friendly agent.

However, due to the high reactivity of these nitroso compounds, that could be oxidized to their respective nitro or dimeric derivatives, azo and/or azoxy arenes, the development of a chemo-selective oxidation of amino to nitroso compounds is of great importance [11,16,19]. In the last years, the most popular methodology to synthesize nitroso compounds was the transition metal-catalyzed oxidation, with tungsten (W) [17], molybdenum (Mo) [20], vanadium (V) [21] as metal, in the presence of H_2O_2 .

Hence, our system is based on the above strategy which combines NaDT with a support to build a ternary system. Although this ternary system has been initially applied, the scientific knowledge and the work on the catalytic principle of such system is still blank. As well known, Nano- Fe_3O_4 particles, a kind of iron oxide, were largely used as support because of their large

surface area, their magnetic properties and their relatively high reactivity [22]. In addition, the use of Fe_3O_4 particles has the advantage to be easy to recover and to reuse for another process.

Herein in this study, we used nano- Fe_3O_4 particles as a support of NaDT in the presence of H_2O_2 to obtain an innovative ternary catalytic system to selectively oxidize amino compounds into nitroso derivatives. This special system was chosen as an example to carry out in-depth research on the reaction mechanism of the ternary catalytic system. Thus, the objectives of this study are **i)** to characterize the prepared NaDT and nano- Fe_3O_4 particles, **ii)** to identify the reactive species in this system, **iii)** to study the efficiency of the oxidation as well as the selectivity in the NaDT/ Fe_3O_4 / H_2O_2 system, **iv)** to optimize the experimental parameters. In addition, cyclic voltammetry (CV) experiments, Fourier transform infrared spectroscopy (FTIR), X-ray photoelectron spectroscopy (XPS) were also set up to study deeply the mechanism of this ternary catalytic system.

2. Experimental

2.1. Materials

Sulfapyridine (SPD) ($\geq 99\%$), sodium tungstate ($\text{Na}_2\text{WO}_4 \cdot 2\text{H}_2\text{O}$), sodium chloride (NaCl), hydrochloric acid (HCl), hydrogen peroxide (H_2O_2 30%), perchloric acid (HClO_4), Iron(III) chloride ($\text{FeCl}_3 \cdot 6\text{H}_2\text{O}$), Iron(II) chloride ($\text{FeCl}_2 \cdot 4\text{H}_2\text{O}$) and sodium hydroxide (NaOH) were purchased from Sigma Aldrich and used as received. Water (Milli-Q) was purified using a reverse osmosis RIOS 5 and Synergy (Millipore) device (resistivity $18\text{ M}\Omega\text{ cm}$, $\text{DOC} < 0.1\text{ mg L}^{-1}$).

2.2. Preparation of sodium decatungstate (NaDT) and Fe₃O₄

The synthesis of sodium decatungstate (Na₄W₁₀O₃₂) was performed according to our previous study [1]. The boiling sodium tungstate solution (50 g of Na₂WO₄·2H₂O dissolved in 300 mL of ultrapure water) was mixed with 1.0 M boiling hydrochloric acid (300 mL) in a beaker, refluxed for 20 seconds to form a green solution. It was followed by adding 150 g of solid sodium chloride, stirring until the solution is re-boiled and keeping for 20 seconds, then rapidly transferred into the ice-water bath. This suspension solution was maintained in a freezer (-18 °C) overnight. The day after, the suspension solution of NaCl and crude Na₄W₁₀O₃₂ was filtered and the solid was dissolved into 150 mL of acetonitrile solution. The latter solution was refluxed for 5 minutes at 79 °C and filtered in order to remove the insoluble NaCl after cooling at ambient temperature. The acetonitrile solution was gently evaporated in hot-water bath (79 °C) to obtain the yellow-green catalyst.

Magnetite (Fe₃O₄) was prepared by following the procedure reported in the literature [23]. A mixture of 27.03 g FeCl₃·6H₂O and 19.88 g FeCl₂·4H₂O in 800 mL Milli-Q water was constantly stirred under nitrogen atmosphere. The pH was adjusted by NaOH aqueous solution to 9-10 and the solution volume was adjusted to 1.0 L with Milli-Q water. Then, the reaction vessel was kept in the dark for 48 h at 60 °C. After centrifugation, the solid was washed with Milli-Q water until the water conductivity after washing was less than 2.0 μS cm⁻¹, and then dried.

The mixture Fe₃O₄/NaDT was obtained by simple addition of the two products in aqueous solution to have the desired concentration.

2.3. Characterization

The X-ray diffraction (XRD) patterns of NaDT and Fe₃O₄ were collected using a X-ray diffractometer (PANalytical X'Pert Pro) with a diffracted beam monochromator Cu K α source (40 kV-40 mA). Patterns were recorded over the form $2\theta = 5$ to 70° , in steps of 0.08° with a count time of 4 seconds. The FTIR spectrum of NaDT and/or Fe₃O₄ were recorded on a Fourier infrared absorption spectrometer (Thermo-Nicolet 380) with an advanced diamond ATR accessory (Specac-Golden Gate). The UV-vis absorption spectra of NaDT were obtained using a Varian Cary 300 UV-vis spectrophotometer. For the characterization of Fe₃O₄, the morphology and the size of the prepared samples were analyzed by transmission electron microscopy (TEM, Hitachi H-7650) at 80 kV acceleration voltage with magnifications up to 200 000. The samples investigated by TEM were suspended in ethanol and dropped onto a 400-mesh holey carbon-coated copper grid and dried at room temperature in air. X-ray photoelectron spectroscopy (XPS) experiments were performed on a Physical Electronics/PHI 5300 X-ray photoelectron spectrometer (S 250 Germany) with a hemispherical analyzer and a single-channel detector that was operated at 300W (15 kV and 20 mA). Mg KR radiation (1253.6 eV) and pass energies of 89.45 eV for survey scans and 17.9 eV for high-resolution scans were employed. The binding energies were calibrated with reference to C1s at 284.8 eV. The BET surface area analyses of adsorbents were carried out in a Quantachrome Nova 3000e Surface Area Analyzer.

2.4. Catalytic tests: sulfapyridine (SPD) oxidation

The conversion of SPD and the formation yield of its corresponding nitroso compound were performed in a batch experiment at room temperature (25°C). 5.0 mg NaDT and 13.2 mg Fe₃O₄ were added into the 50 mL of SPD solution (30 μM). The concentration of NaDT was then equal to 41 μM and the amount of Fe₃O₄ was 0.264 g L⁻¹. The pH of solution was adjusted to 3.0 ± 0.05 using perchloric acid and sodium hydroxide (0.1 M). Hydrogen peroxide was added using a concentrated solution, and so with negligible volume, prior to starting the reaction using the magnetic stirrer at 1100 rpm in order to disperse Fe₃O₄ particles. Then, aliquots of the mixture were taken at different time intervals and were immediately filtrated using PTFE filters of 0.2 μm (CHROMAFIL® Xtra RC-20/25, 25 mm, Macherey-Nagel).

The effect of pH within the range 2.5 - 6.9, of H₂O₂ concentration within the range 1.0 - 20.0 mM, of NaDT concentration within the range 20.0 - 246.0 μM and of the amount of Fe₃O₄ within the range 0.1 - 1.5 g L⁻¹, on the whole mechanistic process were also investigated independently.

In order to prove the hydroxyl radicals generating and reactivity in this ternary catalytic system, 2-propanol was chosen as a trap. It efficiently reacts with hydroxyl radical with a rate constant of 2.3×10⁹ M⁻¹ s⁻¹ [24]. Concentrated isopropanol was added into the solution in order to reach a final concentration of 1.0 mM in the mixture.

2.5. Preparative LC, NMR Spectroscopy, HRMS-UHPLC and HPLC

Preparative liquid chromatography (LC) was used to separate and purify nitroso-sulfapyridine (N-SPD) from the reaction mixture. This separation was obtained with preparative LC (Varian Prep Star 218) equipped with a Varian Pro Star 335 photodiode array detector and an auto sampler. The column was a C18 Varian dynamax Microsorb 60-8 column (250 mm × 41.4 mm, 8 μm particle size). The analyses were performed using acetonitrile and water with 0.1 % of trifluoroacetic acid (TFA), in an isocratic mode at 25/75% respectively, as a mobile phase at a flow rate of 40 mL min⁻¹. After the separation, N-SPD solution was concentrated using a rotary evaporator during 2 hours at 45 °C.

For the characterization and the quantification, NMR spectroscopy was used. 100 μL at 521.9 μM of 3-(Trimethylsilyl) propionic acid-d₄ sodium salt (TSPD₄) in D₂O solution as a reference was added in 900 μL concentrated pure N-SPD solution. NMR data were obtained with a Bruker Avance III 500 MHz Ultrashield™ plus spectrometer (equipped with 5 mm TCI-13C-15N-2H Prodigy Cryoprobe). All spectra were recorded in 600 μL of H₂O (10% D₂O). Chemical shifts (δ) are expressed in ppm relative to residual peak 4.79 (ppm) of water.

The identification of all the products was performed using high resolution mass spectrometry (HRMS) constituted of an Orbitrap QExactive (Thermoscientific) coupled to an ultra-high performance liquid chromatography (UHPLC) instrument Ultimate 3000 RSLC (Thermoscientific). Analyses were carried out in both negative and positive electrospray modes (ESI⁺ and ESI⁻). The elution was performed using the following gradient program: a linear increase of acetonitrile from 5 to 99 % within 7.5 minutes followed by 0.5 minutes at 99 % of

acetonitrile, a decrease of acetonitrile to 5 % in 0.5 minutes and a final step of 5 % within 3 minutes. The column was a Kinetex EVO C18 (100 × 2.1mm; 1.7 μ m particle size (Phenomenex)) and the flow rate was set at 0.45 mL min⁻¹.

The conversion of SPD and the formation of nitroso-sulfapyridine (N-SPD) percentages were obtained by HPLC (Shimadzu NEXERA XR HPL) equipped with a photodiode array detector and an auto sampler. The column was a Macherey Nagel EC 150/2 NUCLEODUR C18ec (150 mm × 2 mm, 2 μ m particle size). The analyses were performed using acetonitrile as mobile phase and water with 0.5 % of phosphoric acid at a flow rate of 0.40 mL min⁻¹. The elution was performed using the following gradient: 5 % of acetonitrile for 2.5 minutes, a linear increase of acetonitrile to 40 % in 4.5 minutes, then an increase of acetonitrile to 95 % in 1.5 minutes, 95 % of acetonitrile for 1 minute and a decrease of acetonitrile to 5 % in 0.5 minute.

2.6. Electrochemical measurements

Cyclic voltammetry (CV) experiments were carried out with a potentiostat Autolab PGSTAT204 controlled by the NOVA software (Metrohm) equipped with a three-electrodes system. An Ag-AgCl electrode was used as the reference electrode and a platinum wire as the auxiliary electrode. The working electrode was a pyrolytic graphite electrode (PGE, A = 0.07 cm²). Before its use, the electrode surface was polished with 1 μ m diamond paste and washed with acetone and then it was polished again with 0.04 μ m alumina slurry to be finally rinsed with ethanol and water. The PGE electrode was modified with a Fe₃O₄ coating (M-PGE) using a solvent casting reference method [25]. A suspension was prepared with 2.0 mg of Fe₃O₄ dispersed in 1.0 mL ethanol by sonication for approximately 15 minutes. Then 10 μ L nafion

solution (5%, Sigma Aldrich) was added in the 1.0 mL Fe₃O₄ suspension followed by sonication for 15 more minutes. 10 μL of the slurry was deposited onto the polished PGE then air dried for 30 minutes. With the aim to deoxygenate the electrolyte solution, the electrolyte solution was bubbling with a for 30 minutes prior to the CV experiments. Cyclic voltammograms were recorded under inert atmosphere (Ar) at a scan rate (v) of 10 mV s⁻¹ in a 0.1 M LiClO₄ (at pH 2.6) in presence or absence of H₂O₂ (5 mM) with a bare PGE or a M-PGE electrode, respectively. The given CVs correspond to the second cycle and CV experiments of two electrodes were performed in the same parameters, each time with fresh LiClO₄ electrolyte solution.

3. Results and Discussion

3.1. Characterization

The powder X-ray diffraction reveals that NaDT is crystallized in the monoclinic lattice with a space group P2(1)/n, as previously reported [26]. The characteristic XRD peaks of NaDT is consistent with the position of the NaDT simulated peaks, which can indicate that the sample has good crystallinity and high purity (**Fig. 1**). In addition, the purity of NaDT can be confirmed by the UV-Vis spectrum (**Fig. S1**), it shows an absorption band with a defined maximum at 321 nm and a molar absorption coefficient of 12365 M⁻¹ cm⁻¹ in perfect agreement with the published literature data [27]. Moreover, the infrared absorption peaks of NaDT are also clearly observed and are consistent with previous stud [28] (**Fig. 2**). The main vibration bands of NaDT are observed at 1007 and 965 cm⁻¹ corresponding to the stretching vibration of the W=O_t bond (O_t - terminal oxygen atoms). The bands at 903 and 775 cm⁻¹ are due to the vibrations of W-

O_b-W (O_b - corner-sharing-oxygen-bridge) and W-O_c-W (O_c - edge-sharing oxygen-bridge) respectively.

The synthesized Fe₃O₄ was characterized using several techniques in order to have a better idea about its physical properties such as material composition and morphology. As shown in the XRD patterns (**Fig. 1**), Fe₃O₄ presents several peaks at $2\theta = 18.44^\circ, 30.30^\circ, 35.67^\circ, 37.18^\circ, 43.32^\circ, 53.78^\circ, 57.29^\circ, 62.95^\circ$. These are found in perfect agreement with those reported in a standard pattern of PDF-#89-6466 leading us to the conclusion that Fe₃O₄ was successfully synthesized. In **Fig. 2**, the red curve represents the infrared spectrum of Fe₃O₄, the infrared absorption peaks of Fe₃O₄ are also clearly observed. The band at 578 cm^{-1} can be assigned to the Fe-O stretching mode of the tetrahedral and octahedral sites [29]. The Fe-OH vibration band is located at 624 cm^{-1} [29]. Moreover, the TEM image (**Fig. S2**) shows that it has a globosity morphology with the particle diameter ranging from 20 to 40 nm. This leads us to the conclusion that we are dealing with a nano Fe₃O₄ particles which presents more likely a large surface area ($74 \pm 1\text{ m}^2\text{ g}^{-1}$) determined by BET. All these analyses show that our Fe₃O₄ has no impurity.

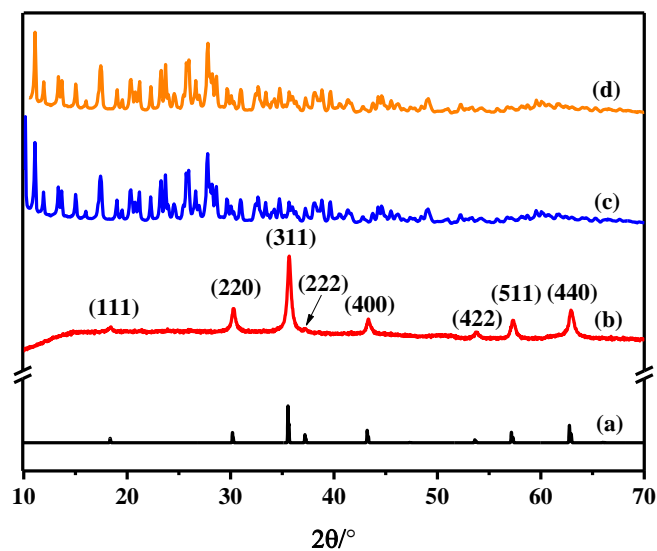


Fig. 1. XRD patterns of Fe_3O_4 and NaDT; a) a standard Fe_3O_4 pattern of PDF-#89-6466. b) the Fe_3O_4 experimental pattern. c) the NaDT experimental pattern. d) the NaDT simulated pattern.

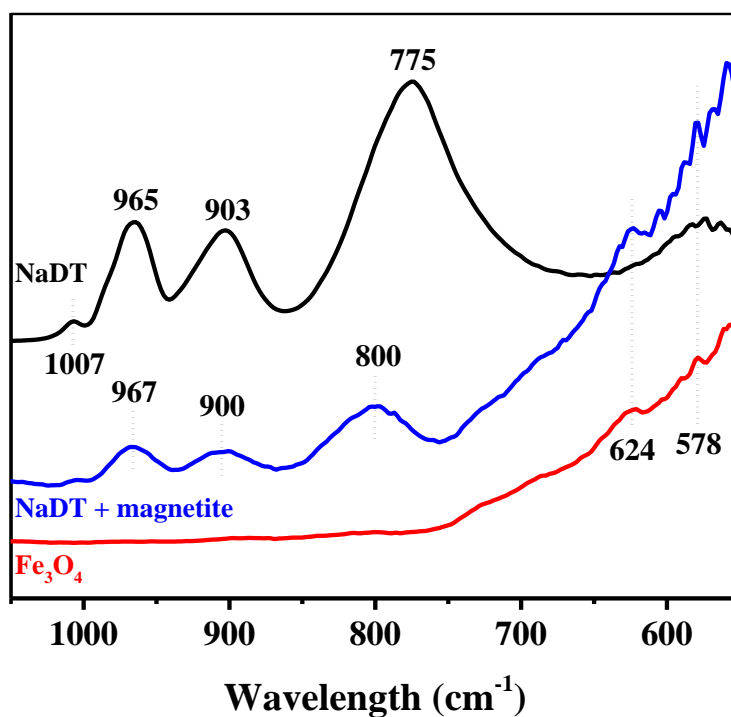


Fig. 2. FTIR spectra of NaDT and/or Fe_3O_4

3.2. Conversion of SPD in different systems

In order to evaluate the efficiency of the sulfapyridine (SPD) oxidation process in aqueous solution at a concentration of 30.0 μM , reactions were performed with H_2O_2 as oxidant in different experimental conditions (H_2O_2 alone, $\text{Fe}_3\text{O}_4/\text{H}_2\text{O}_2$, $\text{NaDT}/\text{H}_2\text{O}_2$ and $\text{NaDT}/\text{Fe}_3\text{O}_4/\text{H}_2\text{O}_2$). As can be seen in **Fig. 3**, in the presence of H_2O_2 alone (5.0 mM), a negligible conversion was obtained. This represents a conversion of roughly 1.5 % within 120 minutes. In the presence of $\text{NaDT}/\text{H}_2\text{O}_2$ (41 $\mu\text{M}/5.0$ mM) and $\text{Fe}_3\text{O}_4/\text{H}_2\text{O}_2$ (0.264 $\text{g L}^{-1}/5.0$ mM), the SPD conversion reached 1.7 % and 4.5 %, respectively within 120 minutes. In contrast, in the presence of a ternary system containing 41 μM of NaDT , 0.264 g L^{-1} of Fe_3O_4 and 5.0 mM of H_2O_2 , a significant increase of the conversion percentage reaching 75.4 % within 120 minutes is obtained demonstrating the oxidation ability of the $\text{NaDT}/\text{Fe}_3\text{O}_4/\text{H}_2\text{O}_2$ system toward SPD. Under our experimental conditions, the conversion appears to follow a pseudo first order kinetic process and the rate constant was estimated to $1.13 \times 10^{-2} \text{ min}^{-1}$ in $\text{NaDT}/\text{Fe}_3\text{O}_4/\text{H}_2\text{O}_2$ system. While for H_2O_2 alone, $\text{Fe}_3\text{O}_4/\text{H}_2\text{O}_2$, $\text{NaDT}/\text{H}_2\text{O}_2$ systems, the rate constants were estimated to 6.92×10^{-5} , 7.72×10^{-5} and $2.97 \times 10^{-5} \text{ min}^{-1}$, respectively. This result shows that the efficiency of SPD conversion was improved by more than two orders of magnitude.

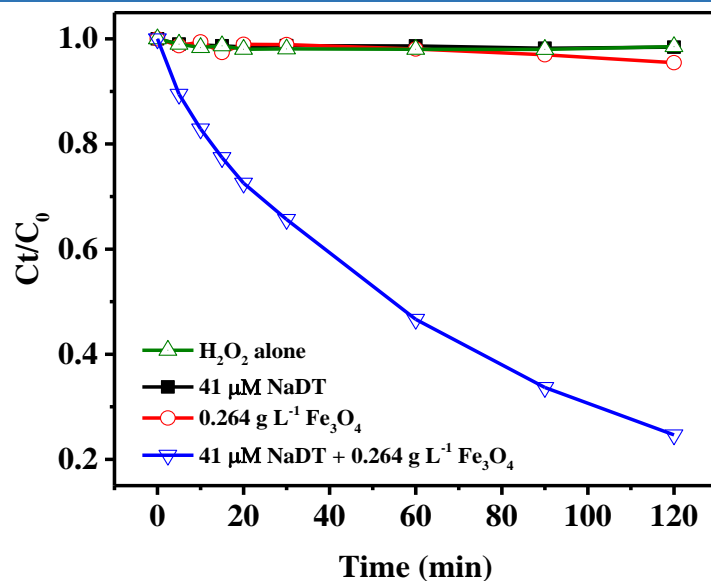


Fig. 3. Conversion kinetics of SPD in the different systems. [SPD] = 30 μM; [H₂O₂] = 5.0 mM; pH = 3.0

It worth noting that for longer experiment time (**Fig. S3**) and in the presence of higher concentrations of NaDT (164 μM)/H₂O₂ (5 mM) and Fe₃O₄ (0.8 g L⁻¹)/H₂O₂ (5 mM), the conversion percentage of SPD increased to 41.7 % and 53.3 % within 72 h, respectively. The rate constants were then estimated at $1.30 \times 10^{-4} \text{ min}^{-1}$ and $3.01 \times 10^{-4} \text{ min}^{-1}$, respectively. Therefore, NaDT /Fe₃O₄/H₂O₂ ternary system demonstrates a much better efficiency when compared to NaDT/H₂O₂ and Fe₃O₄/H₂O₂ (around 90 and 40 times higher, respectively).

In order to elucidate the generated products, we undertook analyses by HRMS/UHPLC. As clearly shown in **Fig. S4**, the disappearance of sulfapyridine (SPD) leads to the formation of mainly five products among them the nitroso-sulfapyridine (N-SPD) ($m/z_{[M+H^+]}$ = 264.0435 (**Table S1**)) is the main product formed in the ternary system. This leads us to the conclusion that the simultaneous presence of Fe₃O₄ and NaDT greatly promotes the amino selective oxidation into nitroso compound.

It's important to mention that hydroxy-sulfapyridine product (**P2 in Table S1**) is observed which may be due to the reactivity of the $\bullet\text{OH}$ radicals with the benzene ring moiety via the electron transfer process and/or a hydrogen abstraction process. This is more likely owing the classical Fenton and Fenton-like processes [30]. In order to prove that the $\bullet\text{OH}$ radicals were generated in this ternary system, the 2-propanol was used as a trap. In **Fig. 4**, the SPD conversion efficiency is lightly inhibited in the presence of isopropanol. This indicates that $\bullet\text{OH}$ radicals are involved in the process. However, only 5.6 % conversion of SPD is contributed by reaction of $\bullet\text{OH}$ radicals and so 94.4% conversion is due to the other processes.

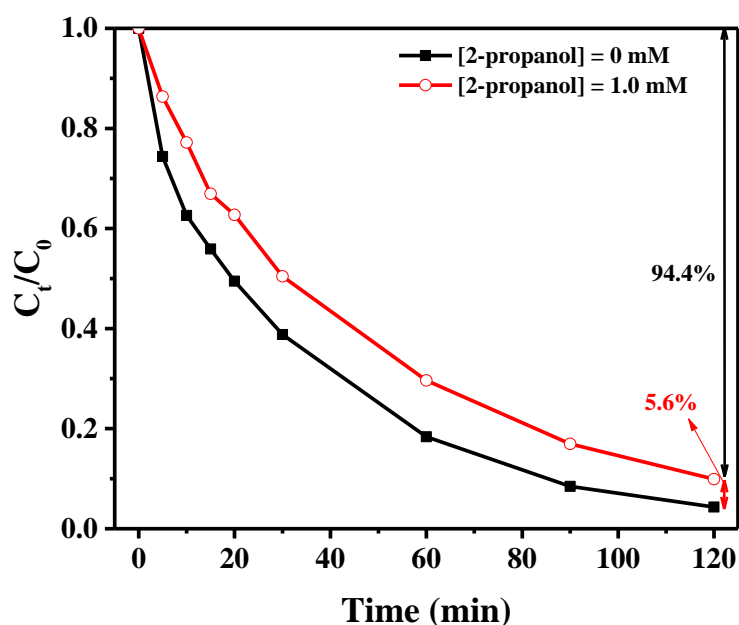


Fig 4. Effect of 2-propanol on the conversion of SPD. $[\text{NaDT}] = 246 \mu\text{M}$; $[\text{Fe}_3\text{O}_4] = 0.4 \text{ g L}^{-1}$; $[\text{H}_2\text{O}_2] = 5.0 \text{ mM}$; $[\text{SPD}] = 30 \mu\text{M}$; $\text{pH} = 3.0$.

The NMR spectrum confirmed this result (**Fig. S5**). The quantification of nitroso-sulfapyridine was performed by using NMR technique according to the procedure given in the materials and methods section. The average concentration of N-SPD calculated after

quantification by NMR is 44.72 μM , and the relative standard deviation is (RSD) 5.1% (Table S2). In addition, the same products were also obtained in NaDT (164 μM)/ H_2O_2 (5 mM) binary system after 72h reaction, which indicates that NaDT plays a key role in oxidation of SPD to N-SPD but in a very low efficiency.

3.3. Optimization of the experimental parameters for the ternary system

In order to optimize the experimental parameters, the different pH (Table S3), concentration of H_2O_2 (Table S4), amount of Fe_3O_4 (Table S5) and concentration of NaDT (Table S6) were investigated. The obtained results demonstrate that the oxidation of SPD into N-SPD is efficient at pH lower than 5.0. As shown in Fig. S6, S7 and S8, the rate constant and the percentage of SPD disappearance reach a plateau when concentrations of H_2O_2 , NaDT and amount of Fe_3O_4 increase and, the limited concentrations are around 10.0 mM, 0.8 g L^{-1} and 41 μM , respectively. The use of higher concentrations is detrimental for the oxidation process. In terms of selectivity for the oxidation of SPD into N-SPD, H_2O_2 concentration has no real impact, the increase of Fe_3O_4 concentration improves slightly the selectivity and as contrary an increase of NaDT concentration decreases the selectivity.

3.4. Recycling experiments

In order to demonstrate that Fe_3O_4 in this ternary system can be recycled, it was collected after each reaction and reemployed for the same experiments. Table 1 shows the conversion of SPD and selectivity for the formation of N-SPD in this system during repeated experiments. The SPD conversion remains between 85 - 87% in 4 times repeated experiments.

The yield of N-SPD formation at first and second cycle is about 75%. A small decrease can be observed after 3 times reusing, which may be mainly due to the accumulation of NaDT on the Fe₃O₄ surface. Indeed, after few cycles, the actual amount of NaDT in the solution is higher than the optimized concentration, which leads to the decrease of the of N-SPD yield. This indicates that the development of the optimal conditions for real application can be the main subject of the more in-depth research work in the future.

Table 1. The conversion and selectivity of SPD in repeated experiments within 2h

Number of cycles	1	2	3	4
Rate constant of SPD disappearance ($\times 10^{-2} \text{ min}^{-1}$)	1.57	1.67	1.54	1.67
Percentage of SPD disappearance (%)	85.4%	86.5%	84.4%	87.1%
Yield of N-SPD formation (%)	74.2%	75.9%	60.2%	59.6%

[NaDT] = 82 μM ; [Fe₃O₄] = 0.4 g L⁻¹; [H₂O₂] = 5.0 mM; [SPD] = 90 μM ; pH = 3.0;

3.5. Investigation of the interactions in the ternary system

According to the above results, NaDT plays a key role in the selective oxidation of SPD, and Fe₃O₄ can greatly increase the reaction rate in the presence of H₂O₂. This is more likely owing to the existence of an interaction between Fe₃O₄ and NaDT. In order to investigate how Fe₃O₄ plays an important role in selective oxidation of SPD to N-SPD, Fourier transform infrared spectroscopy (FTIR), X-ray photoelectron spectroscopy (XPS) and cyclic voltammetry (CV) experiments were performed.

3.5.1. FTIR

Interactions between NaDT and Fe₃O₄ are first investigated by the Fourier Transform infrared spectroscopy (FTIR). By comparing the spectra of NaDT and Fe₃O₄ alone with the mixture of both components, a shift can be noted for the W-O_c-W bond (775 cm⁻¹) which corresponds more likely to the interaction between NaDT and Fe₃O₄ at edge sharing oxygen-bridge (**Fig. 2**). Rakshit et.al indicated that the tungstate can form inner-sphere type bonds on hematite surface [31]. Similarly, Shan et.al indicated that there is a strong interaction between Fe₃O₄ and tungstate [32].

3.5.2. XPS

In order to confirm the interaction between Fe₃O₄ and NaDT and to compare the difference of chemical compositions of Fe₃O₄ before and after reaction, the XPS measurement was performed. A typical full XPS spectrum of Fe₃O₄ (before reaction) is shown in **Fig. 5(a)**. The spectrum indicates the presence of carbon, oxygen and iron arising from Fe₃O₄. This shows that the Fe₃O₄ has no other contaminants, which is consistent with the results of XRD and FTIR. For the Fe₃O₄ after 4 times reuse, the spectrum presents the presence of carbon, oxygen, iron and tungsten, which indicates that the NaDT interacts with the Fe₃O₄ surface.

High resolution Fe 2p spectrum of Fe₃O₄ (after reaction) is shown in **Fig. 5(b)**. **Fig. S10(a)** shows high resolution Fe 2p spectrum of Fe₃O₄ before reaction). Two peaks at 710.55 and 724.10 eV correspond to Fe 2p_{3/2} and Fe 2p_{1/2} peaks of Fe₃O₄, respectively [33]. The spin-orbit split Fe 2p peaks are broad due to a small chemical shift difference between Fe²⁺ and Fe³⁺

present in Fe₃O₄ [34]. These peaks were both well fitted (with low χ^2 -distribution) with two components. For the Fe 2p_{3/2} spectrum, a major peak at 711.92 eV and a minor one at 710.50 eV can be ascribed to Fe³⁺ and Fe²⁺, respectively. Similarly, a major peak at 723.84 eV and a minor one at 725.47 eV were observed in Fe 2p_{1/2} spectrum, which can be also ascribed to Fe³⁺ and Fe²⁺, respectively. In addition, a fitting satellite peak can be observed in **Fig. 5(b)**, which was likely due to iron oxidation generating Fe₂O₃ instead of Fe₃O₄ at the surface³⁶. These results are in accordance with previously published data [35,36].

A Fe³⁺/Fe²⁺ ratio (~2:1) is calculated from the corresponding area of both components under the spectrum of Fe 2p_{3/2} and Fe 2p_{1/2}. This indicates that the Fe₃O₄ is of high purity, which is consistent with XRD result. **Table 2** shows the ratios of Fe²⁺ and Fe³⁺ in Fe₃O₄ (before and after reaction) and the fitting peaks position in Fe 2p_{3/2} and Fe 2p_{1/2} spectra, respectively. It can be clearly observed that the Fe³⁺/Fe²⁺ ratio is similar (the Fe³⁺ percentage increases a little bit after reuse), indicating that the chemical composition and properties of Fe₃O₄ have not significantly changed after 4 times reuse. Moreover, no obvious change is presented at the peaks position of Fe³⁺ in Fe₃O₄ before and after reaction. However, for the peaks position of Fe²⁺ and satellite peak in Fe₃O₄, a small shift which is about 0.3 eV for Fe²⁺ peaks can be observed. This may be due to the interaction between NaDT and Fe²⁺ on the surface of Fe₃O₄. The area of the fitting satellite peak increases comparing the spectra of Fe 2p before and after reaction, which could be due to the further oxidation in the solution in the presence of H₂O₂. This result is consistent with the result of the small increase in the proportion of Fe³⁺ mentioned above.

High resolution O 1s spectra of Fe₃O₄ before and after reaction are shown in (**Fig. S10(b)**) and **Fig. 5(c)**. In **Fig. 5(c)**, the O 1s spectrum can be divided into three component peaks

centered at 529.24, 530.73 and 531.67 eV. The O 1s peak which appears at 531.67 eV is due to the interacted NaDT on the Fe₃O₄ surface [35,36]. The O 1s peaks situated at 529.24 and 530.73 eV correspond to Fe-O in Fe₃O₄ phase and the hydroxyl bonding (Fe-OH) on the surface of Fe₃O₄ [36–38]. **Table 3** shows the fitting peaks position of O 1s in Fe₃O₄ before and after reaction that shows no difference, indicating that the interaction between Fe₃O₄ and NaDT is not established via the oxygen atoms in Fe₃O₄.

High resolution W 4f spectrum is exhibited in magnetite sample after reaction (**Fig. 5(d)**). The two peaks of W 4f_{5/2} and W 4f_{7/2} appear at 39.11 and 36.99 eV, respectively [35,36]. Hence, the results of XPS confirm the interaction between NaDT and Fe₃O₄, which is consistent with the result of FTIR. Therefore, the above results can reveal that there is an interaction between NaDT and Fe₃O₄, and the Fe²⁺ on the surface of Fe₃O₄ establishes an interaction with the edge oxygen atoms shared by sodium decatungstate. There is no significant change in the composition of Fe²⁺ and Fe³⁺ during the reaction process, so Fe₃O₄ can be used repeatedly, and repeated use experiments have also verified this point.

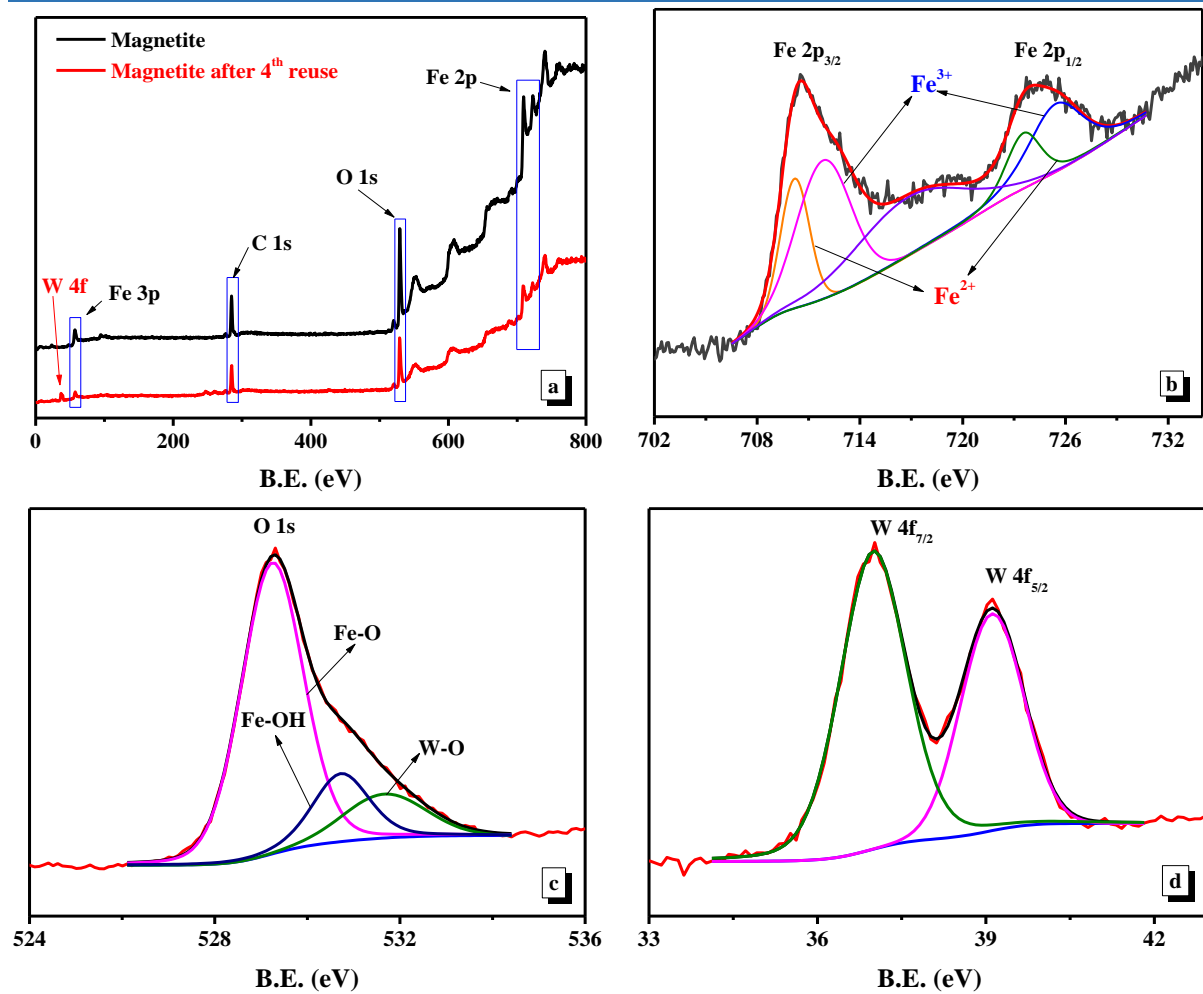


Fig. 5. XPS spectra a) Fe_3O_4 before and after reaction. High resolution spectra of Fe_3O_4 after reaction of (b) Fe 2p, (c) O 1s and (d) W 4f.

Table 2. The ratios of Fe²⁺ and Fe³⁺ in Fe₃O₄ before and after 4 times reuse and the fitting peak position of Fe²⁺, Fe³⁺ and satellite peak in Fe 2p_{3/2} and Fe 2p_{1/2} spectrum respectively

Sample	Atomic ratios			Satellite	Peaks position (eV)			
	Fe ³⁺	Fe ²⁺	χ^2		Fe 2p _{1/2}		Fe 2p _{3/2}	
					Fe ³⁺	Fe ²⁺	Fe ³⁺	Fe ²⁺
Fe ₃ O ₄	0.666	0.334	1.01	717.50	725.47	723.84	711.92	710.50
Fe ₃ O ₄ after 4 th reuse	0.676	0.324	1.17	716.82	725.42	723.54	711.87	710.19

χ^2 represents chi-square distribution, χ^2 -distribution.

Table 3. The fitting peak position of O 1s in Fe₃O₄ before and after 4 times reuse

Sample	W 4f Peak position (eV)			χ^2
	W-O	Fe-O	Fe-OH	
Fe ₃ O ₄	-	529.22	530.77	2.36
Fe ₃ O ₄ after 4 th reuse	531.67	529.24	530.73	0.72

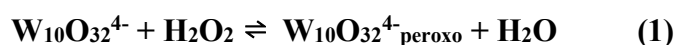
χ^2 represents chi-square distribution, χ^2 -distribution.

3.5.3. CV experiments

In order to confirm this possible interaction between NaDT and Fe₃O₄ that leads to an efficiency of SPD conversion, we have also studied, by cyclic voltammetry, the electrochemical behavior of NaDT at a bare pyrolytic carbon electrode (PGE) and Fe₃O₄ modified electrode (M-PGE) in the presence of H₂O₂.

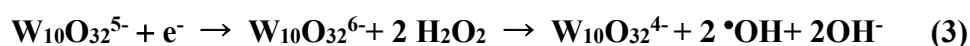
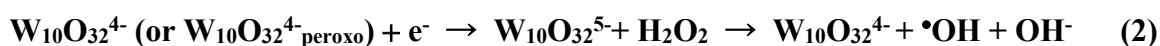
Fig. 6 shows the cyclic voltammograms of 1 mM NaDT in the absence and in the presence of H₂O₂. The curve a represents the baseline recorded at the bare PGE in 0.1 mM LiClO₄ electrolyte without NaDT at pH 2.6 under argon, showing no interference with oxygen reduction. The CV of NaDT (curve b in **Fig. 6**) exhibits two reversible signals. The potential of the first cathodic peak ($E_{pc1} = -0.16$ V/Ag-AgCl) and the second one ($E_{pc2} = -0.36$ V/Ag-AgCl) are consistent with the values reported in the literature [39,40]. The peak separation ($\Delta E = E_{pc} - E_{pa}$) are 69 mV and 76 mV for the first and the second redox couples, showing a good reversibility of the electron transfers which can be assigned to the successive reversible reduction of W₁₀O₃₂⁴⁻ to W₁₀O₃₂⁵⁻ than to W₁₀O₃₂⁶⁻ [39].

The curves c, d, e in **Fig. 6** correspond to the electrochemical signal of NaDT in the presence of H₂O₂ at various concentrations. The shape of the voltammograms changes when H₂O₂ was added in the electrolyte solution. The reversible curve was replaced by a S shape curve, corresponding to a characteristic electrocatalytic process. The two cathodic peaks are shifted to lower cathodic potentials (roughly -0.12V and -0.32V, respectively) that could be due to a specific interaction between NaDT and H₂O₂ forming a decatungstate-peroxo intermediate species (W₁₀O₃₂^{4-peroxo}) [41,42]. The interaction between NaDT and H₂O₂ was confirmed by UV-Vis as shown in **Fig. S12**. The sodium decatungstate-peroxo species (W₁₀O₃₂^{4-peroxo}) generate in the presence of H₂O₂, which can be assigned to the following equation 1:



The current intensity of the two cathodic peaks gradually increased with the H₂O₂ concentration. On contrary, the corresponding anodic peak current decreased when increasing

H₂O₂ concentration. These observations are consistent with an electrocatalytic reaction with H₂O₂. It was noted that the electrocatalytic waves appear on both redox couples: (equation 2 and 3)



The insert of **Fig. 6** represents the current of both cathodic peaks ($I_{p_{c1}}$ and $I_{p_{c2}}$) as a function of the H₂O₂ concentration. It clearly shows that the two current peaks present a linear evolution with H₂O₂ concentration with slopes of 0.537 and 2.522 $\mu\text{A mM}^{-1}$, respectively (correlation coefficient $R^2 = 0.95$ and $R^2 = 0.94$, respectively). Compared to the electrocatalytic current obtained at the first peak ($I_{p_{c1}}$), the second one ($I_{p_{c2}}$) is greater, showing that the reduced species $\text{W}_{10}\text{O}_{32}^{6-}$ is a better electrocatalysts to reduce H₂O₂ than $\text{W}_{10}\text{O}_{32}^{5-}$. The same feature was reported by Kang et al for phosphotungstate [43].

In **Fig. 7**, the electrochemical response of NaDT in the presence of 5 mM H₂O₂, recorded with the bare PGE (curve a) is compared to that obtained with a M-PGE (curve b). It was notable that the catalytic current of NaDT in the presence of H₂O₂ obtained at M-PGE was much higher than the one recorded at the bare PGE. The potential of the first catalytic wave is shifted toward less negative ($E_{p_{c1}} = -0.11 \text{ V/Ag-AgCl}$), corresponding to the $E_{p_{c1}}$ of NaDT at M-PGE (**Fig. S11**), while the catalytic current was increases ($\times 2.5$).

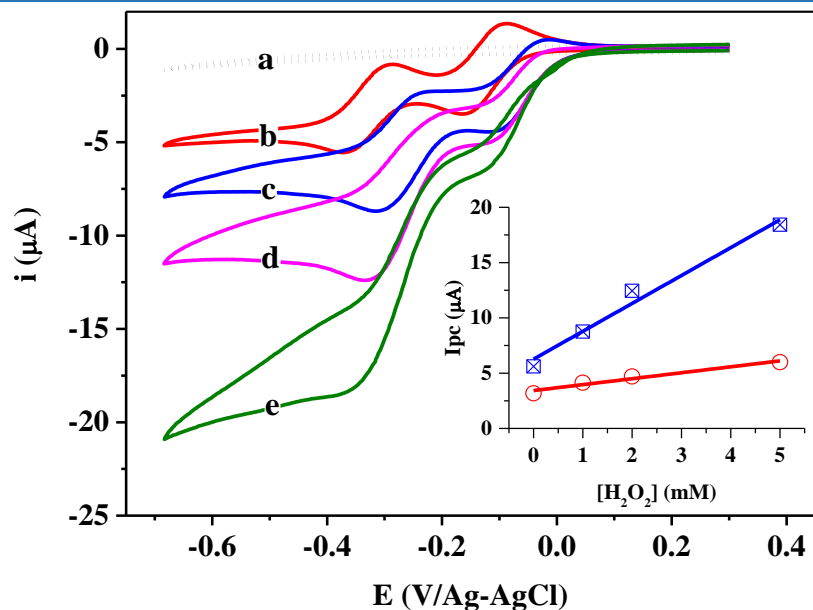
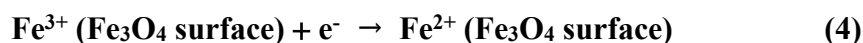


Fig. 6. CVs of PGE baseline in 0.1 M LiClO_4 pH 2.6 under Ar (a), with 1 mM NaDT (b) and in the presence of 1.0 mM (c), 2.0 mM (d), 5.0 mM (e) of H_2O_2 ($\nu = 10 \text{ mV s}^{-1}$). Inset shows the variation of the cathodic currents I_{pc1} (\circ) and I_{pc2} (\boxtimes) as a function of H_2O_2 concentration.

For comparison, the insert of **Fig. 7** shows the CVs recorded using a bare PGE and a M-PGE with 5.0 mM H_2O_2 added in the electrolyte solution and without NaDT. With PEG, no cathodic peak is observed in the presence of H_2O_2 that means no direct reduction of H_2O_2 is occurring at the bare electrode in the investigated potential window. With M-PGE, a well-defined cathodic peak is clearly observed at 0.08 V which is owing an electro-Fenton process [44,45] that occurs on the M-PGE. This process can be expressed by equations (4 and 5):



However, in this case the catalytic current is lower than in the presence of NaDT. This means that with Fe_3O_4 particles on the electrode surface and NaDT in solution, the electrocatalytic process for H_2O_2 reduction is definitively improved. The mechanisms of these electrocatalytic processes are probably not the same on both type of electrodes, implying in the latter case, iron species in interaction with NaDT, as suggested by Dong and Liu for Dawson-type tungstatephosphonate anion [46].

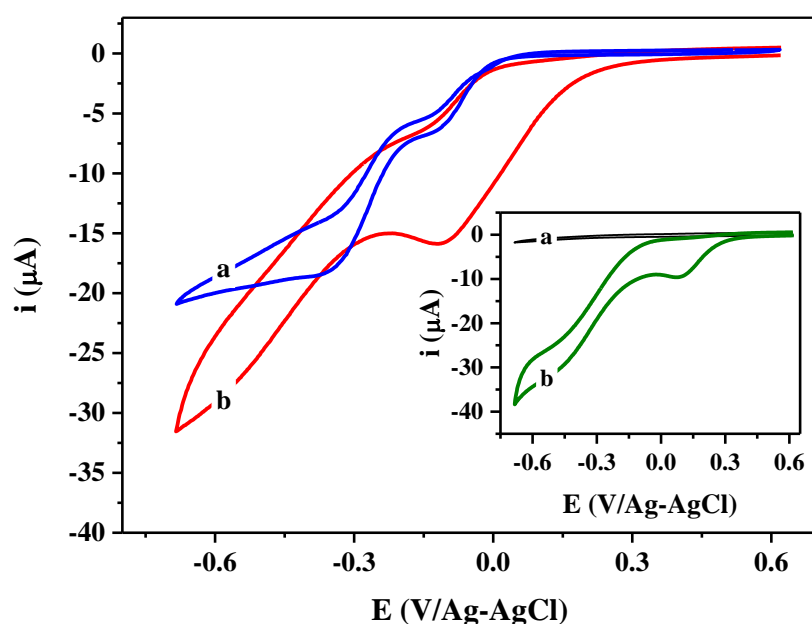


Fig. 7. CVs of 1 mM NaDT in presence of 5.0 mM H_2O_2 recorded at bare PEG (a) and at M-PGE (b). Insert shows CVs (without NaDT) in the presence of 5.0 mM H_2O_2 recorded with bare PEG (a), with a M-PGE (b) (0.1 M LiClO_4 , pH = 2.6, under Ar, $\nu = 10 \text{ mV s}^{-1}$)

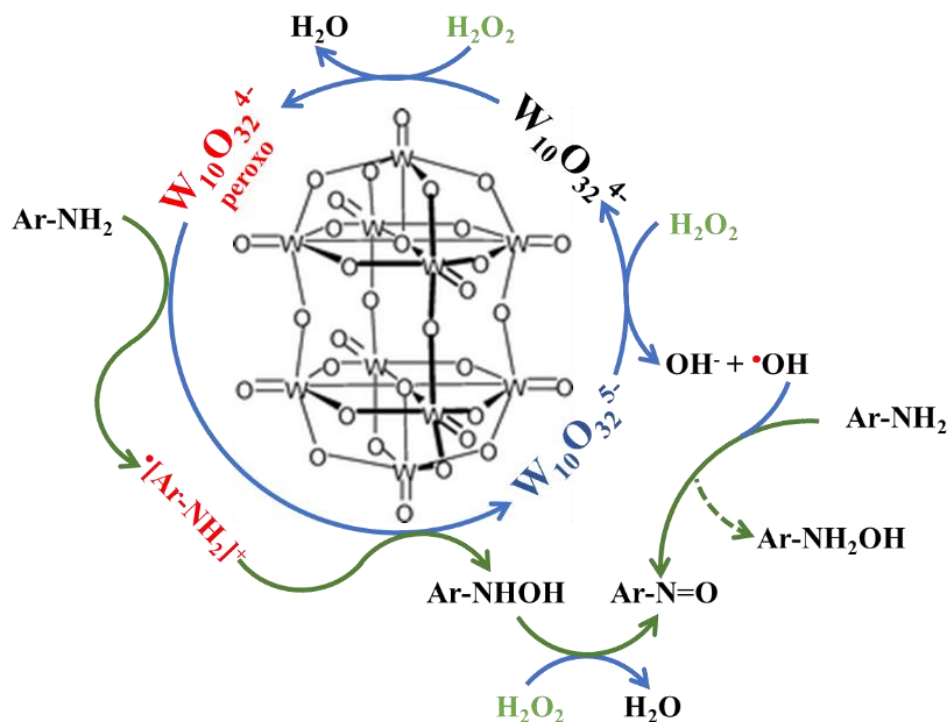
3.6. Mechanistic scheme

According to the above results, the main mechanism of selective oxidation in this ternary system can be proposed. CV experiments reveal that interactions occur between NaDT and

H₂O₂ and also between NaDT and Fe₃O₄. The formation of decatungstate peroxide intermediate species (NaDT_{peroxo}) was shown in UV-Vis.

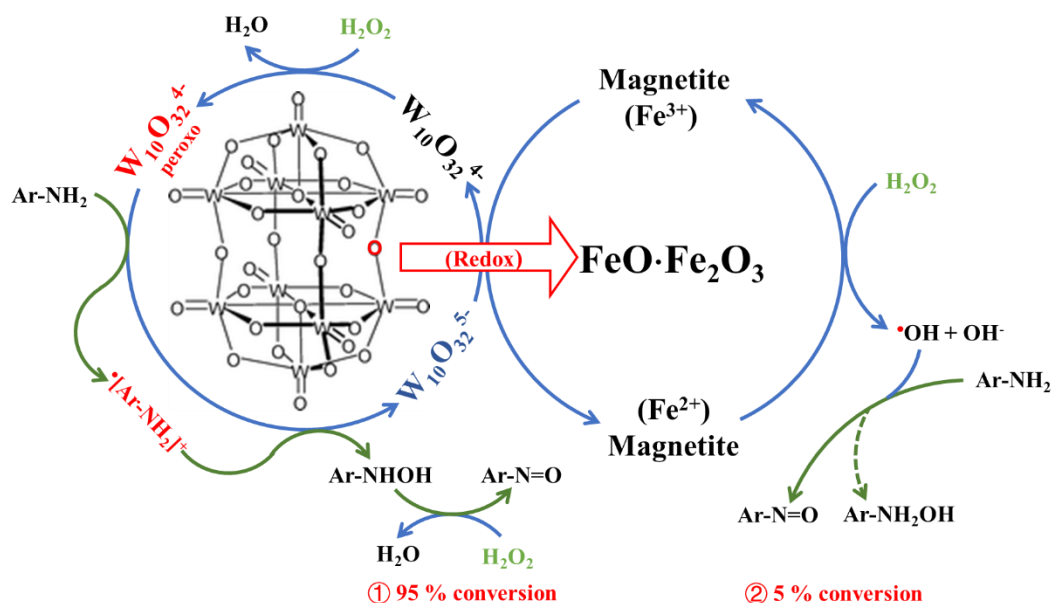
For the interaction between NaDT and Fe₃O₄, IR and XPS characterization clearly show that this interaction is between Fe²⁺ on Fe₃O₄ surface and O element at edge sharing oxygen-bridge of NaDT, which links Fe₃O₄ and NaDT, leading to the formation of NaDT/Fe₃O₄ complex. At the same time, the NaDT reacts with H₂O₂ as well leading to the formation of sodium decatungstate-peroxo (NaDT_{peroxo}). Hence, NaDT/Fe₃O₄/H₂O₂ represents the innovative ternary catalytic system. Such system appears to be a very efficient and interesting catalytic system for the oxidation of amine groups to nitroso derivatives.

In absence of Fe₃O₄, selective oxidation of SPD occurs but with a low efficiency, NaDT_{peroxo} can take an electron from the amine site of sulfapyridine to NaDT giving rise to the formation of the reduced species W₁₀O₃₂⁵⁻ with the simultaneous formation of the radical cation [Ar-NH₂]^{+•} as intermediate which can be oxidized further to Ar-NHOH [7], shown in **Scheme 1**. The latter species may be oxidized in the presence of hydrogen peroxide to form the nitroso derivative (N-SPD). The catalytic activity of NaDT may then be demonstrated by the reduction of H₂O₂ leading to the formation of hydroxyl radicals. However, the efficiency can be highly improved in presence of Fe₃O₄.



Scheme 1. Primary aromatic amines to nitroso aromatic compound through a selective oxidation process in NaDT/H₂O₂ system

While, in the innovative ternary catalytic system (NaDT/Fe₃O₄/H₂O₂), owing to the interaction between NaDT and Fe₃O₄ giving the formation of NaDT/Fe₃O₄ complex, the electron transfer process between Ar-NH₂ and NaDT/Fe₃O₄/H₂O₂ is favored leading to the formation of the reduced species of decatungstate (W₁₀O₃₂⁵⁻) which may regenerate the starting substrate through an electron transfer to Fe₃O₄. The produced radical cation of sulfapyridine is converted, through its oxidation with H₂O₂, to N-SPD. The formation of hydroxyl-sulfapyridine, is clearly a sign for hydroxyl radical formation. This could be produced via a Fenton reaction. The efficiency of the process is mainly owing to the interaction of NaDT with Fe₃O₄ (**Scheme 2**).



Scheme 2. Primary aromatic amines to nitroso aromatic compound through a selective oxidation process in NaDT/Fe₃O₄/H₂O₂ system

4. Conclusion

The ternary system (NaDT/Fe₃O₄/H₂O₂) appears to be a powerful system for the efficient (until 97%) and selective conversion (until 81%) of amine substrates to their nitroso-derivatives. The system consists on a complex material obtained through interaction between Fe₃O₄ and decatungstate on one side and between decatungstate and hydrogen peroxide on the other side as clearly demonstrated by cyclic voltammetry (CV) experiments. This interaction between NaDT and Fe₃O₄ is without any doubt the driving for the electron transfer to occur. The catalytic system proceeds through an electron transfer process between sulfayridine and NaDT leading to the formation of the radical cation on the amine group and the reduced species of NaDT. The regeneration of the W₁₀O₃₂⁴⁻ is obtained via a second electron transfer with Fe₃O₄ owing to the interaction. Thus, during this study we clearly demonstrated that the system NaDT/Fe₃O₄/H₂O₂

is an innovative and powerful process with a high yield of transformation (> 80%) for the generation of nitroso compounds from amine group. It could be used and implemented easily for the synthesis of such chemical compounds in different applications.

Acknowledgements

Peng CHENG thanks the Chinese scholarship council for its financial support and thanks professor Marcello BRIGANTE, engineers Guillaume VOYARD and David BOURGOGNE and Aurélie JOB; and PhD students Yara ARBID and Wengen DENG for their help in some experiments.

References

- [1] P. Cheng, Y. Wang, M. Sarakha, G. Mailhot, Enhancement of the photocatalytic activity of decatungstate, $W_{10}O_{32}^{4-}$, for the oxidation of sulfasalazine/sulfapyridine in the presence of hydrogen peroxide, *J. Photochem. Photobiol. Chem.* 404 (2021) 112890. <https://doi.org/10.1016/j.jphotochem.2020.112890>.
- [2] P.L. Gkizis, I. Kalara-Lafkioti, D. Varelas, I. Tamiolakis, G.S. Armatas, I.N. Lykakis, Efficient and selective oxidation of aromatic amines into nitrosoarenes catalyzed by supported polyoxometalates., *Biointerface Res. Appl. Chem.* 4 (2014) 857–860.
- [3] F. Bigi, A. Corradini, C. Quarantelli, G. Sartori, Silica-bound decatungstates as heterogeneous catalysts for H_2O_2 activation in selective sulfide oxidation, *J. Catal.* 250 (2007) 222–230. <https://doi.org/10.1016/j.jcat.2007.06.019>.
- [4] T. Rassaf, N.S. Bryan, M. Kelm, M. Feelisch, Concomitant presence of N-nitroso and S-nitroso proteins in human plasma, *Free Radic. Biol. Med.* 33 (2002) 1590–1596. [https://doi.org/10.1016/S0891-5849\(02\)01183-8](https://doi.org/10.1016/S0891-5849(02)01183-8).
- [5] J. Huang, Z. Chen, J. Yuan, Y. Peng, Recent Advances in Highly Selective Applications of Nitroso Compounds, *Asian J. Org. Chem.* 5 (2016) 951–960. <https://doi.org/10.1002/ajoc.201600242>.
- [6] M.K. Reddy, I. Ramakrishna, M. Baidya, Divergent Reactivity of gem-Difluoro-enolates toward Nitrogen Electrophiles: Unorthodox Nitroso Aldol Reaction for Rapid Synthesis

- of α -Ketoamides, *Org. Lett.* 20 (2018) 4610–4613.
<https://doi.org/10.1021/acs.orglett.8b01900>.
- [7] J. Ouyang, X. Mi, Y. Wang, R. Hong, Crossing the Ring: A Journey of the Nitroso-ene Reaction, *Synlett.* 28 (2017) 762–772. <https://doi.org/10.1055/s-0036-1588146>.
- [8] A. Menichetti, F. Berti, M. Pineschi, Nitroso Diels-Alder Cycloadducts Derived From N-Acyl-1,2-dihydropyridines as a New Platform to Molecular Diversity, *Molecules.* 25 (2020) 563. <https://doi.org/10.3390/molecules25030563>.
- [9] X. Yu, W. Ding, P. Ge, S. Wang, J. Wang, Oxidative Coupling of Aromatic Amines and Nitrosoarenes: Iodine-Mediated Formation of Unsymmetrical Aromatic Azoxy Compounds, *Adv. Synth. Catal.* 360 (2018) 3150–3156.
<https://doi.org/10.1002/adsc.201800495>.
- [10] M. Dochnahl, G.C. Fu, Catalytic Asymmetric Cycloaddition of Ketenes and Nitroso Compounds: Enantioselective Synthesis of α -Hydroxycarboxylic Acid Derivatives, *Angew. Chem.* 121 (2009) 2427–2429. <https://doi.org/10.1002/ange.200805805>.
- [11] S. Fountoulaki, P.L. Gkizis, T.S. Symeonidis, E. Kaminioti, A. Karina, I. Tamiolakis, G.S. Armatas, I.N. Lykakis, Titania-Supported Gold Nanoparticles Catalyze the Selective Oxidation of Amines into Nitroso Compounds in the Presence of Hydrogen Peroxide, *Adv. Synth. Catal.* 358 (2016) 1500–1508. <https://doi.org/10.1002/adsc.201500957>.
- [12] B.G. Gowenlock, G.B. Richter-Addo, Preparations of C-nitroso compounds, *Chem. Rev.* 104 (2004) 3315–3340.

- [13] R.R. Holmes, R.P. Bayer, A Simple Method for the Direct Oxidation of Aromatic Amines to Nitroso Compounds¹, *J. Am. Chem. Soc.* 82 (1960) 3454–3456. <https://doi.org/10.1021/ja01498a054>.
- [14] B.G. Gowenlock, W. Lüttke, Structure and properties of C-nitroso-compounds, *Q Rev Chem Soc.* 12 (1958) 321–340. <https://doi.org/10.1039/QR9581200321>.
- [15] Y. Shiraishi, H. Sakamoto, K. Fujiwara, S. Ichikawa, T. Hirai, Selective Photocatalytic Oxidation of Aniline to Nitrosobenzene by Pt Nanoparticles Supported on TiO₂ under Visible Light Irradiation, *ACS Catal.* 4 (2014) 2418–2425. <https://doi.org/10.1021/cs500447n>.
- [16] D. Zhao, M. Johansson, J.-E. Bäckvall, In Situ Generation of Nitroso Compounds from Catalytic Hydrogen Peroxide Oxidation of Primary Aromatic Amines and Their One-Pot Use in Hetero-Diels–Alder Reactions, *Eur. J. Org. Chem.* 2007 (2007) 4431–4436. <https://doi.org/10.1002/ejoc.200700368>.
- [17] M. Jadidi Nejad, E. Yazdani, M. Kazemi Miraki, A. Heydari, Tungstate-supported silica-coated magnetite nanoparticles: a novel magnetically recoverable nanocatalyst for green synthesis of nitroso arenes, *Chem. Pap.* 73 (2019) 1575–1583. <https://doi.org/10.1007/s11696-019-00708-x>.
- [18] M. M. Heravi, N. Ghalavand, E. Hashemi, Hydrogen Peroxide as a Green Oxidant for the Selective Catalytic Oxidation of Benzylic and Heterocyclic Alcohols in Different Media: An Overview, *Chemistry.* 2 (2020) 101–178. <https://doi.org/10.3390/chemistry2010010>.

- [19] A. Defoin, Simple Preparation of Nitroso Benzenes and Nitro Benzenes by Oxidation of Anilines with H₂O₂ Catalysed with Molybdenum Salts, *Synthesis*. 2004 (2004) 706–710. <https://doi.org/10.1055/s-2004-815964>.
- [20] A.V. Biradar, T.V. Kotbagi, M.K. Dongare, S.B. Umbarkar, Selective N-oxidation of aromatic amines to nitroso derivatives using a molybdenum acetylide oxo-peroxo complex as catalyst, *Tetrahedron Lett.* 49 (2008) 3616–3619. <https://doi.org/10.1016/j.tetlet.2008.04.005>.
- [21] V. Conte, B. Floris, Vanadium and molybdenum peroxides: synthesis and catalytic activity in oxidation reactions, *Dalton Trans.* 40 (2011) 1419–1436. <https://doi.org/10.1039/C0DT00706D>.
- [22] G. Vilardi, P-aminophenol catalysed production on supported nano-magnetite particles in fixed-bed reactor: Kinetic modelling and scale-up, *Chemosphere*. 250 (2020) 126237. <https://doi.org/10.1016/j.chemosphere.2020.126237>.
- [23] W. Huang, M. Luo, C. Wei, Y. Wang, K. Hanna, G. Mailhot, Enhanced heterogeneous photo-Fenton process modified by magnetite and EDDS: BPA degradation, *Environ. Sci. Pollut. Res.* 24 (2017) 10421–10429. <https://doi.org/10.1007/s11356-017-8728-8>.
- [24] A.J. Elliot, A.S. Simsons, Rate constants for reactions of hydroxyl radicals as a function of temperature, *Radiat. Phys. Chem.* 1977. 24 (1984) 229–231. [https://doi.org/10.1016/0146-5724\(84\)90056-6](https://doi.org/10.1016/0146-5724(84)90056-6).

- [25] H. Liu, Q. Chen, X. Cheng, Y. Wang, Y. Zhang, G. Fan, Sustainable and scalable in-situ fabrication of Au nanoparticles and Fe₃O₄ hybrids as highly efficient electrocatalysts for the enzyme-free sensing of H₂O₂ in neutral and basic solutions, *Sens. Actuators B Chem.* 314 (2020) 128067. <https://doi.org/10.1016/j.snb.2020.128067>.
- [26] Y. Sasaki, T. Yamase, Y. Ohashi, Y. Sasada, Structural Retention of Decatungstates upon Photoreduction, *Bull. Chem. Soc. Jpn.* 60 (1987) 4285–4290. <https://doi.org/10.1246/bcsj.60.4285>.
- [27] D. Attanasio, L. Suber, K. Thorslund, Aerobic photooxidation of substituted benzenes catalyzed by the tungsten isopolyanion [W₁₀O₃₂]⁴⁻, *Inorg. Chem.* 30 (1991) 590–592. <https://doi.org/10.1021/ic00003a053>.
- [28] E.S. Da Silva, V. Prevot, C. Forano, P. Wong-Wah-Chung, H.D. Burrows, M. Sarakha, Heterogeneous photocatalytic degradation of pesticides using decatungstate intercalated macroporous layered double hydroxides, *Environ. Sci. Pollut. Res.* 21 (2014) 11218–11227. <https://doi.org/10.1007/s11356-014-2971-z>.
- [29] S. Nasrazadani, A. Raman, The application of infrared spectroscopy to the study of rust systems—II. Study of cation deficiency in magnetite (Fe₃O₄) produced during its transformation to maghemite (γ-Fe₂O₃) and hematite (α-Fe₂O₃), *Corros. Sci.* 34 (1993) 1355–1365. [https://doi.org/10.1016/0010-938X\(93\)90092-U](https://doi.org/10.1016/0010-938X(93)90092-U).
- [30] Y. Zhang, M. Zhou, A critical review of the application of chelating agents to enable Fenton and Fenton-like reactions at high pH values, *J. Hazard. Mater.* 362 (2019) 436–450. <https://doi.org/10.1016/j.jhazmat.2018.09.035>.

- [31] S. Rakshit, B. Sallman, A. Davantés, G. Lefèvre, Tungstate (VI) sorption on hematite: An in situ ATR-FTIR probe on the mechanism, *Chemosphere*. 168 (2017) 685–691. <https://doi.org/10.1016/j.chemosphere.2016.11.007>.
- [32] G. Shan, Y. Fu, X. Chu, C. Chang, L. Zhu, Highly active magnetic bismuth tungstate/magnetite composite under visible light irradiation in the presence of hydrogen peroxide, *J. Colloid Interface Sci.* 444 (2015) 123–131. <https://doi.org/10.1016/j.jcis.2014.12.068>.
- [33] T. Radu, C. Iacovita, D. Benea, R. Turcu, X-Ray Photoelectron Spectroscopic Characterization of Iron Oxide Nanoparticles, *Appl. Surf. Sci.* 405 (2017) 337–343. <https://doi.org/10.1016/j.apsusc.2017.02.002>.
- [34] S. Tiwari, R. Prakash, R.J. Choudhary, D.M. Phase, Oriented growth of Fe₃O₄ thin film on crystalline and amorphous substrates by pulsed laser deposition, *J. Phys. Appl. Phys.* 40 (2007) 4943–4947. <https://doi.org/10.1088/0022-3727/40/16/028>.
- [35] A. Su, M. Chen, Z. Fu, B. Yang, J. She, F. Wan, C. Zhang, Y. Liu, Hybridizing engineering strategy of non-lacunary (nBu₄N)₄W₁₀O₃₂ by carbon quantum dot with remarkably enhanced visible-light-catalytic oxidation performance, *Appl. Catal. Gen.* 587 (2019) 117261. <https://doi.org/10.1016/j.apcata.2019.117261>.
- [36] B. Yang, Z. Fu, A. Su, J. She, M. Chen, S. Tang, W. Hu, C. Zhang, Y. Liu, Influence of tetraalkylammonium cations on quality of decatungstate and its photocatalytic property in visible light-triggered selective oxidation of organic compounds by dioxygens, *Appl. Catal. B Environ.* 242 (2019) 249–257. <https://doi.org/10.1016/j.apcatb.2018.09.099>.

- [37] Y. Zhong, L. Yu, Z.-F. Chen, H. He, F. Ye, G. Cheng, Q. Zhang, Microwave-assisted synthesis of Fe₃O₄ nanocrystals with predominantly exposed facets and their heterogeneous UVA/Fenton catalytic activity, *ACS Appl. Mater. Interfaces*. 9 (2017) 29203–29212.
- [38] E. Tanasa, C. Zaharia, I.-C. Radu, V.-A. Surdu, B.S. Vasile, C.-M. Damian, E. Andronescu, Novel Nanocomposites Based on Functionalized Magnetic Nanoparticles and Polyacrylamide: Preparation and Complex Characterization, *Nanomaterials*. 9 (2019) 1384. <https://doi.org/10.3390/nano9101384>.
- [39] I. Moriguchi, J.H. Fendler, Characterization and Electrochromic Properties of Ultrathin Films Self-Assembled from Poly(diallyldimethylammonium) Chloride and Sodium Decatungstate, *Chem. Mater.* 10 (1998) 2205–2211. <https://doi.org/10.1021/cm980127b>.
- [40] S.C. Termes, M.T. Pope, Reduction of the decatungstate anion in nonaqueous solution and its confirmation as “polytungstate-Y,” *Inorg. Chem.* 17 (1978) 500–501. <https://doi.org/10.1021/ic50180a064>.
- [41] A.S. Micallef, R.C. Bott, S.E. Bottle, G. Smith, J.M. White, K. Matsuda, H. Iwamura, Brominated isoindolines: precursors to functionalised nitroxides, *J. Chem. Soc. Perkin Trans. 2*. 0 (1999) 65–72. <https://doi.org/10.1039/A806884D>.
- [42] K. Fujitani, T. Mizutani, T. Oida, T. Kawase, Oxidative Cleavage with Hydrogen Peroxide: Preparation of Polycarboxylic Acids from Cyclic Olefins, *J. Oleo Sci.* 58 (2009) 37–42. <https://doi.org/10.5650/jos.58.37>.

- [43] L. Kang, H. Ma, Y. Yu, H. Pang, Y. Song, D. Zhang, Study on amperometric sensing performance of a crown-shaped phosphotungstate-based multilayer film, *Sens. Actuators B Chem.* 177 (2013) 270–278. <https://doi.org/10.1016/j.snb.2012.10.126>.
- [44] P.V. Nidheesh, R. Gandhimathi, Trends in electro-Fenton process for water and wastewater treatment: An overview, *Desalination.* 299 (2012) 1–15. <https://doi.org/10.1016/j.desal.2012.05.011>.
- [45] E. Brillas, I. Sirés, M.A. Oturan, Electro-Fenton process and related electrochemical technologies based on Fenton's reaction chemistry, *Chem. Rev.* 109 (2009) 6570–6631. <https://doi.org/10.1021/cr900136g>.
- [46] S. Dong, M. Liu, Electrochemical and electrocatalytic properties of iron(III)-substituted Dawson-type tungstophosphate anion, *J. Electroanal. Chem.* 372 (1994) 95–100. [https://doi.org/10.1016/0022-0728\(94\)03288-2](https://doi.org/10.1016/0022-0728(94)03288-2).

1 **Supporting Information**

2 **Supporting information**

3 **Oxidation mechanism exploration of an innovative**
4 **ternary catalytic process based on intrasystem**
5 **interaction: Decatungstate/Fe₃O₄/H₂O₂**

6 *Peng Cheng, Mohamed Sarakha, Christine Mousty, Pierre Bonnet and Gilles Mailhot**

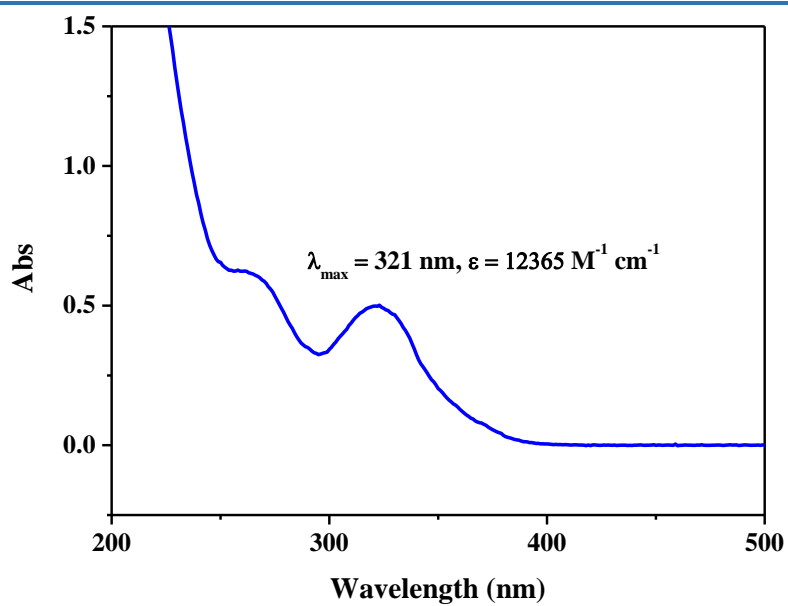
7 Université Clermont Auvergne, CNRS, Clermont Auvergne INP, Institut de Chimie de
8 Clermont Ferrand (ICCF) UMR 6296, BP 80026, F-63171, Aubière cedex, France

9 * Corresponding author. E-mail address: Gilles.Mailhot@uca.fr.

10

11

12

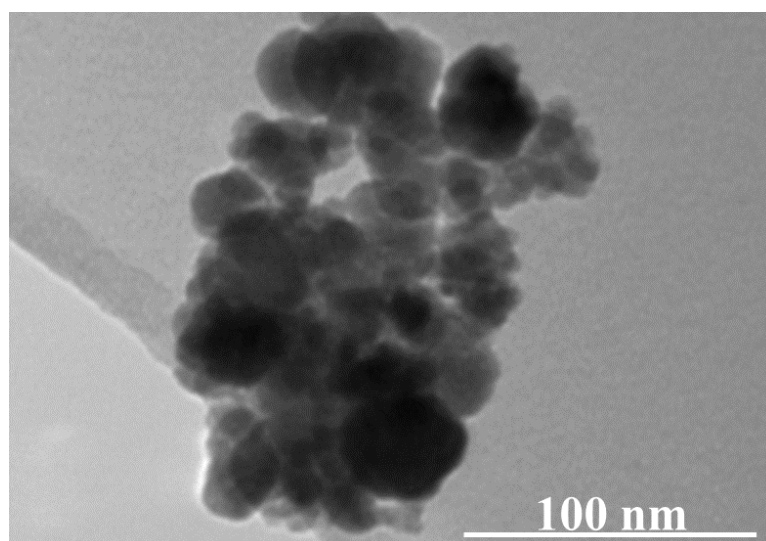


13

14 **Fig. S1.** UV-vis absorption spectrum of sodium decatungstate (NaDT). [NaDT] = 41 μM ;

15

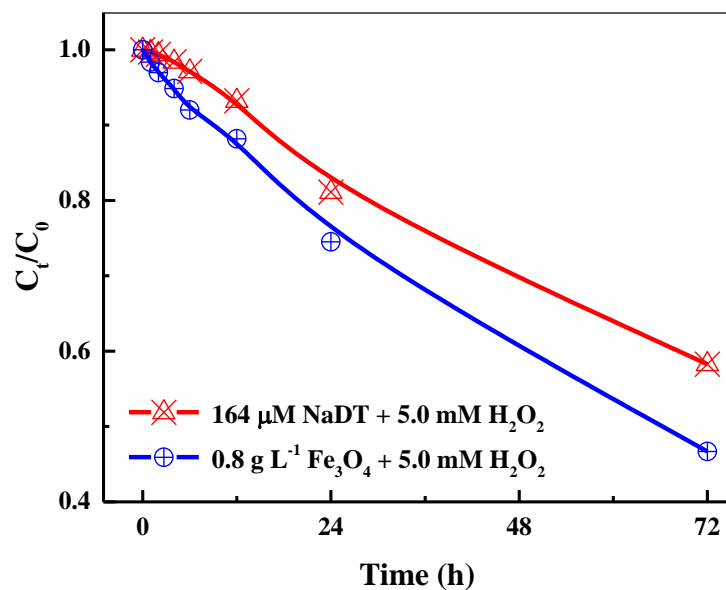
Solvent: ultrapure water; pH = 4.0.



16

17

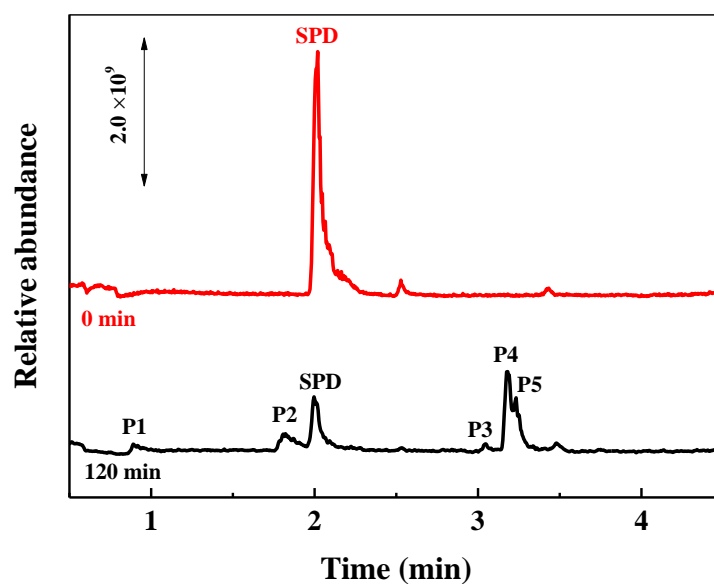
Fig. S2. TEM image of Fe_3O_4



18

19 **Fig. S3.** Longer conversion kinetics of SPD with NaDT or Fe_3O_4 in presence of H_2O_2 . [SPD]

20

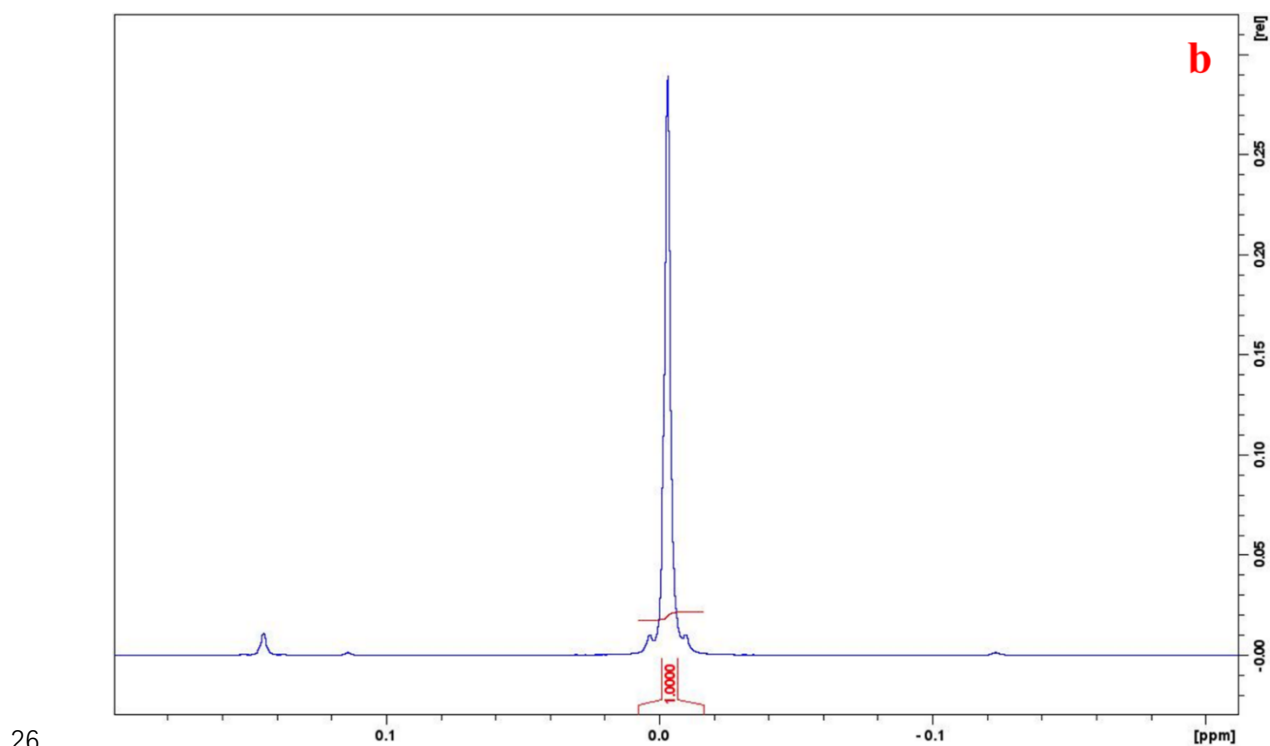
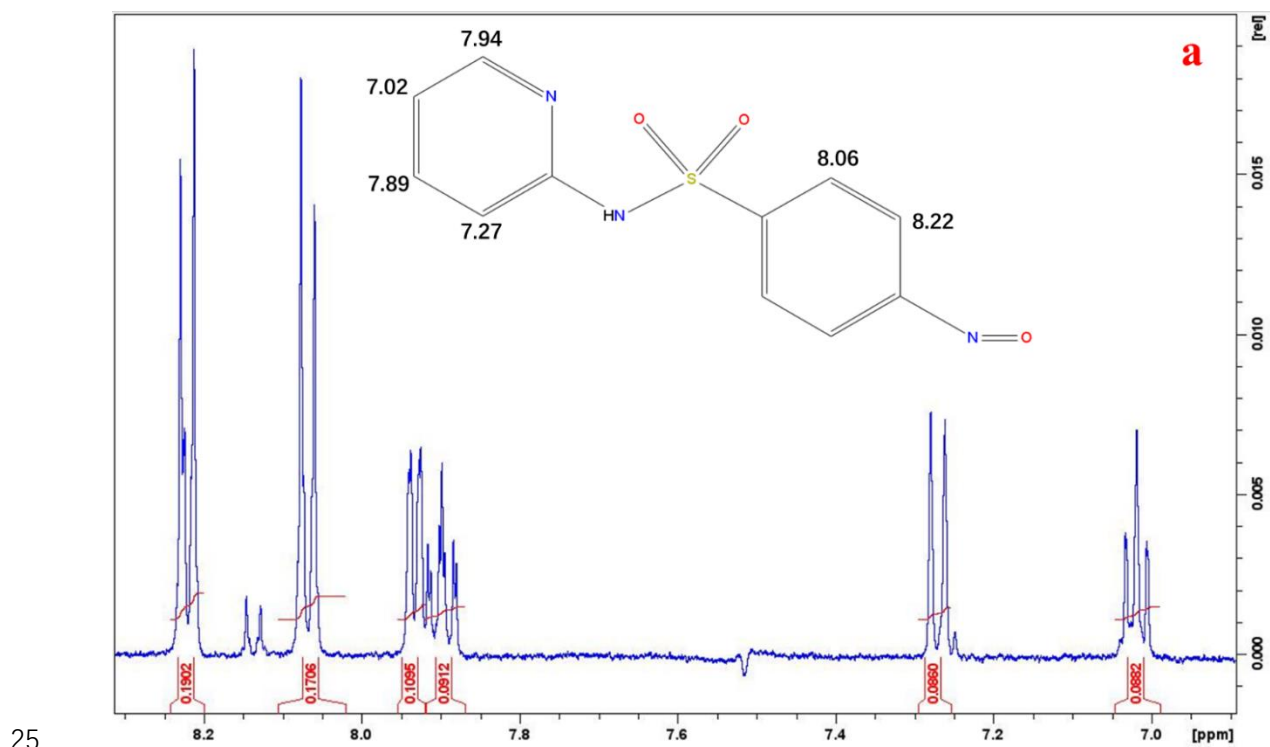
 $= 30.0 \mu\text{M}$; $[\text{H}_2\text{O}_2] = 5.0 \text{ mM}$; $\text{pH} = 3.0$ 

21

22 **Fig. S4.** The UPLC-MS chromatograms of the sulfapyridine (SPD) in the ternary system at 023 min and 120 minutes. $[\text{NaDT}] = 41 \mu\text{M}$; $[\text{Fe}_3\text{O}_4] = 0.4 \text{ g L}^{-1}$; $[\text{H}_2\text{O}_2] = 5.0 \text{ mM}$; $[\text{SPD}] = 120$

24

 μM ; $\text{pH} = 3.0$.



27 **Fig. S5.** NMR spectrum of N-SPD (a) and TPSD₄ (b) after 120 minutes of reaction. (Initial
28 condition [NaDT] = 41 μM; [Fe₃O₄] = 0.4 g L⁻¹; [H₂O₂] = 5.0 mM; [SPD] = 120 μM; pH =
29 3.0.)

¹H NMR (500 MHz, D₂O): δ 8.22 ppm (d, J = 8.8 Hz, 2H), 8.06 ppm (d, J = 8.5 Hz, 2H), 7.94 ppm (d, J = 6.5 Hz, 1H), 7.89 ppm (d d d, J = 1.8, 7.3, 9.0 Hz, 1H), 7.27 ppm (d, J = 9.0 Hz, 1H), 7.02 ppm (t, J = 7.1 Hz, 1H). The chemical shifts and Spin coupling constants are consistent with Castrejon et.al[1]. After normalization, the concentration of N-SPD can be obtained according to the NMR peak area. The average concentration of N-SPD calculated after quantification by NMR is 44.72 mM, and the relative standard deviation (RSD) is 5.1%

Effect of different parameters

a) Effect of pH

The effect of pH was studied within the range 2.5 - 6.9 at constant concentration of NaDT, Fe₃O₄, H₂O₂ and SPD. As clearly seen in **Table S3**, the conversion percentage of SPD decreases when the pH increases. The conversion was estimated to around 77% with a rate of $1.2 \times 10^{-2} \text{ min}^{-1}$ at pH = 2.5 and 46% at pH = 4.9 with a rate of $0.48 \times 10^{-2} \text{ min}^{-1}$. It dropped rapidly to roughly 6% at pH = 6.9 owing more likely to the lower stability of NaDT at pH > 5.5[2]. On the other hand, the acid-base equilibrium of SPD (pK_a = 8.43) may also interfere in the process leading to a change in the solution composition and thus a different reaction processes could occur with the various forms of SPD. Concerning the yield of N-SPD, it is estimated to 70% at pH = 2.5 and increased to reach a maximum at pH = 4.9 (around 90%). No formation of nitroso derivative was observed at higher pH, once again due to the instability of NaDT. NaDT appears then as a key compound in this novel and promising ternary system for the generation of nitroso compound.

50 **b) Effect of H₂O₂ concentration**

51 **Fig. S6** shows the effect of different H₂O₂ concentrations (from 0 to 19.2 mM) on SPD
52 conversion. The results were obtained from NaDT (41 μM) /Fe₃O₄ (0.264 g L⁻¹)/H₂O₂ ternary
53 system at pH 3.0 and in the presence of various hydrogen peroxide concentrations. In the
54 absence of H₂O₂, SPD conversion was found to be very low (0.1 %) while in the presence of
55 H₂O₂, the SPD conversion increased rapidly. The rate constant reached a limit value (1.47×10^{-2}
56 min⁻¹) when the concentration of H₂O₂ is higher than 10.0 mM, leading us to the conclusion
57 that the concentration of H₂O₂ does not represent a limiting step. In addition, the yield of N-
58 SPD remains constant at approximately 70% for the concentration of hydrogen peroxide higher
59 than 5.0 mM (**Table S4**). Thus, in the following experiments, we selected 5.0 mM of H₂O₂.

60 **c) Effect of the amount of Fe₃O₄**

61 As we clearly demonstrated above, Fe₃O₄ and NaDT are the main reactants that lead to the
62 conversion of SPD into N-SPD. In order to find out the optimum concentration of Fe₃O₄,
63 experiments were performed by varying the amount of Fe₃O₄ within the range 0.1 - 1.5 g L⁻¹.
64 The chosen concentrations for the other substrates are [SPD] = 30 μM, [NaDT] = 41 μM in the
65 presence of 5.0 mM H₂O₂ at pH = 3.0.

66 **Table S5**, shows effect of the amount of Fe₃O₄ on the SPD conversion percentage and on
67 the selectivity in the ternary system. Concerning the SPD conversion rate, a rapid increase from
68 43 % to 91 % is observed, when the amount of Fe₃O₄ increases from 0.1 to 0.4 g L⁻¹. The

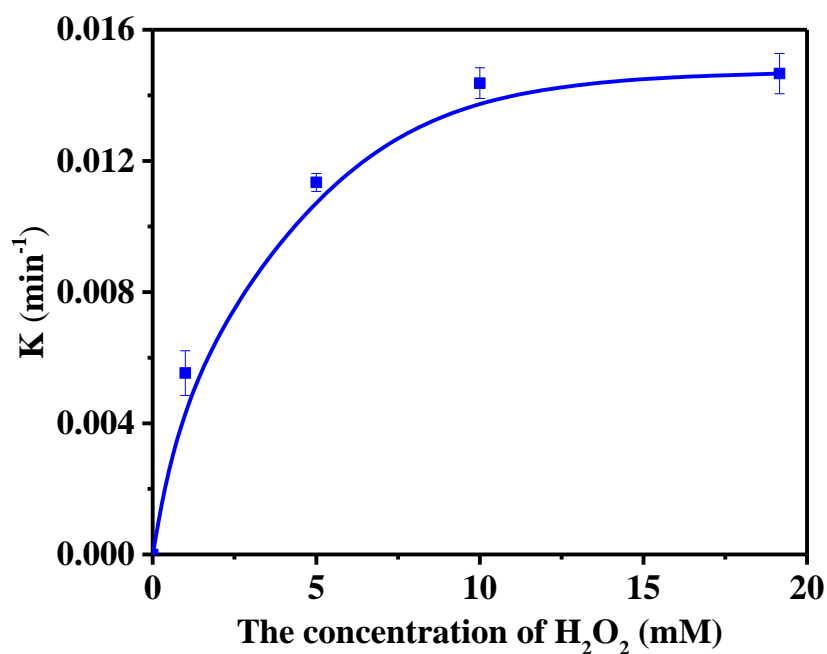
69 conversion reaches a plateau value at about 98% for the amount of Fe_3O_4 higher than 0.8 g L^{-1}
70 with a selectivity that increases to around 81%.

71 Moreover, as shown in **Fig. S7**, an increase of the SPD conversion rate constant is noticed
72 from 0.44×10^{-2} to $3.32 \times 10^{-2} \text{ min}^{-1}$ when the amount of Fe_3O_4 increases from 0.1 to 0.8 g L^{-1} .
73 In this range, the oxidation rate appears to be proportional to Fe_3O_4 amount. When the amount
74 of Fe_3O_4 is increased to 1.5 g L^{-1} , the conversion rate constant slightly increases to 3.58×10^{-2}
75 min^{-1} indicating that a plateau value is reached.

76 **d) Effect of the sodium decatungstate (NaDT) concentration**

77 The effect of the NaDT concentration was studied within the range 0 - $246 \text{ }\mu\text{M}$ by
78 maintaining the amount of Fe_3O_4 at 0.4 g L^{-1} , SPD at a concentration of $30 \text{ }\mu\text{M}$, in the presence
79 of $5.0 \text{ mM H}_2\text{O}_2$ at $\text{pH} = 3.0$. **Table S6** shows Effect of NaDT concentration on SPD conversion
80 and the obtained yield of N-SPD after 2 hours. The percentage of SPD conversion increases
81 rapidly from 9.3 % to 88.6 % with increasing the NaDT concentration from 0 to $21 \text{ }\mu\text{M}$. And a
82 slight increase (to 95.7%) is obtained when the NaDT concentration reaches $246 \text{ }\mu\text{M}$.
83 Concomitantly, a fast increase of SPD disappearance rate constant (0.008×10^{-2} to 1.77×10^{-2}
84 min^{-1}) is observed when NaDT concentration increases from 0 to $21 \text{ }\mu\text{M}$. Then the value rapidly
85 levels off for the range 41 to $246 \text{ }\mu\text{M}$ by reaching a limit rate of approximately $2.5 \times 10^{-2} \text{ min}^{-1}$
86 (**Fig. S8**). Under these experimental conditions, it appears that SPD is efficiently and selectively
87 oxidized even with low NaDT concentration. However, N-SPD selectivity decreases from 77.2 %

88 to 34.9% with increasing the NaDT concentration from 21 to 246 μM . As seen in **Fig. S9**, nitro-
 89 sulfapyridine is generated with higher NaDT concentration, which is due the over-oxidation.

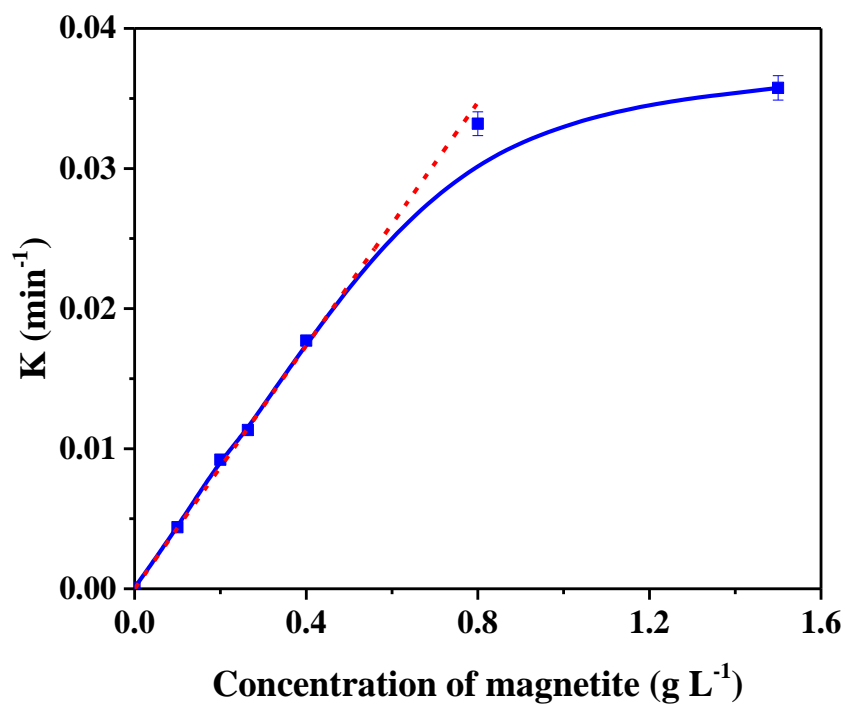


90

91 **Fig. S6.** Effect of H₂O₂ concentration on SPD conversion in NaDT/Fe₃O₄/H₂O₂ system.

92

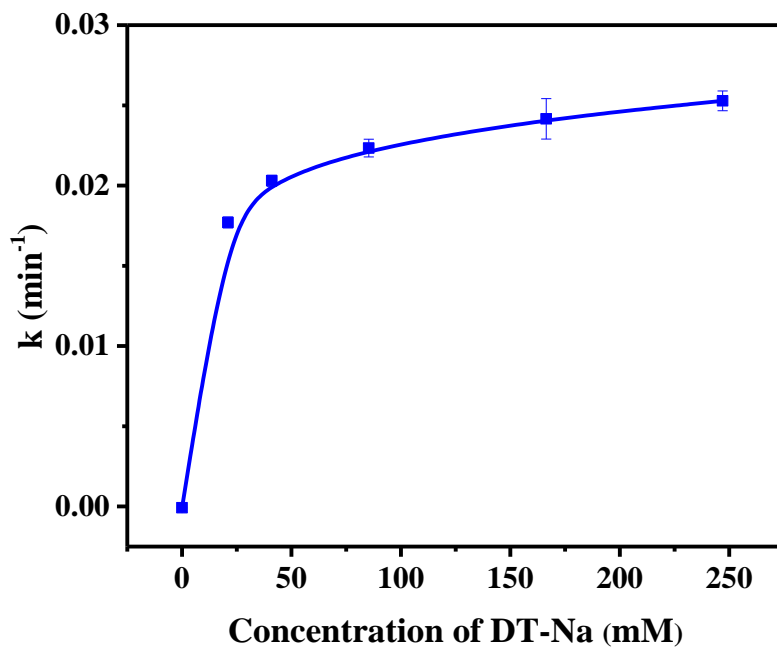
[NaDT] = 41 μM ; [Fe₃O₄] = 0.264 g L⁻¹; [SPD] = 30 μM ; pH = 3.0



93

94 **Fig. S7.** Effect of the amount of Fe₃O₄ on SPD conversion in NaDT/Fe₃O₄/H₂O₂ system.

95

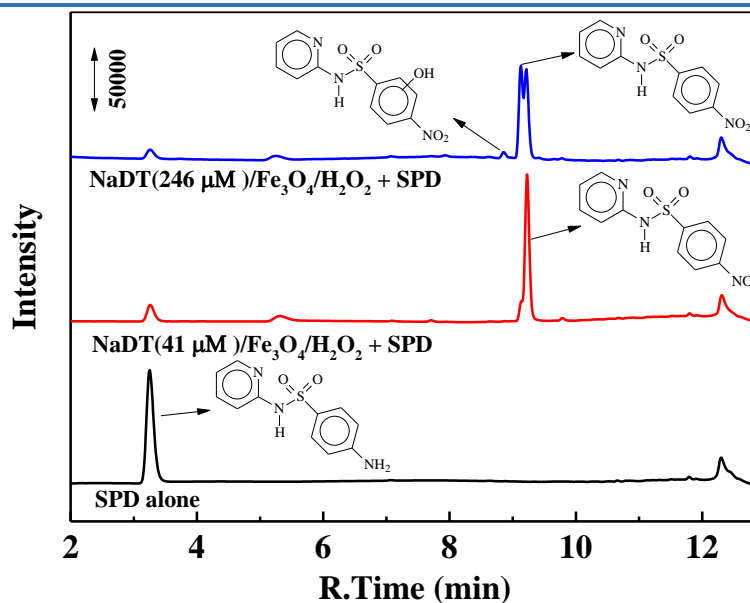
[NaDT] = 41 μM; [H₂O₂] = 5.0 mM; [SPD] = 30 μM; pH = 3.0.

96

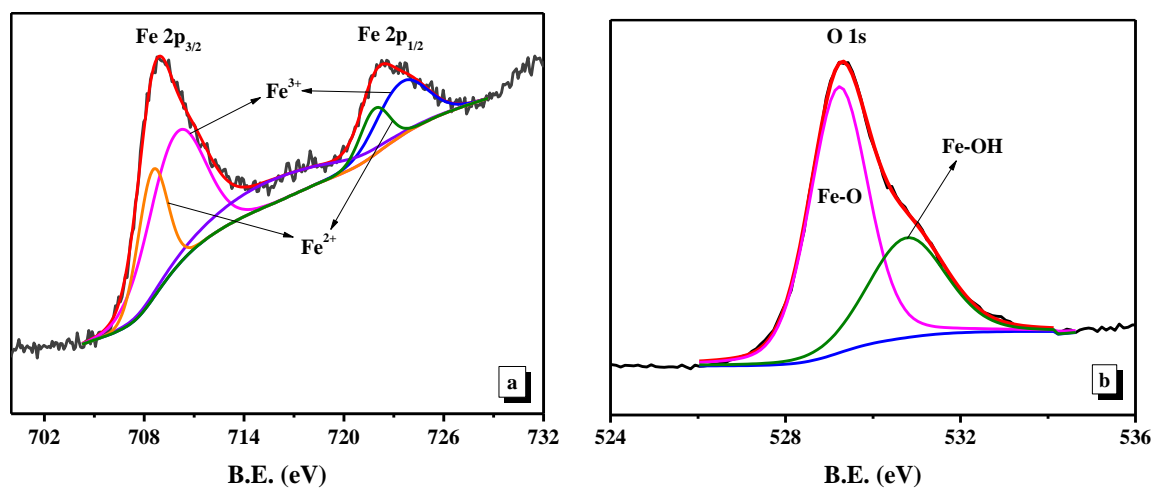
97 **Fig. S8.** Effect of different NaDT concentrations. [H₂O₂] = 5.0 mM; [Fe₃O₄] = 0.4 g L⁻¹;

98

[SPD] = 30 μM; pH = 3.0



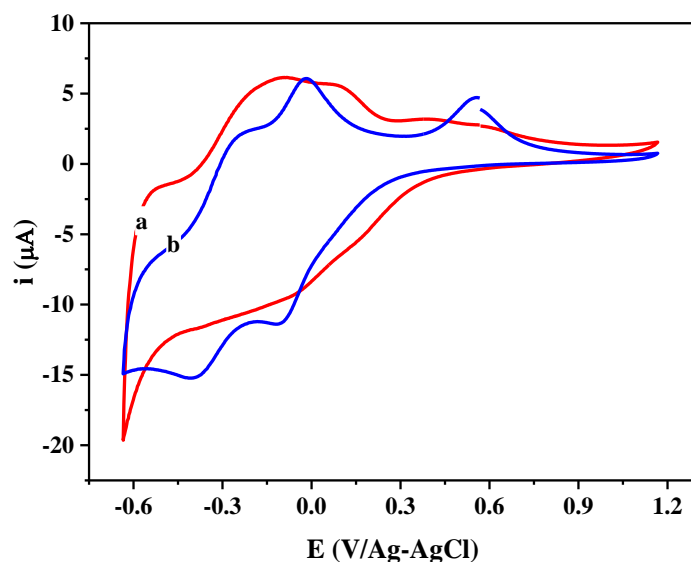
99
 100 **Fig. S9.** The UPLC chromatogram of the sulfapyridine (SPD) in the ternary system. $[\text{H}_2\text{O}_2] =$
 101 5.0 mM ; $[\text{Fe}_3\text{O}_4] = 0.4 \text{ g L}^{-1}$; $[\text{SPD}] = 30 \text{ μM}$; $\text{pH} = 3.0$.



102
 103 **Fig. S10.** High resolution XPS spectra of Fe_3O_4 before reaction of (a) Fe 2p, and (b) O 1s.

104 In **Fig. S11**, the curve **a** corresponds to the CV recorded with a M-PGE in 0.1 mM LiClO_4
 105 electrolyte at $\text{pH} 2.6$ under Ar. The broad signal is related to the electrochemical response of
 106 iron oxide adsorbed on the electrode surface.[3] The curve **b** shows the CV of NaDT recorded
 107 with this M-PGE. Two cathodic peaks are observed at -0.11 V/Ag-AgCl and -0.40 V/Ag-AgCl .

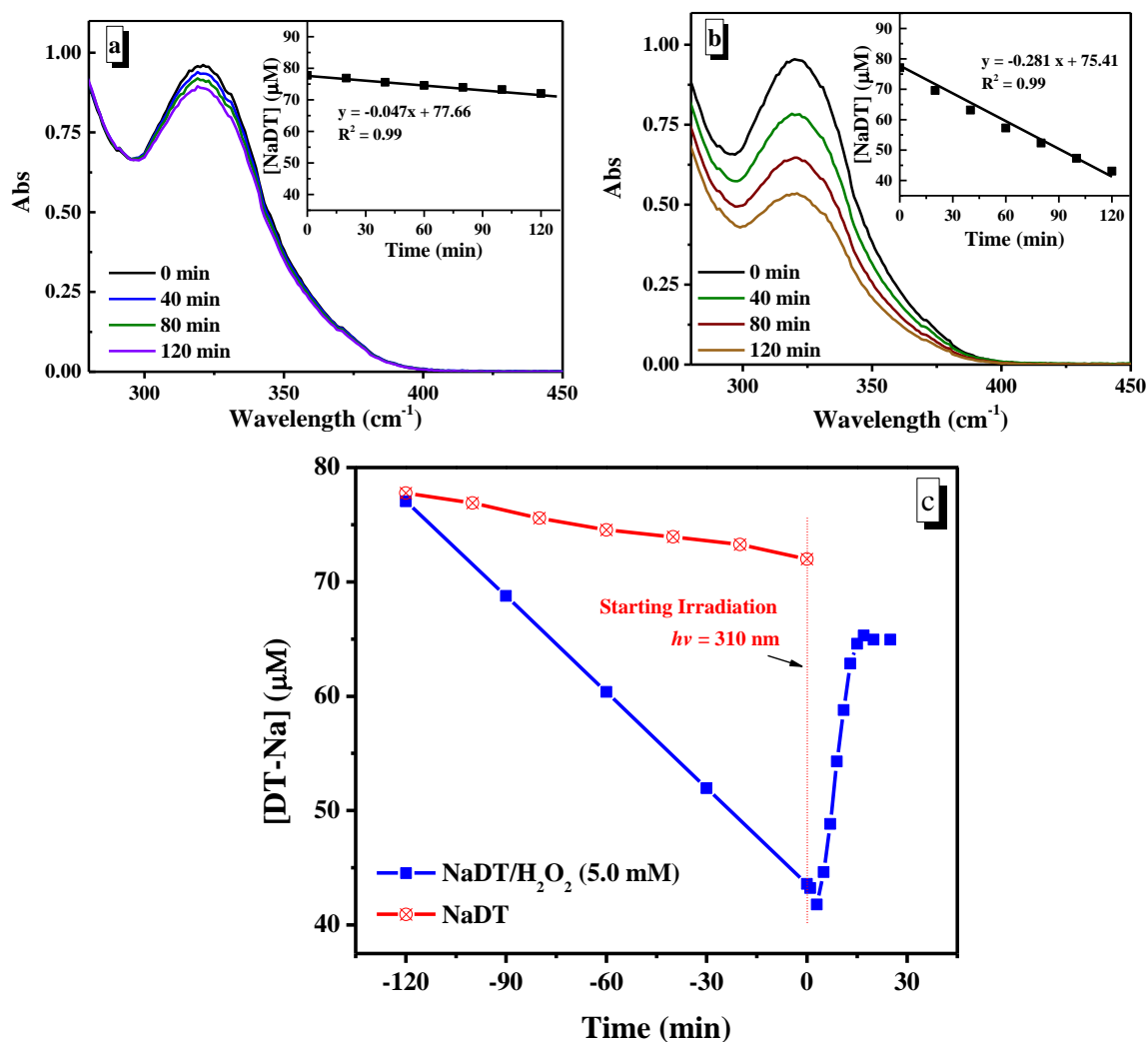
108 These peaks are slightly shifted in comparison to those observed using a bare PGE ($E_{pc1} = -$
109 0.16 V/Ag-AgCl and $E_{pc2} = -0.36$ V/Ag-AgCl). In the reverse scan, three anodic peaks are
110 observed at -0.22 , -0.02 and 0.54 V, respectively. The first two anodic peaks are due to the
111 NaDT regeneration, as previously observed at bare PGE. The origin of the third peak (E_{pa3}),
112 situated at 0.54 V, is not yet identified. These modifications in CV curve of NaDT could be due
113 to specific interactions between surface iron atoms of Fe_3O_4 and NaDT, as described by Dong
114 and Liu for Dawson-type tungstatephosphonate anion [4].



115
116 **Fig. S11.** CVs recorded with M-PGE modified electrode in 0.1 M $LiClO_4$ pH = 2.6 under Ar
117 (a) and in the presence of 1 mM NaDT (b) ($v = 10$ mV s⁻¹).

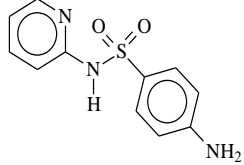
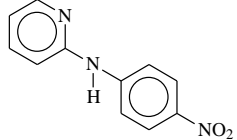
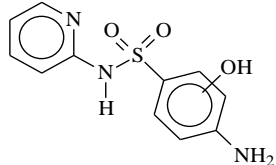
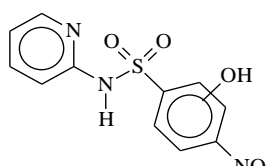
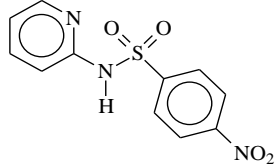
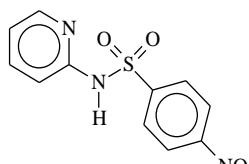
118 In order to confirm the interaction between NaDT and H_2O_2 , NaDT (77 μ M) and H_2O_2
119 (5.0 mM) were mixed in the ultra-pure water. As shown in **Fig. S12(a)**, NaDT disappears slowly
120 in the absence of H_2O_2 with the initial rate of -0.047 μ M min⁻¹. On contrary, the absorbance of
121 NaDT disappears quickly with the initial rate of -0.281 μ M min⁻¹ (**Fig. S12(b)**), which is due
122 to the interaction between NaDT and H_2O_2 leading to the formation of sodium decatungstate-

123 peroxy species ($\text{NaDT}_{\text{peroxy}}$) [5]. The NaDT can regenerate from this peroxide species under
 124 UV ($\lambda = 310 \text{ nm}$) irradiation (**Fig. S12(c)**).



126
 127 **Fig. S12.** The UV-Vis spectra of NaDT in the absence or presence of H_2O_2 within 2 hours at
 128 $\text{pH} = 3.0$. (a) NaDT ($77 \mu\text{M}$), (b) NaDT ($77 \mu\text{M}$) / H_2O_2 (5.0 mM) and (c) The absorbance of
 129 NaDT ($77 \mu\text{M}$) at 321 nm in the presence of H_2O_2 (5.0 mM) before and after irradiation at $\lambda =$
 130 310 nm .

Table S1. MS analysis of SPD products and suggested structures

R-T min	Products	M _{measured} m/z	Molecular formula [M+ H] ⁺	M _{accurate} m/z	Error (ppm)	Chemical structure
1.99	SPD	250.0642	C ₁₁ H ₁₂ O ₂ N ₃ S ⁺	250.0656	-3.008	
0.89	P1	232.0715	C ₁₁ H ₁₀ O ₃ N ₃ ⁺	232.0728	-2.956	
1.81	P2	266.0590	C ₁₁ H ₁₂ O ₃ N ₃ S ⁺	266.0605	-3.559	
3.04	P3	296.0332	C ₁₁ H ₁₀ O ₅ N ₃ S ⁺	296.0347	-3.094	
3.18	P4	280.0383	C ₁₁ H ₁₀ O ₄ N ₃ S ⁺	280.0397	-3.112	
3.22	P5 (N-SPD)	264.0435	C ₁₁ H ₁₀ O ₃ N ₃ S ⁺	264.0448	-3.018	

[NaDT] = 41 μM; [H₂O₂] = 5.0 mM; [SPD] = 120 μM; pH = 3.0.

Table S2. NMR information of N-SPD and TSPD₄

Compounds	TSPD ₄			N-SPD			
H number	9	2	2	1	1	1	1
Chemical shift (ppm)	0.00	8.22	8.06	7.94	7.89	7.27	7.02
Normalized sum of integral	1.0000	0.1902	0.1706	0.1095	0.0912	0.0860	0.0882
Concentration (μM)	52.19	44.67	40.09	51.43	42.84	40.36	41.43
Average [N-SPD] (μM)	44.72			RSD (%)		5.1	

Table S3. Effect of pH on SPD conversion and yield of N-SPD formation in 2h

pH	2.5	3.0	4.1	4.9	6.9
Rate constant of SPD disappearance ($\times 10^{-2} \text{ min}^{-1}$)	1.20	1.13	0.90	0.48	0.004
Percentage of SPD disappearance (%)	77.1	75.4	68.0	45.9	6.0
Yield of N-SPD formation (%)	69.8	71.3	76.7	89.6	0.0

[NaDT] = 41 μM; [H₂O₂] = 5.0 mM; [Fe₃O₄] = 0.264 g L⁻¹; [SPD] = 30 μM;

Table S4. Effect of [H₂O₂] on SPD conversion and yield of N-SPD formation in 2h

[H ₂ O ₂] (mM)	0.0	1.0	5.0	10.0	19.2
Rate constant of SPD disappearance ($\times 10^{-2} \text{ min}^{-1}$)	0.00	0.55	1.13	1.44	1.47
Percentage of SPD disappearance (%)	0.1	49.1	75.4	83.9	84.5
Yield of N-SPD formation (%)	0.0	61.8	71.3	74.4	73.5

[NaDT] = 41 μM ; [Fe₃O₄] = 0.264 g L⁻¹; [SPD] = 30 μM ; pH = 3.0

Table S5. Effect of amount of Fe₃O₄ on SPD conversion and yield of N-SPD formation in 2h

[Fe ₃ O ₄] (g L ⁻¹)	0	0.1	0.2	0.264	0.4	0.8	1.5
Rate constant of SPD disappearance ($\times 10^{-2} \text{ min}^{-1}$)	0.003	0.44	0.92	1.13	1.77	3.32	3.58
Percentage of SPD disappearance (%)	1.7	43.0	67.4	75.4	91.2	98.1	98.5
Yield of N-SPD formation (%)	0	30.2	69.8	71.3	76.8	78.9	81.3

[NaDT] = 41 μM ; [H₂O₂] = 5.0 mM; [SPD] = 30 μM ; pH = 3.0

Table S6. Effect of [NaDT] on SPD conversion and yield of N-SPD formation in 2h

[NaDT] (μM)	0	21	41	82	164	246
Rate constant of SPD disappearance ($\times 10^{-2} \text{ min}^{-1}$)	0.008	1.77	2.03	2.23	2.42	2.53
Percentage of SPD disappearance (%)	9.3	88.6	91.2	93.8	94.5	95.7
Yield of N-SPD formation (%)	0.0	77.2	76.8	67.7	57.7	34.9

$[\text{H}_2\text{O}_2] = 5.0 \text{ mM}$; $[\text{Fe}_3\text{O}_4] = 0.4 \text{ g L}^{-1}$; $[\text{SPD}] = 30 \mu\text{M}$; $\text{pH} = 3.0$

References

- [1] J.L. Castrejon, S.N. Lavergne, A. El-Sheikh, J. Farrell, J.L. Maggs, S. Sabbani, P.M. O'Neill, B.K. Park, D.J. Naisbitt, Metabolic and Chemical Origins of Cross-Reactive Immunological Reactions to Arylamine Benzenesulfonamides: T-Cell Responses to Hydroxylamine and Nitroso Derivatives, *Chem. Res. Toxicol.* 23 (2010) 184–192. <https://doi.org/10.1021/tx900329b>.
- [2] Y. Sasaki, T. Yamase, Y. Ohashi, Y. Sasada, Structural Retention of Decatungstates upon Photoreduction, *Bull. Chem. Soc. Jpn.* 60 (1987) 4285–4290. <https://doi.org/10.1246/bcsj.60.4285>.
- [3] M.A. Gross, S.G.C. Moreira, M.A. Pereira-da-Silva, F.F. Sodré, L.G. Paterno, Multilayered iron oxide/reduced graphene oxide nanocomposite electrode for voltammetric sensing of bisphenol-A in lake water and thermal paper samples, *Sci. Total Environ.* 763 (2021) 142985. <https://doi.org/10.1016/j.scitotenv.2020.142985>.
- [4] S. Dong, M. Liu, Electrochemical and electrocatalytic properties of iron(III)-substituted Dawson-type tungstophosphate anion, *J. Electroanal. Chem.* 372 (1994) 95–100. [https://doi.org/10.1016/0022-0728\(94\)03288-2](https://doi.org/10.1016/0022-0728(94)03288-2).
- [5] R.H. Ingle, N.K.K. Raj, Lacunary Keggin type polyoxotungstates in conjunction with a phase transfer catalyst: An effective catalyst system for epoxidation of alkenes with aqueous H_2O_2 , *J. Mol. Catal. Chem.* 294 (2008) 8–13. <https://doi.org/10.1016/j.molcata.2008.07.003>.

Manuscript 4

Tetra-n-butylammonium decatungstate supported magnetite nanoparticles: a novel magnetically nano-catalyst for green synthesis of nitroso compound

*Peng Cheng, Mohamed Sarakha, Christine Mousty, Pierre Bonnet and Gilles Mailhot**

Université Clermont Auvergne, CNRS, Clermont Auvergne INP, Institut de Chimie de Clermont Ferrand (ICCF) UMR 6296, BP 80026, F-63171, Aubière cedex, France

* Corresponding author, E-mail address: Gilles.Mailhot@uca.fr.

Abstract

The objectives of this study were to prepare a solid decatungstate-magnetite complex (M-T) for the selective oxidation of aromatic amine compounds in the presence of H_2O_2 . The samples were characterized by X-ray diffraction (XRD), transmission electron microscopy (TEM), scanning electron microscopy (SEM) and X-ray photoelectron spectroscopy (XPS). The characterization results show that the TBADT evenly covers the surface of Magnetite, and the interaction between TBADT and magnetite clearly exists. The effects of mixed mass ratios, concentration of H_2O_2 , M-T complex and pH were investigated. 0.2 g L^{-1} M-T complex shows more efficiency on SPD selective oxidation with a rate constant of $6.03 \times 10^{-3} \text{ min}^{-1}$ in the presence of $5 \text{ mM H}_2\text{O}_2$ at $\text{pH} = 2.5$, comparing with the TBADT/ H_2O_2 and magnetite/ H_2O_2 . The M-T/ H_2O_2 selective oxidation system can effectively oxidize SPD to N-SPD in the pH range of 2.5 to 4.6. The heterogeneous M-T/ H_2O_2 system (TBADT-Magnetite- H_2O_2) appears to be a powerful system for the efficient (until 93%) and selective conversion (until 86%) of amine substrates to their nitroso-derivatives. The system consists on a complex material M-T obtained through interaction between magnetite and TBADT as clearly demonstrated by several characterizations and CV experiments. This interaction between TBADT and magnetite is without any doubt the driving force for the electron transfer to occur. The catalytic system proceeds through an electron transfer process between sulfapyridine and TBADT leading to the formation of the radical cation on the amine group and the reduced species of TBADT. The regeneration of the $\text{W}_{10}\text{O}_{32}^{4-}$ is obtained via a second electron transfer with magnetite owing to such interaction. Thus, during this study we clearly demonstrated that the system M-T/ H_2O_2 is an innovative and powerful process with a high yield of transformation for the generation of

nitroso compounds from amine group. It could be used and implemented easily for the synthesis of such chemical compounds in different applications.

Keywords: Tetra-n-butylammonium decatungstate; Magnetite; Hydrogen peroxide; Selective oxidation; Electron transfer process.

1. Introduction

Nitroso compounds are known to be highly valuable chemical intermediates, which are versatile building blocks in polymer, dyes, agrochemical and pharmaceutical industries [1]. Nitroso compounds can be prepared easily from inexpensive starting material [2]. Among the preparation methods, catalytic oxidation of primary amines appears to be one of the widely used method with a variety of oxidizing agents [3–5]. H_2O_2 known as a milder oxidant is widely used in “green synthesis”, since H_2O and O_2 represent the main reaction products [2,6]. In addition, the less amount of complex mixtures of over-oxidized, non-regio and chemo-selective side products is produced with H_2O_2 [2].

In the last years, the most popular methodology to prepare nitroso compounds was the transition metal-catalyzed oxidation, with tungstate (W) [2,7], molybdenum (Mo) [1,8], vanadium (V) [8], zirconium (Zr) [9], gold (Au) [10] as metal, in combination with the hydrogen peroxide. However, these catalytic oxidation procedures show low efficiency and it might lead to the formation of undesired products such as azo or azoxy derivatives as well as to over-oxidation to the nitro compounds [11]. Nowadays, improving the high activity and selectivity attracts more attentions and immobilization transition metal on a solid support became an interesting and excellent strategy. Moreover, heterogeneous catalysis has a high potential for the recycling of the catalyst. This might be used efficiently for large-scale production. Fountoulaki, et al. studied the catalytic activity of titania-supported gold nanoparticles (Au/TiO_2) for the selective oxidation of amines into nitroso compound using H_2O_2 , and they clearly illustrated that the titania (TiO_2) promotes the selective formation of variety of nitroso arenes in high yields and selectivity, even in a large-scale synthesis [10].

Gkizis, et al. investigated the selective oxidation of various aryl amines using decatungstate supported by mesoporous TiO₂ nanoparticle assemblies in combination with H₂O₂ [7]. The experiment showed, in short reaction time, an exceptionally high activity of these catalyst toward aryl amines oxidation with high yields and selectivity at ambient conditions. As an example, with series of substituted anilines high yield (up to 99%) and selectivity (> 90%) were obtained. These studies show high efficiency and selectivity of transition metal complex catalyzed oxidation. Catalytic oxidation of tungstate-activated complex has received considerable interest owing to their high activity and selectivity. Jadidi Nejad, et al. studied selective oxidation with tungstate-supported silica-coated magnetite nanoparticles [2]. This new complex can be reused for the preparation of nitroso compounds up to 6 times in presence of H₂O₂ with a yield of roughly 70%.

Decatungstate (DT) is a catalyst commonly used often in organic selective synthesis, especially in photo-catalyzed oxidation [12]. In addition, a variety of methods have been developed to prepare heterogeneous DT photocatalysts, including dipping DT on a solid substrate [13], incorporating it into a sol-gel network [14], and combining it on silica [15], connecting to ion exchange resins [16] or polymer membrane [17], respectively. These heterogeneous DT photocatalysis systems are easier to treat and recover catalyst than in a homogeneous DT solution.

Considering the selection of the support material, magnetite as on kind of iron oxide has high value of surface area, and it is often used as support for complex [18]. In addition, previous study proved that the interaction exist between iron oxide and tungstate oxide, which could made the electron more easily transfer from W⁶⁺ sites to Fe³⁺ [19]. Rakshit et, al. indicated that

tungsten forms inner-sphere type bonds on hematite surface and the strength of the interaction increased with decreasing pH using in situ ATR-FTIR [20]. Sallman, et al illustrate that tungsten surface complexation mode on iron oxide can be affected by pH and phosphate ion [21].

Hence, based on the well understanding interaction between these two species, we used, in this study, nano-magnetite (M) as a support of tetra-n-butylammonium decatungstate (TBADT) to synthesis the magnetite-decatungstate (M-T) complex. We used M-T complex to obtain an innovative catalytic system to selectively oxidize amino compounds into nitroso derivatives in the presence of H₂O₂. In addition, the use of heterogeneous complex particles presents the advantage to be easy to recover and reusable. Experiments were performed as a function of various parameters, such as pH, the ratio of TBADT and magnetite, the concentrations of H₂O₂ and M-T complex. In order to identify the reactive species, to understand the mechanism of the reaction and also to optimize i) the efficiency of the oxidation of the substrate to nitroso compound as well as the ii) selectivity in the M-T/H₂O₂ system. Moreover, cyclic voltammetry (CV) experiments were also performed to deeply study the mechanism of this catalytic system.

2. Materials and Methods

2.1. Materials

Sulfapyridine (SPD) ($\geq 99\%$), sodium tungstate (Na₂WO₄·2H₂O), tetra-n-butylammonium bromide (TBABr), hydrochloric acid (HCl), hydrogen peroxide (H₂O₂ 30%), perchloric acid (HClO₄), Iron(III) chloride (FeCl₃·6H₂O), Iron(II) chloride (FeCl₂·4H₂O) and sodium

hydroxide (NaOH) were purchased from Sigma Aldrich and used without any further purifications. Water (Milli-Q) was purified using a reverse osmosis RIOS 5 and Synergy (Millipore) device. Its resistivity was 18 M Ω cm and the dissolved organic carbon (DOC) was estimated to < 0.1 mg L⁻¹.

2.2. Preparation of magnetite, TBADT and M-T complex

The preparation of tetra-n-butylammonium decatungstate (TBADT) was performed using the method described elsewhere [22]. To a boiling sodium tungstate solution (8 g of Na₂WO₄·2H₂O dissolved in 100 mL of ultrapure water) was added 16.75 mL boiling hydrochloric acid (3.0 M). The temperature was maintained at 95 °C for 5 min till the change of the solution color to green. Then, the addition of an aqueous solution (95 °C) of tetra-n-butylammonium bromide (TBABr, 6.4 g/10 mL) leads to the immediate formation of a white precipitate. The mixture was kept under stirring at a temperature of 95 °C. This suspension solution was then filtered after cooling at ambient temperature. The solid was dissolved into dichloromethane and filtered with the aim to remove the insoluble particles. Finally, the obtained dichloromethane solution was gently evaporated at 38 °C to obtain the yellow-green catalyst.

Magnetite was prepared by following the procedure reported in the literature [23]. A mixture of 27.03 g FeCl₃·6H₂O and 19.88 g FeCl₂·4H₂O in 800 mL Milli-Q water was constantly stirred under nitrogen atmosphere. The pH was adjusted by NaOH aqueous solution to 9–10 and the solution volume was adjusted to 1.0 L with Milli-Q water. The reaction vessel

was then kept in the dark for 48 h at 60 °C. After centrifugation, the solid was carefully washed with Milli-Q water until the water conductivity was less than 2.0 $\mu\text{S cm}^{-1}$ and then dried.

The complex magnetite-TBADT (M-T) was prepared by the following procedure. A mixture of 1.0 g tetra-n-butylammonium decatungstate (TBADT) and 2.0 g magnetite was vigorously stirred in 10.0 mL acetonitrile solution. The reaction vessel was then kept in the dark for 24 hours at ambient temperature. After centrifugation the solid was washed with Milli-Q water three times and then dried in the oven at 50 °C. The different ratios of magnetite /TBADT (20/1, 10/1, 5/1, 2/1) were prepared using similar process with the equivalent quantities of magnetite.

2.3. Characterization

In order to characterize the purity of the synthesized TBADT, the UV–Vis absorption spectra of TBADT were obtained using a Varian Cary 300 UV–vis spectrophotometer. The X-ray diffraction (XRD) patterns of TBADT, magnetite and magnetite-TBADT complex (M-T) were collected using a Siemens Model D500 X-ray diffractometer with a diffracted beam monochromator Cu $K\alpha$ source (40 kV-40 mA). Patterns were recorded over the form $2\theta = 5$ to 70° , in steps of 0.08° with a count time of 4 seconds. The FTIR spectra of TBADT, magnetite and M-T complex were recorded with fourier infrared absorption spectrometer (FTIR, Thermo-Nicolet 380) with an advanced diamond ATR accessory (Specac-Golden Gate). For the characterization of the morphology and the size of magnetite, TBADT and M-T complex, the prepared samples were analyzed by transmission electron microscopy (TEM, Hitachi H-7650) at 80 kV acceleration voltage with magnifications up to 200 000. The samples investigated by

TEM were suspended in ethanol and dropped onto a 400-mesh holey carbon-coated copper grid and dried at room temperature. With the objective to check whether TBADT is uniformly covered on the surface of nano-magnetite, SEM-EDS element mapping experiment was used to visually study the distribution of elements recording on scanning electron microscopy (SEM, JEOL JSM-6490LV). X-ray photoelectron spectroscopy (XPS) studies were performed on a Physical Electronics/PHI 5300 X-ray photoelectron spectrometer (S 250 Germany) with a hemispherical analyzer and a single-channel detector that was operated at 300 W (15 kV and 20 mA). Mg KR radiation (1253.6 eV) and pass energies of 89.45 eV for survey scans and 17.9 eV for high-resolution scans were used. The BET surface area analyses of adsorbents were carried out in a Quantachrome Nova 3000e Surface Area Analyzer.

2.4. Catalytic tests: sulfapyridine (SPD) oxidation

The conversion of SPD and the formation yield of its corresponding nitroso compound were performed in a batch experiment at room temperature (roughly 25°C). 20 mg M-T complex was added into the 50 mL of SPD solution (30 µM). The pH of solution was adjusted to 3.0 ± 0.05 using perchloric acid and sodium hydroxide (0.1 M). Hydrogen peroxide was added using a known volume of a concentrated solution, and so with negligible volume, prior to starting the reaction using the magnetic stirrer at 1100 rpm min⁻¹ in order to disperse magnetite particles. Then, aliquots of the mixture were taken at different time intervals and were immediately filtrated using PTFE filters of 0.2 µm (CHROMAFIL® Xtra RC-20/25, 25 mm, Macherey-Nagel).

The effect of ratio magnetite/TBADT (20/1, 10/1, 5/1 and 2/1), pH (1.9, 2.5, 3.0, 4.0, 4.6, 5.2 and 7.2), of H₂O₂ (1, 5, 10, 20, 30, 40 and 50 mM) and M-T (0.1, 0.2, 0.4 and 0.8 g L⁻¹) concentration were also investigated.

2.5. Preparative liquid chromatography, NMR Spectroscopy and HPLC

(1) Preparative liquid chromatography (LC)

Preparative liquid chromatography (LC) was used to separate and purify nitroso-sulfapyridine (N-SPD) from the reaction mixture. This separation was obtained using preparative LC (Varian Prep Star 218) equipped with a Varian Pro Star 335 photodiode array detector and an auto sampler. The column was a C18 Varian dynamax Microsorb 60-8 column (250 mm × 41.4 mm, 8 μm particle size). The analyses were performed using an eluent composed of acetonitrile (ACN) and water with 0.1 % of trifluoroacetic acid (TFA), in an isocratic mode at 25/75% and at a flow rate of 40 mL min⁻¹. N-SPD was finally collected after the evaporation of the solvent.

(2) NMR spectroscopy

For the characterization and also the quantification, NMR spectroscopy was used. 100 μL at 5 mM of 3-(Trimethylsilyl) propionic acid-d₄ sodium salt (TSPd₄) in D₂O solution as a reference was added in 900 μL concentrated pure N-SPD solution. NMR data were obtained with a Bruker Advance III 500 MHz UltrashieldTM plus spectrometer (equipped with 5 mm TCI-13C-15N-2H Prodigy Cryoprobe). All spectra were recorded in 600 μL of H₂O (10% D₂O). Chemical shifts (δ) are expressed in ppm relative to residual peak 4.79 (ppm) of water.

The concentration of nitroso-sulfapyridine was calculated via the following equation (1):

$$[\text{N-SPD}] = \frac{9A_0 \times [\text{TSPd}_4]}{b \times A_{\text{ref}}} \times 1.1 \quad (1)$$

Where [N-SPD] is the concentration of nitroso-sulfapyridine (N-SPD), A_0 is the area of nitroso-sulfapyridine resonance in the ^1H NMR spectrum, $[\text{TSPd}_4]$ is the concentration of the reference, A_{ref} is the area of reference resonance in the ^1H NMR spectrum, b is the number of protons of N-SPD in the signal integrated, and 9 is the number of protons resonating of TSPd_4 at 0 ppm. The 1.1 factor is owing to dilution of TSPd_4 .

(3) High Performance Liquid Chromatography (HPLC)

The conversion of SPD and the formation of nitroso-sulfapyridine (N-SPD) percentages were obtained by HPLC (Shimadzu NEXERA XR HPL) equipped with a photodiode array detector and an auto sampler. The column was a Macherey Nagel EC 150/2 NUCLEODUR C18ec (150 mm \times 2 mm, 2 μm particle size). The analyses were performed using acetonitrile (ACN) as mobile phase and water with 0.5 % of phosphoric acid at a flow rate of 0.40 mL min^{-1} . The elution was performed using the following gradient: 5 % of ACN for 2.5 min, linear increase of ACN to 40 % in 4.5 min, then increase of ACN to 95 % in 1.5 min, 95 % of ACN for 1 min and decrease of ACN to 5 % in 0.5 min.

(4) Ultra-high performance liquid chromatography mass spectrometry (UPLC-MS)

The identification of all the byproducts was performed using high resolution mass spectrometry (HRMS) constituted of an Orbitrap QExactive (ThermoScientific) coupled to an

ultra-high performance liquid chromatography (UHPLC) instrument Ultimate 3000 RSLC (ThermoScientific). Analyses were carried out in both negative and positive electrospray modes (ESI⁺ and ESI⁻). Sulfapyridine and its byproducts were separated using the same elution gradient as previously indicated. The column was a Macherey Nagel EC 150/2 NUCLEODUR C18ec (150 mm × 2 mm, 2 μm particle size) and the flow rate was set at 0.40 mL min⁻¹.

2.6. Electrochemical measurement

Cyclic voltammetry (CV) experiments were carried out with a potentiostat Autolab PGSTAT204 controlled by the NOVA software (Metrohm) equipped with a three-electrodes system. An Ag-AgCl electrode was used as the reference electrode and a platinum wire as the auxiliary electrode. The working electrodes were a pyrolytic graphite electrode (PGE, A = 0.07 cm²) modified with a TBADT coating (T-PGE), with a magnetite coating (M-PGE), and with a mixed magnetite and TBADT coating (M-T-PGE) prepared by adapted solvent casting methods. Before its use, the electrode surface was polished with 1 μm diamond paste and washed with acetone and then it was polished again with 0.04 μm alumina slurry to be finally rinsed with ethanol and water. To prepare the T-PGE, a TBADT solution was prepared with 40.0 mg of TBADT diluted in 1.0 mL acetonitrile by sonication for 2 minutes. The 10 μL TBADT solution was deposited onto the polished PGE then air dried for 120 min. The M-PGE was also prepared using a solvent casting method [24]. A suspension was prepared with 80 mg of magnetite dispersed in 1.0 mL ethanol by sonication for approximately 30 minutes. Then 10 μL nafion solution (5%, Sigma Aldrich) was added in the 1.0 mL magnetite suspension followed by sonication for 15 more minutes. 10 μL of the slurry was deposited onto the polished

PGE then air dried for 120 minutes. Finally, for the M-T-PGE a suspension was prepared in a centrifuge tube with 40.0 mg of TBADT and 80.0 mg of magnetite (TBADT/M = 1/2) dispersed in 1.0 mL acetonitrile for 24 hours on a rotating reactor (45 rpm min^{-1}) at ambient temperature. After centrifugation the solid was washed three times with acetonitrile and Milli-Q water and then dry in the oven at $50 \text{ }^\circ\text{C}$. After getting the fresh M-TBADT mixture (110 mg), 1 mL ethanol was added in this centrifuge tube with sonication for approximately 30 min, then 10 μL nafion solution (5%, Sigma Aldrich) was added in the 1.0 mL M-TBADT suspension followed by sonication for 30 min more. 10 μL of the slurry was deposited onto the polished PGE then air dried for 120 minutes. Cyclic voltammograms were recorded under inert atmosphere (Ar) at a scan rate (ν) of 10 mV s^{-1} in a 0.1 M LiClO_4 (at pH 3.5) in presence or absence of H_2O_2 (5 mM) with a T-PGE, M-TBADT or M-T-PGE electrode, respectively. The CVs shown correspond to the 10th cycle. Recycle of M-TBADT-PGE electrode was also performed in the same parameters, each time with fresh LiClO_4 electrolyte solution.

3. Result and Discussions

3.1. Characterization

(1) UV-Vis spectrometer of TBADT

The purity of tetra-n-butyllummonium decatungstate (TBADT) can be confirmed by the UV-Vis spectra shown in **Fig. S1**. It shows that TBADT at low concentration exhibits two characteristic peaks in the range of 250-350 nm in UV-vis spectra, in agreement with the previous works [25,26]. The peak at 320 nm is ascribed to oxygen to tungsten charge transition

(LMCT) of four linear W-O-W bridge bonds in the $W_{10}O_{32}^{4-}$ structure [25–27] and the other weak peak at 264 nm likely corresponds to LMCT process of the unstable structural subunit $[W_5O_{16}]^{2-}$ [28]. The molar absorption coefficient of TBADT ($W_{10}O_{32}^{4-}$) at 320 nm of $11983 \text{ M}^{-1} \text{ cm}^{-1}$ is in perfect agreement with the published literature data [29–31]. This can illustrate that TBADT has high purity.

(2) XRD

X-ray diffractometer is used to analyze qualitatively the phase composition of the TBADT, magnetite and M-T complex before and after reaction. As shown in the XRD patterns (**Fig. 1**), magnetite (black curve) presents several peaks at $2\theta = 18.44^\circ, 30.30^\circ, 35.67^\circ, 37.18^\circ, 43.32^\circ, 53.78^\circ, 57.29^\circ, 62.95^\circ$. These are in perfect agreement with those reported in a standard pattern of PDF-#89-6466 leading us to the conclusion that magnetite was successfully synthesized. The green curve represents the XRD pattern of the pure TBADT, which shows two high intensity peaks at 7.33° and 7.62° and several small peaks from 5° to 40° , which is quite similar to the previous study [32]. For the XRD pattern of M-T complex (before reaction), the characteristic peaks of magnetite and TBADT can be observed, which means that TBADT was successfully attached to the surface of magnetite. In addition, the intensity of TBADT in M-T complex after reaction did not decrease, which indicate the immobilization of TBADT is quite stable on the surface of magnetite. While the interaction between magnetite and TBADT is not obviously shown in XRD patterns, so more characterization should be used to study.

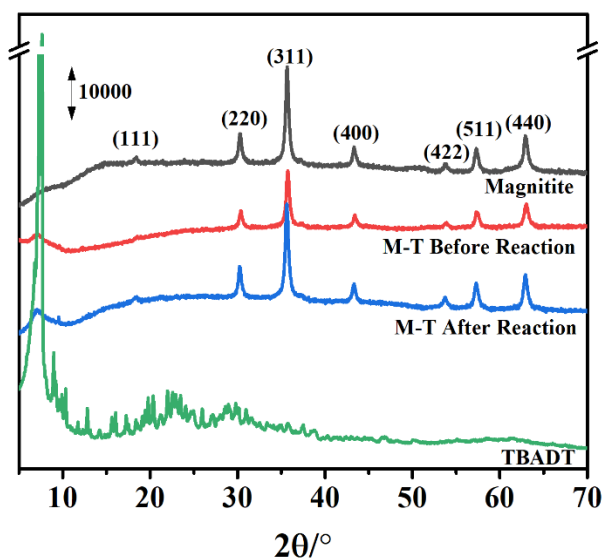


Fig. 1. XRD patterns of TBADT, magnetite and M-T complex before and after reaction.

(3) FTIR

In order to confirm that the interaction existing between magnetite and TBADT, the Fourier infrared spectroscopy (FTIR) was used to characterize the M-T complex. **Fig. 2** shows the FTIR spectra of TBADT, magnetite and M-T complex. The main vibration bands (**in curve a**) of tetra-n-butylammonium decatungstate (TBADT) are observed at 992, 953, 944 and 571 cm^{-1} corresponding to the stretching vibration of the $\text{W}=\text{O}_t$ bond (O_t - terminal oxygen atoms), and at 886 and 776 cm^{-1} are due to the vibrations of $\text{W}-\text{O}_b-\text{W}$ (O_b - corner-sharing-oxygen-bridge) and $\text{W}-\text{O}_c-\text{W}$ (O_c - edge-sharing oxygen-bridge) [33]. Additionally, three characteristic vibrations resulting from tetra-n-butylammonium (TBA^+) between 1600 to 1100 cm^{-1} are also observed [34]. The vibrations at a range of 2800 - 3000 cm^{-1} are similar to the previous study [33], which is due to C-H bond stretching [14]. In the **curve b**, the band at 577 cm^{-1} can be assigned to the Fe-O stretching mode of the tetrahedral and octahedral sites [35]. The Fe-OH wide vibration band is ranged at 612 - 626 cm^{-1} [36]. By comparing the spectrum of the M-T

complex with TBADT, a blue shift (about 19 cm^{-1}) can be noted for the W-O_c-W bond (795 cm^{-1}) in **curve c**, which corresponds more likely to the interaction between TBADT and magnetite at edge sharing oxygen-bridge.

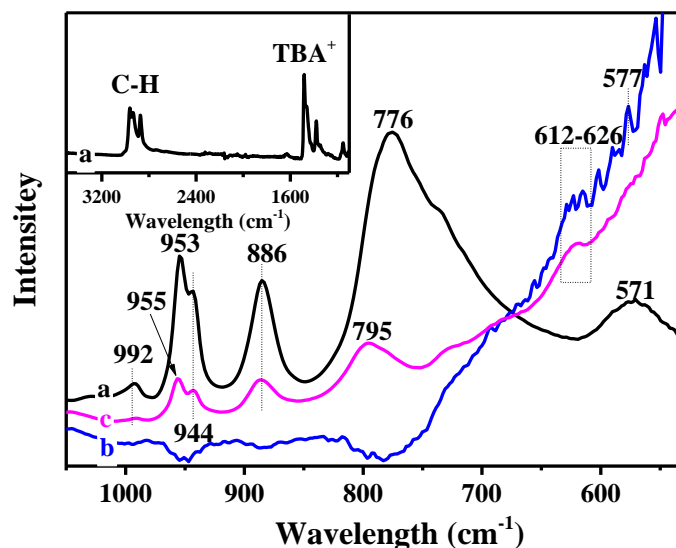


Fig. 2. The FTIR spectra of TBADT(a), magnetite (b) and M-T complex (c). Insert shows the FTIR spectrum of TBADT at the range of $1100 - 3500\text{ cm}^{-1}$

(4) XPS

In order to confirm the interaction between magnetite and TBADT and to determine the chemical compositions and electronic structure of M-T complex, XPS measurements were performed on magnetite, TBADT and M-T complex (before and after reaction). A typical full XPS spectrum of M-T complex (before reaction) is shown in **Fig. 3(a)**. The spectrum indicates the presence of carbon, oxygen, iron, tungsten, arising from internal magnetite and external TBADT. This shows that the M-T complex has no other contaminants, which is consistent with the results of XRD and FTIR. Because the atomic sensitivity factor of Fe is much higher than

those of C and O, the negligible and weak peaks of Fe imply that the Fe_3O_4 is uniformly and continuously coated by TBADT shells [37].

High resolution Fe 2p spectrum of M-T complex (before reaction) is shown in **Fig. 3(b)**. Two peaks at 710.16 and 724.18 eV correspond to Fe $2p_{3/2}$ and Fe $2p_{1/2}$ peaks of Fe_3O_4 , respectively [38]. The spin-orbit split Fe 2p peaks are broad due to a small chemical shift difference between Fe^{2+} and Fe^{3+} present in Fe_3O_4 [39]. In **Fig. 3(b)**, the Fe $2p_{3/2}$ and Fe $2p_{1/2}$ spectra were both well fitted with two peaks respectively. For the Fe $2p_{3/2}$ spectrum, a major peak at 711.25 eV and a minor one at 709.80 eV are observed, which can be ascribed to Fe^{3+} and Fe^{2+} , respectively. In addition, like the Fe $2p_{3/2}$ spectrum, a major peak at 724.50 eV and a minor one at 723.09 eV were observed in Fe $2p_{1/2}$ spectrum, which can be ascribed to Fe^{3+} and Fe^{2+} , respectively. This result is in accordance with the previous research [40]. $\text{Fe}^{3+}/\text{Fe}^{2+}$ ratio is calculated from the corresponding area under the spectrum of Fe $2p_{3/2}$ and Fe $2p_{1/2}$ to be 2:1. This indicates that the magnetite is of high purity, which is consistent with XRD result. **Table 1** shows the ratios of Fe^{2+} and Fe^{3+} in magnetite and M-T (before and after reaction) and the fitting peak position of Fe^{2+} and Fe^{3+} in Fe $2p_{3/2}$ and Fe $2p_{1/2}$ spectra respectively. It can be clearly observed that the $\text{Fe}^{3+}/\text{Fe}^{2+}$ ratio and peak position in M-T complex (before and after reaction) and pure magnetite show no difference. This illustrates that the chemical composition and properties of magnetite have not significantly changed after M-T complex synthesis and after reaction.

High resolution O 1s spectrum of M-T complex (before reaction) is shown in **Fig. 3(c)**. The O 1s spectrum can be divided into three component peaks centered at 529.25, 530.00 and 531.65 eV. **Table 2** shows the fitting peak position of O 1s in TBADT, magnetite and M-T

complex (before and after reaction). In **Table 2**, the O 1s peak of TBADT appears at 528.98 eV [12,26] and those of magnetite concentrate at 530.00 and 531.48 eV correspond to Fe-O in magnetite phase [41,42] and the hydroxyl bonding (Fe-OH) on the surface of magnetite, respectively [42]. While in M-T complex, a small shift at O 1s peak of W-O (increased 0.26-0.27 eV) and Fe-OH (increased 0.16-0.17 eV) can be observed (The data was red bold marked in **Table 2**), comparing the peaks position of M-T complex with pure magnetite and TBADT. This small shift could be due to the interaction between TBADT and the iron hydroxyl group on the surface of magnetite. This result is consistent with above FTIR results. In addition, this interaction is established by oxygen atoms, and iron atoms and tungsten atoms are combined with oxygen atoms. This can be clearly inferred from the results of infrared and XPS.

In **Fig. 3(d)**, High resolution W 4f spectrum is exhibited. The two peaks of W 4f_{5/2} and W 4f_{7/2} in TBADT appear at 37.01 and 34.92 eV, respectively [12,26], which show no difference with pure TBADT (**Table S1**). Hence, the results of XPS confirm the interaction between TBADT and magnetite, which is consistent with the FTIR results.

Moreover, the small shift of O 1S spectrum in the M-T complex after reaction can still clearly be observed via XPS, which means this interaction still makes Fe and W atom combine with each other. This suggests that this interaction is quite strong. Rakshit et, al. indicated that tungsten forms inner-sphere type bonds on hematite surface and the strength of the interaction can be affected by pH, which studied using in situ ATR-FTIR technique [20].

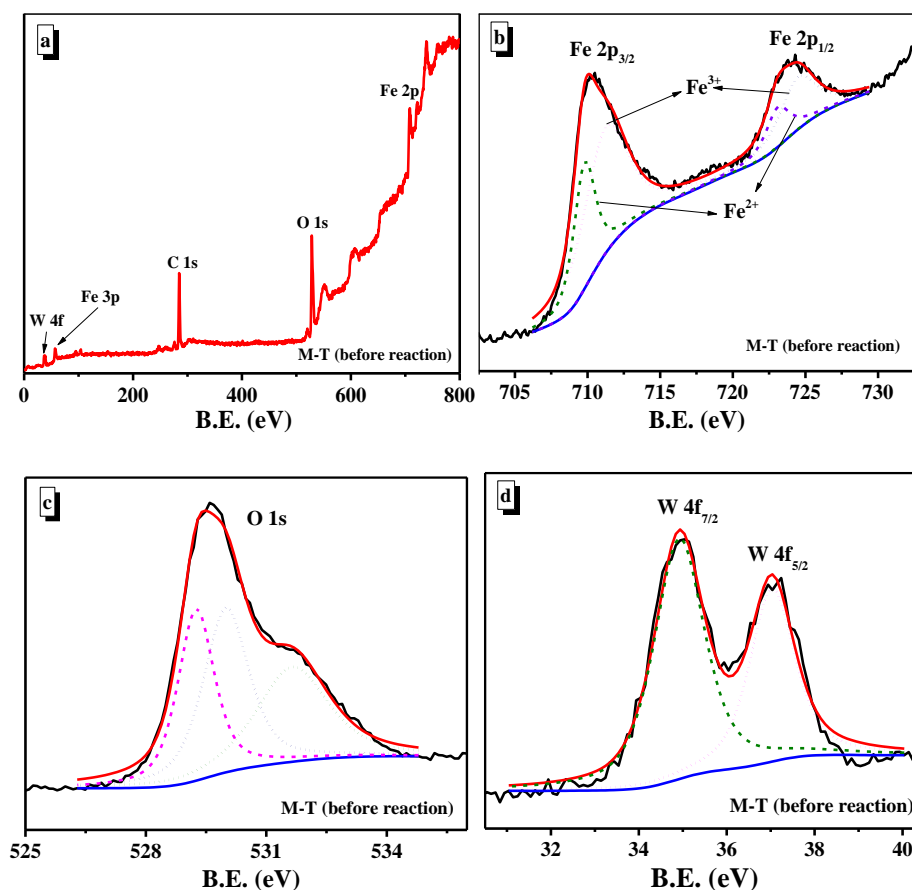


Fig. 3. The XPS profile of M-T complex (before reaction) (a), and the high-resolution spectra of Fe 2p (b), O 1s (c) and W 4f (d)

(5) TEM

The morphology information was obtained by the transmission electron microscopy (TEM). The **Fig. S2** shows the TEM images of magnetite, TBADT and the M-T complex before and after reaction. The TEM image (**Fig. S2(a)**) of magnetite shows that it has a globosity morphology with the particle diameter ranging from 20 to 40 nm. This leads us to the conclusion that we are dealing with a nano magnetite material which presents more likely a large surface area ($74 \pm 1 \text{ m}^2 \text{ g}^{-1}$). All these analyses (XRD, FTIR, XPS and TEM) show that our magnetite has no impurity. **Fig. S2(b)** shows the TEM image of TBADT, TBADT presents a short rod-

like morphology with a length of 100 nm. **Fig. S2(c)** shows the M-T complex before the reaction. The morphology of M-T complex keeps the same with the morphology of magnetite, while the short rod-like TBADT is not observed in the M-T complex. This is because that in the preparation process of the M-T complex, TBADT is first dissolved in acetonitrile, and then individual clusters of TBADT will be wrapped on the surface of the magnetite through the interaction (inner-sphere type bonds) with magnetite. So we can infer that M-T has a core-shell structure with magnetite as the core and TBADT wrapped in the outer layer. In addition, the morphology of M-T complex does not change after the reaction (**Fig. S2 (c)**), which proves that the M-T complex has a certain degree of durability.

Table 1. The ratios of Fe²⁺ and Fe³⁺ in magnetite and M-T complex. The fitting peak position of Fe²⁺ and Fe³⁺ in Fe 2p_{3/2} and Fe 2p_{1/2} spectrum respectively.

Sample	Atomic ratios			Peak position (eV)			
				Fe 2P _{1/2}		Fe 2P _{3/2}	
	Fe ³⁺	Fe ²⁺	χ^2	Fe ³⁺	Fe ²⁺	Fe ³⁺	Fe ²⁺
magnetite	0.668	0.332	3.74	724.46	723.05	711.29	709.83
M-T (before reaction)	0.667	0.333	3.18	724.50	723.09	711.25	709.80
M-T (after reaction)	0.667	0.333	5.70	724.44	723.03	711.25	709.79

χ^2 represent chi-square distribution, χ^2 -distribution.

Table 2. The fitting peak position of O 1s in TBADT, magnetite and M-T complex

Sample	O 1s Peak position (eV)			χ^2
	W-O	Fe-O	Fe-OH	
TBADT	528.98	-	-	4.04
Magnetite	-	530.00	531.48	13.12
M-T (before reaction)	529.25	530.00	531.65	7.43
M-T (after reaction)	529.24	530.00	531.64	10.93

χ^2 represent chi-square distribution, χ^2 -distribution.

(6) SEM-EDS

In order to verify whether TBADT is uniformly covered on the surface of nano-magnetite, SEM-EDS element mapping technology is used to visually study the distribution of elements. **Fig. 4** shows the SEM image and SEM-EDS element mapping of M-T complex before and after reaction. The elements such as Fe, O, and W have the same distribution both in the M-T complex before and after reaction, indicating that TBAD is evenly distributed on the surface of nano-magnetite. The W element did not decrease or even disappear after the reaction, which shows that the M-T material has a certain degree of stability. Hence, this result illustrates that the interaction between TBADT and magnetite can ensure the strength of the connection between the two substances.

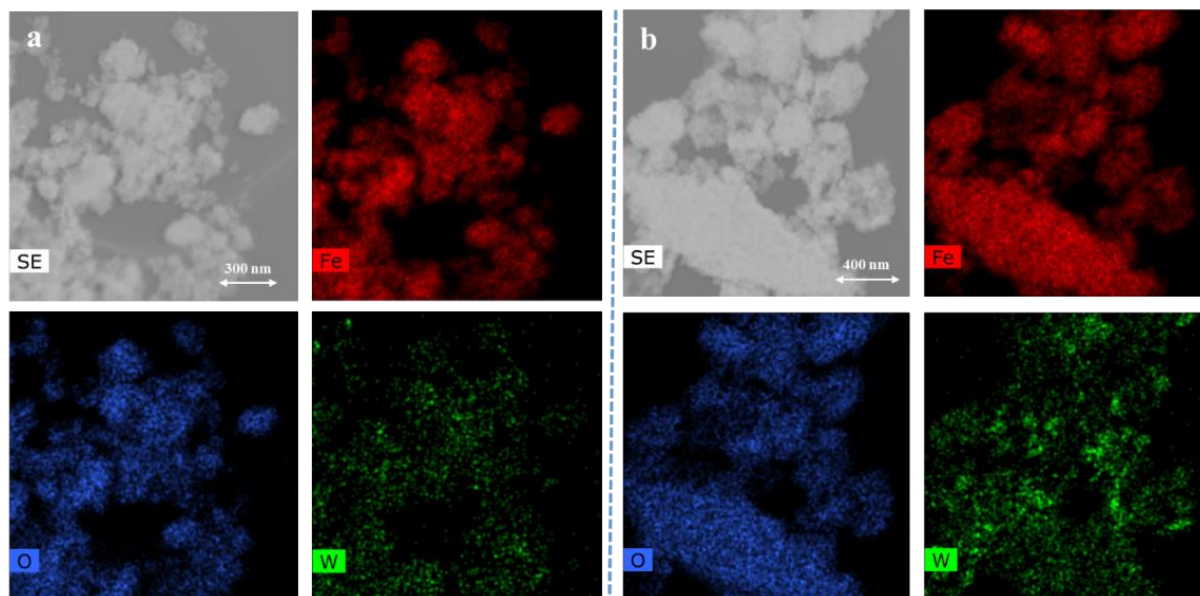


Fig. 4. SEM images and SEM-EDS element mapping of M-T complex before and after reaction

3.2. Comparison experiment of sulfapyridine conversion

The synthesized complex M-T associated with hydrogen peroxide was used for the oxidation of sulfapyridine (SPD) and the efficiency was evaluated. With this objective, aqueous solution of SPD at a concentration of $30.0 \mu\text{M}$ was mixed first with M-T₂₋₁ and H₂O₂ (5.0 mM) at pH =3.0. For the sake of comparison, experiments were also performed with H₂O₂ alone, magnetite/H₂O₂, TBADT/H₂O₂ under the same experimental conditions. **Fig. 5,** show that in the presence of hydrogen peroxide alone (5.0 mM), almost no SPD oxidation (<1.5% within 2 hours) was obtained under our experimental conditions. Within the same time, the conversion was estimated to 0.4 % with TBADT/H₂O₂ ($0.4 \text{ g L}^{-1}/5.0 \text{ mM}$) and to 9.3 % magnetite/H₂O₂ ($0.4 \text{ g L}^{-1}/5.0 \text{ mM}$). However, in the presence of 0.4 g L^{-1} synthesized M-T₂₋₁ (Magnetite/TBADT = 2/1) complex and 5.0 mM of H₂O₂, the conversion reached 75.8 % within 2 hours which clearly demonstrates the important and interesting oxidation ability of the M-

T/H₂O₂ system toward SPD. Under our experimental conditions, the conversion appears to follow a pseudo first order kinetics and the rate constant was estimated to $1.20 \times 10^{-2} \text{ min}^{-1}$. While performing the experiments in the absence of hydrogen peroxide, we can easily evaluate the SPD adsorption ability of the solid support. As shown in **Fig. S3** no adsorption of SPD was observed on TBADT, magnetite and M-T within 2 hours.

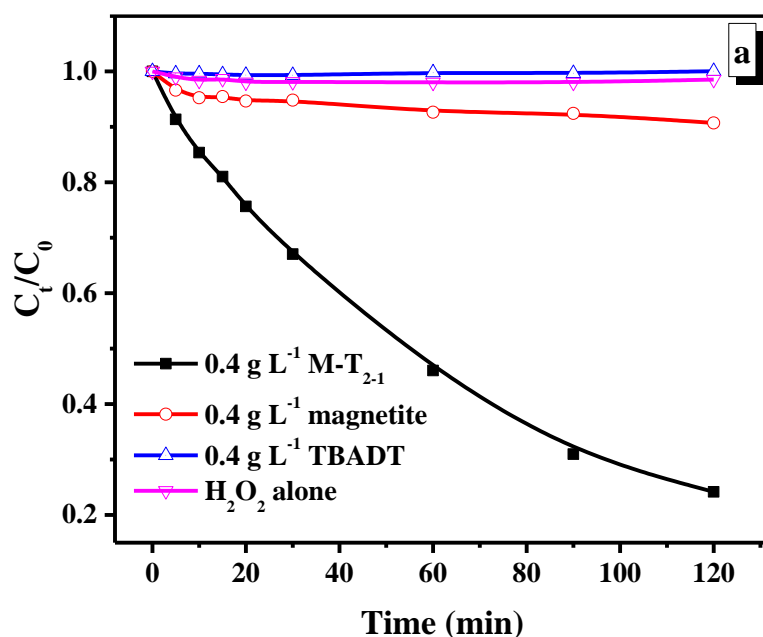


Fig. 5. Kinetics of sulfapyridine (SPD) disappearance under various experimental conditions.

$$[\text{SPD}] = 30 \mu\text{M}; \text{H}_2\text{O}_2 = 5.0 \text{ mM}; \text{pH} = 3.0.$$

The generated products in the M-T/H₂O₂ systems were analyzed by HRMS/UHPLC and NMR. The disappearance of sulfapyridine leads to the formation of mainly three products among them the nitroso-sulfapyridine (N-SPD) ($m/z_{[\text{M}+\text{H}^+]} = 264.0435$ (**Table S2**)) and, the hydroxyl-sulfapyridine product (P1) which was mainly formed in magnetite/H₂O₂ system, more likely owing the classical Fenton and Fenton-like processes²⁷. As a contrary, the N-SPD is the main product formed in the M-T/H₂O₂ system leading us to the conclusion that the simultaneous

presence of magnetite and TBADT greatly promotes the amino selective oxidation into nitroso compound. The NMR spectrum confirmed this result (**Fig. S4**). The quantification of nitroso-sulfapyridine was performed by using NMR technique according to the procedure given in the materials and methods section. The average concentration of N-SPD calculated after quantification by NMR is 52.03 μM , and the relative standard deviation is (**RSD**) 4.8% (**Table S3**).

In order to optimize such oxidation process of SPD, the effect of various ratio of magnetite/TBADT (20/1, 10/1, 5/1 and 2/1), concentration of H_2O_2 (1, 5, 10, 20, 30, 40 and 50 mM), pH (1.9, 2.5, 3.0, 4.0, 4.6, 5.2 and 7.2), and amount of M-T (0.1, 0.2, 0.4 and 0.8 g L^{-1}) were investigated.

3.3. Effect of main experimental parameters

(1) Effect of the ratio between magnetite and TBADT

To study the effect of the different ratio of magnetite and TBADT on SPD conversion, we prepared different M-T samples at a range of the ratio of magnetite and TBADT from 20/1 to 2/1 (M/T = 20/1, 10/1, 5/1 and 2/1). In **Fig. S5**, SPD conversion percentage increases from 7.8 to 51.5% with the increase of the percentage of TBADT in M-T complex from 4.8% to 33.3%. Under these conditions, the pseudo first order rate constant increased from 0.69×10^{-3} to $6.3 \times 10^{-3} \text{ min}^{-1}$ (**Table 3**). Moreover, concerning the yield of nitroso derivative (N-SPD), **Table 3** clearly shows it remains constant to roughly 78%-86%. Such results are clearly in agreement with the fact that M-T complex presents a good and interesting selectivity for the oxidation of

SPD. For the coming experiments, M-T with a ratio at 2/1 which is marked as M-T₂₋₁ was chosen.

(2) Effect of pH

The solution pH is a very important parameter for selective oxidation of sulfapyridine. This was studied within the range 1.9 - 7.2 at constant concentration of M-T₂₋₁ (0.2 g L⁻¹), H₂O₂ (5 mM) and SPD (30.0 μM). As observed in **Fig. S6**, the efficiency of SPD conversion decreases with the increase of the solution pH. Meanwhile, the conversion percentage of SPD decreases also when the pH increases (**Table 4**). The conversion was estimated to around 58.9% with a rate constant of $7.31 \times 10^{-3} \text{ min}^{-1}$ at pH = 1.9 and 36.6% at pH = 4.0 with a rate constant of $3.66 \times 10^{-3} \text{ min}^{-1}$. It dropped rapidly to roughly 7.2 % at pH = 7.2 owing more likely to the lower stability of decatungstate at pH > 5.5, and also due to the interaction between Fe and W decreases when pH increases [20]. On the other hand, the protolytic equilibrium of SPD (pK_a = 8.43) may also interfere in the process leading to a change in the solution composition and thus, different reaction processes could occur with the various forms of SPD. Concerning the yield of N-SPD, it is estimated to 82.55 % at pH = 2.5 and small decrease can be observed for pHs between 3.0 and 4.6 (around 75%). While the yield of N-SPD formation (%) is 0% at pH = 1.9, which is due to the excessive oxidation of amino compounds to nitro compounds.

(3) Effect of H₂O₂ concentration

The effect of H₂O₂ was investigated up to the concentration of 50 Mm (**Fig. S7**). As observed in **Table 5**, SPD conversion percentage reaches a maximum 36.6% (with a rate

constant of $3.66 \times 10^{-3} \text{ min}^{-1}$) with H_2O_2 concentration of 5.0 mM. The SPD conversion percentage levelled off at roughly 35% within the range of 5-20 Mm with a slight increase of the rate constant that reaches $3.82 \times 10^{-3} \text{ min}^{-1}$. However, for higher concentrations, a decrease of the yield was observed (roughly 25 %) with a rate constant of about $2.60 \times 10^{-3} \text{ min}^{-1}$. Concerning the selectivity of the reaction, namely nitroso-sulfapyridine (N-SPD) formation, its yield increases from 65.5% to 83.7% when H_2O_2 concentration increases from 1.0 to 20.0 mM. In addition, unlike the trend of SPD conversion percentage, the yield of N-SPD remains constant at about 85% when H_2O_2 concentration increases from 30.0 to 50.0 mM

Table 3. Effect of the ratio between magnetite and TBADT on SPD conversion and N-SPD production in 2h

M-T complex	20-1	10-1	5-1	2-1
Rate constant (min^{-1})	0.69×10^{-3}	3.00×10^{-3}	4.53×10^{-3}	6.03×10^{-3}
Conversion (%)	7.8	29.1	40.7	51.5
Yield of N-SPD formation (%)	78.6	86.3	86.0	82.6

$[\text{M-T}] = 0.2 \text{ g L}^{-1}$; $[\text{H}_2\text{O}_2] = 5.0 \text{ mM}$; $[\text{SPD}] = 30 \text{ }\mu\text{M}$; $\text{pH} = 2.5$.

Table 4. Effect of pH on SPD conversion and N-SPD production in 2h

pH	1.9	2.5	3.0	4.0	4.6	5.2	7.2
Rate constant ($\times 10^{-3} \text{ min}^{-1}$)	7.30	6.03	5.84	3.66	2.09	2.07	0.68
Conversion (%)	58.9	51.5	49.8	36.6	21.9	21.8	7.2
Yield of N-SPD formation (%)	0	82.6	75.8	74.6	75.0	6.1	0

$[\text{M-T}_{2-1}] = 0.2 \text{ g L}^{-1}$; $[\text{H}_2\text{O}_2] = 5.0 \text{ mM}$; $[\text{SPD}] = 30 \text{ }\mu\text{M}$.

Table 5. Effect of H₂O₂ concentration on SPD conversion and N-SPD production in 2h

[H ₂ O ₂] (mM)	0	1.0	5.0	10.0	20.0	30.0	40.0	50.0
Rate constant ($\times 10^{-3} \text{ min}^{-1}$)	0	1.55	3.66	3.7	3.8	2.6	2.60	2.62
Conversion (%)	0	16.4	36.6	35.3	36.6	26.7	25.6	26.6
Yield of N-SPD formation (%)	0	65.5	74.6	74.3	83.7	85.1	85.0	84.5

[M-T₂₋₁] = 0.2 g L⁻¹; [SPD] = 30 μM; pH = 4.0.

(4) Effect of the amount of M-T complex

The effect of the amount of synthesized M-T was investigated within the range of 0 - 0.8 g L⁻¹ (**Fig. S8**). The SPD conversion percentage increases to reach 93.4% as the M-T concentration increases from 0 to 0.8 g L⁻¹ (**Table 6**). Under these conditions the rate constant increased from 2.5×10^{-3} up to $22.5 \times 10^{-3} \text{ min}^{-1}$. This effect shows an interesting benefit for the oxidation of SPD. Moreover, an increase of the yield for nitroso-sulfapyridin formation is also observed (roughly 78.7% for 0.8 g L⁻¹ of M-T), indicating an important selectivity of the process under these conditions.

Table 6. Effect of H₂O₂ concentration on SPD conversion and yield in 2h

[M-T ₂₋₁] (g L ⁻¹)	0	0.1	0.2	0.4	0.8
Rate constant ($\times 10^{-3} \text{ min}^{-1}$)	0	2.5	5.8	12.	22.5
Conversion (%)	1.5	27.0	49.8	75.8	93.4
Yield of N-SPD formation (%)	0	66.2	66.8	73.8	78.7

[H₂O₂] = 5.0 mM; [SPD] = 30 μM; pH = 3.0

3.4. Investigation of Electrochemical behavior of M-T, magnetite and TBADT

In order to confirm the possible interaction between TBADT and magnetite that leads to an efficient conversion SPD, we have compared, the electrochemical behavior of TBADT deposited on a pyrolytic carbon electrode (T-PGE), magnetite modified electrode (M-PGE), and mixed M-T modified electrode (M-T-PGE) in the absence and the presence of H_2O_2 .

Fig. 6 shows cyclic voltammograms (CVs) of T-PGE (A) and M-T-PGE (B) in the absence and in the presence of H_2O_2 . The dash line represents the baseline recorded at the bare PGE in 0.1 mM LiClO_4 electrolyte at pH 3.5 under argon, showing no interference with oxygen reduction.

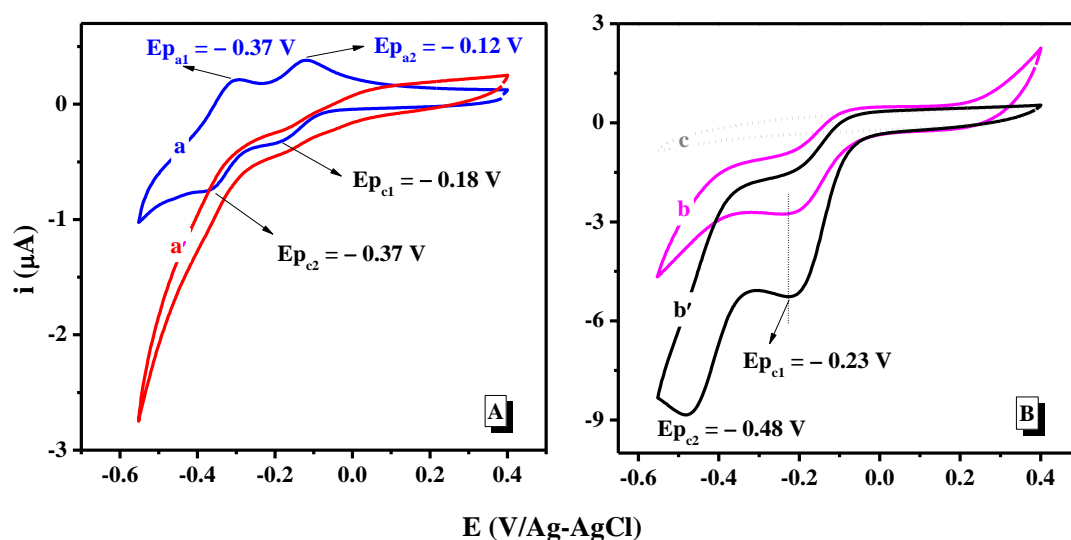
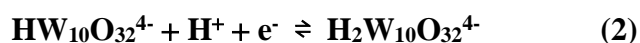


Fig. 6. The CVs of A) T-PGE and B) M-T-PGE in the absence (a and a') or presence of 5 mM (b, b') H_2O_2 in 0.1 M LiClO_4 (pH = 3.5) under Ar, $v = 10 \text{ mV s}^{-1}$. The dash line (curve c) corresponds to the PGE baseline in 0.1 M LiClO_4 pH 3.5 under Ar.

The CV of TBADT deposited on PGE (**Fig. 6 A, curve a**) exhibits two reversible signals. The potential of the first cathodic peak ($\text{Ep}_{c1} = -0.18 \text{ V/Ag-AgCl}$) and the second one ($\text{Ep}_{c2} = -$

0.37 V/Ag-AgCl) are consistent with the values, reported in the literature [27,43] for sodium decatungstate (NaDT) in aqueous solution. While Yang, et al reported the first cathodic at 0.06 V/ SCE for TBADT dissolved in a mixed solvent (HCl (12 M, 1.0 mL) and MeCN (9.0 mL)) [12], which is due the different polarity of solvent [44]. The peak separation ($\Delta E = E_{pc} - E_{pa}$) are 60 mV for the first and the second redox couples, showing a good reversibility of the electron transfers which can be assigned to the following reactions:

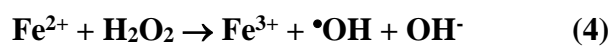


The curve **a'** in **Fig. 6A** corresponds to the electrochemical signal of TBADT in the presence of 5 mM H_2O_2 . The shape of the voltammograms changes when hydrogen peroxide (H_2O_2) was added in the electrolyte solution. Although the two cathodic peaks were not obvious, the current intensity of these two peaks seems to increase slightly (current at $E_{pc1} = -0.18\text{V}$ and $E_{pc1} = -0.37\text{V}$ are $-0.43 \mu\text{A}$ and $-1.10 \mu\text{A}$, respectively), while the corresponding anodic peak current decreased. The electrocatalytic reaction with H_2O_2 seems to be less efficient than with NaDT in solution for which the electrocatalytic waves appear on both redox couples of NaDT [to be published].

The curve **b** in **Fig. 6B** represents the CV of the M-T-PGE in 0.1 mM LiClO_4 electrolyte at pH 3.5 under argon. A cathodic peak can be observed at $E_{pc1} = -0.23 \text{ V/Ag-AgCl}$ ($I_{c1} = -2.77 \mu\text{A}$). The presence of H_2O_2 in the electrolyte causes an increase of the cathodic current ($I_{pc1} \times$ approximately 2 times) and the appearance of a second irreversible peak at $E_{pc2} = -0.48 \text{ V/Ag-AgCl}$. The shape of those catalytic waves is similar to those we have previously reported using

M-PGE and NaDT in solution [to be published]. Even if the peak intensities cannot be compared directly, since the same amount of TBADT was not deposited on both electrode surface, it was notable that the catalytic currents in the presence of H₂O₂ obtained at M-T-PGE was much higher than the one recorded at the T-PGE. This indicates that there is an interaction between TBADT and magnetite leading to an enhancement of the electrocatalytic process.

For comparison, **Fig. S9** shows the CVs recorded using a M-PGE with and without 5.0 mM H₂O₂ added in the electrolyte solution. With M-PGE, a well-defined cathodic peak is clearly observed at -0.08 V which is owing to an electro-Fenton process [45,46]. This process can be expressed by equations (3 and 4):



However, in this case the catalytic current ($I_{p_c} = 2.05 \mu\text{A}$) is lower than with M-T-PGE. This means that with the mixture of M-T particles on the electrode surface, the electrocatalytic process for H₂O₂ reduction is definitively improved. The mechanisms of these electrocatalytic processes are probably not the same on both type of electrodes (M-PGE and M-T-PGE), implying in the latter case, iron species from magnetite in interaction with TBADT, as suggested by Dong and Liu for Dawson-type tungstatephosphonate anion [47].

The current stability of M-T-PGE was investigated in CV in absence (a) and in presence of H₂O₂ (b) for 10 potential cycles (**Fig. S10**). In absence of H₂O₂, a cathodic peak at -0.18 V/Ag-AgCl ($I_{p_{c1}} = -7.87 \mu\text{A}$) can be observed in the first cycle and then the signal was stabilized with the cathodic peak $E_{p_{c1}}$ at -0.23V/Ag-AgCl. The higher current in the first cycle may be

due the reduction of some O_2 molecules adsorbed on the modified electrode. In the presence of H_2O_2 , the current stabilized also rapidly, showing that the M-T coating on the PGE surface is relatively stable. The appearance of the second cathodic peak (E_{pc2}) seems to be limited by diffusion restrictions through the film which seems to be solved after 2 or 3 cycles.

In order to investigate the recycling performance of the M-T solid mixture, the same M-T-PGE was used to perform the CVs experiment six times in a fresh electrolyte solution under Ar in the presence of 5.0 mM H_2O_2 (**Fig. S11**). The second cathodic peak (E_{pc2}) can be seen after the second use, which is consistent with the above result. Insert shows the evolution of the cathodic current (I_{pc1} and I_{pc2}) as function of the electrode uses confirming the good reproducibility of the electrocatalytic process occurring at the M-T-PGE electrode.

3.5. Comparison between soluble decatungstate with insoluble decatungstate

In order to understand the work of selective catalysis more deeply, this part systematically compares the results of selective oxidation of SPD in soluble decatungstate (NaDT) and insoluble decatungstate (TBADT). **Table 7** shows the SPD selective oxidation reaction parameters in NaDT/Magnetite/ H_2O_2 and M-T/ H_2O_2 system. It is clearly observed that the results of the selective oxidation of SPD, like the rate constant of SPD disappearance ($\times 10^{-3} \text{ min}^{-1}$), the percentage of SPD disappearance (%) and yield of N-SPD formation (%) show no significant difference, when the reaction parameters, such as concentration of decatungstate, Magnetite, H_2O_2 , SPD and pH are the same in abovementioned two systems. In addition, the optimal parameters of reaction show some similarities. For example, the optimal pH for both systems is in a range of 2.5-4.0, and optimal concentration of H_2O_2 is in a range of 5.0 - 20.0

mM. These similarities can let us infer that the two systems have the same reaction mechanism and process.

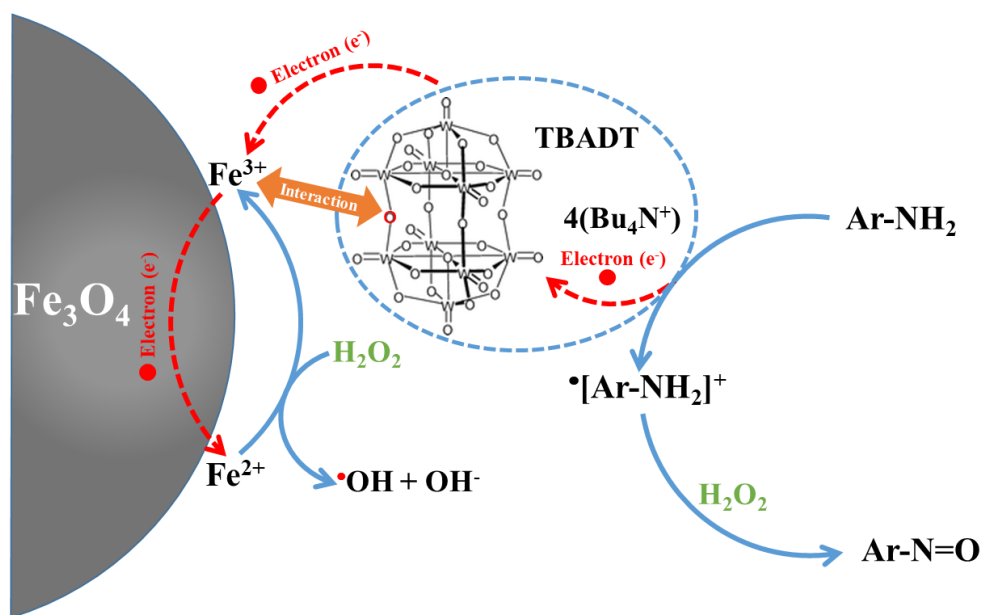
Table 7. Comparison of selective oxidation parameters in soluble and insoluble $W_{10}O_{32}^{4-}$

Parameters	NaDT/Magnetite	M-T ₂₋₁ System
	System	
$[W_{10}O_{32}^{4-}]$ (μ M)	41 (NaDT)	40.2 (TBADT)
$[Magnetite]$ ($g\ L^{-1}$)	0.264	0.266
$[H_2O_2]$ (mM)	5.0	5.0
$[SPD]$ (μ M)	30	30
pH	3.0	3.0
Rate constant of SPD disappearance ($\times 10^{-3}\ min^{-1}$)	11.3	12.0
Percentage of SPD disappearance (%)	75.4	75.8
Yield of N-SPD formation (%)	71.3	73.8

3.6. Mechanistic scheme

The obtained results demonstrate that the oxidation of SPD into N-SPD is efficient at pH lower than 5.0 in M-T/ H_2O_2 system. The rate constant and the percentage of SPD disappearance increase, while the yield of N-SPD formation reach to a plateau, when concentrations of M-T and H_2O_2 increase, while the use of higher concentrations of H_2O_2 is detrimental for the yield of N-SPD formation. The characterization results and CV experiments analysis clearly show that there is an interaction between magnetite and TBADT. The mechanism in M-T/ H_2O_2

system could be explained by an electron transfer from the amine site of sulfapyridine to TBADT giving rise to the formation of the reduced species TBADT^{1-} with the simultaneous formation of the radical cation $[\text{Ar-NH}_2]^{\bullet+}$. The radical cation $[\text{Ar-NH}_2]^{\bullet+}$ further reacts with H_2O_2 to form N-SPD. Owing to the interaction between W and Fe atom, the electron can efficiently transfer to magnetite. At the same time, the Fe^{3+} on the surface become Fe^{2+} , and the regeneration of Fe^{3+} happens in presence of H_2O_2 in the solution. The formation of hydroxyl-sulfapyridine, is clearly a sign for hydroxyl radical formation. This could be produced via a Fenton reaction. The efficiency of the process is mainly owing to the interaction of NaDT with magnetite (**Scheme. 1**).



Scheme 1. Primary aromatic amines to nitroso aromatic compound through a selective oxidation process using M-T complex in the presence of H_2O_2 .

4. Conclusion

The heterogeneous M-T/H₂O₂ system (TBADT-Magnetite-H₂O₂) appears to be a powerful system for an efficient (until 93%) and selective conversion (until 86%) of amine substrates into their nitroso-derivatives. The system consists on a complex material M-T obtained through interaction between magnetite and TBADT as clearly demonstrated by several characterization and CV experiments. This interaction between NaDT and magnetite is without any doubt the driving for the electron transfer to occur. The catalytic system proceeds through an electron transfer process between sulfapyridine and TBADT leading to the formation of the radical cation on the amine group and the reduced species of TBADT. The regeneration of the W₁₀O₃₂⁴⁻ is obtained via a second electron transfer with magnetite owing to the interaction. Thus, during this study we clearly demonstrated that the system M-T/H₂O₂ is an innovative and powerful process with a high yield of transformation (> 86%) for the generation of nitroso compounds from amine group. It could be used and implemented easily for the synthesis of such chemical compounds in different applications.

5. Proposal

1. ESR spectroscopy will be used to identify the •OH radicals.
2. The reuse catalytic experiment will be performed to test the stability of M-T complex.
3. The iron leaching experiment should be performed later.

References

- [1] A.V. Biradar, T.V. Kotbagi, M.K. Dongare, S.B. Umbarkar, Selective N-oxidation of aromatic amines to nitroso derivatives using a molybdenum acetylide oxo-peroxo complex as catalyst, *Tetrahedron Letters*. 49 (2008) 3616–3619. <https://doi.org/10.1016/j.tetlet.2008.04.005>.
- [2] M. Jadidi Nejad, E. Yazdani, M. Kazemi Miraki, A. Heydari, Tungstate-supported silica-coated magnetite nanoparticles: a novel magnetically recoverable nanocatalyst for green synthesis of nitroso arenes, *Chem. Pap.* 73 (2019) 1575–1583. <https://doi.org/10.1007/s11696-019-00708-x>.
- [3] R.R. Holmes, R.P. Bayer, A Simple Method for the Direct Oxidation of Aromatic Amines to Nitroso Compounds¹, *J. Am. Chem. Soc.* 82 (1960) 3454–3456. <https://doi.org/10.1021/ja01498a054>.
- [4] B.G. Gowenlock, W. Lüttke, Structure and properties of C-nitroso-compounds, *Q. Rev. Chem. Soc.* 12 (1958) 321–340. <https://doi.org/10.1039/QR9581200321>.
- [5] Y. Shiraishi, H. Sakamoto, K. Fujiwara, S. Ichikawa, T. Hirai, Selective Photocatalytic Oxidation of Aniline to Nitrosobenzene by Pt Nanoparticles Supported on TiO₂ under Visible Light Irradiation, *ACS Catal.* 4 (2014) 2418–2425. <https://doi.org/10.1021/cs500447n>.
- [6] M. M. Heravi, N. Ghalavand, E. Hashemi, Hydrogen Peroxide as a Green Oxidant for the Selective Catalytic Oxidation of Benzylic and Heterocyclic Alcohols in Different Media: An Overview, *Chemistry*. 2 (2020) 101–178. <https://doi.org/10.3390/chemistry2010010>.

- [7] P.L. Gkizis, I. Kalara-Lafkioti, D. Varelas, I. Tamiolakis, G.S. Armatas, I.N. Lykakis, Efficient and selective oxidation of aromatic amines into nitrosoarenes catalyzed by supported polyoxometalates., *Biointerface Research in Applied Chemistry*. 4 (2014) 857–860.
- [8] V. Conte, B. Floris, Vanadium and molybdenum peroxides: synthesis and catalytic activity in oxidation reactions, *Dalton Trans.* 40 (2011) 1419–1436. <https://doi.org/10.1039/C0DT00706D>.
- [9] K. Krohn, Zirconium Alkoxide Catalyzed Oxidation of Phenols, Alcohols, and Amines, *Synthesis*. 1997 (1997) 1115–1127. <https://doi.org/10.1055/s-1997-1333>.
- [10] S. Fountoulaki, P.L. Gkizis, T.S. Symeonidis, E. Kaminioti, A. Karina, I. Tamiolakis, G.S. Armatas, I.N. Lykakis, Titania-Supported Gold Nanoparticles Catalyze the Selective Oxidation of Amines into Nitroso Compounds in the Presence of Hydrogen Peroxide, *Advanced Synthesis & Catalysis*. 358 (2016) 1500–1508. <https://doi.org/10.1002/adsc.201500957>.
- [11] D. Zhao, M. Johansson, J.-E. Bäckvall, In Situ Generation of Nitroso Compounds from Catalytic Hydrogen Peroxide Oxidation of Primary Aromatic Amines and Their One-Pot Use in Hetero-Diels–Alder Reactions, *European Journal of Organic Chemistry*. 2007 (2007) 4431–4436. <https://doi.org/10.1002/ejoc.200700368>.
- [12] B. Yang, Z. Fu, A. Su, J. She, M. Chen, S. Tang, W. Hu, C. Zhang, Y. Liu, Influence of tetraalkylammonium cations on quality of decatungstate and its photocatalytic property in visible light-triggered selective oxidation of organic compounds by dioxygens, *Applied*

- Catalysis B: Environmental. 242 (2019) 249–257.
<https://doi.org/10.1016/j.apcatb.2018.09.099>.
- [13] M.D. Tzirakis, I.N. Lykakis, G.D. Panagiotou, K. Bourikas, A. Lycourghiotis, C. Kordulis, M. Orfanopoulos, Decatungstate catalyst supported on silica and γ -alumina: Efficient photocatalytic oxidation of benzyl alcohols, *Journal of Catalysis*. 252 (2007) 178–189.
<https://doi.org/10.1016/j.jcat.2007.09.023>.
- [14] A. Molinari, A. Bratovcic, G. Magnacca, A. Maldotti, Matrix effects on the photocatalytic oxidation of alcohols by $[\text{nBu}_4\text{N}]_4\text{W}_{10}\text{O}_{32}$ incorporated into sol–gel silica, *Dalton Trans.* 39 (2010) 7826–7833. <https://doi.org/10.1039/C003282D>.
- [15] L. Ni, J. Ni, Y. Lv, P. Yang, Y. Cao, Photooxygenation of hydrocarbons over efficient and reusable decatungstate heterogenized on hydrophobically-modified mesoporous silica, *Chem. Commun.* (2009) 2171–2173. <https://doi.org/10.1039/B821987G>.
- [16] E. Fornal, C. Giannotti, Photocatalyzed oxidation of cyclohexane with heterogenized decatungstate, *Journal of Photochemistry and Photobiology A: Chemistry*. 188 (2007) 279–286. <https://doi.org/10.1016/j.jphotochem.2006.12.023>.
- [17] M. Carraro, M. Gardan, G. Scorrano, E. Drioli, E. Fontananova, M. Bonchio, Solvent-free, heterogeneous photooxygenation of hydrocarbons by Hyflon® membranes embedding a fluorine-tagged decatungstate, *Chem. Commun.* (2006) 4533–4535.
<https://doi.org/10.1039/B610551C>.
- [18] M.B. Gawande, P.S. Branco, R.S. Varma, Nano-magnetite (Fe_3O_4) as a support for recyclable catalysts in the development of sustainable methodologies, *Chem. Soc. Rev.* 42 (2013) 3371–3393. <https://doi.org/10.1039/C3CS35480F>.

- [19] H. Wang, Z. Qu, S. Dong, H. Xie, C. Tang, Superior Performance of $\text{Fe}_{1-x}\text{W}_x\text{O}_8$ for the Selective Catalytic Reduction of NO_x with NH_3 : Interaction between Fe and W, *Environ. Sci. Technol.* 50 (2016) 13511–13519. <https://doi.org/10.1021/acs.est.6b03589>.
- [20] S. Rakshit, B. Sallman, A. Davantés, G. Lefèvre, Tungstate (VI) sorption on hematite: An in situ ATR-FTIR probe on the mechanism, *Chemosphere.* 168 (2017) 685–691. <https://doi.org/10.1016/j.chemosphere.2016.11.007>.
- [21] B. Sallman, S. Rakshit, G. Lefèvre, Influence of phosphate on tungstate sorption on hematite: A macroscopic and spectroscopic evaluation of the mechanism, *Chemosphere.* 213 (2018) 596–601. <https://doi.org/10.1016/j.chemosphere.2018.09.157>.
- [22] H. Li, X. Jiang, W. Zhu, J. Lu, H. Shu, Y. Yan, Deep Oxidative Desulfurization of Fuel Oils Catalyzed by Decatungstates in the Ionic Liquid of $[\text{Bmim}]\text{PF}_6$, *Ind. Eng. Chem. Res.* 48 (2009) 9034–9039. <https://doi.org/10.1021/ie900754f>.
- [23] W. Huang, M. Luo, C. Wei, Y. Wang, K. Hanna, G. Mailhot, Enhanced heterogeneous photo-Fenton process modified by magnetite and EDDS: BPA degradation, *Environmental Science and Pollution Research.* 24 (2017) 10421–10429. <https://doi.org/10.1007/s11356-017-8728-8>.
- [24] H. Liu, Q. Chen, X. Cheng, Y. Wang, Y. Zhang, G. Fan, Sustainable and scalable in-situ fabrication of Au nanoparticles and Fe_3O_4 hybrids as highly efficient electrocatalysts for the enzyme-free sensing of H_2O_2 in neutral and basic solutions, *Sensors and Actuators B: Chemical.* 314 (2020) 128067. <https://doi.org/10.1016/j.snb.2020.128067>.

- [25] F. Bigi, A. Corradini, C. Quarantelli, G. Sartori, Silica-bound decatungstates as heterogeneous catalysts for H₂O₂ activation in selective sulfide oxidation, *Journal of Catalysis*. 250 (2007) 222–230. <https://doi.org/10.1016/j.jcat.2007.06.019>.
- [26] A. Su, M. Chen, Z. Fu, B. Yang, J. She, F. Wan, C. Zhang, Y. Liu, Hybridizing engineering strategy of non-lacunary (nBu₄N)₄W₁₀O₃₂ by carbon quantum dot with remarkably enhanced visible-light-catalytic oxidation performance, *Applied Catalysis A: General*. 587 (2019) 117261. <https://doi.org/10.1016/j.apcata.2019.117261>.
- [27] S.C. Termes, M.T. Pope, Reduction of the decatungstate anion in nonaqueous solution and its confirmation as “polytungstate-Y,” *Inorg. Chem.* 17 (1978) 500–501. <https://doi.org/10.1021/ic50180a064>.
- [28] K. Nomiya, Y. Sugie, K. Amimoto, M. Miwa, Charge-transfer absorption spectra of some tungsten(VI) and molybdenum(VI) polyoxoanions, *Polyhedron*. 6 (1987) 519–524. [https://doi.org/10.1016/S0277-5387\(00\)81018-9](https://doi.org/10.1016/S0277-5387(00)81018-9).
- [29] D.C. Duncan, T.L. Netzel, C.L. Hill, Early-Time Dynamics and Reactivity of Polyoxometalate Excited States. Identification of a Short-Lived LMCT Excited State and a Reactive Long-Lived Charge-Transfer Intermediate following Picosecond Flash Excitation of [W₁₀O₃₂]⁴⁻ in Acetonitrile, *Inorg. Chem.* 34 (1995) 4640–4646. <https://doi.org/10.1021/ic00122a021>.
- [30] P. Cheng, Y. Wang, M. Sarakha, G. Mailhot, Enhancement of the photocatalytic activity of decatungstate, W₁₀O₃₂⁴⁻, for the oxidation of sulfasalazine/sulfapyridine in the presence of hydrogen peroxide, *Journal of Photochemistry and Photobiology A: Chemistry*. 404 (2021) 112890. <https://doi.org/10.1016/j.jphotochem.2020.112890>.

- [31] D. Dondi, A.M. Cardarelli, M. Fagnoni, A. Albini, Photomediated synthesis of β -alkylketones from cycloalkanes, *Tetrahedron*. 62 (2006) 5527–5535. <https://doi.org/10.1016/j.tet.2006.03.028>.
- [32] A. Su, M. Chen, Z. Fu, B. Yang, J. She, F. Wan, C. Zhang, Y. Liu, Hybridizing Engineering Strategy of Decatungstate. 2. Regulated Effect of Doping Transition Metal Ions on Photocatalytic Oxidation Performance of $(n\text{Bu}_4\text{N})_4\text{W}_{10}\text{O}_{32}$, *Inorg. Chem.* 59 (2020) 7520–7530. <https://doi.org/10.1021/acs.inorgchem.0c00390>.
- [33] D. Shi, Z. Ming, Q. Wu, T. Lai, K. Zheng, C. He, J. Zhao, A novel photosensitizing decatungstate-based MOF: Synthesis and photocatalytic oxidation of cyclohexane with molecular oxygen, *Inorganic Chemistry Communications*. 100 (2019) 125–128. <https://doi.org/10.1016/j.inoche.2018.12.024>.
- [34] J. Desilvestro, S. Pons, The cathodic reduction of carbon dioxide in acetonitrile: An electrochemical and infrared spectroelectrochemical study, *Journal of Electroanalytical Chemistry and Interfacial Electrochemistry*. 267 (1989) 207–220. [https://doi.org/10.1016/0022-0728\(89\)80249-9](https://doi.org/10.1016/0022-0728(89)80249-9).
- [35] S. Nasrazadani, A. Raman, The application of infrared spectroscopy to the study of rust systems—II. Study of cation deficiency in magnetite (Fe_3O_4) produced during its transformation to maghemite ($\gamma\text{-Fe}_2\text{O}_3$) and hematite ($\alpha\text{-Fe}_2\text{O}_3$), *Corrosion Science*. 34 (1993) 1355–1365. [https://doi.org/10.1016/0010-938X\(93\)90092-U](https://doi.org/10.1016/0010-938X(93)90092-U).
- [36] M. Stoia, R. Istrate, C. Păcurariu, Investigation of magnetite nanoparticles stability in air by thermal analysis and FTIR spectroscopy, *J Therm Anal Calorim.* 125 (2016) 1185–1198. <https://doi.org/10.1007/s10973-016-5393-y>.

- [37] F. Han, L. Ma, Q. Sun, C. Lei, A. Lu, Rationally designed carbon-coated Fe₃O₄ coaxial nanotubes with hierarchical porosity as high-rate anodes for lithium ion batteries, *Nano Research*. 7 (2014) 1706–1717.
- [38] T. Radu, C. Iacovita, D. Benea, R. Turcu, X-Ray Photoelectron Spectroscopic Characterization of Iron Oxide Nanoparticles, *Applied Surface Science*. 405 (2017) 337–343. <https://doi.org/10.1016/j.apsusc.2017.02.002>.
- [39] S. Tiwari, R. Prakash, R.J. Choudhary, D.M. Phase, Oriented growth of Fe₃O₄ thin film on crystalline and amorphous substrates by pulsed laser deposition, *J. Phys. D: Appl. Phys.* 40 (2007) 4943–4947. <https://doi.org/10.1088/0022-3727/40/16/028>.
- [40] T. Yamashita, P. Hayes, Analysis of XPS spectra of Fe²⁺ and Fe³⁺ ions in oxide materials, *Applied Surface Science*. 254 (2008) 2441–2449. <https://doi.org/10.1016/j.apsusc.2007.09.063>.
- [41] F. Márquez, G.M. Herrera, T. Campo, M. Cotto, J. Ducongé, J.M. Sanz, E. Elizalde, Ó. Perales, C. Morant, Preparation of hollow magnetite microspheres and their applications as drugs carriers, *Nanoscale Research Letters*. 7 (2012) 210. <https://doi.org/10.1186/1556-276X-7-210>.
- [42] E. Tanasa, C. Zaharia, I.-C. Radu, V.-A. Surdu, B.S. Vasile, C.-M. Damian, E. Andronescu, Novel Nanocomposites Based on Functionalized Magnetic Nanoparticles and Polyacrylamide: Preparation and Complex Characterization, *Nanomaterials*. 9 (2019) 1384. <https://doi.org/10.3390/nano9101384>.

- [43] I. Moriguchi, J.H. Fendler, Characterization and Electrochromic Properties of Ultrathin Films Self-Assembled from Poly(diallyldimethylammonium) Chloride and Sodium Decatungstate, *Chem. Mater.* 10 (1998) 2205–2211. <https://doi.org/10.1021/cm980127b>.
- [44] A. Kozytskiy, Y.V. Panasyuk, A.M. Mishura, Photocatalytic Monofluorination of Unactivated C(sp³)–H Bonds by N-Fluorobenzenesulfimide Involving the Decatungstate Anion and the Effect of Water Additives on These Reactions, *Theoretical and Experimental Chemistry*. (2018). <https://doi.org/10.1007/s11237-018-9577-3>.
- [45] P.V. Nidheesh, R. Gandhimathi, Trends in electro-Fenton process for water and wastewater treatment: An overview, *Desalination*. 299 (2012) 1–15. <https://doi.org/10.1016/j.desal.2012.05.011>.
- [46] E. Brillas, I. Sirés, M.A. Oturan, Electro-Fenton process and related electrochemical technologies based on Fenton’s reaction chemistry, *Chem Rev.* 109 (2009) 6570–6631. <https://doi.org/10.1021/cr900136g>.
- [47] S. Dong, M. Liu, Electrochemical and electrocatalytic properties of iron(III)-substituted Dawson-type tungstophosphate anion, *Journal of Electroanalytical Chemistry*. 372 (1994) 95–100. [https://doi.org/10.1016/0022-0728\(94\)03288-2](https://doi.org/10.1016/0022-0728(94)03288-2).

Supporting Information

Tetra-n-butylammonium decatungstate supported magnetite nanoparticles: a novel magnetically nano-catalyst for green synthesis of nitroso compound

*Peng Cheng, Mohamed Sarakha, Christine Mousty, Pierre Bonnet and Gilles Mailhot**

Université Clermont Auvergne, CNRS, Clermont Auvergne INP, Institut de Chimie de
Clermont Ferrand (ICCF) UMR 6296, BP 80026, F-63171, Aubière cedex, France

* Corresponding author. E-mail address: Gilles.Mailhot@uca.fr.

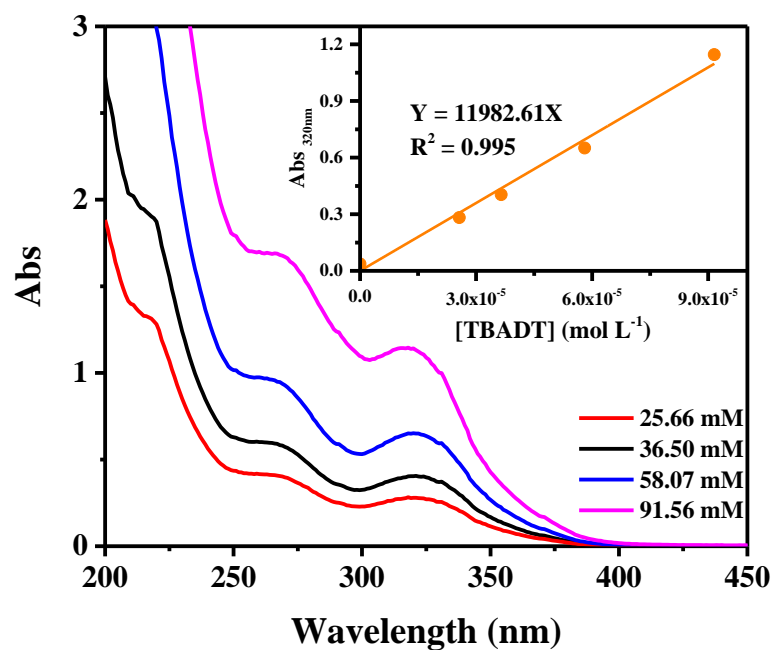


Fig. S1. UV-vis spectra of TABDT at different concentrations. Insert shows the calibration curve of the molar absorption coefficient of TABDT

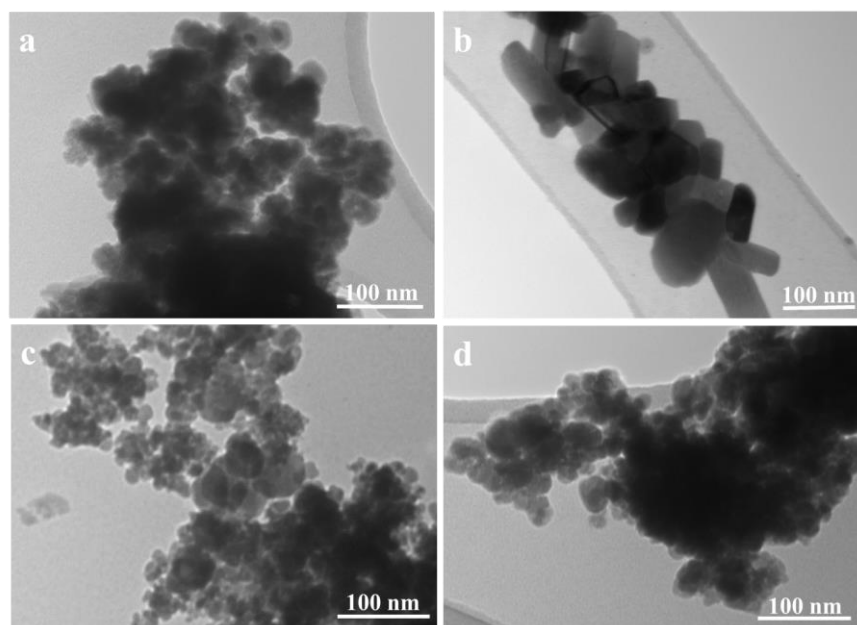


Fig. S2. TEM images of the magnetite (a), TABDT (b) and the M-T complex before (c) and after (d) reaction

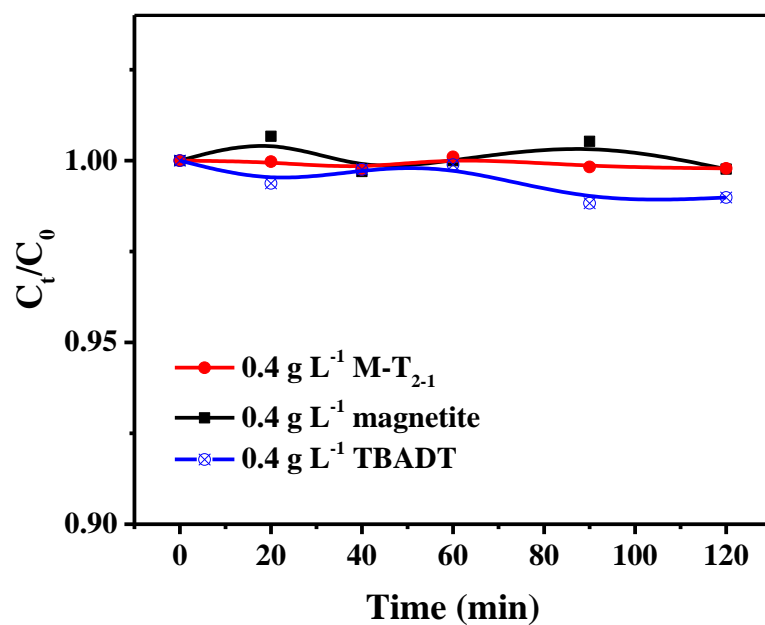


Fig. S3. Adsorption experiments of SPD on TBADT, magnetite and M-T complex. [SPD] = 30 μ M; H₂O₂ = 5.0 mM; pH = 3.0.

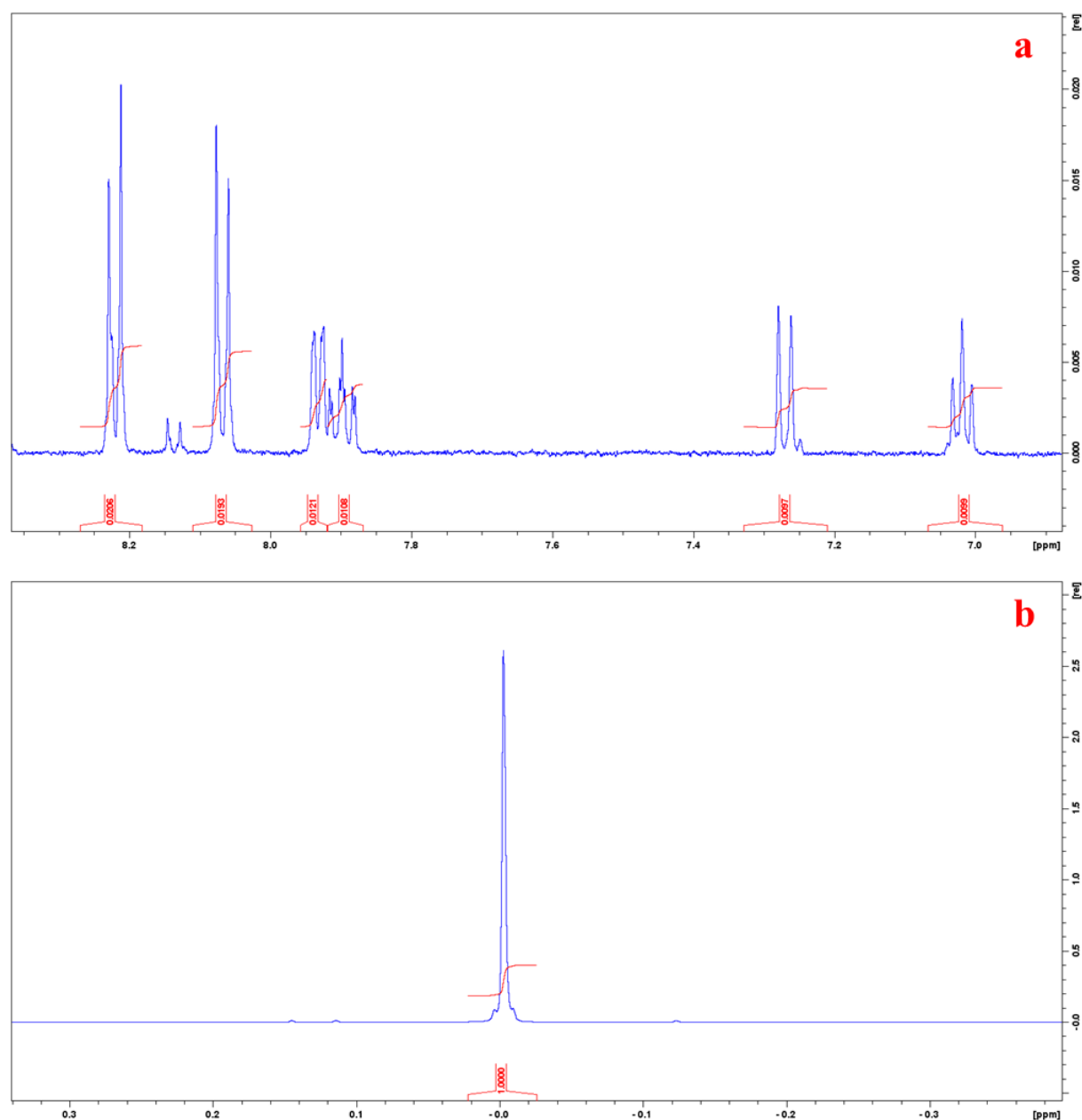


Fig. S4. NMR spectra of N-SPD (a) and TSPd₄ (b)

¹H NMR (500 MHz, D₂O): δ 8.22 ppm (d, J = 8.5 Hz, 2H), 8.06 ppm (d, J = 8.6 Hz, 2H), 7.93 ppm (d, J = 6.2 Hz, 1H), 7.90 ppm (d d d, J = 1.9, 7.3, 9.1 Hz, 1H), 7.27 ppm (d, J = 9.0 Hz, 1H), 7.03 ppm (t, J = 6.7 Hz, 1H). The chemical shifts and Spin coupling constants are consistent with the our previous work [to be published] and Castrejon et.al study [3]. After normalization, the concentration of N-SPD can be obtained according to the NMR peak area.

The concentration of nitroso-sulfapyridine was calculated with the following equation:

$$[\text{N-SPD}] = \frac{9A_0 \times [\text{TSPd}_4]}{b \times A_{\text{ref}}} \times 1.1$$

Where [N-SPD] is the concentration of nitroso-sulfapyridine (N-SPD), A_0 is the area of nitroso-sulfapyridine resonance in the ^1H NMR spectrum, $[\text{TSPd}_4]$ is the concentration of the reference, A_{ref} is the area of reference resonance in the ^1H NMR spectrum, b is the number of protons of N-SPD in the signal integrated, and 9 is the number of protons resonating of TSPd_4 at 0 ppm. The 1.1 factor came from dilution of TSPd_4 . The average concentration of N-SPD calculated after quantification by NMR is 52.03 mM (dropping a sample with a chemical shift of 7.93 ppm), and the relative standard deviation (RSD) is 4.8%.

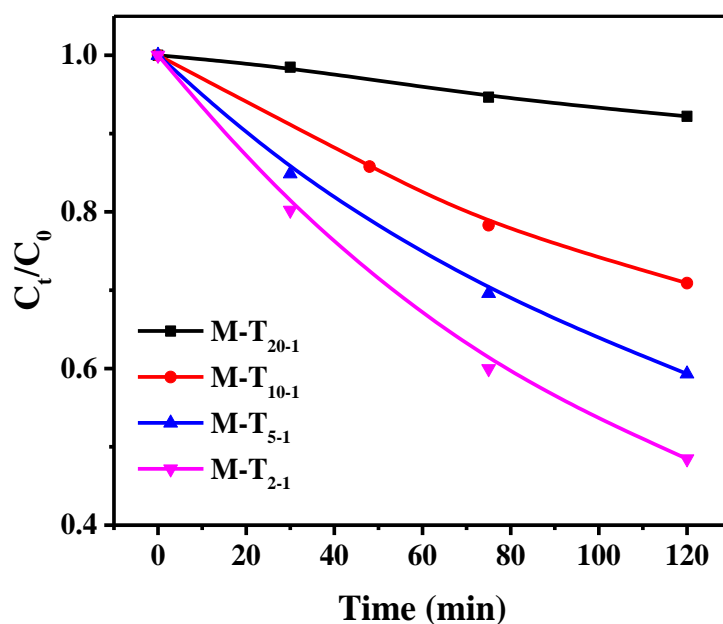


Fig. S5. Effect of the ratio between magnetite and TBADT on the conversion of SPD. [M-T]

= 0.2 g L⁻¹, [H₂O₂] = 5.0 mM; [SPD] = 30 μM; pH = 2.5.

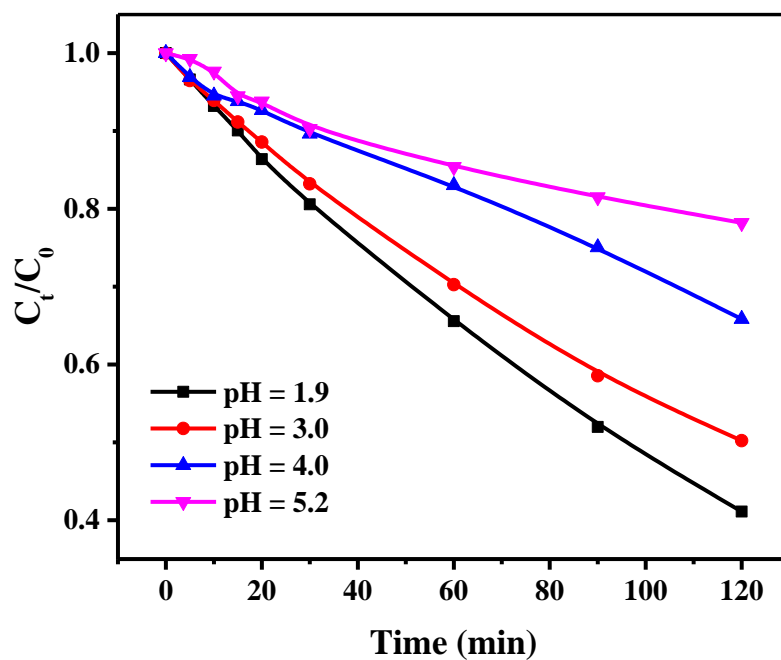


Fig. S6. Effect of pH on the conversion of SPD. $[M-T_{2-1}] = 0.2 \text{ g L}^{-1}$; $[H_2O_2] = 5.0 \text{ mM}$;
 $[SPD] = 30 \text{ mM}$.

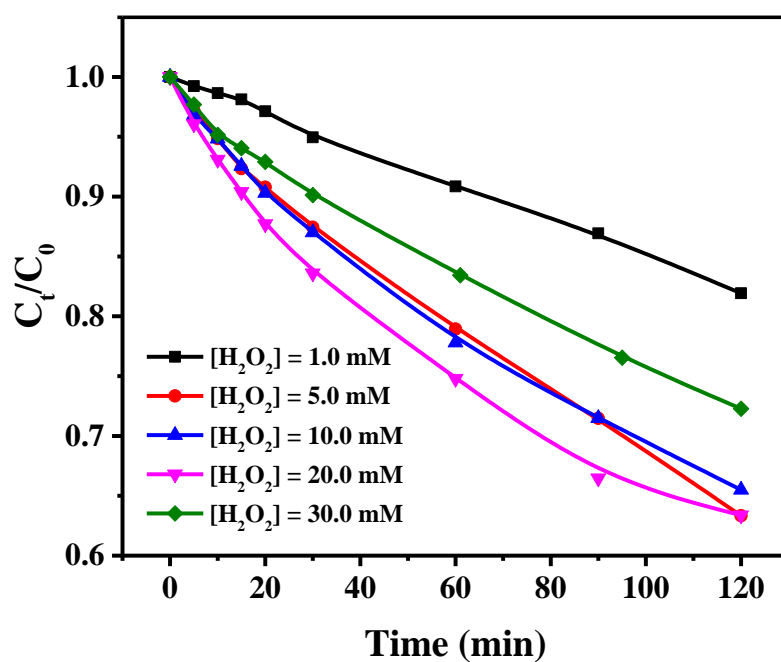


Fig. S7. Effect of hydrogen peroxide concentration on the conversion of SPD. $[M-T_{2-1}] = 0.2 \text{ g L}^{-1}$; $[SPD] = 30 \text{ μM}$; $\text{pH} = 4.0$.

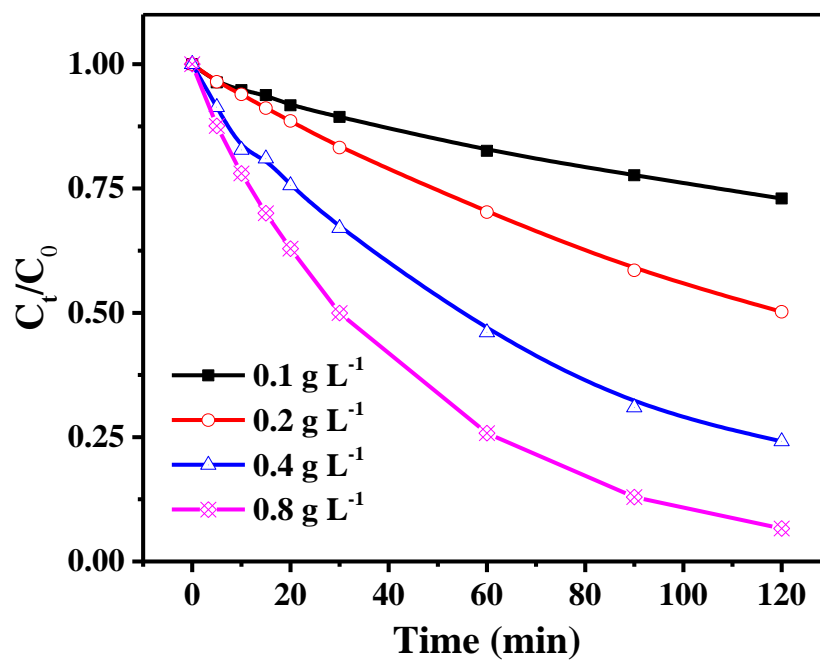


Fig. S8. Effect of the amount of M-T₂₋₁ on the conversion of SPD. [H₂O₂] = 5.0 mM; [SPD] = 30 μM; pH = 3.0.

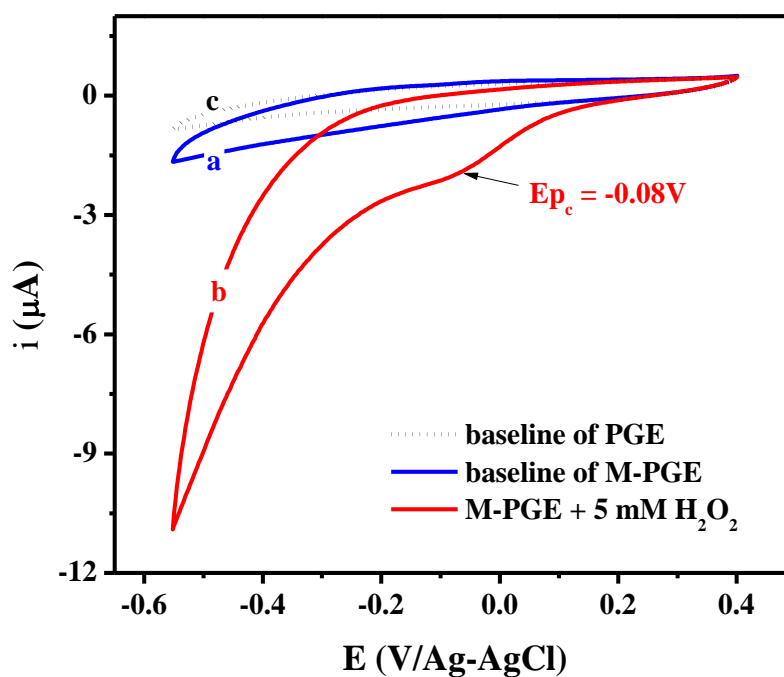


Fig. S9. The CVs of M-PGE in the absence (a) and in the presence (b) of 5 mM H₂O₂ in 0.1 M LiClO₄ (pH = 3.5) under Ar, $v = 10 \text{ mV s}^{-1}$. The dash line (curve c) corresponds to the PGE baseline in 0.1 M LiClO₄ pH 3.5 under Ar.

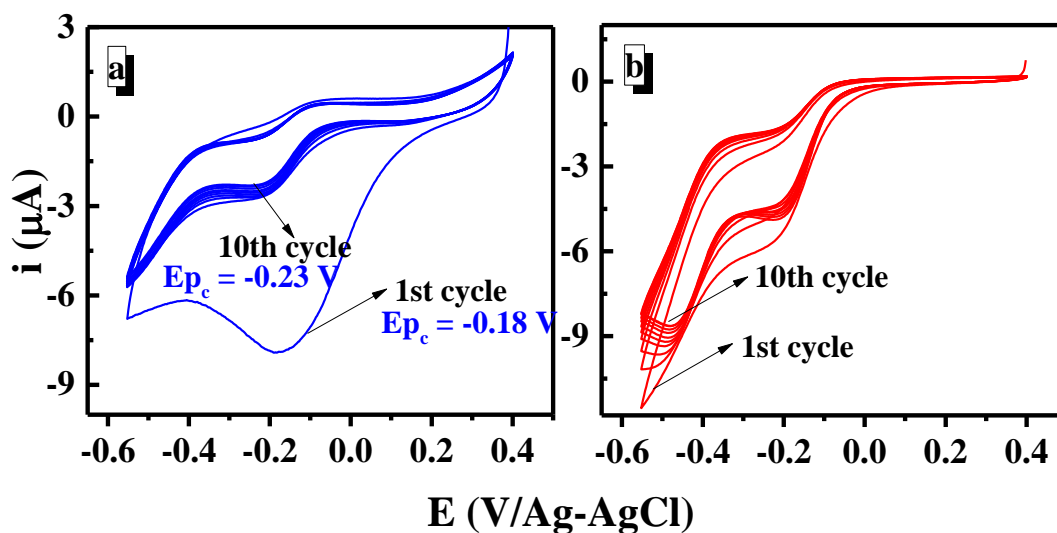


Fig. S10. Ten cycles of CVs of M-T-PGE in the absence (a) and presence of 5mM H_2O_2 (b) in 0.1 M LiClO_4 (pH = 3.5) under Ar, $v = 10$ mV s^{-1} .

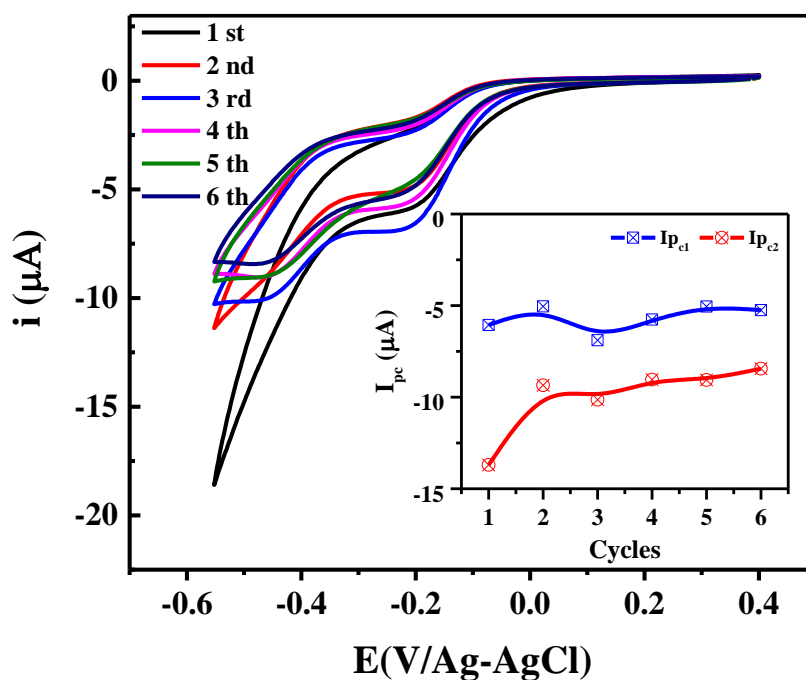


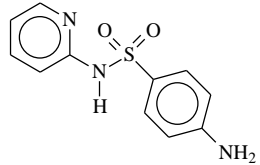
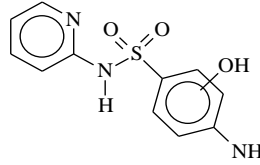
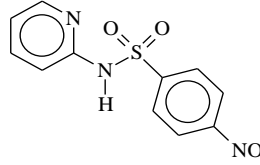
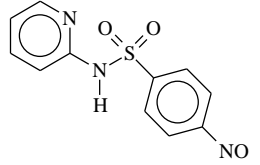
Fig. S11. Six consecutive CVs of M-T-PGE in the presence of 5mM H_2O_2 in 0.1 M LiClO_4 (pH = 3.5) under Ar, $v = 10$ mV s^{-1} . Insert shows the cathodic currents I_{pc1} (\otimes) and I_{pc2} (\boxtimes) at each cycle time.

Table S1. The fitting peak position of W_{4f} in TBADT and M-T complex

Sample	W 4f Peak position (eV)		χ^2
	W 4f _{5/2}	W 4f _{7/2}	
TBADT	37.03	34.92	10.96
M-T (before reaction)	37.01	34.92	3.07
M-T (after reaction)	36.99	34.92	4.78

χ^2 represent chi-square distribution, χ^2 -distribution.

Table S2. MS analysis of SPD products and suggested structures

R-T min	Products	M _{measured} m/z	Molecular formula [M+ H] ⁺	M _{accurate} m/z	Error (ppm)	Chemical structure
5.75	SPD	250.0642	C ₁₁ H ₁₂ O ₂ N ₃ S ⁺	250.0656	-0.935	
5.30	P1	266.0591	C ₁₁ H ₁₂ O ₃ N ₃ S ⁺	266.0605	-1.159	
8.03	P2	280.0384	C ₁₁ H ₁₀ O ₄ N ₃ S ⁺	280.0397	-0.832	
8.11	P3 (N-SPD)	264.0435	C ₁₁ H ₁₀ O ₃ N ₃ S ⁺	264.0448	-1.054	

[M-T₂₋₁] = 0.2 g L⁻¹; [H₂O₂] = 5.0 mM; [SPD] = 30 μM; pH = 4.0.

Table S3. NMR information of N-SPD and TSPD₄

Compound	TSPD ₄			N-SPD			
H number	9	2	2	1	1	1	1
Chemical shift (ppm)	0.00	8.22	8.06	7.93	7.90	7.27	7.03
Normalized sum of integral	1.0000	0.0206	0.0193	0.0121	0.0108	0.0097	0.0099
Concentration(μM)	521.90	53.22	49.86	62.52	55.80	50.12	51.15
Average [N-SPD] (μM)	52.03		RSD (%)		4.8		

Reference

- [1] J.L. Castrejon, S.N. Lavergne, A. El-Sheikh, J. Farrell, J.L. Maggs, S. Sabbani, P.M. O'Neill, B.K. Park, D.J. Naisbitt, Metabolic and Chemical Origins of Cross-Reactive Immunological Reactions to Arylamine Benzenesulfonamides: T-Cell Responses to Hydroxylamine and Nitroso Derivatives, *Chem. Res. Toxicol.* 23 (2010) 184–192.
<https://doi.org/10.1021/tx900329b>.

Chapter 5: Conclusion

In the present Ph.D manuscript, the isopolyoxometalates catalyst decatungstate ($W_{10}O_{32}^{4-}$), soluble sodium decatungstate (NaDT) and insoluble tetra-n-butylammonium decatungstate (TBADT), were synthesized. Their performances in photodegradation (NaDT combined with H_2O_2 or persulfate to degrade antibiotics) and selective oxidation of organic substrate were deeply investigated. NaDT and TBADT combined with magnetite and H_2O_2 to selectively oxidize aromatic amine compounds.

➤ Photocatalytic degradation

Decatungstate (DT) as photocatalyst combining with oxidant (H_2O_2 and PS) can promote the efficiency of antibiotics degradation. The substrate can be oxidized by excited NaDT, simultaneously, the oxidant can be reduced and produce the reactive oxygen species (ROS), which can oxidize substrate as well.

In the first part of this thesis, the combination of $W_{10}O_{32}^{4-}$ and H_2O_2 at pH = 4.0 under UVA irradiation permitted an efficient degradation of the pollutants (sulfasalazine (SSZ) and sulfapyridine (SPD)). Regarding the results, the combination of NaDT and H_2O_2 showed more efficient degradation of SPD and SSZ with an initial rate at $1.6 \times 10^{-7} \text{ mol}^{-1} \text{ L s}^{-1}$ and $7.0 \times 10^{-7} \text{ mol}^{-1} \text{ L s}^{-1}$ in the presence of 1.0 mM H_2O_2 , comparing with the NaDT and H_2O_2 alone. The initial rate and the percentage of substrate disappearance increased with the increase of NaDT concentration and reach to a plateau when the concentration of NaDT, is around 40 μM . When increasing the H_2O_2 concentration, the degradation efficiency increases, detrimental effect of the oxidation process was not observed at higher concentrations. The NaDT/ H_2O_2 /hv degradation system can effectively degrade pollutants in the pH range of 3 to 6, while the initial

rate of SPD and SSZ disappearance decrease when pH value increases. The degradation process involves two ways of reaction for the oxidation of the organic compounds i) an electron transfer reaction with the excited state of decatungstate and ii) also the hydroxyl radical reactivity. $\bullet\text{OH}$ is formed from the Fenton like reaction with the reduced species of decatungstate, $\text{W}_{10}\text{O}_{32}^{5-}$ and H_2O_2 . The latter process represents under our experimental conditions the main process for the disappearance of the pollutants and it is also a way for the regeneration of starting catalyst, decatungstate. The main primary reactions were found to be hydroxylation, desulfurization and scission at the azo group $-\text{N}=\text{N}-$ moiety. For prolonged irradiations, the mineralization of the solution was observed which highlights the point that $\text{W}_{10}\text{O}_{32}^{4-}/\text{H}_2\text{O}_2$ and light represents an interesting AOP's system for water depollution. Indeed, the two possible pathways for the oxidation of organic compounds in this system are important asset for treating polluted waters leading us to the conclusion that this system could be considered in the future as a promising process for the decontamination of water. As a perspective of this work, the immobilization of the photocatalyst decatungstate on solid supports will be a goal in order to recycle the photocatalyst after treatment.

At second part of the thesis, the photochemical conversion of NaDT into its reduced species ($\text{NaDT}^{1-}/\text{NaDT}^{2-}$) was investigated. The NaDT^{1-} and NaDT^{2-} are formed under irradiation in oxygen-free aqueous solution in the presence of methanol with rate of $3.8 \times 10^{-5} \text{ M min}^{-1}$ and $0.3 \times 10^{-5} \text{ M min}^{-1}$, respectively. The molar absorption coefficients (ϵ) of $\text{NaDT}/\text{NaDT}^{1-}/\text{NaDT}^{2-}$ were estimated at 321, 360, 635 and 775nm. Those molar absorption coefficients (ϵ) appear to be of great help for the determination of the concentration of each NaDT species in the solution. These two reduced forms of decatungstate can be oxidized by the

persulfate as observed by the UV-Vis spectroscopy. The combination of $W_{10}O_{32}^{4-}$ and persulfate (PS) under UVA irradiation appears to be more efficient on SPD degradation with a rate constant of $7.7 \times 10^{-2} \text{ min}^{-1}$ in the presence of 2 mM PS, comparing with the NaDT ($5.0 \times 10^{-2} \text{ min}^{-1}$) and PS ($0.3 \times 10^{-2} \text{ min}^{-1}$) alone in the degradation system at pH = 3.

➤ Selective oxidation

DT can also work as catalyst for selective oxidation amine compound into nitroso compound efficiently combining with magnetite and H_2O_2 . The electron transfer from amine compound to DT and magnetite is an important process of the reaction. The interaction between magnetite and DT, which contributes to the acceleration of the electron transfer, was observed. Both soluble (NaDT) and insoluble decatungstate (TBADT) combine with H_2O_2 and magnetite can efficiently oxidize amine compound to nitroso compound with a similar reaction rate and a selectivity of N-SPD formation yield. This illustrates that it could be used and implemented easily for the synthesis of such chemical compounds in different applications.

In the third part of the thesis, the combination of $W_{10}O_{32}^{4-}$, magnetite and H_2O_2 was used as a novel ternary catalytic system to selectively oxidize aromatic amine compounds (sulfapyridine, SPD) into nitroso compounds (nitroso-sulfapyridine, N-SPD). According to the XRD patterns, NaDT and magnetite were successfully synthesized. Regarding the results, the combination of $W_{10}O_{32}^{4-}$, magnetite appears to be more efficient on SPD selective oxidation with a rate constant of $1.13 \times 10^{-2} \text{ min}^{-1}$ in the presence of 5 mM H_2O_2 , when compared with the system NaDT/ H_2O_2 and magnetite/ H_2O_2 . The ternary system (NaDT/ Fe_3O_4 / H_2O_2) appears to be a powerful system for an efficient (up to 97%) and selective conversion (up to 81%) of

amine substrates to their nitroso-derivatives. The system consists on a complex material obtained through interaction between magnetite and decatungstate as clearly demonstrated by FTIR and cyclic voltammetry (CV) experiments. The high efficiency of SPD selective oxidation to N-SPD is due to the interaction between NaDT and magnetite.

The catalytic system proceeds through an electron transfer process between sulfapyridine and NaDT leading to the formation of the radical cation on the amine group and the reduced species of NaDT. The regeneration of the $W_{10}O_{32}^{4-}$ is obtained via a second electron transfer with magnetite owing to the interaction. The magnetite can be reused up to 4 times with high percentage of SPD disappearance and yield of N-SPD formation. Thus, during this study we clearly demonstrated that the system NaDT/Magnetite/ H_2O_2 is an innovative and powerful process with a high yield of transformation for the generation of nitroso compounds from amine group.

In the fourth part of this thesis, a solid decatungstate and magnetite complex (M-T) was synthesized to selectively oxidize the aromatic amine compounds. According to the XRD, the tetra-n-butylammonium decatungstate (TBADT) and magnetite was successfully synthesized. The TBADT-magnetite complex (M-T) was prepared when mixing the both compounds in acetonitrile solution. Characterization (XRD, TEM, SEM-EDS mapping, XPS) shows that the TBADT evenly covers the surface of Magnetite, and the interaction between TBADT and magnetite clearly exists. The M-T was used to selectively oxidize aromatic amine compounds (sulfapyridine, SPD) to form nitroso compounds (nitroso-sulfapyridine, N-SPD) in the presence of H_2O_2 . Regarding the results, 0.2 g L^{-1} M-T is more efficient on SPD selective oxidation with a rate constant of $6.03 \times 10^{-3} \text{ min}^{-1}$ in the presence of $5 \text{ mM } H_2O_2$ at $\text{pH} = 2.5$, comparing with

Conclusion

the TBADT/H₂O₂ and magnetite/H₂O₂. The heterogeneous M-T/H₂O₂ system (TBADT-Magnetite-H₂O₂) appears to be a powerful system for the efficient (until 93%) and selective conversion (until 86%) of amine substrates to their nitroso-derivatives. The system consists on a complex material M-T obtained through interaction between magnetite and TBADT as clearly demonstrated by several characterization and CV experiments. This interaction between TBADT and magnetite is without any doubt the driving force for the electron transfer to occur. The catalytic system proceeds through an electron transfer process between sulfapyridine and TBADT leading to the formation of the radical cation on the amine group and the reduced species of TBADT. The regeneration of the W₁₀O₃₂⁴⁺ is obtained via a second electron transfer with magnetite owing to such interaction. Thus, during this study we clearly demonstrated that the system M-T/H₂O₂ is an innovative and powerful process with a high yield of transformation for the generation of nitroso compounds from amine group.